



HAL
open science

WDM transmission of 400 Gbps and beyond using multi-band OFDM & Nyquist-WDM

Mengdi Song

► **To cite this version:**

Mengdi Song. WDM transmission of 400 Gbps and beyond using multi-band OFDM & Nyquist-WDM. Networking and Internet Architecture [cs.NI]. Télécom ParisTech, 2016. English. NNT : 2016ENST0059 . tel-03701644

HAL Id: tel-03701644

<https://pastel.hal.science/tel-03701644>

Submitted on 22 Jun 2022

HAL is a multi-disciplinary open access archive for the deposit and dissemination of scientific research documents, whether they are published or not. The documents may come from teaching and research institutions in France or abroad, or from public or private research centers.

L'archive ouverte pluridisciplinaire **HAL**, est destinée au dépôt et à la diffusion de documents scientifiques de niveau recherche, publiés ou non, émanant des établissements d'enseignement et de recherche français ou étrangers, des laboratoires publics ou privés.



EDITE – ED 130

THÈSE

pour obtenir le grade de docteur délivré par

Télécom ParisTech
Spécialité « **Communications et Electronique** »

présentée et soutenue publiquement par

Mengdi SONG

le 13 octobre 2016

Transmission WDM à 400 Gbps et au-delà au moyen de modulations multi-bandes OFDM & Nyquist-WDM

Directeurs de thèse : **Yves JAOUEN & Raphaël LE BIDAN**

Co-encadrement : **Erwan PINCEMIN**

Jury

Sergeï TURITSYN, Aston University, United Kingdom
Ioannis TOMKOS, Athens Information Technology, Greece
Juerg LEUTHOLD, ETH Zurich, Switzerland
Antonio NAPOLI, Coriant, Germany
Erwan PINCEMIN, Orange Labs, France
Yves JAOUEN, Telecom ParisTech, France
Raphael LE BIDAN, Telecom Bretagne, France

Rapporteur
Rapporteur
Examineur
Examineur
Examineur
Directeur de thèse
Directeur de thèse

**T
H
È
S
E**

Abstract

In the context of ever increasing traffic demand, future long-haul optical transmission systems will evaluate towards higher capacity and will be able to support more flexible optical networking. In this thesis, we study the potential of multi-band OFDM, which is a credible alternative of the industrial single-carrier solutions for future generations of beyond 100 Gbps systems. After presenting a brief overview of long-haul transmission systems and OFDM digital signal processing techniques, we show the experimental implementation of 16QAM-OFDM as well as its transmission performance. Some implementation constraints of 16QAM-OFDM related to hardware impairments have been investigated. The transmission performance has been compared with that of Nyquist-WDM format. After that, in the context of superchannel and flexible optical networking, we have carried out an experimental proof-of-concept of sub-wavelength optical switching. We have demonstrated the feasibility of such optical add-drop operations inside OFDM and Nyquist-WDM superchannels. At last, we have addressed some short-term research topics that concern telecom companies, such as the potential application scenarios of the low-cost and power-efficient coherent CFP interface based on Silicon photonics integration technology.

Résumé

Avec une croissance soutenue de trafic internet, les futurs systèmes de transmission optique longue-distance vont évoluer vers plus de capacité et d'avantage de flexibilité. Dans ce manuscrit, nous étudions le potentiel des formats OFDM multi-bandes, qui sont une alternative crédible aux solutions industrielles de type mono-porteuse pour les futures générations de systèmes au-delà de 100 Gbps. Nous commençons par une rapide présentation des systèmes de transmission longue distance et des techniques de traitement numérique d'un signal OFDM, suivie par une description de l'implémentation expérimentale d'un signal 16QAM-OFDM ainsi que des performances obtenue en transmission. Les contraintes d'implémentation d'un signal 16QAM-OFDM liées aux imperfections matériel ont été analysées. Les performances en transmission de l'OFDM ont été comparées avec celle du Nyquist-WDM. Par la suite, dans le contexte de superchannel et de réseaux optiques flexibles, nous avons réalisé une démonstration expérimentale du concept de commutation optique sous-longueur d'onde. La faisabilité des fonctions insertion et extraction d'une sous-bande à l'intérieur de superchannels OFDM et Nyquist-WDM a été démontrée. Finalement, nous concluons par des perspectives à court terme susceptible d'intéresser les industriels du domaine, tel que l'étude d'interfaces CFP cohérent, l'intégration photonique sur Silicium apportant des réductions de coût importantes et une faible consommation énergétique.

Acknowledgements

I would like to thank Pr. Sergeï Turitsyn from Aston University and Pr. Ioannis Tomkos from Athens Information Technology Center for accepting to be reporters of my PhD defense. Also I would like to thank Pr. Juerg Leuthold from ETH Zurich and M. Antonio Napoli from Coriant R&D for accepting to be part of my PhD defense committee.

I would like to express my sincere gratitude to my thesis supervisor Erwan Pincemin. I really appreciated the way that you guided me and the large amount of time that you put on my PhD work. I enjoyed the many fruitful discussions. Many thanks for your continuous encouragement.

I am grateful to my thesis co-director Yves Jaouen. Thank you very much for your continuous guide in my PhD work. You were always available. I really appreciated your precious suggestions and advices.

I would like to show my sincere appreciation to the help of my thesis co-director Raphaël Le Bidan. You were always available for my questions and thank you very much for the many valuable answers.

I would like to thank all members of the SOAN team (Synchronization and Optical Agile Network) of Orange Labs, where I worked during three years for my PhD thesis. I enjoyed working in this adorable team. Thanks to all of you for your help.

I would like to thank my family for your love and encouragement. Also I would like to thank Jianghao for your continuous support.

Table of contents

Introduction	1
CHAPTER 1 Long-haul optical transmission systems	3
1.1 Main physical impairments in single-mode fiber	4
1.1.1 Fiber loss	4
1.1.2 Chromatic dispersion	5
1.1.3 Polarization mode dispersion	6
1.1.4 Nonlinear effects	7
1.2 Evolution of long-haul optical transmission systems	8
1.2.1 Intensity-modulation / direct detection-based systems	8
1.2.2 Coherent detection-based systems	9
1.3 Beyond 100 Gbps technologies	9
1.3.1 High order modulation formats	9
1.3.2 Amplification schemes	11
1.3.3 Optical fibers	14
1.3.4 Advanced FEC solutions	15
1.3.5 Nonlinear equalizers	16
1.4 Conclusion	19
CHAPTER 2 OFDM for WDM transmission systems	21
2.1 OFDM principle	22
2.2 Transmitter DSP procedures	24
2.2.1 Frame structure and notations	24
2.2.2 Cyclic prefix	25
2.2.3 Clipping and PAPR reduction	27
2.3 Receiver DSP procedures	28
2.3.1 Time synchronization	29
2.3.2 Frequency synchronization	32
2.3.3 Channel estimation	37
2.3.4 Phase noise compensation	38
2.4 OFDM dimensioning	40
2.4.1 Calculation of overheads	40
2.4.2 Cyclic prefix dimensioning	41
2.4.3 Multi-band approach	42
2.4.4 400 Gbps OFDM dimensioning considering experimental constraints	43

2.5	OFDM variants with improved features	45
2.6	State of art of OFDM transmission experiments	46
2.7	OFDM versus single-carrier formats	47
2.8	Conclusion.....	48
CHAPTER 3 Experimental implementation and performance evaluation of 16QAM-OFDM		49
3.1	Sensitivity to hardware impairments of QPSK- and 16QAM-OFDM	50
3.1.1	Simulation set-up.....	50
3.1.2	Results and discussions	51
3.2	Back-to-back performance of QPSK- and 16QAM-OFDM.....	54
3.2.1	Electrical and optical back-to-back performance	54
3.2.2	CD and PMD tolerance	59
3.2.3	Multi-band OFDM transmitter	61
3.3	Transmission experiments over G.652 and G.655 fibers	62
3.3.1	Experimental set-up.....	62
3.3.2	Results and discussions	63
3.4	Transmission experiments adopting nonlinear mitigation techniques.....	66
3.4.1	Experimental set-up.....	66
3.4.2	Results and discussions	68
3.5	Experimental comparison of OFDM and Nyquist-WDM	70
3.5.1	Experimental set-up.....	70
3.5.2	Signal processing of Nyquist-WDM	71
3.5.3	Experimental results	72
3.6	Conclusion.....	74
CHAPTER 4 Towards flexible optical transport networks: OFDM sub-wavelength optical switching		75
4.1	Context and motivation	76
4.2	Concept of sub-wavelength optical switching.....	77
4.3	Sub-wavelength optical switching inside 100 Gbps MB-OFDM.....	79
4.3.1	Structure of sub-wavelength OADM.....	80
4.3.2	Back-to-back characterization	80
4.3.3	Straight-line transmission	82
4.3.4	Cascadability of the sub-wavelength OADM.....	84
4.4	Sub-wavelength optical switching inside 1 Tbps MB-OFDM & Nyquist-WDM superchannel.....	87
4.4.1	Structure of the FOX-C node.....	87

4.4.2	Back-to-back characterization	89
4.4.3	Straight-line Transmission.....	92
4.4.4	Cascadability of sub-wavelength OADM.....	95
4.5	Conclusion.....	97
CHAPTER 5 Next generations of ultra-high bit rate transceivers and technologies.....		99
5.1	100 Gbps digital coherent CFP interface for short reach, regional, and ultra-long-haul optical communications.....	101
5.1.1	100 Gbps digital coherent CFP module.....	101
5.1.2	Passive interconnection of distant NE.....	102
5.1.3	100 Gbps up-grade of metro-regional 10 Gbps WDM systems	103
5.1.4	Full 100 Gbps ULH WDM transmission.....	104
5.2	Performance comparison of G.657.A2 and G.652.D fibers	106
5.2.1	G.657.A2 versus G.652.D fibers	106
5.2.2	Experimental set-up.....	107
5.2.3	Results and discussion.....	108
5.3	400 Gbps real-time coherent Nyquist-WDM DP-16QAM transmission over legacy G.652 or G.655 fiber infrastructure with 2 dB margins	110
5.3.1	Experimental setup.....	110
5.3.2	Back-to-back characterization, transmission performances and discussions	111
5.4	Conclusion.....	114
Conclusions and perspectives.....		115
Conclusions		115
Perspectives		116
Appendix		119
References		125
Publications		133

List of abbreviations

A

ADC	Analog to Digital Convertor
ARPU	Average Revenue Per User
ASE	Amplified Spontaneous Emission
AWG	Arbitrary Waveform Generator
AWGN	Additive White Gaussian Noise

B

BER	Bit Error Rate
BERT	BER Tester
BtB	Back-to-Back

C

CAUI	100G Attachment Unit Interface
CD	Chromatic Dispersion
CFO	Carrier Frequency Offset
CFP	C-form Factor Pluggable
CMA	Constant Modulus Algorithm
CMZM	Complex Mach-Zehnder Modulator
CP	Cyclic Prefix
CPE	Common Phase Error

D

DAC	Digital to Analog Convertor
DBP	Digital Back-Propagation
DCF	Dispersion Compensation Fiber
DCO-CFP	Digital COherent CFP
DD-LMS	Decision-Directed Least Mean Square
DFT	Discrete Fourier Transform
DGD	Differential Group Delay
DGE	Dynamic Gain Equalizer
DP	Dual-Polarization
DPO	Digital Phosphor Oscilloscope
DP-QPSK	Dual Polarization QPSK
DRS	Double Rayleigh Scattering
DSF	Dispersion-Shifted Fiber
DSP	Digital Signal Processing
DVB	Digital Video Broadcasting

E

ECL	External Cavity Laser
EDFA	Erbium-Doped Fiber Amplifier
ENOB	Effective Number Of Bits
EON	Elastic Optical Networking

F

FDE	Frequency Domain Equalizer
FEC	Forward Error Correction
FFT	Fast Fourier Transform
FOPMD	First-Order PMD
FPC	Fiber Polarization Controller
FTTH	Fiber-To-The-Home
FWM	Four Wave Mixing

G

GB	Guard-Band
GbE	GbEthernet
GVD	Group Velocity Dispersion

H

HD-FEC	Hard-Decision FEC
HSR	High Spectral Resolution

I

I	In-phase
ICI	Inter-Carrier Interference
IDFT	Inverse Discrete Fourier Transform
IFFT	Inverse Fast Fourier Transform
IM/DD	Intensity Modulation Direct Detection
ISI	Inter-Symbol Interference
ITU	International Telecommunication Union
IVSTF-NLE	Inverse Volterra Series Transfer Function NonLinear Equalizer

J

K

L

LCoS	Liquid Crystals on Silicon
LDPC	Low-Density Parity-Check
LEAF	Large Effective Area Fiber
LO	Local Oscillator
LPF	Low Pass Filter
LTE	Long-Term Evolution

M

MB-OFDM	Multi-Band OFDM
MCF	Multi-Core Fiber
MI	Modulation Index
MIMO	Multiple-Input Multiple-Output
MLSE	Maximum Likelihood Sequence Estimation
MMF	Multi-Mode Fiber
MPI	Multiple-Path Interference
MSA	Multi-Source Agreement
MSE	Mean Squared Error

N

NCG	Net Coding Gain
NE	Network Element
NF	Noise Figure
NLSE	NonLinear Schrodinger Equation
NRZ-OOK	Non-Return-to-Zero On-Off-Keying
N-WDM	Nyquist-Wavelength Division Multiplexing
NZDSF	Non-Zero Dispersion Shifted Fiber

O

ODL	Optical Delay Line
OFDM	Orthogonal Frequency Division Multiplexing
Offset-QAM	Offset-Quadrature Amplitude Modulation
OIF	Optical Internetworking Forum
OLT	Optical Line Terminal
ONU	Optical Network Unit
OPBF	Optical Pass-Band Filter
OSA	Optical Spectrum Analyzer
OSBF	Optical Stop-Band Filter
OSNR	Optical Signal-to-Noise Ratio
OXC	Optical Cross-Connect

P

PAPR	Peak-to-Average Power Ratio
------	-----------------------------

PBC	Polarization Beam Combiner
PBS	Polarization Beam Splitter
PDG	Polarization-Dependent Gain
PDM	Polarization Division Multiplexing
PM	Polarization-Maintaining
PMD	Polarization Mode Dispersion
PRBS	Pseudo-Random Bit Sequence
PS	Polarization Scrambler
PSP	Principle State of Polarization
PSR	Pilot-to-Signal Ratio

Q

Q	Quadrature
QAM	Quadrature Amplitude Modulation
QPSK	Quadrature Phase-Shift Keying

R

RDE	Radius-Directed Equalization
RF	Radio-Frequency
RGI-OFDM	Reduced-Guard-Interval OFDM
ROADM	Reconfigurable Optical Add-Drop Multiplexer
ROPA	Remote Optically Pumped Amplifier

S

Sb-Ch	Sub-Channel
SD-FEC	Soft-Decision FEC
SDM	Spatial-Division Multiplexing
SE	Spectral Efficiency
SER	Symbol Error Rate
SNR	Signal-to-Noise Ratio
SOP	State-Of-Polarization
SOPC	Simple Odd Parity Code
SOPMD	Second-Order PMD
SP	Single-polarization
Sp-Ch	Super-Channel
SPM	Self-Phase Modulation
SpS	Samples per Symbol
SPS	Synchronous Polarization Scrambler
SRS	Stimulated Raman Scattering
SSF	Split-Step Fourier method
SSMF	Standard Single Mode Fiber

T

TPC Turbo Product Code

U

ULH Ultra-Long-Haul
ULL-LAF Ultra-Low Loss Large effective Area Fiber

V

VOA Variable Optical Attenuator
VPI-TM VPI Transmission Maker

W

WDM Wavelength Division Multiplexing
WSS Wavelength Selective Switch

X

XPM Cross-Phase Modulation
XPoIM Cross-Polarization Modulation

Y

Z

ZGI-OFDM Zero-Guard-Interval OFDM

INTRODUCTION

Optical fiber systems play an important role in modern communication networks. The characteristics of optical fiber make it the most suited transmission media for long-haul high bit rate communications. Since its introduction in the 1970's, the capacity of optical fiber systems has dramatically increased thanks to various technology breakthroughs. The invention of EDFA makes long-haul transmission possible without the need of expensive periodic electrical regeneration. The large amplification window of EDFA enables the introduction of wavelength division multiplexing (WDM), allowing the transmission of 80 channels in one optical fiber and 10 Gbps NRZ-OOK signals in each channel in the 1990's. The application of coherent detection in optical systems is another major breakthrough, permitting the use multilevel modulation formats, polarization multiplexed signal and digital signal processing techniques. The 100 Gbps coherent DP-QPSK systems deployed on a 50-GHz grid WDM infrastructure began to be deployed since 2012. They are capable of offering long-haul reach of ~2000 km and providing ten times of data rate capacity with respect to 10 Gbps NRZ-OOK systems.

Due to the ever growing traffic demands, capacity increase over optical systems is still required. According to Cisco visual networking index [1], the global IP traffic will increase nearly threefold between 2015 and 2020. The next generation of long-haul optical systems will target a per channel bit rate of 400 Gbps or 1 Tbps or even higher. The use of high order modulation formats, such as 16-QAM, is a way of increasing the spectral efficiency, but at the expense of transmission reach. To avoid the expensive electrical regeneration, the long-haul reach of a transmission system is very important for telecom operators. The performance of a high bit rate signal could be further improved through the upgrade of optical fiber infrastructure (such as novel optical fibers and hybrid amplification schemes) or more powerful digital signal processing techniques (such as advanced forward error correction algorithms and nonlinear mitigation techniques).

Besides single-carrier modulation formats, coherent orthogonal frequency division multiplexing (OFDM) began to draw attention since the arrival of coherent detection and the possibility of performing digital signal processing in transmitter and receiver. It has been proven to have equivalent transmission performance with respect to single-carrier formats. OFDM format presents several interesting characteristics. OFDM signal has intrinsically quasi-rectangular spectrum. Adjacent channels can be placed close to each other without generating serious spectral crosstalk, permitting a high spectral efficiency. Thanks to the insertion of cyclic prefix, CD and PMD can be compensated with very low computational complexity through single tap equalizer. OFDM also allows an easy implementation of space-time coding techniques capable of mitigating polarization dependent loss (PDL). In addition, OFDM signal is composed of a large number of individually modulated subcarriers. Bit and power loading can be realized on each subcarrier in case of performance nonhomogeneity, for example due to optical filtering effect.

Due to the bandwidth limitation of electrical and optical components, the future 400 Gbps or 1 Tbps capacity can no longer be carried by one single channel. "Superchannel", composed of a number of low bit rate sub-channels, becomes a promising approach to cope with the

demand of ultra-high bit rate. The 50-GHz fixed grid will be replaced by flex grid granularity. Future optical superchannels will be elastic, capable of adapting the superchannel capacity to the traffic demand variable over time. OFDM and Nyquist-WDM are two promising candidates for this future flexible high capacity optical network.

In this thesis, we intend to investigate the potential of OFDM in the context of superchannel and flexible optical networking. We have first investigated the performance of 400 Gbps and 1 Tbps 16QAM-OFDM in various configurations, and compared to that of Nyquist-WDM. We have then carried out a novel study of sub-wavelength optical switching through experimental proof-of-concept, intending to offer a more flexible optical network by exploiting the intrinsically rectangular-like spectral shape of OFDM. We have also studied some short-term research topics that concern telecom operators using real-time interfaces.

Chapter 1: provides an overview of long-haul optical transmission systems. We start by introducing the main physical impairments of single-mode optical fiber. We then describe the evolution of the currently deployed WDM transmission systems and beyond 100 Gbps technologies.

Chapter 2: gives an overview of OFDM technique for long-haul optical transmission systems. We present transmitter & receiver DSP algorithms, dimensioning of OFDM signal, OFDM formats with improved features, state-of-art of OFDM transmission experiments as well as comparisons with single-carrier techniques.

Chapter 3: studies the experimental implementation of 16QAM-OFDM. We present the sensitivity of 16QAM-OFDM to practical hardware impairments, back-to-back performance, tolerance to CD and PMD, transmission performance over two types of fibers, performance of nonlinear mitigation techniques and experimental comparisons with 16QAM-Nyquist-WDM.

Chapter 4: studies the feasibility of sub-wavelength optical switching inside OFDM and Nyquist-WDM superchannel. We present the structure of sub-wavelength add/drop node, the optimization of optical bandpass and bandstop filter bandwidths, and the cascability of sub-wavelength optical add/drops inside QPSK and 16-QAM modulated superchannels.

Chapter 5: focuses on short-term research topics that concern telecom operators. We present the performance of 100 Gbps digital coherent CFP based on Silicon photonics technologies, the capacity of ITU-T G.657.A2 fiber to address long-haul transmission, and the performance of 400 Gbps coherent dual-carrier DP-16QAM real-time interface.

CHAPTER 1

LONG-HAUL OPTICAL TRANSMISSION SYSTEMS

This chapter is an overview of long-haul optical transmission systems. We will start by introducing the main physical impairments of single-mode optical fiber. We will then describe the evolution of long-haul transmission systems with a focus on two detection techniques: direct detection and coherent detection. At last, we will discuss about beyond 100 Gbps technologies: high order modulation formats as well as hardware and signal processing improvements.

1.1 Main physical impairments in single-mode fiber

Optical signals suffer from several impairments when propagating along the fiber. We will first describe main linear effects consisting of fiber loss, chromatic dispersion (CD) and polarization mode dispersion (PMD). The principal nonlinear phenomenon: Kerr effect will also be briefly introduced.

1.1.1 Fiber loss

An important fiber parameter is the power loss during signal propagation inside the fiber. The signal power $P(z)$ at the output of the fiber can be expressed as

$$P(z) = P(0)\exp(-\alpha z) \quad \text{Eq. 1-1}$$

where $P(0)$ is the signal power at the input of the fiber, z is the fiber length and α is the fiber loss coefficient in neper/m. The fiber loss coefficient is usually expressed in dB/km with the relation of 1 neper/m = 8686 dB/km.

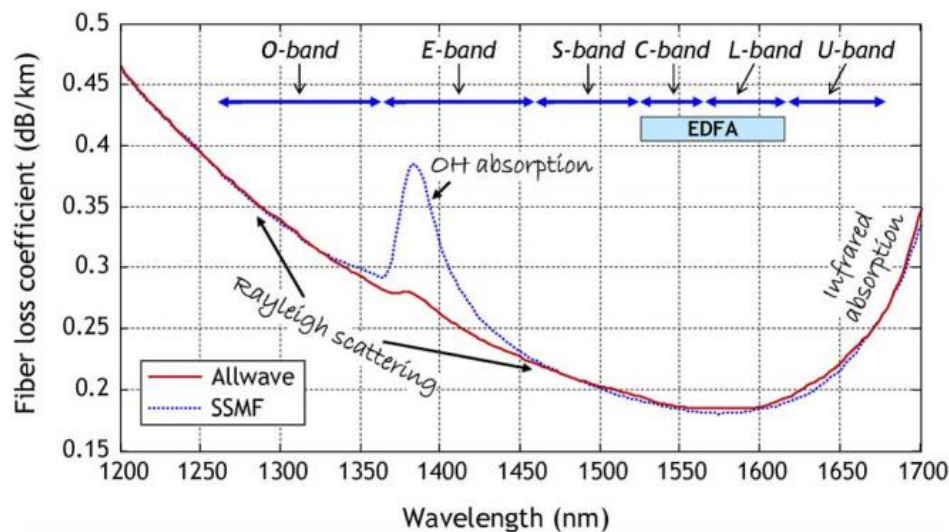


Figure 1-1: Spectral dependence of the fiber loss coefficient for standard single-mode fiber (SSMF) and a fiber without the water absorption peak (Allwave). [2]

The fiber loss depends on the signal wavelength as depicted in Fig. 1-1. The main sources governing the attenuation profile are Rayleigh scattering and absorption of the material. Rayleigh scattering arises from density fluctuations frozen into the fused silica during manufacture. Resulting local fluctuations in the refractive index scatter light in all directions. It affects short wavelengths more than long ones in the near infrared region (1200-1715 nm). Besides Rayleigh scattering, the absorption of silica glass, strong at long fiber wavelengths as well as the presence of impurities also contribute to fiber loss. The OH absorption is

responsible for the peak at 1380 nm shown in Fig. 1-1 over SSMF. The OH peak can be eliminated in current fiber manufacturing.

The wavelengths with moderate fiber loss (from 1300 to 1700 nm) are considered usable for long distance transmission. In practical implementations, the usable bandwidth is limited by the bandwidth of amplification technologies. Erbium doped fiber amplifiers (EDFA) cover C-band and L-band, which coincide with the minimum fiber loss wavelength zones.

1.1.2 Chromatic dispersion

Chromatic dispersion (CD) represents the fact that different colors or wavelengths travel at different velocities in optical fiber. The total dispersion is essentially the combination of material dispersion and waveguide dispersion. Material dispersion is caused by variations of refractive index of the fiber material with respect to wavelength. Waveguide dispersion refers to differences in the signal speed depending on the distribution of the optical power over the core and cladding of the optical fiber. When the wavelength of the optical signal increases, more signal will be carried by the cladding, which has a different refractive index with respect to the fiber core.

The effect of fiber dispersion is accounted by expanding the propagation constant β into a Taylor series around the central frequency ω_0

$$\beta(\omega) = n(\omega) \frac{\omega}{c} = \beta_0 + \beta_1(\omega - \omega_0) + \frac{1}{2}\beta_2(\omega - \omega_0)^2 + \dots \quad \text{Eq. 1-2}$$

where $n(\omega)$ is the refractive index and c is the velocity of light in vacuum. The propagation constant β , also named as phase constant, represents the change of phase per unit length along the path travelled by the wave at any instant. The coefficient β_0 is a constant phase shift and β_1 is the inverse of the group velocity ($\beta_1 = 1/V_g$), or in other words the group delay per unit length. The second derivative, β_2 , is responsible for CD and is called the group velocity dispersion (GVD) parameter. The most commonly used parameter to indicate the amount of dispersion in fiber is the dispersion parameter D , defined as the variation of the group delay per unit length with the wavelength. It is related to β_2 by the relation

$$D = \frac{d\beta_1}{d\lambda} = -\frac{2\pi c}{\lambda^2} \beta_2 \quad \text{Eq. 1-3}$$

Fig. 1-2 shows the dispersion profile along the wavelength for the international telecommunication union (ITU) G.652 standard single mode fiber (SSMF), which is the most widely deployed fiber for long-haul application, as well as the profile of its two contributors: material dispersion and waveguide dispersion. The zero dispersion falls on the wavelength of ~1310 nm. It has a D of ~17 ps/(nm·km) at the wavelength of 1550 nm.

CD causes pulse broadening and leads to inter-symbol interference (ISI). In legacy 10 Gbps non-return-to-zero on-off-keying (NRZ-OOK) systems with intensity modulation direct detection (IM/DD), CD is managed by inserting dispersion compensation fiber (DCF) with a negative dispersion coefficient after each fiber span. Another approach is to change the dispersion profile of the fiber. Dispersion-shifted fiber (DSF) with zero dispersion at 1550 nm is defined in ITU G.653. The manufacturing of DSF can be realized by modifying the refractive index of the core. However, zero dispersion fiber is very sensitive to the nonlinear effect of four-wave mixing (FWM), making it unsuitable for WDM transmission. The non-

zero dispersion shifted fiber (NZDSF) defined in ITU G.655 shifts the zero dispersion to around 1510 nm, in order to achieve both low dispersion and lower nonlinear effects with respect to DSF. The dispersion quantities at 1550nm and other characteristics of several NZDSF are given in Table 1-1 in sub-section 1.3.3. With the arrival of coherent detection, the chromatic dispersion, being a quasi-deterministic effect, can be entirely compensated through digital signal processing.

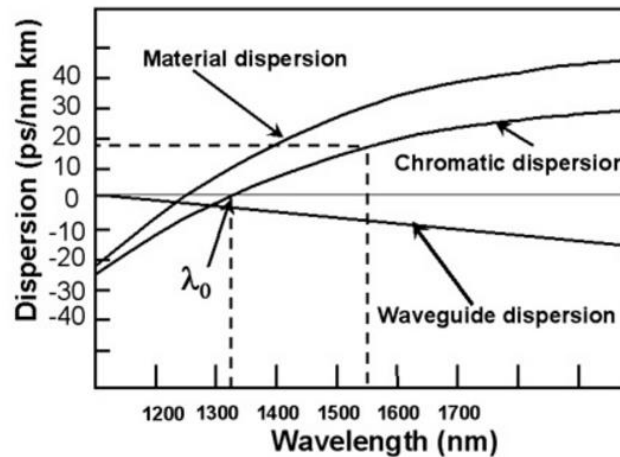


Figure 1-2: Profile of chromatic dispersion of a G.652 SSMF as well its two contributors: material dispersion and waveguide dispersion. [3]

1.1.3 Polarization mode dispersion

A beam of light can be thought of as being composed of two orthogonal polarization modes. In perfectly circular fiber, the two polarization states possess the same propagation characteristics. However, in reality, the imperfections in the waveguide geometry combined with mechanical stress and temperature variations in the field result in birefringence. In a birefringent medium, signals propagating over the two polarization modes experience different refractive index, therefore travel at different group velocity.

Based on [4], there exists two orthogonal principle states of polarization (PSPs). When an optical signal is aligned with one of the PSPs, its output polarization is invariant to first order with changes in frequency, meaning that the spectral components of the output signal all have the same state of polarization. PSPs are also referred to as the fast and slow polarization modes. The fast polarization mode maximizes the group velocity and the slow one minimizes it. The difference in propagation time between two PSPs is named as differential group delay (DGD).

The PSPs vary randomly along the fiber and change over time, so that DGD is also random. For long fiber which is the case for long-haul transmission, it is found that the DGD values follow Maxwellian distribution [5] whose average is proportional to the square root of fiber length. The first-order polarization mode dispersion coefficient (PMD), usually expressed in $\text{ps}/\sqrt{\text{km}}$, is used to characterize the average dispersion of a given fiber. The typical PMD of a G.652 SSMF is $0.1 \text{ ps}/\sqrt{\text{km}}$. The impact of PMD over an optical signal depends on both the differential group delay and the relative intensities of light in the PSPs. The impairment is maximal when equal amounts of light are coupled into the two PSPs, and the impairment is negligible when all of the light is coupled to a single PSP.

Besides first-order PMD, birefringence effects are wavelength dependent. This feature results in second-order PMD, including a dependency of the PMD with the wavelength named as polarization dependent chromatic dispersion and a shift of PSPs with the wavelength.

1.1.4 Nonlinear effects

Fiber loss, CD and PMD are linear effects whose impact is independent of the optical power. Besides linear effects, the refractive index of fiber also changes with the intensity of light. This phenomenon is known as Kerr effect [6, 7]. The refractive index n depending on the optical power inside the fiber is expressed by

$$n(\omega, P) = n(\omega) + n_2 \cdot I = n(\omega) + n_2 \frac{P}{A_{eff}} \quad \text{Eq. 1-4}$$

where n is the linear part of the refractive index, n_2 is the nonlinear refractive index, I is the optical intensity, P is the optical power and A_{eff} is the effective core area. The value of n is approximately 1.5 and n_2 has typical values of $2\text{-}3 \cdot 10^{-20} \text{ m}^2/\text{W}$. A_{eff} of G.652 SSMF is around $80\text{-}100 \mu\text{m}^2$ at 1550 nm depending on the fiber design. From Eq. 1-4, we can deduce that either high optical power or small A_{eff} increase the impact of Kerr effect. The nonlinear coefficient γ is expressed by

$$\gamma = \frac{n_2 \omega}{c A_{eff}} \quad \text{Eq. 1-5}$$

Within a fiber span, the optical power is important for the first kilometres and drops to a low value at the end of the span. As a result, nonlinear effect decreases along the fiber span. The effective fiber length, taking into account the fiber attenuation is expressed as

$$L_{eff} = \frac{1 - \exp(-\alpha L)}{\alpha} \quad \text{Eq. 1-6}$$

where L is the total length of the fiber span and α is the attenuation coefficient. The nonlinear phase shift introduced by a fiber of length L is given by

$$\phi_{NL} = \gamma \cdot L_{eff} \cdot P_0 \quad \text{Eq. 1-7}$$

where P_0 is the peak power within the span.

In a WDM system, we are interested in the impact of Kerr effect over each individual channel. For a given channel, the phase shift induced by its own power variation is named as self-phase modulation (SPM). The refractive index also depends on the power variation of other co-propagating channels and results in cross-phase modulation (XPM) effect. Another inter-channel effect is the four-wave mixing (FWM), shown as co-propagating channels interacting with each other to create signals at new frequencies. Furthermore, the PSPs of a channel can be affected by the PSPs of other co-propagating channels. This effect is named as cross-polarization modulation (XPoIM).

The impairment created by nonlinear effects is also related to the amount of fiber dispersion. High dispersion fibers have better nonlinear performance. It is demonstrated that G.652 SSMF ($D = 17 \text{ ps/nm/km}$) outperforms G.655 LEAF ($D = 4.3 \text{ ps/nm/km}$) in coherent 40 Gbps and 100 Gbps WDM transmissions [8]. Coherent systems achieve better performance over DCF-free fiber line with respect to the legacy dispersion-managed fiber line [9].

1.2 Evolution of long-haul optical transmission systems

1.2.1 Intensity-modulation / direct detection-based systems

Optical fiber was introduced in the first half of the 1970's. In its early years, optical fiber systems saw smooth capacity increase and the transmission window was gradually switched from 800 to 1300 to 1550 nm towards the lowest attenuation wavelengths. The modulation scheme was intensity modulation / direct detection (IM/DD). At the transmitter, information is encoded onto the amplitude of the signal; at the receiver, decision is made according to the signal intensity by means of a photo-detector. Non-return-to-zero on-off-keying (NRZ-OOK) is the most commonly used IM/DD modulation format.

The invention of Erbium-doped fiber amplifiers (EDFA) in the late 1980's is a great breakthrough for long-haul optical communications. It allows the attenuated signal to be periodically amplified, thus avoiding the expensive electrical regeneration. EDFA presents a large amplification window that coincides with the low attenuation window of optical fiber. Multiple channels at different wavelengths can be simultaneously amplified through single EDFA, enabling the introduction of wavelength division multiplexing (WDM).

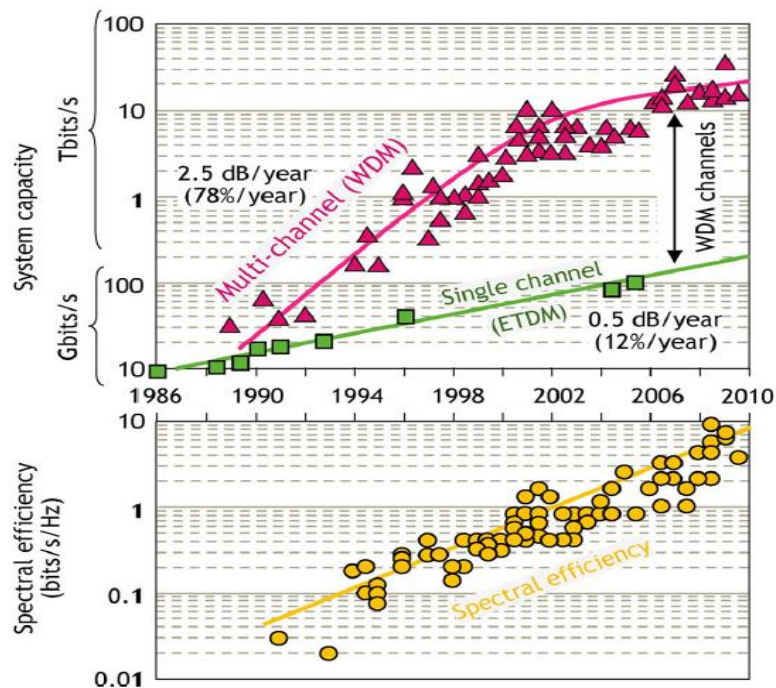


Figure 1-3: Demonstrated system capacities (green squares: single-channel systems, red triangles: WDM systems) and spectral efficiency evolutions. [2]

2.5 Gbps NRZ-OOK was the first deployed format in the WDM systems constituted of 40 channels. The transmission reach was ~800 km over G.652 SSMF. Further increase of data rate was limited by the accumulated CD. The impairment generated by CD is proportional to the square of baud rate. The data rate increase from 2.5 Gbps to 10 Gbps was made possible through the deployment of dispersion compensation fiber (DCF) and the use of forward error correction (FEC) codes. 10 Gbps NRZ-OOK deployed in the WDM systems of 80 channels offers a data rate of ~1 Tbps per fiber. Fig. 1-3 shows the demonstrated system capacities of single-channel and WDM systems, as well as the evolution of spectral efficiencies from 1986 to 2010.

1.2.2 Coherent detection-based systems

Coherent communications were first introduced by DeLange in 1970 [10] and studied extensively in the 1980's because of their higher receiver sensitivity (10-15 dB) with respect to direct detection schemes. However, their development was interrupted for nearly 20 years, due to the deployment of EDFA and WDM systems which made IM/DD the simple and perfect format to achieve long-haul reach and to cope with traffic demand. In the 2000's, the traffic load continued increasing, so that the per fiber capacity needed to follow up. The number of channels in the WDM systems is limited by the amplification bandwidth of EDFA. The most straightforward approach would be to increase the per channel bit rate of IM/DD systems.

The capacity increase from 10 Gbps NRZ-OOK to 40 Gbps NRZ-OOK faced several challenges: Firstly, 40 Gbps requires 6 dB of extra-OSNR with respect to 10 Gbps in order to obtain the same bit error rate. In other words, on the same fiber link, the transmission reach of 40 Gbps is about four times shorter than that of 10 Gbps. In addition, legacy fibers present high PMD values. The sensitivity to PMD impairment is proportional to the baud rate. While the 10 Gbps receiver has a PMD tolerance of 10 ps which corresponds to 10% of the symbol duration, the tolerance of 40 Gbps receiver is only 2.5 ps. Furthermore, 40 Gbps NRZ-OOK channel occupies a spectral range of more than 50 GHz, making it non-compliant with the 80-channel 50-GHz grid WDM system, especially with 50-GHz grid configurable optical add-drop multiplexers (ROADM) deployed in the network.

Facing the difficulties of 40 Gbps NRZ-OOK and with the availability of high speed ADCs, coherent detection regained attention. 40 Gbps dual-polarization quadrature phase-shift keying (DP-QPSK) real-time coherent systems were first demonstrated by Nortel in 2008 [11]. Coherent detection allows access to both amplitude and phase of the optical signal, permitting use of the advanced modulation formats with increased spectral efficiency. The per channel capacity is further doubled by polarization multiplexing. In addition, coherent detection makes the digital signal processing (DSP) possible, giving the possibilities of combating linear and nonlinear effects numerically. CD can be compensated in the electrical domain, avoiding the use of DCF. 100 Gbps DP-QPSK systems, having a transmission reach of ~2000 km and compliant with the 50-GHz WDM grid, are being deployed in long-haul networks since 2012.

1.3 Beyond 100 Gbps technologies

The next generation of long-haul systems will have a per channel capacity of beyond 100 Gbps. The direct way of increasing per channel capacity would be the use of high order modulation formats. However, their transmission reach is largely reduced with respect to QPSK. Improving the fiber infrastructure and developing advanced DSP techniques are potential approaches of increasing the transmission reach. Recent developments over optical fibers, optical amplification schemes, forward error correction codes and nonlinear mitigation techniques will be described in this section.

1.3.1 High order modulation formats

Increasing the spectral efficiency (SE), which consists in transmitting more bits per second per hertz, is a direct way to cope with the increasing traffic demand. The currently deployed 100 Gbps DP-QPSK systems in a 50 GHz fixe grid channel have a SE of 2 bits/s/Hz. QPSK

modulation, also named as 4-QAM, whose constellation diagram is shown in Fig.1-4, has 4 constellation points and carries 2 bits per symbol. Higher order modulation formats permit to carry more bits per symbol. 8-QAM, 16-QAM, 32-QAM and 64-QAM carry 3, 4, 5 and 6 bits per symbol, respectively. They achieve a SE of 3, 4, 5 and 6 bits/s/Hz, respectively, if we adopt the same symbol rate as in 100 Gbps DP-QPSK systems.

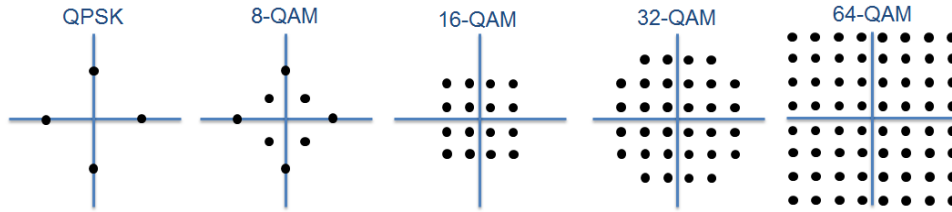


Figure 1-4: Examples of M-QAM constellations.

Increasing modulation order means to make adjacent constellation points closer to each other, making it more sensitive to noise. The bit error rate (BER) versus signal-to-noise ratio (SNR) per bit curves of QPSK, 16-QAM and 64-QAM are plotted in Fig. 1-5a, according to the BER expression of QAM formats provided in [12]. For example, to achieve a BER of 10^{-3} , the theoretical SNR per bit required by QPSK, 16-QAM and 64-QAM are ~ 6 dB, ~ 10 dB and ~ 15 dB, respectively. It means that, at the same bit rate, we need to provide 4 dB of extra-SNR for 16-QAM and 9 dB of extra-SNR for 64-QAM, in order to achieve the same BER performance as QPSK.

We would also want to compare the SNR requirement of different modulation formats at the same symbol rate. The BER versus SNR per symbol curves are plotted in Fig. 1-5b. This time, to achieve a BER of 10^{-3} , the theoretical SNR per symbol required by QPSK, 16-QAM and 64-QAM are ~ 9 dB, ~ 16 dB and ~ 22 dB, respectively. At the same symbol rate, for example 100 Gbps QPSK, 200 Gbps 16-QAM and 300 Gbps 64-QAM signals, 16-QAM needs 7 dB of extra-SNR and 64-QAM requires 13 dB of extra-SNR with respect to QPSK.

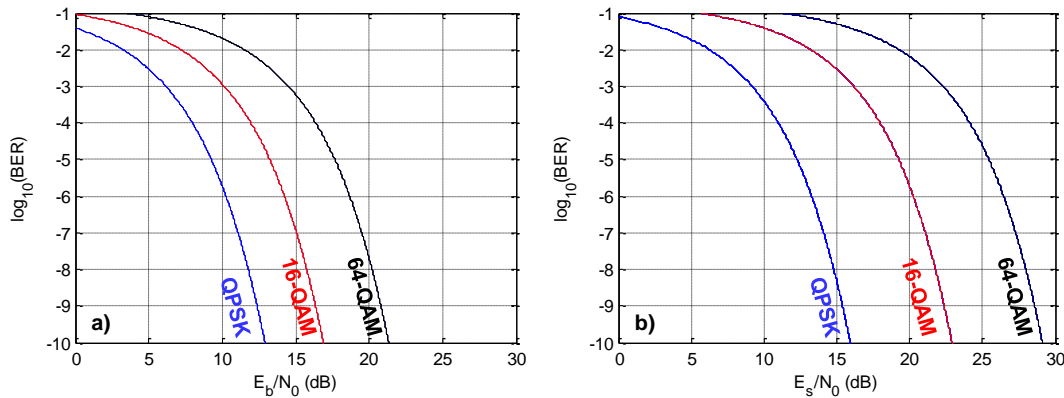


Figure 1-5: a) BER as a function of the SNR per bit; b) BER as a function of the SNR per symbol.

The transmission reach of current 100 Gbps DP-QPSK systems is around 2000 km, which satisfies the needs of European backbone network without electrical regeneration. In absence of nonlinear effects, requiring 7 dB extra-SNR means dividing the transmission reach by a factor of 5, which means the reach of 200 Gbps DP-16-QAM systems will be only around 400 km. This theoretical prediction is verified by various field trials with real-time 16-QAM transponders and legacy fiber infrastructure (SSMF with EDFA amplification) [13-15].

Moreover, higher order modulation formats are also more sensitive to hardware impairments, such as the effective number of bits (ENOB) in digital-to-analog converters (DAC) and analog-to-digital converters (ADC), which will be presented in section 3.1 through numerical simulation.

High order modulation formats permit an increase of SE, but have a major problem of transmission reach. Improvements over fiber infrastructure (such as amplification schemes and optical fibers) and digital signal processing algorithms (such as forward error correction codes and nonlinear equalizers) will play an important role to push the implementation of high order modulation formats in long-haul networks.

1.3.2 Amplification schemes

Optical amplifier is an important element in long-haul optical transmission systems. EDFA is by far the most widely used optical amplifier. It can efficiently amplify light in the 1550 nm region where fiber loss is minimal. The distributed Raman amplification offers lower noise figure and larger amplification window. We will briefly introduce the principle and characteristics of EDFA and Raman amplifiers.

1.3.2.1 EDFA

In an EDFA, the signal amplification is realized inside a few-meters long single-mode Erbium-doped fiber. Laser pumps around 980 nm or 1480 nm excite the erbium ions (Er^{3+}) into a higher energy level. The energy level diagram is shown in Fig. 1-6. Amplification occurs when incoming photons stimulate the erbium ions in the excited state to relax, at the same time releasing photons that have the same energy and phase as the incoming photons. These photons will repeat the process, thus providing gain to the signal. The conventional amplification range of an EDFA is the C-band (from 1530 nm to 1565 nm). It can also be optimized for the amplification of L-band (from 1565 nm to 1625 nm) signal.

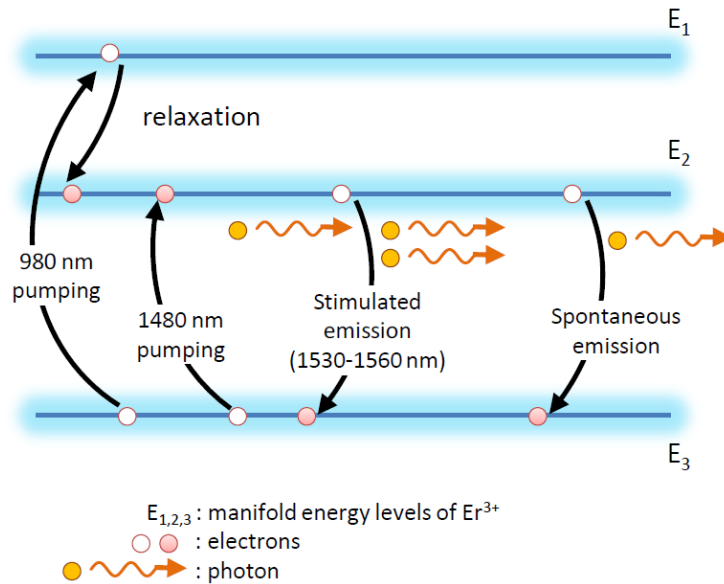


Figure 1-6: Energy level diagram of an EDFA. [16]

In addition to stimulated emission, a few of the excited Er^{3+} ions decay to the ground level through spontaneous emission. In this case, noisy photons with a random phase are emitted

and further amplified through the relaxation of Er^{3+} ions. This process is called amplified spontaneous emission (ASE). The ASE noise is commonly assumed as additive white Gaussian noise. It is characterized by noise figure NF which is defined as the ratio of the input and output OSNR. NF can also be expressed in terms of gain G and spontaneous emission factor (or population inversion factor) n_{sp} [17]

$$NF = 2n_{sp} \frac{(G-1)}{G} \approx 2n_{sp} \quad \text{Eq. 1-8}$$

At high G , which is the case for a fiber span of 50-100 km, the NF can be approximated as $2n_{sp}$. A perfect amplifier with $n_{sp} = 1$ has a NF of 2, corresponding to 3 dB in decibel unit. In practice, EDFAs have a NF of between 4 and 6 dB.

A long-haul transmission is composed of a certain number of spans, each of which followed by an EDFA. As a consequence, the ASE noise is accumulated. Assuming a link with fibers of equal span length and amplifiers with the same gain and noise figure, the optical signal-to-noise ratio (OSNR) at the output of the link can be expressed as

$$OSNR = \frac{GP_{in}}{2N_{spans}N_{ASE}B_{ref}} \quad \text{with } N_{ASE} \approx \frac{1}{2}NF \cdot hfG \quad \text{Eq. 1-9}$$

where P_{in} is the signal power at the input of the EDFA, N_{spans} is the number of spans in the link, N_{ASE} is the power spectral density of ASE noise in one polarization, B_{ref} is the reference bandwidth, h is the Planck constant and f is the frequency of the light. From Eq. 1-9, the OSNR in dB can be written as

$$OSNR_{dB} = P_{in,dB} - NF_{dB} - 10 \log_{10}(N_{spans}) - 10 \log_{10}(hfB_{ref}) \quad \text{Eq. 1-10}$$

We notice that the signal-to-noise ratio is positively related to the signal power at the input of the EDFA $P_{in,dB}$, and negatively related to the noise figure of the EDFA NF_{dB} and the number of spans N_{spans} .

1.3.2.2 Raman amplifier

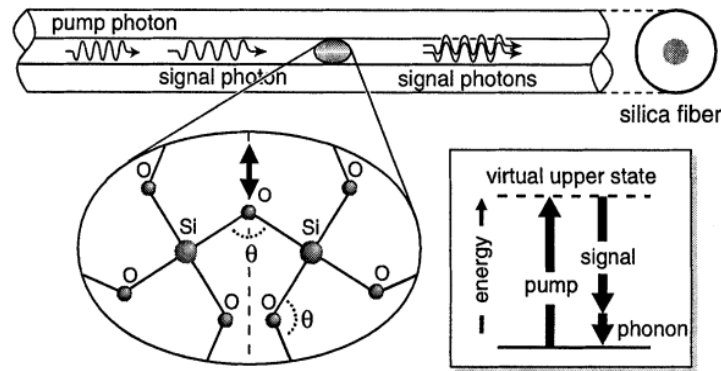


Figure 1-7: Schematic depicting amplification by Raman scattering in optical fiber. The Raman Stokes interaction between a pump, signal photon and the silica molecules converts the pumps into a replica of the signal photon, producing an optical phonon. [18]

Spontaneous Raman scattering was first discovered by Raman [19], for which he received the Nobel Prize in Physics in 1930. Optical photons are inelastically scattered by molecular vibrations called optical phonons [18]. Raman scattering can occur in all materials. In silica

glass, it is dominated by the bending motion of the Si-O-Si bond (see bond angle θ in Fig. 1-7). Raman scattering can be stimulated by signal light at an appropriate frequency shift from a pump, leading to stimulated Raman scattering (SRS). The energy level diagram is shown in Fig. 1-7. In this process, a pump photon is converted into an exact replica of the signal photon, and the remaining energy produces an optical phonon. Therefore, the initial signal photon is amplified.

There are a number of different configurations in which Raman amplification can be utilized on a fiber span. The Raman pumps may counter-propagate with the signal (backward Raman) and/or co-propagate with the signal (forward Raman). Additionally, residual pump power from Raman can power a remote optically pumped amplifier (ROPA). A ROPA is typically Erbium-doped fiber placed between 60 and 140 km from the equipment node and basically performs the function of an EDFA mid-span [20]. Fig. 1-8 shows different signal power profiles for different amplification schemes.

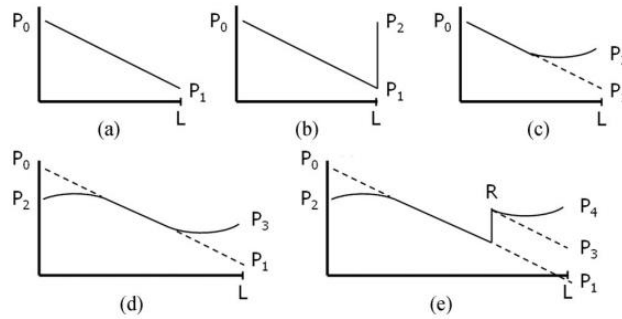


Figure 1-8: Signal power profiles (dBm) for different span amplification schemes in a span of length L (km). Dashed lines show power profiles without Raman amplification (not to scale). (a) span, (b) EDFA, (c) backward Raman, (d) forward + backward Raman, (e) forward + backward Raman + ROPA. [20]

Raman amplification has spectral flexibility, because Raman gain depends on the frequency separation between a pump and signal. As long as pump light with the appropriate wavelength is available, one can build amplifiers for any band of signal wavelengths. By combining multiple pump wavelengths, Raman systems are compatible with a wideband transmission window (up to 100 nm wide). Another benefit of Raman amplification is its low noise figure. Let's take the case of backward Raman as an example, as shown in Fig. 1-8c, and assume that the rest of the loss is balanced by an EDFA. This configuration can be modelled as the cascade of two amplifiers. The total noise figure of a cascaded amplifier chain is given by [17]

$$NF_{total} = NF_1 + \frac{NF_2 - 1}{G_1} + \frac{NF_3 - 1}{G_1 G_2} + \dots \quad \text{Eq. 1-11}$$

where NF_i and G_i are the noise figure and gain (in linear units) for the i th amplifier in the chain. If the gain of the first amplifier (G_1) is sufficiently high, the total noise figure will be dominated by the noise figure of the first amplifier (NF_1) which is the noise figure of the backward Raman in our case. Whereas the noise figure of pure EDFA is always higher than 3 dB, the total noise figure of hybrid Raman-EDFA can be negative in decibel unit. [20] demonstrates an OSNR benefit of about 4.75 dB using hybrid Raman-EDFA with respect to pure EDFA.

There are several effects causing transmission penalties when using Raman amplification. One of the penalties comes from multiple-path interference (MPI), which occurs when signal light reaches the receiver by more than one optical path. MPI is mainly caused by double

Rayleigh scattering (DRS) and can be treated as an additional noise source. In practice, MPI should be kept below -20 dB [20]. The level of MPI is related to the signal power, which restricts the Raman gain of the amplifier to about 25 dB. The MPI for Raman gain less than 15 dB is fairly insignificant. Other impairments, such as polarization-dependent gain (PDG), FWM with Raman pumps, and noise transfer from pumps to signal, also need to be taken into account when designing Raman amplifiers.

Compared to EDFA, Raman or hybrid Raman-EDFA amplifiers have a higher cost and more complicated engineering procedures, such as stricter safety requirements due to high-power pumps. In return, it provides larger amplification window and lower noise figure with respect to EDFA, making it one of the potential enablers of long-haul transmission with ultra-high bit rate.

1.3.3 Optical fibers

The transmission media: optical fiber has great impact on the transmission performance in long-haul systems. As described in section 1.1, several key parameters (i.e. fiber loss, CD, PMD and nonlinear effects) characterize the fiber.

- **Attenuation coefficient α** : determines the fiber loss of a given span length. It directly affects the $P_{in_{dB}}$ in Eq. 1-10, so as the OSNR of the received signal.
- **CD**: was considered as an undesirable effect in DD/IM systems. We intended to design fibers with lower CD, in order to reduce the length of dispersion compensation fiber. In coherent systems, CD is no longer an undesirable impairment, since it is a quasi-deterministic process and can be compensated through digital signal processing. Besides, the presence of CD reduces the fiber nonlinear effects, so that fibers with large dispersion coefficient are desired.
- **PMD**: was another undesirable effect in DD/IM systems, leading to performance degradation. In coherent systems, PMD can be compensated in the polarization demultiplexing process in the receiver.
- **Effective area**: has been defined for the purposes of calculating nonlinear effects which depends on the power density of the light injected into the fiber. The larger the effective area, the lower the power density and so the impact of nonlinear effects.

Different types of fibers have been designed to achieve best output in different use cases. ITU has developed a number of standards to classify various types of fibers, among which G.652, G.655 and G.654 are the most widely studied and deployed for long-haul systems. G.652 represents standard single-mode fiber (SSMF) with an α of ~0.2 dB/km and a dispersion of ~16-18 ps/(nm.km) at 1550 nm. G.655 stands for non-zero dispersion shifted fiber (NZDSF) with an α of ~0.2 dB/km and a dispersion of ~4-10 ps/(nm.km). G.654 denotes cut-off shifted fiber with large effective area, so that low nonlinear effects. It was initially designed for submarine transmission systems to reach ultra-long-haul distance. Table 1-1 shows key parameters of some industrial fibers designed within G.652, G.655 and G.654 ITU standards.

Table 1-1: Key parameters of some industrial fibers

Product	ITU standard	α @1550 nm (dB/km)	CD @1550 nm (ps/nm/km)	PMD (ps/km ^{1/2})	Effective area @1550 nm (μm^2)
Corning SMF-28e+	G.652	≤ 0.20	≤ 18.0	≤ 0.06	85
Corning LEAF	G.655	≤ 0.19	4.5-6.0	≤ 0.04	72
Draka TeraLight	G.655	≤ 0.22	5.5-10	≤ 0.04	63
TrueWave REACH	G.655	≤ 0.20	5.5-8.9	≤ 0.04	55
Draka LongLine	G.654	≤ 0.19	≤ 23	≤ 0.04	120
Corning Vascade EX2000	G.654	0.160	20.2	≤ 0.05	112
Corning Vascade EX3000	G.654	0.158	20.8	≤ 0.05	150

Most of the fibers currently deployed in terrestrial long-haul systems are G.652 and G.655 fibers with an α of ~ 0.2 dB/km and an effective area of less than $85 \mu\text{m}^2$. There is room for improving the OSNR as well as the nonlinear performance by adopting ultra-low loss, large CD and large effective area fibers. However, it should be noted that changing fiber infrastructure demands huge investments for operators. As a consequence, this option will be considered only if all the other less expensive solutions have been implemented.

1.3.4 Advanced FEC solutions

Forward error correction (FEC) is based on adding redundant information to the information bit sequence. After transmission over a noisy channel such as optical fiber, a decoding system tries to exploit the redundant information for fully recovering of the source bit sequence. FEC is an essential element in today’s high bit rate optical transmission. An “error-free” transmission requires a post-FEC BER down to 10^{-12} or 10^{-15} .

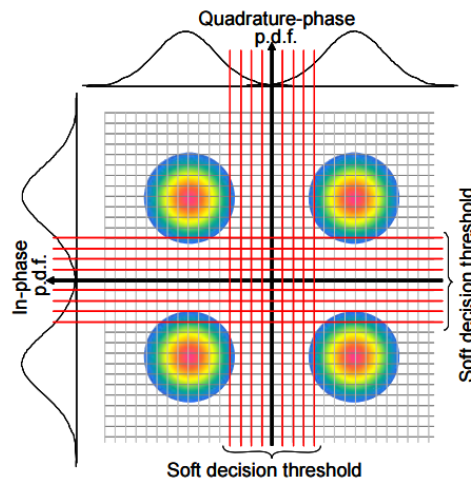


Figure 1-9: Typical 3-bit soft decision for QPSK signal. [21]

FEC decoding can be carried out with two decision schemes: hard-decision (HD) and soft-decision (SD). A HD-FEC works with data sequence coming out of demodulation (symbol demapping) consisting only of “1” and “0”. A soft-decision does not only give the conventional ‘1’ versus ‘0’ decision, but also indicates how certain we are about the decision. A typical soft-decision structure of a QPSK modulation is depicted in Fig. 1-9. The 2^N-1 decision thresholds are placed between constellation points. In the case of $N = 3$, the demodulated bit will be represented by a binary vector ranging from [000] to [111]. The left-most bit corresponds to the hard-decision, and the other two bits are information digits indicating the probability of ‘1’ or ‘0’. The theoretical net coding gain (NCG) of HD-and SD-

FEC as a function of the overhead is plotted with black and red lines in Fig. 1-10. The theoretical limit of SD-FEC is ~2 dB higher with respect to HD-FEC.

The evolution of FECs in optical communication systems is commonly classified into three generations. The first generation uses classical hard decision codes. The most representative is Reed-Solomon (255,239) code standardized by ITU-T G.709, which has an overhead of ~7% and a NCG at BER = 10^{-12} of ~6 dB. The second generation FEC schemes are based on concatenated product code, meaning that the bit stream is first encoded by a simple algebraic code and that several of these code words are interleaved; after partitioning, the interleaver output is again encoded by a simple algebraic code [22]. Second generation FECs, represented by the FEC schemes standardized by ITU-T G.975.1, usually have a NCG from 7 to 9 dB. With the utilization of coherent detection and high resolution ADCs, the third generation FEC: SD-FEC becomes an attractive means to increase the NCG. Two types of SD-FEC codes are the most widely implemented: low-density parity-check (LDPC) codes and turbo product codes (TPC). At 20% overhead, the NCG reaches ~11 dB. Fig. 1-10 shows the NCG of G.975.1 FECs and some recently published advanced FECs.

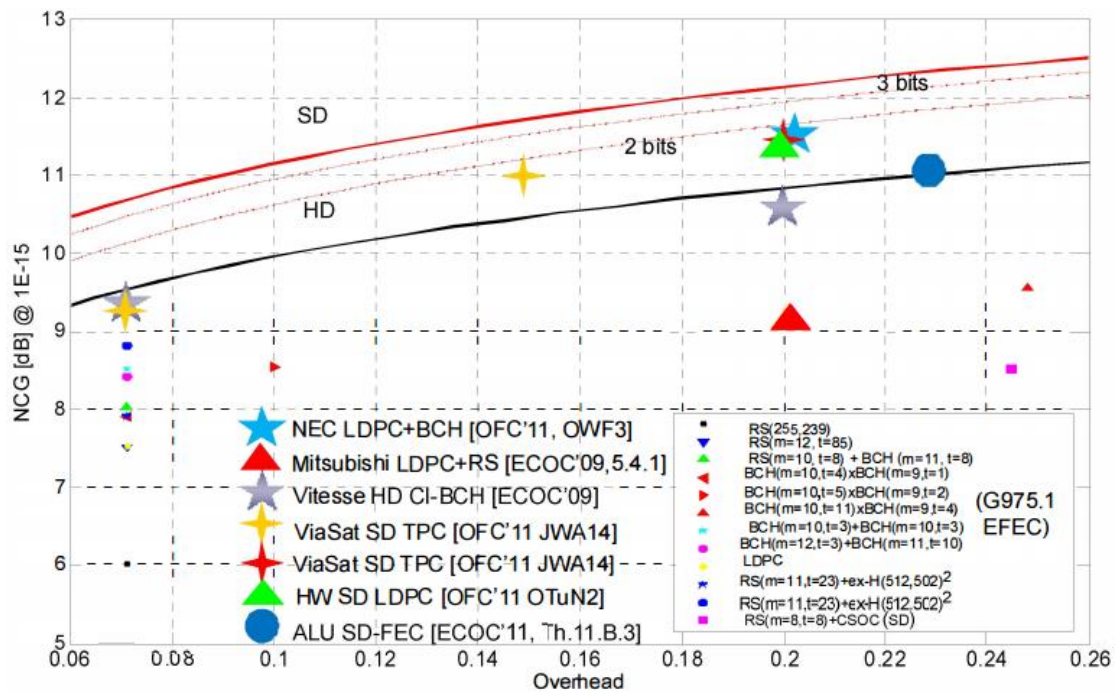


Figure 1-10: Theoretical NCG of HD-FEC and SD-FEC for additive white Gaussian noise (AWGN) channel as well as the NCG of G.975.1 FECs and recently published advanced FECs. [23]

Powerful FEC is one of the enablers of ultra-high bit rate in long-haul systems. The performance of new FEC codes is approaching the Shannon limit. One approach to further increase the NCG is to create FECs with higher overhead, but at the expense of data rate. Some other research axis, such as optimal decoding to non-AWGN nonlinear channel, and joint coding and modulation, may help future FECs to provide more coding gain.

1.3.5 Nonlinear equalizers

The transmission performance over optical fiber is limited by the signal to noise ratio at low launch power, and restricted by the fiber nonlinear effects at high power. Numerical nonlinear equalizations are developed to mitigate intra-channel fiber nonlinearities. Digital back-

propagation (DBP) realized through split-step Fourier (SSF) method [24, 25] is the most studied and commonly considered as reference benchmark of nonlinear compensation algorithms. Recently, 3rd order inverse Volterra series transfer function nonlinear equalizer (IVSTF-NLE) [26, 27] has drawn attention due to its parallel structure, allowing for simultaneous linear and nonlinear compensation. The principle of DBP-SSF and IVSTF-NLE will be detailed in this sub-section.

1.3.5.1 Digital back-propagation

The signal propagation in the optical fiber can be described by the nonlinear Schrodinger equation (NLSE)

$$\frac{\partial E}{\partial z} - j \frac{\beta_2}{2} \frac{\partial^2 E}{\partial t^2} + \frac{\alpha}{2} E = -j\gamma |E|^2 E \quad \text{Eq. 1-12}$$

where $E = E(t, z)$ is the electric field envelope of the optical signal, β_2 is the second-order dispersion parameter, α is the fiber attenuation coefficient, and γ is the fiber nonlinear coefficient. The NLSE can be solved numerically using the SSF method in a noniterative asymmetric way, where the fiber is modeled as a concatenation of nonlinear and linear sections, as depicted in Fig. 1-11. h corresponds to the step size of the SSF method. The accuracy of the model improves when the step size is decreased. The signal power is strongest at the input of the fiber section, so as the fiber nonlinearities. That is why the nonlinear section is usually modeled before the linear section. Eq. 1-13 shows the signal transformation inside the nonlinear section. It corresponds to a phase rotation in the time domain. Eq. 1-14 shows the effect of fiber attenuation and CD in the linear section, which is a phase rotation in the frequency domain. $E_n(w, z + h)$ and $E(w, z + h)$ correspond to the frequency domain representations of $E_n(t, z + h)$ and $E(t, z + h)$.

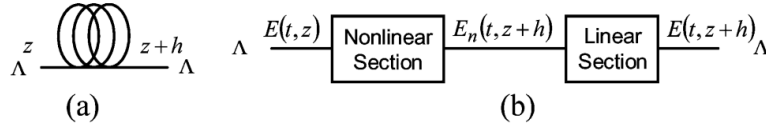


Figure 1-11: (a) Fiber section from z to $z + h$; (b) Mathematical model. [24]

$$E_n(t, z + h) = E(t, z) \exp(j\gamma h |E(t, z)|^2) \quad \text{Eq. 1-13}$$

$$E(w, z + h) = E_n(w, z + h) \times \exp\left(-\left(\frac{\alpha}{2} + j \frac{\beta_2}{2} \omega^2\right) h\right) \quad \text{Eq. 1-14}$$

In the case of dual polarization, signal propagation along the fiber can be described by Manakov equation with $\gamma' = \frac{8}{9}\gamma$:

$$\frac{\partial E_{x/y}}{\partial z} - j \frac{\beta_2}{2} \frac{\partial^2 E_{x/y}}{\partial t^2} + \frac{\alpha}{2} E_{x/y} = -j\gamma' (|E_x|^2 + |E_y|^2) E_{x/y} \quad \text{Eq. 1-15}$$

The output signals of the nonlinear and linear sections become:

$$E_{n,x/y}(t, z + h) = E_{x/y}(t, z) \exp(j\gamma' h (|E_x(t, z)|^2 + |E_y(t, z)|^2)) \quad \text{Eq. 1-16}$$

$$E_{x/y}(w, z + h) = E_{n,x/y}(w, z + h) \times \exp\left(-\left(\frac{\alpha}{2} + j \frac{\beta_2}{2} \omega^2\right) h\right) \quad \text{Eq. 1-17}$$

The digital backpropagation using SSF method consists in performing numerically the inverse operation to estimate the transmitted signal, so that:

$$E'_{n,x/y}(w, z + h) = E_{x/y}(w, z + h) \times \exp\left(\left(\frac{\alpha}{2} + j\frac{\beta_2}{2}\omega^2\right)h\right) \quad \text{Eq. 1-18}$$

$$E'_{x/y}(t, z) = E'_{n,x/y}(t, z + h)\exp(-j\varepsilon\gamma' L_{eff}(|E'_{n,x}(t, z)|^2 + |E'_{n,y}(t, z)|^2)) \quad \text{Eq. 1-19}$$

where $E'_{n,x/y}(t, z + h)$ and $E'_{x/y}(t, z)$ are the estimated intermediate and transmitted signals of a given step. L_{eff} represents the effective length of the step which equals to $\frac{1-\exp(-\alpha h)}{\alpha}$. An empirical parameter ε ($0 < \varepsilon < 1$) is generally applied for optimal BER performance.

DBP usually requires small compensation steps, meaning several steps per span to achieve good equalization performance, which results in high computational complexity. Several studies have been carried out to simplify the hardware implementation of DBP [28-31].

1.3.5.2 3rd order inverse Volterra based equalizer

The solution of the NLSE can be written with VSTF kernels of up to third order as [27]:

$$E(\omega, z) = H_1(\omega, z)E(\omega) + \int_{-\infty}^{\infty} \int_{-\infty}^{\infty} H_3(\omega_1, \omega_2, \omega - \omega_1 + \omega_2, z) \times E(\omega_1)E^*(\omega_2)E(\omega - \omega_1 + \omega_2)d\omega_1d\omega_2 \quad \text{Eq. 1-20}$$

$$H_1(\omega, z) = \exp(-\alpha z/2)\exp(-j\omega^2\beta_2 z/2) \quad \text{Eq. 1-21}$$

$$H_3(\omega_1, \omega_2, \omega - \omega_1 + \omega_2, z) = -\frac{j\gamma}{4\pi^2}H_1(\omega, z) \times \frac{1-\exp(-[\alpha + j\beta_2(\omega_1 - \omega)(\omega_1 - \omega_2)]z)}{\alpha + j\beta_2(\omega_1 - \omega)(\omega_1 - \omega_2)} \quad \text{Eq. 1-22}$$

where $E(\omega) = E(\omega, 0)$ is the optical signal in the frequency domain at the input of the fiber, $H_1(\omega, z)$ and $H_3(\omega_1, \omega_2, \omega - \omega_1 + \omega_2, z)$ are the first and the third order Volterra kernels, respectively. A third order IVSTF-NLE calculates the inverse of $H_3(\omega_1, \omega_2, \omega - \omega_1 + \omega_2, z)$ as nonlinear compensator.

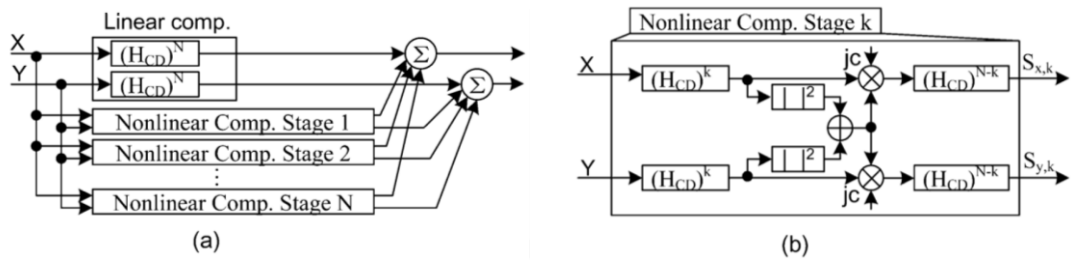


Figure 1-12: Realization of the third order IVSTF-NLE for dual-polarization. (a) Block diagram of the overall compensation scheme. (b) Detailed realization of the nonlinear compensation stage k. [26]

Fig. 1-12a shows the block diagram of a dual-polarization third order IVSTF-NLE proposed in [26]. The equalizer considers an optically amplified N-span fiber link without in-line dispersion compensating. A simplification in the formula of the third order inverse is obtained by ignoring the waveform distortion within a span. The compensation is composed of a linear part and a nonlinear part operating in parallel. The linear part compensates the chromatic dispersion. The nonlinear part contains N stages, where N is the number of spans.

The detailed realization of the nonlinear compensation stage k is shown in Fig. 1-12b. $H_{CD} = \exp\left(\frac{j\omega^2\beta_2L}{2}\right)$ compensates the CD of each span, where L denotes the span length. c is a constant whose theoretical value equals to γL_{eff} . In practical implementation over experimental test-bed, the optimum value of c is usually different from its theoretical value and needs to be optimized for each set-up. In the k th nonlinear compensation stage, we first recover the dispersion effect of k spans by applying $(H_{CD})^k$, and then calculate the nonlinearities through $jc(|\cdot|_x^2 + |\cdot|_y^2)(\cdot)_x$ and $jc(|\cdot|_x^2 + |\cdot|_y^2)(\cdot)_y$, where the signal is multiplied by a constant jc and by the total power of the two polarizations. At last, we remove the residual dispersion by applying $(H_{CD})^{N-k}$.

The linear compensation stage and each stage of the nonlinear compensation are respective realizations of:

$$K_1(\omega) = H_1^{-1}(\omega) = \exp\left(\frac{j\omega^2\beta_2NL}{2}\right) \quad \text{Eq. 1-23}$$

$$K_{3,k}(\omega_1, \omega_2, \omega - \omega_1 + \omega_2) \approx \frac{j\gamma'}{4\pi^2} \times \frac{1 - \exp(-\alpha L)}{\alpha} \times K_1(\omega) \exp(jk\beta_2L\Delta\Omega) \quad \text{Eq. 1-24}$$

where K_p denotes the p th order inverse of a given nonlinear system H , γ' assumes the value of $\frac{8}{9}\gamma$ present in the Manakov equation for dual-polarization and $\Delta\Omega = (\omega_1 - \omega)(\omega_1 - \omega_2)$.

Nonlinear equalizers significantly improve the transmission reach of high bit rate signal, especially in single channel configuration. [28] demonstrates a reach improvement of 68% and 43% over 112 Gbps DP-16QAM systems by applying DBP of 4 steps per span and 0.2 steps per span, respectively. Nonlinear equalization is one of the potential enablers of implementing high order modulation format in long-haul systems. However, its computational complexity is still a barrier preventing its real time implementation. Besides, the bandwidth of the currently developed ADCs only allows the detection of single channel, making it unable for the receiver DSP to get the knowledge of adjacent channels. As a consequence, SPM is the only nonlinear effect mitigated. In WDM systems with a large number of co-propagating channels, the performance of intra-channel nonlinear equalizers is very limited. Few experiments have compared their performance in single channel and WDM configurations. In section 3.4, we will investigate the performance of DBP-SSF and IVSTF-NLE over 400 Gbps OFDM signal and compare their performance in three scenarios with different quantities of inter-channel nonlinearities.

1.4 Conclusion

In this chapter, we have presented main physical impairments in single-mode optical fiber, including fiber loss, chromatic dispersion, polarization mode dispersion and Kerr effect. We have then provided a brief description of the evolution of long-haul optical transmission systems. WDM was the first major breakthrough enabled by the invention of EDFA. The evolution from 10 Gbps to 40 Gbps with IM/DD approach faced several technical difficulties, promoting the revival of coherent detection. 100 Gbps coherent DP-QPSK systems are currently under massive deployment. The next generation beyond 100 Gbps long-haul systems will use high order modulation formats to provide high spectral efficiency. Their transmission reach becomes the major barrier. Long-haul transmission with high order modulation formats may be enabled by some fiber infrastructure or DSP improvements, such

as ultra-low loss large effective area fiber, new amplification schemes, advanced forward error correction codes and nonlinear mitigation techniques. In the next chapter, we will give an overview of OFDM technique for WDM optical transmission systems.

CHAPTER 2

OFDM FOR WDM TRANSMISSION SYSTEMS

The concept of using orthogonal frequencies for transmission was proposed by Chang of Bell Labs in 1966 [32]. The proposal to generate orthogonal signals using an FFT came in 1969 [33]. The cyclic prefix, which is an important aspect of almost all practical OFDM implementations, was proposed in 1980 [34]. These are the three key aspects that form the basis of most OFDM systems [35]. During the last 20 years, OFDM has been adopted by a wide range of communication standards, such as European Digital Video Broadcasting (DVB), wireless local area networks (WiFi, IEEE 802.11a/g), asymmetric digital subscriber line (ADSL, ITU G.992.1) and fourth generation mobile communications technology long-term evolution (LTE) [36].

OFDM has received considerable attention in the recent past in the field of optical communication. Its quasi-rectangular spectral form allows locating adjacent channels with small guard-band, yielding to a high spectral efficiency. Some OFDM DSP algorithms require less computational capacity than those of single-carrier systems: the CD and PMD can be directly absorbed by cyclic prefix and the polarization demultiplexing can be realized by a single tap equalizer. OFDM also allows an easy implementation of space-time coding techniques capable of mitigation polarization dependent loss (PDL) [16]. In addition, since the OFDM signal is composed of a large number of low symbol rate subcarriers, it is capable of overcoming some frequency domain impairments and thereby maximizing link capacity through appropriate subcarrier bit and power loading.

This chapter is an overview of OFDM for long-haul optical transmission systems. We will start by introducing the principle of OFDM which relies on the IFFT/FFT operation. A description of the key transmitter and receiver DSP procedures follows, illustrated by experimental results which demonstrate the impact of inaccurate time and frequency synchronization. Afterwards, we will present a methodology for defining OFDM parameters. The dimensioning of a 400 Gbps OFDM channel which takes into account experimental constraints is used as an illustrative example. Later on, OFDM formats with improved features, such as DFT-spread OFDM and offset-QAM, will be briefly introduced. At last, we will present a state-of-art review of OFDM transmission experiments and comparisons with single-carrier techniques.

2.1 OFDM principle

The idea of OFDM is to divide the channel into a large number of low-rate orthogonal subcarriers. Each subcarrier occupies a different central frequency and is characterized by a sinc spectrum. Their orthogonality is guaranteed if the subcarrier spacing Δf is multiple of the inverse of symbol duration. The property of orthogonality permits to demodulate each subcarrier free from any interference from the other subcarriers. Fig. 2-1 shows examples for waveform orthogonality in time and frequency.

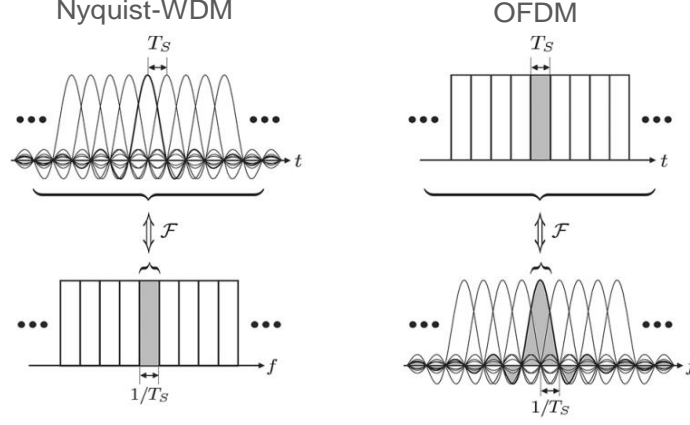


Figure 2-1: Examples for waveform orthogonality in time (on the left hand side) and in frequency (on the right hand side). [37]

Unlike single carrier systems, whose symbol mapping is carried out in the time domain, OFDM modulates each subcarrier in the frequency domain. Inverse Discrete Fourier Transform (IDFT), usually computed with Inverse Fast Fourier Transform (IFFT) algorithm, is carried out in the transmitter. Discrete Fourier Transform (DFT), usually computed with Fast Fourier Transform (FFT) algorithm, is carried out in the receiver. Throughout this thesis, the abbreviation of IFFT and FFT will be used to represent IDFT and DFT. The input of the IFFT can be expressed as a complex vector $\mathbf{X} = [X_0 X_1 X_2 \dots X_{N-1}]^T$, where N is the size of the IFFT. Each element of \mathbf{X} represents the data to be carried on the corresponding subcarrier, so for example X_k represents the data to be carried on the k th subcarrier. The output of the IFFT is [35]

$$x_m = \frac{1}{\sqrt{N}} \sum_{k=0}^{N-1} X_k \exp\left(\frac{j2\pi km}{N}\right) \quad \text{for } 0 \leq m \leq N-1 \quad \text{Eq. 2-1}$$

The $\frac{1}{\sqrt{N}}$ coefficient makes the discrete signals at the input and the output of the transform for each symbol the same average power.

At the receiver, a forward FFT will be performed

$$Y_k = \frac{1}{\sqrt{N}} \sum_{m=0}^{N-1} y_m \exp\left(\frac{-j2\pi km}{N}\right) \quad \text{for } 0 \leq k \leq N-1 \quad \text{Eq. 2-2}$$

where $\mathbf{y} = [y_0 y_1 y_2 \dots y_{N-1}]^T$ is the vector representing the sampled time domain signal at the input of the receiver FFT and $\mathbf{Y} = [Y_0 Y_1 Y_2 \dots Y_{N-1}]^T$ is the discrete frequency domain vector at the FFT output. If we only consider AWGN in the channel, then

$$y_m = x_m + w_m \quad \text{Eq. 2-3}$$

where w_m is a sample of white Gaussian noise. From Eq. 2-2 and Eq. 2-3, we find

$$Y_k = \frac{1}{\sqrt{N}} \sum_{m=0}^{N-1} y_m \exp\left(\frac{-j2\pi km}{N}\right) = \frac{1}{\sqrt{N}} \sum_{m=0}^{N-1} (x_m + w_m) \exp\left(\frac{-j2\pi km}{N}\right) = X_k + W_k \quad \text{Eq. 2-4}$$

where W_k is the noise component of the k th output of the receiver FFT. Eq. 2-4 shows that, if there is only additive noise in the channel, the received signal Y_k also suffers from additive noise.

2.2 Transmitter DSP procedures

The typical OFDM transmitter (Tx) DSP procedures in long-haul optical communication systems are shown in Fig. 2-2. First of all, a high bit-rate binary data stream is split into a high number of low bit-rate binary data tributaries by a serial-to-parallel conversion. Each low bit-rate tributary feeds one OFDM subcarrier. Then, symbol mapping, also called modulation, converts binary data to complex samples. Following the pilot tones, training sequence insertion and synchronization symbol insertion, the signal is transformed from frequency to time domain through IFFT. After adding cyclic prefix in front of each symbol and parallel-to-serial conversion, clipping is carried out to take full advantage of the effective number of bits (ENOB) of digital-to-analog converter (DAC).

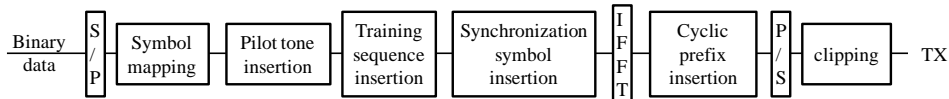


Figure 2-2: Typical OFDM Tx DSP block diagram in long-haul optical communication systems.

Some of the Tx DSP blocks will be described in detail in the following sub-sections. We will begin by introducing the OFDM frame structure which indicates the location of pilot tones, training sequence and synchronization symbol. We will also provide the abbreviations of various OFDM frame parameters. The cyclic prefix concept and clipping techniques will be presented in the second and third sub-sections.

2.2.1 Frame structure and notations

The OFDM signal processing is carried out by the unity of “frame” which has a two dimensional structure, as depicted in Fig. 2-3. The horizontal and vertical axis represent the time and frequency dimension, respectively. From the time point of view, one OFDM frame is composed of a certain number of “symbols”. From the frequency point of view, one OFDM frame consists of a certain number of “subcarriers”.

Since we use data aided signal processing techniques, some of the symbols and subcarriers are not used for transmitting useful data but reserved for signal processing. A “synchronization symbol”, in charge of time and frequency synchronization, is usually placed at the front of the frame. It is followed by training symbols, also called “training sequence”, which makes polarization demultiplexing easier. In data symbols, some of the subcarriers are reserved for “pilot tones” whose task is to compensate for the common phase error generated by laser phase noise. Zero-padding subcarriers are placed at low and high frequencies in order to avoid aliasing problem.

The smallest digital signal processing element is called “sample” represented by a complex value. Note that there are frequency domain samples and time domain samples. The OFDM frame depicted in Fig. 2-3 is composed of frequency domain samples, whose values are calculated in the symbol mapping stage. Each sample is located on a specific subcarrier and occupies an entire symbol duration. After performing the IFFT in the Tx DSP procedures, an OFDM frame will be represented by time domain samples. Each time domain sample covers all the frequency components but represents a specific instant inside the symbol.

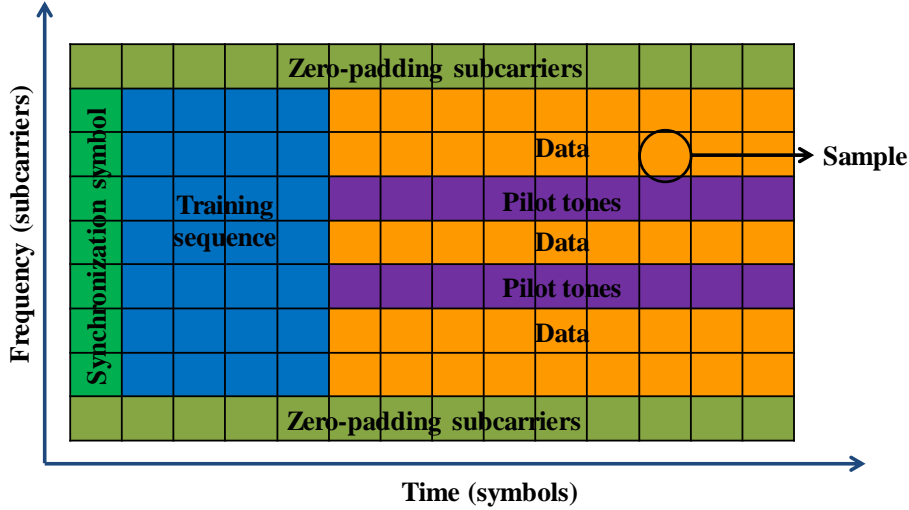


Figure 2-3: Typical OFDM frame structure.

Throughout this manuscript, we will use N_{XX} to denote the number of subcarriers and L_{XX} to denote the number of symbols. For example, N_{data} , N_P and N_{ZP} represent the number of data subcarriers, pilot tones subcarriers and zero-padding subcarriers, respectively. The total number of subcarriers N , which is also the IFFT size at the transmitter side and the FFT size at the receiver side, is calculated as $N = N_{data} + N_P + N_{ZP}$. As it will be described in the sub-section 2.2.2 of cyclic prefix concept, at the output of the transmitter IFFT, a cyclic prefix of N_{CP} time domain samples will be added in front of each symbol. The symbol length including cyclic prefix will become $N + N_{CP}$. L_{TS} and L_{data} denote the number of symbols in the training sequence and in the data, respectively. The number of symbols in the synchronization symbol, which is usually 1, is not calculated apart but included in L_{TS} . The number of symbols in an OFDM frame is calculated as $L_{frame} = L_{data} + L_{TS}$. Finally, the number of time domain samples in an OFDM frame including cyclic prefix is expressed as $L_{frame} \cdot (N + N_{CP})$.

2.2.2 Cyclic prefix

In optical fiber, the pulse spreading generated by CD and PMD will cause signal inter-symbol interference (ISI) and inter-carrier interference (ICI). As OFDM symbol duration is much longer than the pulse spreading, cyclic prefix (CP) is an easy way to completely eliminate ISI and ICI. The transmitted OFDM frame consists of a sequence of symbols. Let $\mathbf{x}(i) = [x_0(i) \ x_1(i) \ x_2(i) \ \dots \ x_{N-1}(i)]^T$ be the output of the IFFT of the i th symbol. In most OFDM systems, the CP is added to the front of each time domain OFDM symbol before transmission. In other words, a number of samples from the end of the symbol are appended to the start of the symbol.

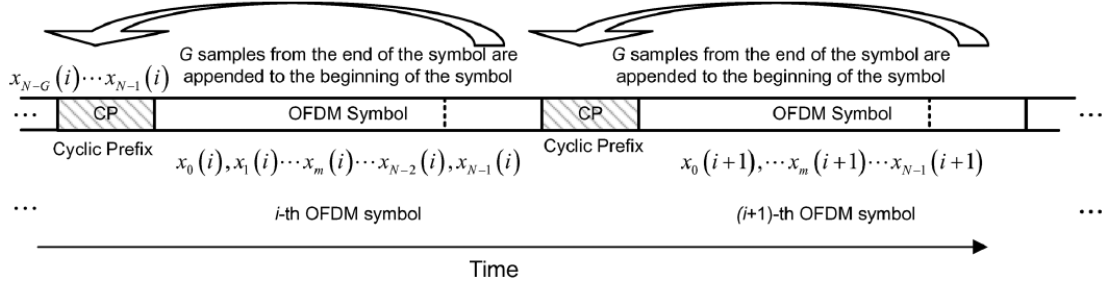


Figure 2-4: Time domain sequence of OFDM symbol showing the cyclic prefix, with $G = N_{CP}$. [35]

As shown in Fig. 2-4, instead of transmitting $\mathbf{x}(i)$, the following sequence is transmitted

$$\mathbf{x}_{CP}(i) = [x_{N-N_{CP}}(i) \dots x_{N-1}(i), x_0(i) x_1(i) x_2(i) \dots x_{N-1}(i)]^T \quad \text{Eq. 2-5}$$

where N_{CP} is the length of the CP. The received sequence after CP removal is

$$\mathbf{y}(i) = [y_0(i) y_1(i) y_2(i) \dots y_{N-1}(i)]^T \quad \text{Eq. 2-6}$$

Supposing that there is a shift to an earlier time of q samples in the time synchronization stage, the signal after CP removal becomes

$$\mathbf{y}'(i) = [y_{N-q}(i) \dots y_{N-1}(i), y_0(i) y_1(i) y_2(i) \dots y_{N-1-q}(i)]^T \text{ with } q \leq N_{CP} \quad \text{Eq. 2-7}$$

After performing the FFT, we find

$$Y'_k(i) = \frac{1}{\sqrt{N}} \sum_{m=0}^{N-1} y'_m(i) \exp\left(\frac{-j2\pi km}{N}\right) = \frac{1}{\sqrt{N}} \sum_{m=q}^{N-1+q} y_{m-q}(i) \exp\left(\frac{-j2\pi km}{N}\right) \quad \text{Eq. 2-8}$$

Supposing that $p=m-q$, we get

$$\begin{aligned} Y'_k(i) &= \frac{1}{\sqrt{N}} \sum_{p=0}^{N-1} y_p(i) \exp\left(\frac{-j2\pi k(p+q)}{N}\right) = \exp\left(\frac{-j2\pi kq}{N}\right) \cdot \frac{1}{\sqrt{N}} \sum_{p=0}^{N-1} y_p(i) \exp\left(\frac{-j2\pi kp}{N}\right) \\ &= \exp\left(\frac{-j2\pi kq}{N}\right) \cdot Y_k(i) \end{aligned} \quad \text{Eq. 2-9}$$

As shown in Eq. 2-9, the frequency domain samples are affected by a phase rotation which depends on the subcarrier index k but is independent of the symbol number i . As long as the shift q is constant in each OFDM frame, which is the case if the same timing correction is applied to the whole frame, each subcarrier k in training sequence suffers the same phase rotation as the subcarrier k in data sequence. As a result, this phase rotation can be estimated and compensated by the single tap channel estimation using training sequence. The channel estimation method will be described in the section 2.3.3. For the simplicity of illustration, the shift q is integer number of samples. The upper illustration is also valid for a shift with fractional number of samples.

Fig. 2-5 presents the addition of CP to accommodate the spreading of the subcarriers in time caused by CD. The receiver FFT window is carefully chosen so that the ISI part is out of the window. ISI can be completely eliminated, provided that the spreading is shorter than CP length.

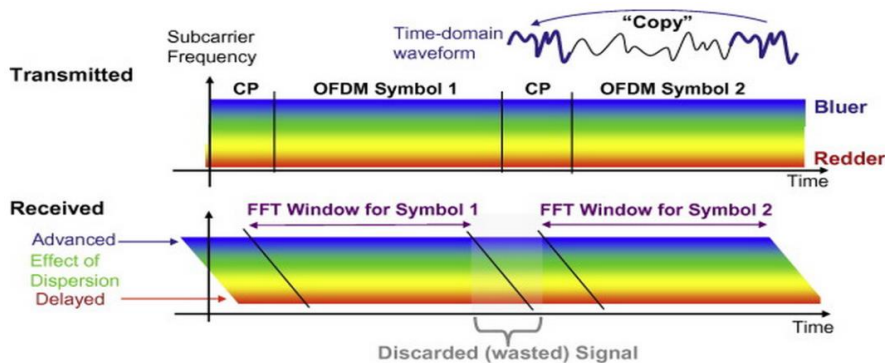


Figure 2-5: Addition of CP to accommodate the spreading of the subcarriers in time, due to chromatic dispersion in an optical fiber, for example. [38]

In optical transmission, CP should be long enough to cover the spreading created by CD and PMD. As CP introduces redundancy and reduces the overall data rate, it puts some constraints over the OFDM dimensioning. The relation between CP length, FFT size, sampling frequency and CP overhead will be discussed in the section 2.4.2 of cyclic prefix dimensioning.

2.2.3 Clipping and PAPR reduction

Clipping is carried out at the last stage of the transmitter DSP in order to reduce the peak-to-average power ratio (PAPR) of the signal. There are several reasons for PAPR reduction. First of all, the ENOB of DAC is limited, so that in the AWG there is a quantization effect. If the PAPR is very high, part of the ENOB will be used only by very few high power samples. The quantization noise will become very high. The average signal power at the output of the AWG will also be very small. Another reason of doing PAPR reduction is the linearity issue of electrical components, such as radio-frequency (RF) amplifier. The response of these components becomes very non-linear for high power signals, yielding to large distortion. Besides, it is also demonstrated that low PAPR OFDM formats, such as DFT-spread-OFDM, suffer less from fiber nonlinearity, leading to better transmission performance over conventional OFDM [39, 40]. Nevertheless, the PAPR increases rapidly with the accumulation of dispersion in the fiber and stabilizes around a certain value which is independent of signal format [41]. The impact of initial PAPR on the transmission performance is very limited over high dispersion fiber.

Among the PAPR reduction techniques, clipping is the simplest one. It consists in defining a largest representable amplitude (A_{max}), so that all the samples whose the amplitude is larger than A_{max} are cut down to A_{max} . Signal distortion will be created by the clipping process. Fig. 2-6 shows the effect of clipping for different DAC resolutions [42]. The signal distortion is characterized by mean squared error (MSE) defined as the average of the squares of the deviations (i.e. the difference between the clipped sample and its initial value). The clipping ratio is defined as the A_{max} divided by the samples' standard deviation. As shown in Fig. 2-6, there is an optimum tradeoff between the clipping and rounding error that minimizes the total distortion. At a DAC ENOB of 5 which is a typical value for current commercial DACs, the optimum clipping ratio is around 7 dB.

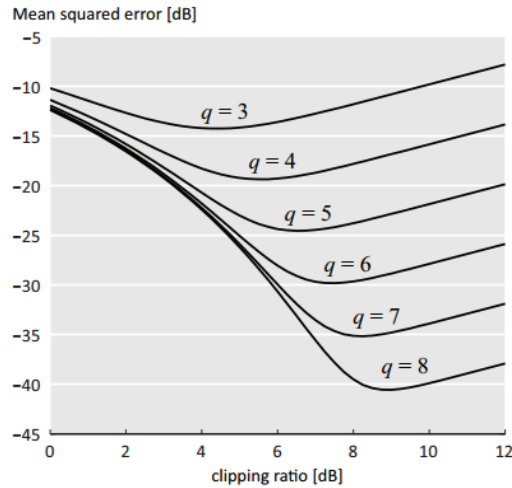


Figure 2-6: Effect of clipping ratio for varying DAC resolution (MSE versus clipping ratio), with q =ENOB of DAC. [42]

Besides clipping, many other techniques are proposed for OFDM signal PAPR reduction [43]. They can be classified into two categories: 1) specific coding schemes and phase optimization before/during/after the symbol mapping; 2) transforms of the time domain signal.

When N signals are added with the same phase, they produce a peak power, which is N times the average power. Therefore, PAPR reduction can be obtained by reducing the possibility of occurrence of the same phase within the N signals, which is the key idea of the coding schemes [44-47]. A simple block coding scheme was introduced by Jones et al. [46], and its basic idea is to map 3 bits data into 4 bits codeword by adding a Simple Odd Parity Code (SOPC) in the last bit. The main disadvantage of this method is the loss of coding rate. Another PAPR reduction technique by implementing CAZAC sequence was recently demonstrated [47]. It consists in multiplying the OFDM symbols by a specific CAZAC sequence called Zadoff-Chu sequence after the symbol mapping stage. This technique does not decrease the coding rate.

The other category consists in making changes over the time domain signal. Nonlinear companding transforms have drawn much attention. The most typical one is μ -law companding [48]. It focuses on enlarging signals with small amplitude and keeping peak signal unchanged, so that the average power of the transmitted signals is increased. Other nonlinear companding transforms, based on error function and exponential function, have been proposed in [49, 50]. They make less impact on the original OFDM power spectrum than the μ -law companding technique, so as to keep the spectrum sharp and rectangular-like after nonlinear companding.

2.3 Receiver DSP procedures

The typical OFDM receiver (Rx) DSP algorithms in long-haul optical communication systems are shown in Fig. 2-7. The first step is time synchronization in charge of identifying the beginning of OFDM symbols. Then, the carrier frequency offset (CFO), which is the frequency difference between the transmitter laser and the local oscillator, is estimated and compensated. The following operations (serial-to-parallel conversion, cyclic prefix removal, FFT, channel estimation using training sequence, phase noise estimation and compensation using pilot tones, demodulation and parallel-to-serial) are carried out in order.

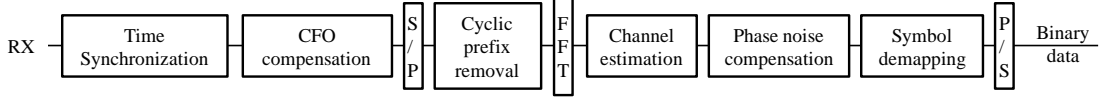


Figure 2-7: Typical OFDM Rx DSP procedures in long-haul optical communication systems.

Some of the Rx DSP procedures will be described in detail. We will start by time synchronization. The impact of time synchronization error is investigated by theoretical calculations and experimental studies. Two time synchronization algorithms, based on OFDM training symbol composed of repeated identical parts, are introduced. The CFO compensation, also called frequency synchronization, is detailed in sub-section 2.3.2, showing the impact of CFO as well as CFO compensation algorithms. The principle of polarization multiplexed channel and a particular training sequence are described in sub-section 2.3.3. Finally, we will present the impact of laser phase noise and phase noise compensation algorithms.

2.3.1 Time synchronization

Doing time synchronization for OFDM consists in finding an estimate of where the symbols start. It is usually the first stage of the receiver DSP. The following DSP steps, such as FFT, channel estimation, phase noise estimation and symbol demapping, are carried out symbol by symbol. Timing estimation error will result in ISI and ICI, because part of the information from adjacent symbols is taken into account for the signal processing of the current symbol. There is some tolerance for timing estimation error when cyclic prefix is over dimensioned for CD and PMD.

The impact of time synchronization error is first shown by theoretical calculation. Experimental demonstration compares the sensitivity of QPSK- and 16QAM-OFDM to inaccurate synchronization, by depicting the constellation and BER degradation. Later on, timing algorithms, based on OFDM training symbol composed of repeated identical parts, will be described.

2.3.1.1 Impact of time synchronization error

As shown in the sub-section 2.2.2 of cyclic prefix concept, in absence of CD and PMD, a shift to an earlier time of q samples with $q \leq N_{CP}$ creates only a phase rotation which can be compensated by training sequence. When the shift of q to an earlier time is larger than CP duration or the shift of q is to a later time, it can no longer be covered by CP. ISI and ICI will be generated. Let's take the second case for illustration: supposing that there is a shift of q to a later time in time synchronization stage, the signal after CP removal becomes

$$\mathbf{y}''(i) = [y_q(i) y_{q+1}(i) y_{q+2}(i) \dots y_{N-1}(i), y_{N-N_{CP}}(i+1) \dots y_{N-N_{CP}+q-1}(i+1)]^T$$

with $q \leq N_{CP}$ Eq. 2-10

For the sake of clarity, here we only consider the case of $q \leq N_{CP}$, i.e. the signal $\mathbf{y}''(i)$ contains part of the CP of the $(i+1)$ th symbol. After performing the FFT, we find

$$\begin{aligned} Y''_k(i) &= \frac{1}{\sqrt{N}} \sum_{m=0}^{N-1} y''_m(i) \exp\left(\frac{-j2\pi km}{N}\right) \\ &= \frac{1}{\sqrt{N}} \sum_{m=0}^{N-1-q} y_{m+q}(i) \exp\left(\frac{-j2\pi km}{N}\right) + \frac{1}{\sqrt{N}} \sum_{m=N-q}^{N-1} y_{m+q-N_{CP}}(i+1) \exp\left(\frac{-j2\pi km}{N}\right) \end{aligned}$$

Let $p=m+q$, we get

$$Y''_k(i) = \frac{1}{\sqrt{N}} \sum_{p=q}^{N-1} y_p(i) \exp\left(\frac{-j2\pi k(p-q)}{N}\right) + \frac{1}{\sqrt{N}} \sum_{p=N}^{N-1+q} y_{p-N_{CP}}(i+1) \exp\left(\frac{-j2\pi k(p-q)}{N}\right)$$

$$= \exp\left(\frac{j2\pi kq}{N}\right) \cdot Y_k(i) + I_k^{ICI}(i) + I_k^{ISI}(i)$$

$$\text{with } I_k^{ICI}(i) = -\frac{1}{\sqrt{N}} \sum_{p=0}^{q-1} y_p(i) \exp\left(\frac{-j2\pi k(p-q)}{N}\right)$$

$$I_k^{ISI}(i) = \frac{1}{\sqrt{N}} \sum_{p=N}^{N-1+q} y_{p-N_{CP}}(i+1) \exp\left(\frac{-j2\pi k(p-q)}{N}\right)$$

As shown in Eq. 2-12, the signal recovered for the k th subcarrier of the i th symbol is constituted of its original signal $Y_k(i)$ with a phase rotation, inter-carrier inference component $I_k^{ICI}(i)$ and inter-symbol interference component $I_k^{ISI}(i)$. The phase rotation depends on the subcarrier number k , but it is independent of symbol number i , so that it can be corrected in the channel estimation stage by training sequence. The ISI and ICI components cannot be compensated, yielding to degraded system performance. It is thus mandatory for OFDM signal to get correct time synchronization.

Fig. 2-8 shows the effect of synchronization error on the constellation of QPSK- and 16QAM-OFDM signal. The constellations are obtained by back-to-back experiments without any noise loading. The FFT size equals to 256 and the number of cyclic prefix samples is fixed at 16. The first couple of constellations shows the signal quality under perfect time synchronization. The following couples depict the signal degradation when the inter-symbol interference is from 1 to 5 samples. The degradation caused by ISI = 1 sample can already be clearly noticed by the eyes. An error of several samples destroys the constellation.

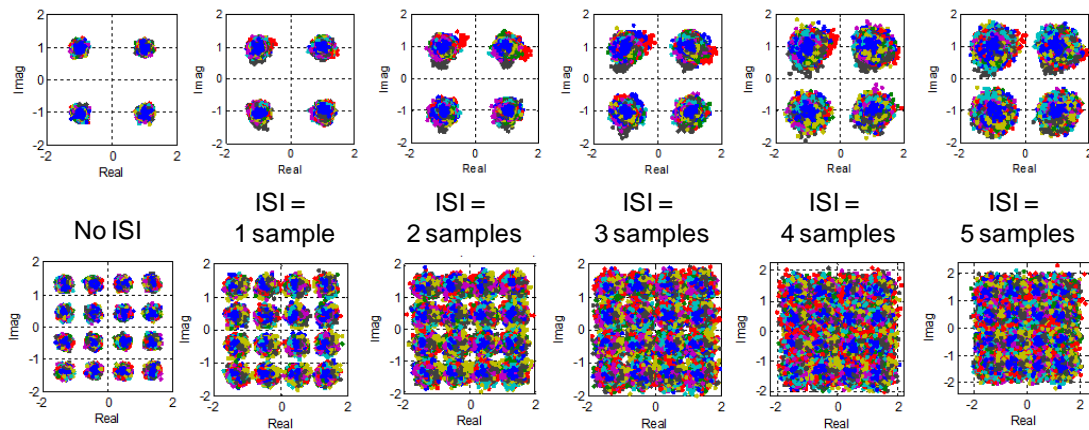


Figure 2-8: Effect of ISI on the constellation of QPSK- and 16QAM-OFDM in experimental back-to-back without any noise loading.

The sensitivity to synchronization error of QPSK- and 16QAM-OFDM is compared in Fig. 2-9. In a back-to-back configuration, the BER of both QPSK- and 16QAM-OFDM with perfect time synchronization is set to 2×10^{-3} by means of noise loading. Then, we add from 1 to 5 samples of synchronization error and record its BER. There is clear BER degradation when ISI is only 1 sample, showing the importance of accurate time synchronization. 16QAM-

OFDM, whose BER is degraded by one decade with an ISI of 4 samples, shows much higher sensibility to synchronization error with respect to QPSK-OFDM.

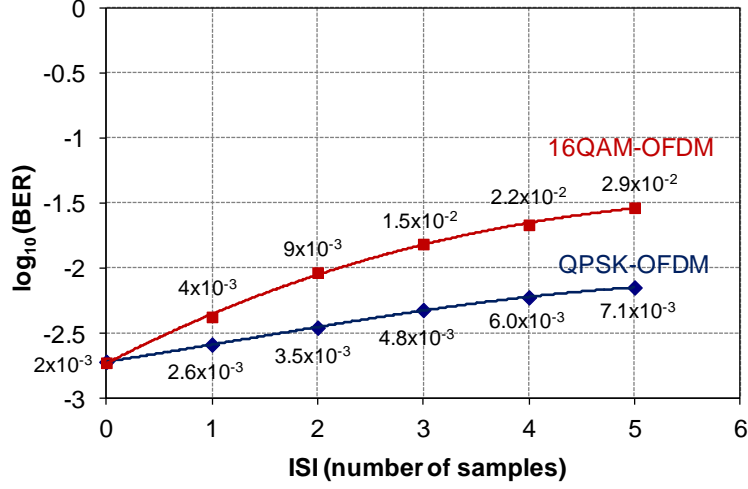


Figure 2-9: BER versus ISI (expressed by number of samples) for QPSK- and 16QAM-OFDM.

2.3.1.2 Time synchronization algorithms

Several time synchronization algorithms have been proposed in the literature. In this work, we will focus on a particular family of timing algorithms based on OFDM training symbol composed of repeated identical parts. The periodicity nature equips time synchronization with robustness against frequency offset. The same symbol can also be used for frequency offset estimation which will be described in the next sub-section. The simplest technique was proposed by Schmidl & Cox in [51]. It consists in using one symbol which has two identical halves in the time domain. The generation of this synchronization symbol can be carried out by two manners. The two halves of the symbol are made identical in the time domain by transmitting a pseudo-random sequence on the even frequencies, while zeros are used on the odd frequencies. In order to maintain approximately constant signal energy for each symbol, the frequency components of this training symbol are multiplied by $\sqrt{2}$ at the transmitter. The other method of generating this synchronization symbol is to use an IFFT of half the normal size to generate the time domain samples. The repetition is now generated using the IFFT, so instead of just using the even frequencies, a random sequence would be transmitted on all of the subcarriers to generate the time domain samples which are half a symbol in duration. Then, time domain samples are repeated to form the synchronization symbol.

The two halves will remain identical after passing through the channel, except that there will be a phase difference between them caused by the carrier frequency offset. If the conjugate of a sample from the first half is multiplied by the corresponding sample from the second half, the result will have a phase of approximately $\phi = \pi T \Delta_{CFO}$, where T is the OFDM symbol duration without CP and Δ_{CFO} is the carrier frequency offset. At the start of the frame, the products of each of these pairs of samples will have approximately the same phase, so the magnitude of the sum will be a large value. Let L be the number of samples in half of the synchronization symbol excluding the CP, the timing metric is defined as in [51]

$$M(d) = \frac{|\sum_{m=0}^{L-1} (r_{d+m}^* r_{d+m+L})|^2}{\sum_{m=0}^{L-1} |r_{d+m+L}|^2} \quad \text{Eq. 2-15}$$

The timing metric reaches a plateau which has a length equal to the length of the CP minus the length of the channel impulse response since there is no ISI and ICI within this plateau to distort the signal. As a result, the OFDM symbol beginning point (excluding the CP) can be set to any point on the plateau. The timing metric of a back-to-back experimental dual-polarization (DP) OFDM signal is shown in Fig. 2-10a. At the transmitter side, the DP signal is emulated by a polarization division multiplexing unit (PDM-unit), in which the second polarization (y polarization) is created by duplicating the first polarization (x polarization) signal and by putting a delay of one symbol duration. Fig. 2-10a only depicts the timing metric of the received x polarization. Due to the polarization mixing in the fiber, there are two plateaus on the timing metric. The first plateau corresponds to the frame beginning point of the x polarization and the second one corresponds to that of the y polarization. The two plateaus are spaced by one symbol duration. Depending on the degree of polarization mixing, the first plateau can be taller or shorter than the second one.

In low OSNR, the accuracy of timing metric is affected by noise, so it is difficult to determine the starting and ending point of the plateau. One of the methods is to simply find the maximum of the timing metric. Another approach is to find the maximum, find the points to the left and right in the time domain, which are 90% of the maximum, and average these two 90% times to find the symbol timing estimate. The averaging method performs better than simply finding the peak of the timing metric [51].

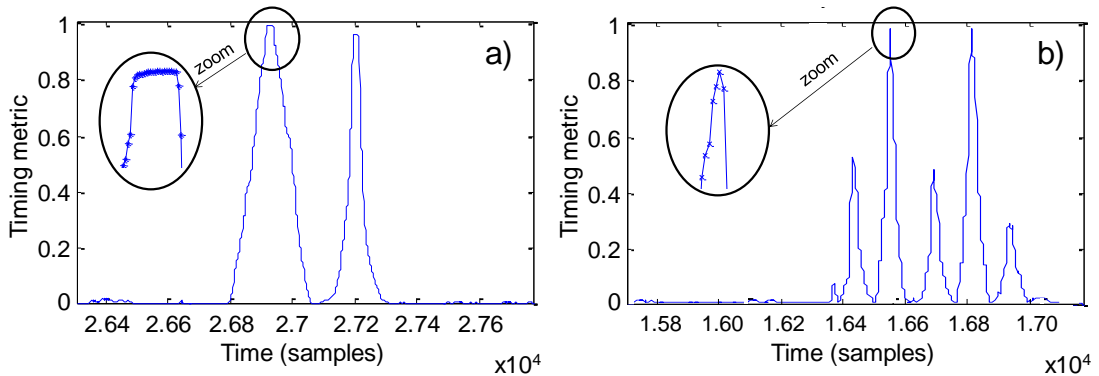


Figure 2-10: The timing metric of the x polarization of a back-to-back experimental DP-OFDM signal a) using Schmidl & Cox synchronization symbol, b) using Minn & Barghava for a synchronization symbol made of L=4 repetitions.

Another approach proposed by Minn & Bhargava [52] extends the Schmidl and Cox original technique by allowing more than 2 repetitions of the basic pattern, and by introducing sign inversion between certain repetitions. These two modifications improve timing estimation by ruling out the plateau problem, yielding timing metrics with steeper roll-off. [52] is focused on the cases of 4, 8 and 16 repetitions, and found that the best performance were obtained with training symbols of the form [+B +B +B-B], [+B +B -B -B +B -B -B -B], and [+B -B -B +B +B +B -B -B +B -B +B -B -B], respectively. The timing metric of the x polarization of a back-to-back experimental DP-OFDM signal using 4 repetitions is shown in Fig. 2-10b.

2.3.2 Frequency synchronization

In general, frequency synchronization comes after time synchronization in the receiver DSP algorithms. In optical communications, frequency synchronization is in charge of compensating the carrier frequency offset (CFO) between transmitter laser and receiver laser

(also called local oscillator). One of the main drawbacks of OFDM is its high sensitivity to frequency offset [35]. Since the OFDM signal is constituted of large number of closely spaced subcarriers with sinc form, each subcarrier has significant side-lobes over a frequency range which includes many other subcarriers. Only at the exact frequency position of each subcarrier, there is no frequency component from other subcarriers. In contrast to the large time synchronization tolerance of OFDM enabled by CP, ICI comes up with the presence of small quantity of CFO.

In this sub-section, the impact of CFO will be illustrated by theoretical calculation and experimental demonstration. CFO estimation algorithms that use the synchronization symbol composed of repeated identical sub-symbols will be presented, as well as the performance of such algorithms evaluated by back-to-back experiments. At last, we will briefly describe a solution for the estimation of large CFO.

2.3.2.1 Impact of CFO

At the receiver, the time domain signal with CFO can be expressed as follows

$$y_m^{CFO}(i) = \exp\left(\frac{j2\pi\Delta_{CFO}((N+N_{CP})i+m)}{f_s}\right) y_m(i) \quad \text{for } 0 \leq m \leq N-1 \quad \text{Eq. 2-16}$$

where Δ_{CFO} is the carrier frequency offset, f_s is the sampling frequency of the discrete signal and $y_m(i)$ is the equivalent time domain signal in absence of CFO. According to Eq. 2-16, the CFO results in a constant phase rotation $\exp\left(\frac{j2\pi\Delta_{CFO}}{f_s}\right)$ between two successive time domain samples. The CFO compensation is usually carried out in two steps: one step compensates the CFO which is multiple of the subcarrier spacing and the other step compensates the rest of the CFO which is less than one subcarrier spacing. As a result, the frequency offset is usually normalized (here noted as ε) with respect to the subcarrier spacing with the following relation

$$\varepsilon = \frac{\Delta_{CFO}N}{f_s} \quad \text{Eq. 2-17}$$

Eq.2-16 can also be written as

$$y_m^{CFO}(i) = \exp\left(\frac{j2\pi\varepsilon((N+G)i+m)}{N}\right) y_m(i) \quad \text{for } 0 \leq m \leq N-1 \quad \text{Eq. 2-18}$$

At the FFT output, we obtain

$$\begin{aligned} Y_k^{CFO}(i) &= \frac{1}{\sqrt{N}} \sum_{m=0}^{N-1} \exp\left(\frac{j2\pi\varepsilon((N+G)i+m)}{N}\right) y_m(i) \exp\left(\frac{-j2\pi km}{N}\right) \\ &= \underbrace{\exp\left(\frac{j2\pi\varepsilon((N+G)i)}{N}\right)}_{\exp(j\phi_i)} \cdot \frac{1}{\sqrt{N}} \sum_{m=0}^{N-1} y_m(i) \exp\left(\frac{-j2\pi(k-\varepsilon)m}{N}\right) \end{aligned} \quad \text{Eq. 2-19}$$

Supposing that the CFO is of integer number of subcarrier spacing, the expression becomes

$$Y_k^{CFO}(i) = \exp(j\phi_i) \cdot \frac{1}{\sqrt{N}} \sum_{m=0}^{N-1} y_m(i) \exp\left(\frac{-j2\pi pm}{N}\right) = \exp(j\phi_i) \cdot Y_{k-\varepsilon}(i) \quad \text{for } \varepsilon \leq k \leq N \quad \text{Eq. 2-20}$$

The signal on the k th subcarrier that we obtain is actually the information of the $(k-\varepsilon)$ th subcarrier rotated by a phase ϕ_i . If the CFO is not an exact integer number of subcarrier spacing, the expression becomes

$$Y_k^{CFO}(i) = Y_k(i) \cdot \exp(j\phi_i) \cdot \underbrace{\frac{1}{N} \sum_{m=0}^{N-1} \exp\left(\frac{j2\pi\varepsilon m}{N}\right)}_{\alpha(\varepsilon)} + \underbrace{\exp(j\phi_i) \cdot \frac{1}{N} \sum_{m=0}^{N-1} \sum_{\substack{l=0 \\ l \neq k}}^{N-1} \exp\left(\frac{j2\pi((l-k+\varepsilon)m)}{N}\right)}_{ICI} Y_l(i)$$

Eq. 2-21

The resulting signal $Y_k^{CFO}(i)$ is the initial signal that we would get in absence of CFO $Y_k(i)$ multiplied by a phase rotation which is common to all subcarriers, attenuated by $|\alpha(\varepsilon)|$ and added by an ICI.

The impact of CFO on QPSK- and 16QAM-OFDM is shown in Fig. 2-11. Experiments are carried out in back-to-back with homodyne detection (same laser for the transmitter and the local oscillator), so that the initial CFO equals to zero. The BER of both formats is set to 2×10^{-3} through noise loading. Then, we add CFO numerically in the receiver. The x-axis represents the CFO normalized to the subcarrier spacing according to Eq. 2-17. From Fig. 2-11, we notice significant BER degradation when the CFO increases. As a consequence, it is essential to have accurate CFO estimation and compensation mechanism. Besides, 16QAM-OFDM is much more sensitive to the frequency offset than QPSK-OFDM. The BER is degraded to 3×10^{-3} at a CFO of 0.007 times of subcarrier spacing for 16QAM-OFDM compared to 0.013 times of subcarrier spacing for QPSK-OFDM.

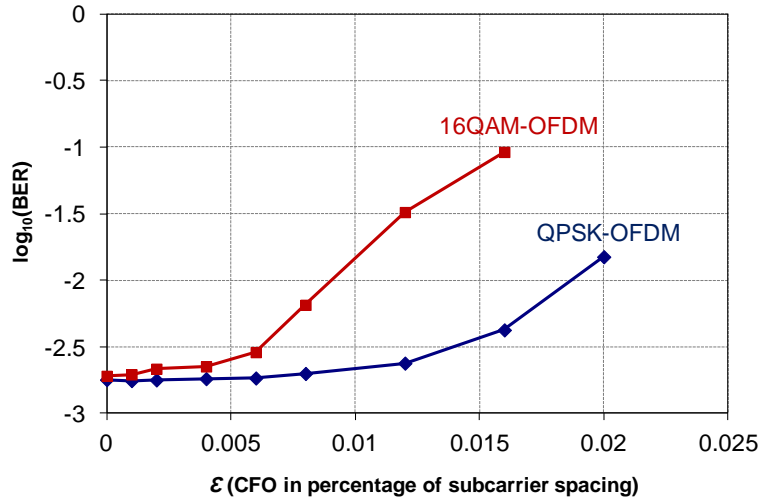


Figure 2-11: BER versus ε (CFO in percentage of subcarrier spacing) for QPSK- and 16QAM-OFDM.

2.3.2.2 CFO estimation algorithms

As mentioned in the sub-section 2.3.1 of time synchronization, training symbol constituted of repeated identical sub-symbols can be used for both time synchronization and CFO estimation. Since CFO creates a constant phase rotation $\exp\left(\frac{j2\pi\Delta_{CFO}}{f_s}\right)$ between two successive samples whose quantity is related to Δ_{CFO} , it is possible to estimate the Δ_{CFO} by calculating the phase difference ϕ between the i th samples of two identical sub-symbols. The CFO estimated is

$$\Delta_{CFO} = \frac{\phi f_s}{2\pi L} \quad \text{for } 0 \leq \phi < 2\pi \quad \text{Eq. 2-22}$$

where f_s is the sampling frequency and L is the distance in terms of number of samples between the two samples calculated. If the training symbol is composed of two identical sub-symbols, then L will be half the FFT size N . The Δ_{CFO} estimated using each sample of the sub-symbol is usually averaged to increase the estimation accuracy.

In order to study the accuracy of CFO estimation using Schmidl & Cox and Minn & Bhargava symbol, we have carried out back-to-back experiments with homodyne detection. Accurate time synchronization is ensured in these experiments. If the CFO estimation performed by the algorithms would be perfect, the CFO estimated should be exactly zero in the homodyne detection configuration. As a result, the value of CFO estimated by the algorithms can be considered as CFO estimation error. Fig. 2-12 and Fig. 2-13 depict the histograms of the CFO estimation error of both algorithms. 1000 iterations are carried out to build the histograms. Fig. 2-12 shows the estimation error of Schmidl & Cox approach at high OSNR without any noise loading and at BER = 2×10^{-3} achieved by noise loading. We notice that the CFO estimation reaches the same accuracy independent of the OSNR. The estimation errors of most iterations are lower than 0.02 times of subcarrier spacing. Fig. 2-13 compares the estimation accuracy of Schmidl & Cox and Minn & Bhargava symbol. We notice that the two algorithms reach equivalent performance.

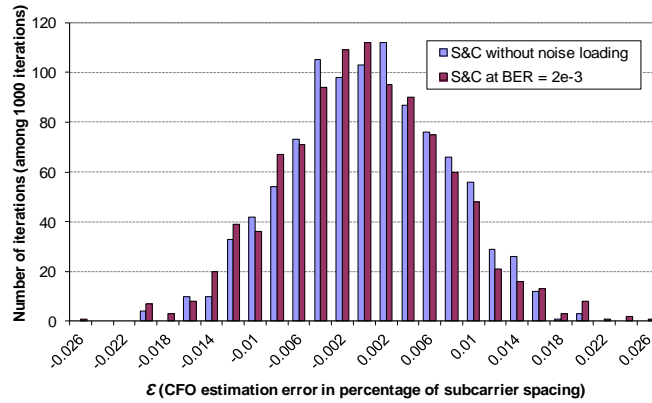


Figure 2-12: Histograms of ϵ (CFO estimation error in percentage of subcarrier spacing) for Schmidl & Cox (S&C) approach at high OSNR without noise loading and at BER = 2×10^{-3} .

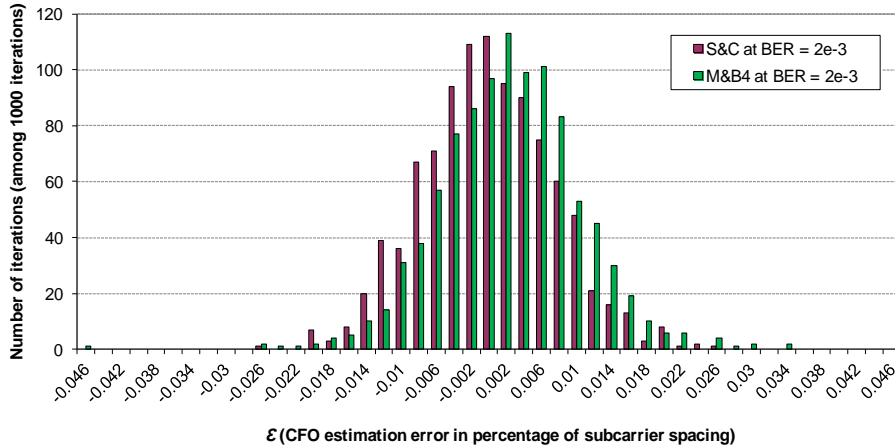


Figure 2-13: Histograms of ε (CFO estimation error in percentage of subcarrier spacing) for Schmidl & Cox (S&C) and Minn & Bhargava (M&B) approach at BER = 2×10^{-3} .

By combining Eq. 2-17 and Eq. 2-22, the CFO ε normalized to the number of subcarrier spacing is

$$\varepsilon = \frac{\phi N}{2\pi L} \quad \text{for } 0 \leq \phi < 2\pi \quad \text{Eq. 2-23}$$

As the phase rotation estimated is between 0 and 2π , the CFO estimated ε also has a range which is between 0 and $\frac{N}{L}$ times of subcarrier spacing. For the Schmidl & Cox approach [51], as two identical semi-symbols are used, the estimation range is between 0 and 2 times of subcarrier spacing. Supposing that the sampling frequency is 32 GHz and the FFT size is equal to 1024, the maximum CFO that can be estimated is 62.5 MHz. For the Minn & Bhargava approach [52], the maximum CFO estimated is 130 MHz, 260 MHz and 520 MHz respectively for the cases of 4, 8 and 16 repetitions. It is thus necessary to keep the CFO within a low value to get right estimation. As ECLs are used for OFDM high data rate transmission, which are not very stable in frequency, it is not easy to keep the CFO always smaller than 500 MHz. As a result, a second estimation algorithm is needed to estimate large quantity of CFO.

2.3.2.3 Large CFO estimation

When the phase rotation between the i th samples of two identical sub-symbols exceeds 2π , only the remainder of the phase rotation divided by 2π is compensated by the upper described method. The phase rotation multiple of 2π remains uncompensated. For the Schmidl & Cox approach, this uncompensated CFO is equal to an even multiple of subcarrier spacing. For Minn & Bhargava, it is also multiple of subcarrier spacing. In Julie Karaki's thesis [53], it is proposed a simple method to estimate CFO of integer subcarrier spacing. It exploits the presence of zero-padding subcarriers on both sides of the spectrum, and attempts to locate the edges of the signal spectrum at the FFT output. First, the average received signal power P_k on each subcarrier over M successive OFDM symbols is computed as

$$P_k = \frac{1}{M} \sum_{i=0}^{M-1} |y_k(i)|^2 \quad \text{for } 0 \leq k \leq N-1 \quad \text{Eq. 2-24}$$

Then, this average power spectrum is cross-correlated with an appropriate frequency mask in order to detect the edges of the signal spectrum and deduce the corresponding frequency shift from the initial location of the edges. It consists in finding the subcarrier index d which maximizes the cross-correlation function

$$M(d) = \max_d \left\{ \sum_{l=0}^{w-1} G_l^* P_{k+l} \right\} \quad \text{Eq. 2-25}$$

where G_l^* is complex conjugate of the l th sample in the frequency mask and w represents length of the frequency mask. One example of frequency mask is (here w is an even number)

$$G_l = \begin{cases} 1 & l = 0 \dots \frac{w}{2} - 1 \\ -1 & l = \frac{w}{2} \dots w - 1 \end{cases} \quad \text{Eq. 2-26}$$

The integer CFO is obtained by subtracting the two subcarrier indices d calculated at the receiver and transmitter side.

2.3.3 Channel estimation

Another important step of the receiver DSP is the channel estimation of dual-polarization OFDM. The coherent transmission with polarization multiplexed signal is a multiple-input multiple-output (MIMO) system with two inputs and two outputs. Assuming perfect time and frequency synchronization, the received signal on the subcarrier k is expressed as

$$\begin{bmatrix} Y_k^{polx}(i) \\ Y_k^{poly}(i) \end{bmatrix} = \begin{bmatrix} H_k^{xx} & H_k^{xy} \\ H_k^{yx} & H_k^{yy} \end{bmatrix} \cdot \begin{bmatrix} X_k^{polx}(i) \\ X_k^{poly}(i) \end{bmatrix} + \begin{bmatrix} N_k^{polx}(i) \\ N_k^{poly}(i) \end{bmatrix} \quad \text{Eq. 2-27}$$

The signal received on each polarization is a linear combination (mixing) of the two polarization-multiplexed transmitted signals. Specifically, for a given subcarrier k , H_k^{xx} and H_k^{yx} represent the energy transferred from the transmitted x polarization towards the received x and y polarizations, respectively. Similarly, H_k^{xy} and H_k^{yy} represent the energy transferred from transmitted y polarization towards received x and y polarizations, respectively.

In single-carrier polarization multiplexed systems, blind MIMO channel estimation using four multi-taps adaptive filters is proven to be an effective approach [54]. When we transpose this method to OFDM, which is multicarrier and requires four multi-taps adaptive filters for each subcarrier, a huge number of filters would be needed, resulting in extremely high computational complexity. It is demonstrated that in a multicarrier system, the computational complexity of a MIMO detector can be greatly reduced by data-aided channel estimation using known training symbols [55]. It is essential that the training symbols of the transmitters are orthogonal so that they can be uniquely identified at the receiver. A simple and typical structure suggested by Jansen [56] has the form

$$\begin{bmatrix} X_k^{polx}(i) & 0 \\ 0 & X_k^{poly}(i+1) \end{bmatrix}$$

Each training period consists of two OFDM training symbols. In each symbol, only one of the two polarizations is filled with known data. The received signal becomes

$$\begin{bmatrix} Y_k^{polx}(i) & Y_k^{polx}(i+1) \\ Y_k^{poly}(i) & Y_k^{poly}(i+1) \end{bmatrix} = \begin{bmatrix} H_k^{xx} & H_k^{xy} \\ H_k^{yx} & H_k^{yy} \end{bmatrix} \cdot \begin{bmatrix} X_k^{polx}(i) & 0 \\ 0 & X_k^{poly}(i+1) \end{bmatrix} + \begin{bmatrix} N_k^{polx}(i) & N_k^{polx}(i+1) \\ N_k^{poly}(i) & N_k^{poly}(i+1) \end{bmatrix} \quad \text{Eq. 2-28}$$

Channel coefficients are estimated by

$$\tilde{H}_k^{xx} = \frac{Y_k^{polx}(i)}{X_k^{polx}(i)} ; \tilde{H}_k^{yx} = \frac{Y_k^{poly}(i)}{X_k^{polx}(i)} ; \tilde{H}_k^{xy} = \frac{Y_k^{polx}(i+1)}{X_k^{poly}(i+1)} ; \tilde{H}_k^{yy} = \frac{Y_k^{poly}(i+1)}{X_k^{poly}(i+1)} \quad \text{Eq. 2-29}$$

An effective method to reduce the impact of the error caused by the noise term is to apply averaging with a moving average algorithm over time and/or frequency [56]. In [53], it is demonstrated that time domain averaging significantly improves the performance. Frequency averaging over 3 subcarriers appears to be helpful. No significant improvement is observed for averaging more subcarriers. Due to the CD, subcarriers far apart from each other experience different phase rotations and thus the channel can no longer be considered as constant in such frequency ranges.

2.3.4 Phase noise compensation

Laser phase noise is a major impairment limiting the performance of OFDM systems. It is a random process caused by the fast frequency fluctuation of the transmitter and receiver lasers. Its effect over OFDM signal is similar to that of the CFO, except that the CFO can be considered as constant within an OFDM frame and creates a constant phase rotation $\exp\left(\frac{j2\pi\Delta_{CFO}}{f_s}\right)$ between two successive time domain samples whereas the laser phase noise, which is a fast frequency fluctuation, creates a random phase rotation between two samples. The phase rotation affecting the k th sample of the i th OFDM symbol can be decomposed into a mean rotation of the i th symbol $\Phi(i)$, also called common phase error (CPE) and a random fluctuation $\Delta\Phi_k(i)$ around the mean:

$$\Phi_k(i) = \Phi(i) + \Delta\Phi_k(i) \quad \text{Eq. 2-30}$$

Supposing perfect time and frequency synchronization, phase noise transfers the receiver frequency domain signal into

$$Y_k^{FN}(i) = Y_k(i) \cdot \exp(j\Phi(i)) \cdot \underbrace{\frac{1}{N} \sum_{m=0}^{N-1} \exp(j\Delta\Phi_k(i))}_{\alpha(i)} + \underbrace{\exp(j\Phi(i)) \cdot \frac{1}{N} \sum_{m=0}^{N-1} \sum_{\substack{l=0 \\ l \neq k}}^{N-1} \exp\left(\frac{j2\pi((l-k)m)}{N} + j\Delta\Phi_k(i)\right) Y_l(i)}_{ICI} \quad \text{Eq. 2-31}$$

Similarly to what is observed with a CFO, the signal is rotated, attenuated and suffers from an ICI. The laser phase noise can be modeled as a Wiener process for which $E[\Phi_k(i)] = 0$ and $E[\Phi_k(i+1) - \Phi_k(i)]^2 = \frac{2\pi\beta}{f_s}$, where β [Hz] denotes the 3-dB linewidth of the power density spectrum of the free-running laser. In [57], the sensitivity of OFDM and single-carrier signal to laser phase noise is compared. Supposing that the CPE is perfectly estimated and compensated, with respect to the $SNR = \frac{E_s}{N_0}$ in absence of carrier phase impairment, a performance degradation D in dB can be approximated by [57]

$$D \approx \begin{cases} \frac{10}{\ln 10} \frac{11}{60} \left(4\pi N \frac{\beta}{f_s}\right) \frac{E_s}{N_0} & \text{OFDM} \\ \frac{10}{\ln 10} \frac{1}{60} \left(4\pi \frac{\beta}{f_s}\right) \frac{E_s}{N_0} & \text{single-carrier} \end{cases} \quad \text{Eq. 2-32}$$

As expected, the performance degradation D of both OFDM and single-carrier decreases with the laser linewidth β . OFDM is more sensitive to phase noise, since its approximate performance degradation contains a multiplicative factor $\frac{11}{60}$ instead of $\frac{1}{60}$ for single-carrier. Besides its performance degradation is also proportional to the FFT size N , which is usually at least 64 or 128. For OFDM, we also notice that the performance degradation is proportional to the symbol duration $\frac{N}{f_s}$, so that increasing the OFDM symbol duration will enhance the ICI caused by phase noise.

Essentially two methods have been proposed in the literature in order to compensate for the laser phase noise. The first one is the use of pilot tones [58] which consists in inserting a certain number of known subcarriers all over the data symbols at the transmitter, as shown in

Fig. 2-3 and Fig. 2-14a. Since these pilot tones suffer the same CPE as data subcarriers, the CPE is estimated by averaging the phase rotation of the pilot tones at the receiver. The temporal fluctuations of the phase inside one OFDM symbol is not taken into account, so the ICI component of Eq. 2-31 remains uncompensated.

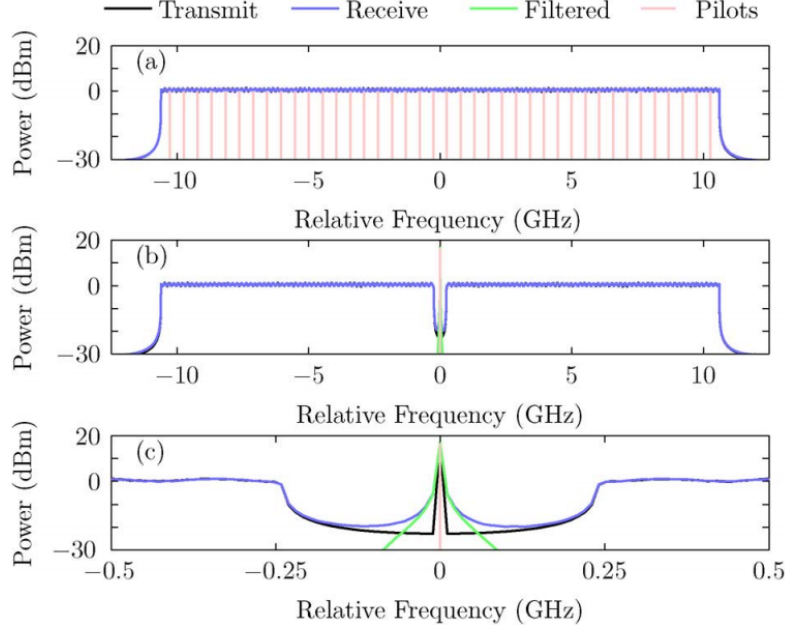


Figure 2-14: (a) Transmitted and received 112-Gbps DP-OFDM spectra with distributed pilots for CPE estimation. (b) Transmitted and received 112-Gbps DP-OFDM spectra and pilot for RF-pilot-based phase noise estimation as well as filtered pilot. (c) Zoomed version of (b). [59]

The other method referred to as RF pilot proposed in [60] concerns both CPE and ICI. It consists in inserting a high power pure tone in the middle of the spectrum, as depicted in Fig. 2-14b. A zoom over the RF pilot is shown in Fig. 2-14c, with the transmitted spectrum drawn in black color and received spectrum in blue. A certain number of subcarriers around this pure tone are set to zero, in order to deal with the spectrum broadening produced by phase noise. At the receiver, a low-pass filter is used to extract the RF pilot. In the time domain, each sample of the RF pilot has experienced the same phase rotation as the data at the same instant, so this method does not only compensate for the CPE but also addresses the fast temporal fluctuations of the phase. Another advantage of RF pilot is that the CFO, including both the fractional and the integer part, is compensated at the same time. To obtain a good estimation quality at the presence of noise and to ensure that the RF pilot does not take too much power compared to data-carrying subcarriers, the power of RF pilot tone needs to be carefully optimized. In [60], a metric of pilot-to-signal ratio (PSR) is proposed

$$PSR[dB] = 10 \log_{10} \frac{P_{RF}}{P_{OFDM}} \quad \text{Eq. 2-33}$$

where P_{RF} and P_{OFDM} represent the electrical power of the RF-pilot and the OFDM baseband, respectively. The optimum PSR is about -15 dB for a back-to-back configuration using ECL lasers [60].

2.4 OFDM dimensioning

As described above, the typical OFDM DSP procedures comprise data-aided dispersion compensation, time & frequency synchronization, MIMO channel estimation and phase noise compensation. Data-aided approaches add overheads to the useful data, thus reducing the available data rate. The overhead percentage is proportional to the number of samples allocated for these data-aided algorithms (i.e. CP, training sequence and pilot tones) and also related to some other OFDM frame parameters, such as FFT size and sampling frequency. The objective of OFDM dimensioning is to achieve a good balance between overhead and DSP performance.

In this section, we will start by indicating the relation between raw bit rate and nominal bit rate, as well as the calculation of each overhead produced by data-aided DSP procedures. The dimensioning of cyclic prefix, which needs to cover the entire pulse spreading produced by CD and PMD, is detailed. We will then introduce the multi-band approach which relaxes the hardware requirement of some electrical components and enables a novel switching scheme: sub-wavelength optical switching. At last, we will present a dimensioning of 400 Gbps OFDM channel by taking laboratory experimental constraints into consideration. The dimensioning considers three modulation formats (QPSK, 8-QAM and 16-QAM) in order to target different spectral efficiency and transmission reach.

2.4.1 Calculation of overheads

The raw bit rate of an OFDM signal is expressed as

$$R_{raw} = f_s \cdot \frac{N - N_{ZP}}{N} \cdot \log_2 M \cdot N_p = B \cdot \log_2 M \cdot N_p \quad \text{Eq. 2-34}$$

where f_s is the sampling frequency, N is the FFT size, N_{ZP} is the number of zero-padding subcarriers, B is the OFDM signal bandwidth, M is the number of points on the constellation and N_p is the number of polarizations which equals to 2 for dual-polarization signal. As the OFDM spectrum has quasi-rectangular form, in the case without zero-padding subcarriers, the signal bandwidth equals to the sampling frequency. Since zero-padding subcarriers are added on the left and right edges of the spectrum, they are not counted into the signal bandwidth and not considered as overhead. The nominal bit rate after removing various overheads is expressed as

$$R_{nominal} = (1 - \varepsilon_{FEC})(1 - \varepsilon_P)(1 - \varepsilon_{TS})(1 - \varepsilon_{CP})R_{raw} \quad \text{Eq. 2-35}$$

where ε_{FEC} , ε_P , ε_{TS} , ε_{CP} represent the overheads of FEC, pilots, training sequence and cyclic prefix, respectively. In our dimensioning, ε_{TS} counts both the overhead of training sequence and synchronization symbol. The overheads are calculated as follows:

$$\varepsilon_{FEC} = \frac{R}{1+R} ; \varepsilon_P = \frac{N_P}{N_{data} + N_P} ; \varepsilon_{TS} = \frac{L_{TS}}{L_{data} + L_{TS}} ; \varepsilon_{CP} = \frac{N}{N + N_{CP}} \quad \text{Eq. 2-36}$$

where R represents the code redundancy of FEC, which is ~7% for typical HD-FECs and ~20% for SD-FECs implemented in actual 100 Gbps / 400 Gbps transceivers. 20% FEC redundancy is equivalent to an overhead of 16.67%.

Pilots overhead is related to the number of pilot subcarriers and the number of data subcarriers. Either using pilot tones or RF-pilot as phase noise estimation method, increasing

the number of pilot subcarriers improves the estimation accuracy but also increases overhead. It is shown that 5 pilot subcarriers achieve good estimation performance for QPSK modulated OFDM signal [53]. Higher modulation formats, such as 16-QAM have higher requirement over the phase estimation quality. Through experimental validation, we found that averaging the phase rotation over 16 pilot tones achieves a good estimation quality for 16QAM-OFDM. When using RF-pilot approach, the reserved subcarriers for phase estimation is composed of RF-pilot subcarrier and the subcarriers switched off on its left / right-hand side. One way to reduce overhead ε_p consists in increasing the data subcarriers, i.e. increasing FFT size.

Training sequence overhead is related to the number of training symbols and data symbols within an OFDM frame. 16-QAM modulation requires approximately 35 training symbols to achieve good channel estimation. Increasing OFDM frame length is a good way to decrease the overhead ε_{TS} , as long as the channel response and the carrier frequency offset remain stationary within the frame duration.

The overhead of CP is related to the number of CP samples and the FFT size. Given the fiber length and the signal bandwidth, the minimum CP duration can be calculated, as detailed in the following sub-section.

2.4.2 Cyclic prefix dimensioning

In order to avoid ISI and ICI, the duration of the cyclic prefix (T_{CP}) has to be larger than the total dispersion introduced by the fiber. This condition can be written as:

$$T_{CP} > \tau_{max} \quad \text{Eq. 2-37}$$

The number of samples in the cyclic prefix N_{CP} is equal to $T_{CP} \cdot 10^9 \cdot f_s$ with f_s expressed in GHz. The former condition becomes:

$$N_{CP} > \tau_{max} \cdot 10^9 \cdot f_s \quad \text{Eq. 2-38}$$

To simplify the dimensioning, we consider that the total dispersion in time is the sum of CD and PMD. By doing so, the worst case is considered. In practice, the accumulated effect of those two dispersions usually is less than their sum. So we have:

$$\tau_{max} = \tau_{max,CD} + \tau_{max,PMD} \quad \text{Eq. 2-39}$$

The chromatic dispersion is caused by the group velocity difference between the various frequencies which constitute the OFDM signal. As a consequence, the maximum accumulated chromatic dispersion corresponds to the group velocity difference between the highest and the lowest frequency in the OFDM signal bandwidth, which can be expressed as:

$$\tau_{max,CD} = LD\Delta\lambda = LD \frac{cB}{f_0^2} \quad \text{Eq. 2-40}$$

where D is the chromatic dispersion parameter in ps/(nm.km), L is the fiber length in km, $\Delta\lambda$ is the bandwidth expressed in wavelength in nm, c is the light velocity in m/s and f_0 is the central frequency of the signal in GHz.

The PMD is caused by the difference of group propagation velocity between the two principal polarization axes of the fiber. At the end of the link, it results in a differential group delay (DGD) between these two polarization states, noted as τ_{DGD} . This delay follows a Maxwellian

distribution, whose maximum value is infinite. The average value of this distribution is defined as the PMD of the fiber link. So, we will dimension the system for a maximum DGD value. The probability that this value be over-passed is called unavailability. In this dimensioning, we consider that the maximum DGD value, $\tau_{max,PMD}$, is equal to 3.3 times the average DGD value, which results in an unavailability of 4.14×10^{-6} and equals to 2 minutes per year. The maximum DGD is thus expressed as:

$$\tau_{max,PMD} = 10^{-12} * 3.3 * P\sqrt{L} \quad \text{Eq. 2-41}$$

where P is the PMD fiber coefficient in ps/km^{1/2} and L is the fiber length in km.

From Eq. 2-39, Eq. 2-40 and Eq. 2-41, the total dispersion in time is equal to:

$$\tau_{max} = 10^{-12} \left(LD \frac{cB}{f_0^2} + 3.3 * P\sqrt{L} \right) \quad \text{Eq. 2-42}$$

For typical fibers and typical transmission distances, $\tau_{max,CD}$ is several hundreds of times higher than $\tau_{max,PMD}$, so chromatic dispersion is dominant. From Eq. 2-40, we notice that $\tau_{max,CD}$ is linearly proportional to the chromatic dispersion parameter D . As a consequence, more CP samples are needed for G.652 fiber (with a $D = 17$ ps/nm/km) than for G.655 fiber (with a $D = 4.3$ ps/nm/km) if other parameters are equal. Besides, $\tau_{max,CD}$ is also linearly proportional to the transmission distance L and signal bandwidth B .

From Eq. 2-38 and Eq. 2-42, the condition on N_{CP} becomes:

$$N_{CP} > 10^{-3} \left(LD \frac{cBf_s}{f_0^2} + 3.3 * BP\sqrt{L} \right) \quad \text{Eq. 2-43}$$

It is worth noticing that the minimum number of CP samples is proportional to the multiplication of the signal bandwidth B and the sampling frequency f_s . f_s is always larger than B , so increasing B means increasing f_s . As a result, the minimum number of CP samples is approximately proportional to the square of B , which means increasing B will increase rapidly the number of CP samples. One way to reduce CP overhead is to increase the FFT size N , which leads to increased computational complexity and increased sensitivity to phase noise. It is thus necessary to make a trade-off between the CP overhead, the computational complexity and impairment created by phase noise.

2.4.3 Multi-band approach

As shown by Eq. 2-34, the raw bit rate of an OFDM channel is related to its bandwidth, modulation order and number of polarizations. Increasing the modulation order will shorten the transmission reach, which may not be suitable for long-haul transmission. The number of polarizations equals to 2 for a polarization multiplexed coherent system. As a consequence, the only way to form high bit rate channel is to increase its bandwidth. It is constrained in turn by the availability of analog to digital (ADC) and digital to analog (DAC) convertors operating with the required bandwidth. Bandwidth and sampling speed limitations prevent the generation of an OFDM signal with high spectral occupancy, which limits the increase of data rate carried by one band. Besides, the ENOBs of DAC and ADC are smaller at high frequencies compared to low frequencies. As a result, a back-to-back performance penalty, i.e. an error floor, could appear over large bandwidth signal.

Conversely, the multi-band OFDM (MB-OFDM) approach decreases considerably the constraints put on the bandwidth and sampling speed of DAC/ADC and is more suitable for long-haul transmission applications. It consists in splitting the global data rate into several OFDM sub-bands generated by several transmitters. Each OFDM band is characterized by low bandwidth and low data rate and is carried by different carriers. Afterwards, the sub-bands are combined together and transmitted. At the receiver each band is detected separately; a filter with bandwidth slightly larger than the bandwidth of each band can be used to select the desired band. MB-OFDM transmission was experimentally demonstrated in [61]. Instead of creating a single-band 120 Gbps DP-OFDM using single DAC, four 30 Gbps DP-OFDM sub-bands are generated by separate DACs. The bandwidth requirement is thus divided by four.

Besides relaxing DAC/ADC bandwidth, an OFDM channel composed of multiple sub-bands of small bandwidth also enables a novel switching scheme, referred to as sub-wavelength optical switching, in the context of elastic optical network (EON). It consists in performing optical aggregation and switching of individual OFDM sub-band inside the channel using ultra-selective optical filters. The proposed ultra-fine switching granularity achieves reduced CAPEX cost for the overall network as well as spectrum saving. A thorough experimental study of the sub-wavelength optical switching will be presented in chapter 4.

2.4.4 400 Gbps OFDM dimensioning considering experimental constraints

In Julie Karaki's thesis [53], a thorough OFDM dimensioning is carried out for 100 Gbps OFDM channel by taking into consideration the experimental constraints of laboratory. A multi-band approach using four sub-bands is adopted in order to relax the bandwidth requirement of DAC/ADC. At the time of her dimensioning, Tektronix 7122B AWG with a sampling frequency of 12 Gsa/s is used for the 100 Gbps experiments. QPSK modulation and HD-FEC are adopted. The bandwidth per sub-band is 8 GHz and the FFT size is fixed at 256. The objective of this dimensioning is to investigate different possibilities for 400 Gbps OFDM channel, in particular using different modulation formats: QPSK, 8-QAM and 16-QAM to achieve different spectral efficiency and transmission reach. The generation of 400 Gbps OFDM in a single-band configuration requires very large bandwidth DAC, so that it will be dimensioned in a multi-band manner. It will also be suitable for the sub-wavelength optical switching study presented in chapter 4.

At the time of the present work, Keysight AWG, with a sampling frequency of 64 GSa/s and a 3-dB bandwidth of ~15 GHz in baseband, is available in our laboratory, permitting higher bandwidth per sub-band. Optical bandwidth is the double of baseband bandwidth, meaning that 15 GHz in baseband corresponds to 30 GHz of optical band. A sub-band bandwidth $B = 18$ GHz is chosen in this 400 Gbps dimensioning. The signal quality at this bandwidth is guaranteed by the new AWG and it permits to transmit 400 Gbps in four 16-QAM modulated sub-bands. The bandwidth B is approximately doubled compared to the former value of 8 GHz.

We will start by the dimensioning of one OFDM sub-band. As shown in Eq. 2-43, the minimum number of CP samples is approximately proportional to the square of signal bandwidth B , so the CP overhead increases significantly with B . Assuming a maximum transmission distance of 1000 km, G.652 fiber (with $D = 17$ ps/nm/km and $P = 0.1$ ps/km^{1/2})

and a sampling frequency of 32 GHz, the maximum dispersion is 2.46 ns and the minimum N_{CP} avoiding ISI is 79 samples. To increase the security margin, we choose $N_{CP} = 128$, which is the minimum power of 2 greater than 79. The CP overhead versus FFT size is shown in Table 2-1. In order to limit the overhead to approximately 10%, to limit the computational complexity and to control the impairment created by phase noise, $N = 1024$ is chosen for the following 400 Gbps experiments.

Table 2-1: CP overhead as a function of FFT size

FFT size (N)	CP overhead (ϵ_{CP})
256	33.33%
512	20.00%
1024	11.11%
2048	5.88%

Table 2-2 summarizes the key OFDM parameters and overheads determined according to the aforementioned formulas. The number of pilots and training symbols are fixed at 16 and 35, respectively, in order to ensure good estimation performance for the three modulation formats: QPSK, 8-QAM and 16-QAM. The frame length is fixed at 1000 symbols, corresponding to a frame duration of 36 μ s. Using the current OFDM parameters, it is demonstrated through experimentation that the channel response remains stationary within one frame. Among the four overheads, FEC and CP are the two that add more than 10% of redundancy.

Table 2-2: Key OFDM parameters and overheads

Frequency parameters	
Sampling frequency (f_s)	32 GSa/s
Bandwidth (B)	18 GHz
Symbol parameters	
FFT size (N)	1024
Number of data subcarriers (N_{data})	560
Number of pilots (N_P)	16
Number of zero-padding subcarriers (N_{ZP})	448
Number of CP (N_{CP})	128
Frame parameters	
Frame length (L_{frame})	1000
Number of training symbols (L_{TS})	35
Number of data symbols (L_{data})	965
Overheads	
FEC overhead (ϵ_{FEC})	16.67%
Pilots overhead (ϵ_P)	2.78%
Training sequence overhead (ϵ_{TS})	3.50%
CP overhead (ϵ_{CP})	11.11%

After fixing the OFDM sub-band parameters, we will determine the number of sub-bands that is required to achieve 400 Gbps of nominal bit rate for each modulation order. The nominal bit rate per sub-band is 50 Gbps, 75 Gbps and 100 Gbps when modulated with QPSK, 8-QAM and 16-QAM, respectively. In order to have minimum 400 Gbps of nominal bit rate, they need 8, 5.33 and 4 sub-bands, respectively. An integer number of sub-bands, which is immediately higher than 5.33, is assigned to 8-QAM, so that the number of sub-bands is fixed at 6, yielding to a nominal bit rate of 450 Gbps. The parameters of MB-OFDM for the three different modulation orders are shown in Table 2-3. A guard-band of 2 GHz is reserved between adjacent sub-bands in order to avoid crosstalk. The spectral efficiencies are 2.53,

3.81 and 5.13, respectively, for the three modulation formats. The 400 Gbps 16-QAM MB-OFDM channel, composed of four sub-bands, is generated experimentally in chapter 3 according to this dimensioning and its spectrum is shown in Fig. 3-26.

Table 2-3:400 Gbps MB-OFDM parameters using QPSK, 8-QAM and 16-QAM

Modulation formats	QPSK	8-QAM	16-QAM
Nominal bit rate per sub-band	50 Gbps	75 Gbps	100 Gbps
Number of sub-bands	8	6	4
Nominal bit rate ($R_{nominal}$)	400 Gbps	450 Gbps	400 Gbps
Raw bit rate (R_{raw})	576 Gbps	648 Gbps	576 Gbps
Sub-band bandwidth	18GHz		
Guard-band	2 GHz		
Total bandwidth	158 GHz	118 GHz	78 GHz
Spectral efficiency (SE)	2.53 bit/s/Hz	3.81 bit/s/Hz	5.13 bit/s/Hz

2.5 OFDM variants with improved features

Apart from the conventional electrical OFDM presented up to now, several OFDM formats with improved features were recently proposed in the literature. As demonstrated in the OFDM dimensioning section, as we increase the signal bandwidth to achieve higher data rate, longer cyclic prefix is needed, leading to an increased overhead and a reduced spectral efficiency. RGI-OFDM, ZGI-OFDM and Offset-QAM have been introduced to eliminate large CP. Another drawback of OFDM is its high transmitter PAPR, leading to high linearity requirement for transmitter components and high fiber nonlinear impairments. Low PAPR formats, such as DFT-Spread-OFDM, have been intensively investigated in the literature.

In Reduced-Guard-Interval (RGI)-OFDM [62], a frequency domain equalizer (FDE) compensates for CD prior to OFDM signal processing at the receiver, as is done in single-carrier FDE equalization. A reduced guard-interval or CP between adjacent OFDM symbols is used to accommodate ISI with short memory, such as that induced by transmitter bandwidth limitations or fiber PMD. This approach enables the reduction of CP to only ~2% in a typical long-haul 100 Gbps OFDM system [62]. Zero-guard-interval (ZGI)-OFDM, which completely remove the CP, is demonstrated in [63]. It uses the channel transfer function estimated from OFDM channel estimation to update the coefficients of the FDE, and thus enables the FDE to compensate for not only CD but also residual linear effects.

Offset-Quadrature Amplitude Modulation (Offset-QAM) [64, 65] is another OFDM variant to eliminate CP. In the single-carrier case of offset-QAM, the principle is to delay the quadrature signal by $T/2$ with respect to the in-phase signal, where T is the symbol period. Offset-QAM OFDM multiplexes multiple sub-channels carrying offset-QAM data, with $\pi/2$ phase difference between adjacent sub-channels. This scheme has been shown to exhibit greatly reduced crosstalk levels due to the relaxed requirements for sub-channel orthogonality. The principle of encoding and decoding of DFT-spread offset-QAM OFDM is described in [64]. In addition to the delay of $T/2$ and the phase different of $\pi/2$ between odd and even subcarriers, FIR filters are applied to the signal at the output of the transmitter IFFT. The required GI length for dispersion compensation in offset-QAM OFDM is twice the subcarrier spacing compared to full OFDM bandwidth for conventional OFDM. In absence of GI, negligible penalty with respect to conventional OFDM is achieved in experimental validations [64].

Discrete Fourier Transform (DFT)-spread-OFDM is a technique used in wireless uplink applications and offers lower PAPR than OFDM. It has recently been adopted in optical transmission. The additional DSP expense paid for the lower PAPR is an additional pair of DFT and inverse DFT (IDFT), with the DFT implemented at the transmitter and the IDFT at the receiver. Higher nonlinear tolerance of DFT-spread-OFDM over conventional OFDM is demonstrated [39, 40]. Nevertheless, the PAPR increases rapidly with the accumulation of dispersion in the fiber and stables around a certain value which is independent of signal format [41]. The impact of initial PAPR on the transmission performance is very limited over high dispersion fiber.

The aforementioned OFDM variants offer slight improvement with respect to conventional OFDM when focusing on spectral efficiency or transmitter PAPR. These are not critical features in the studies carried out in the present thesis, so that we will only implement conventional OFDM in the following simulation and experimental studies.

Besides electrical OFDM whose time domain data is obtained through electronic IFFT, all-optical (AO)-OFDM [66-69] is another approach for generating an OFDM signal. Individual laser sources at equidistant frequencies serve as subcarriers onto which IQ modulators encode the information to be transmitted. The modulated subcarriers are then combined with an optical coupler or WDM combiner to form the OFDM signal. We will only study electrical OFDM in this thesis.

2.6 State of art of OFDM transmission experiments

A number of laboratory experiments have been carried out to evaluate the potential of OFDM for future long-haul and submarine transmission systems. The results of some typical experiments are listed in Table 2-4. Advanced modulation formats, such as 8-QAM, 16-QAM and 32-QAM, are adopted in order to carry high data rate. Low ASE noise amplifications schemes, ultra-low loss large effective area fiber (ULL-LAF), short span length and advanced DSP algorithms are investigated to increase the transmission reach. Three amplification methods: EDFA-only, Raman/EDFA hybrid and Raman-only are chosen in the experiments. A majority of them use ULL-LAF instead of SSMF and a span length shorter than 100 km. Most of them use SD-FEC with 20% overhead and some have even higher overhead (33.75% and 37.1%). Nonlinearity compensation algorithms are also implemented to improve the nonlinear tolerance of high order modulation formats.

Transoceanic distance is achieved using 8-QAM and 16-QAM formats. For 8-QAM, as demonstrated in [70], the use of ULL-LAF with 60.6 km span length and 20% overhead SD-FEC is sufficient. Whereas for 16-QAM, as shown in [71], the use of 33.75% overhead SD-FEC and nonlinearity compensation algorithm is necessary. The possibility of using even higher modulation levels, such as 32-QAM, is also demonstrated. A 256-QAM modulated transmission is shown in [72], which has twice the SE of 16-QAM and four times of QPSK. Its transmission distance is very limited (800 km) even using Raman amplification, ULL-LAF, very high overhead SD-FEC and nonlinearity compensation algorithm.

Table 2-4: Examples of OFDM transmission experiments using high order modulation formats

Ref.	Modulation format	Amplification technique	Fibre type	Span length	FEC	Nonlinearity compensation	Transmission distance
[61]	8-QAM	Raman/EDFA hybrid	SSMF	82 km	7% HD-FEC	No	1,000 km

[70]	8-QAM	EDFA only	ULL-LAF	60.6 km	20% SD-FEC	No	10,181 km
[73]	16-QAM	Raman only	ULL-LAF	100 km	7% HD-FEC	Pre- and post-DBP	2,000 km
[74]	16-QAM	EDFA only	SSMF	75 km	20% SD-FEC	No	2,175 km
[75]	16-QAM	EDFA only	ULL-LAF	60.6 km	20% SD-FEC	No	4,242 km (with > 1.6-dB Q-factor margin)
[76]	16-QAM	Raman only	ULL-LAF	100 km	20.5% SD-FEC	Pre- and post-DBP	4,800 km
[71]	16-QAM	EDFA only	ULL-LAF	60.6 km	33.75% SD-FEC	Multi-band DBP	10,181 km
[77]	32-QAM	Raman only	ULL-LAF	100 km	20.5% SD-FEC	Pre- and post-DBP	1,600 km
[75]	32-QAM	EDFA only	ULL-LAF	60.6 km	20% SD-FEC	Multi-band DBP	4,242 km
[72]	256-QAM (with constellation shaping)	Raman only	ULL-LAF	100 km	37.1% SD-FEC	Pre- and post-DBP	800 km

In [78], the transmission performance of 16-QAM modulated OFDM using two types of fibers: SSMF & ULL-LAF, called ULAF (ultra-large-area fiber) in the paper, are compared, as well as two amplification schemes: EDFA-only & Raman/EDFA hybrid amplification. The span length is fixed at 80 km. It has been shown that the optimum signal launch power is about 2 dB higher in ULAF than in SSMF for transmission over 1600 km under both amplification schemes. As shown in Table 2-5, ULAF offers better performance than SSMF, measured here by the Q^2 factor. Hybrid amplification offers better performance than EDFA. We can note that ULL-LAF and EDFA-only scheme offers better transmission performance than that of SSMF and Raman/EDFA hybrid amplification scheme. Nevertheless, the fiber infrastructure for long-haul core network of most operators is based on SSMF or LEAF. Changing to more efficient fiber requires huge investment.

Table 2-5: OFDM performance comparison after 1600 km's transmission [78]

	Optimum power	Received OSNR (dB)	Received Q^2 (dB)	Q^2 Margin (dB)
ULAF, Hybrid	0 dBm	29	9.3	2.9
SSMF, Hybrid	-2 dBm	28	8.3	1.9
ULAF, EDFA	3 dBm	27	8.7	2.3
SSMF, EDFA	1 dBm	25	6.5	0.1

2.7 OFDM versus single-carrier formats

100 Gbps DP-QPSK single-carrier transceivers are under massive deployment. 100 Gbps DP-QPSK is replacing 10 Gbps NRZ-OOK technique and is becoming the new generation of long-haul technology. 16-QAM modulated single-carrier approach is then investigated for transmitting 200 Gbps channel or 400 Gbps dual-carrier superchannel [13, 79]. To achieve 400 Gbps and 1 Tbps superchannel with optimum spectral efficiency, Nyquist-WDM (N-WDM) is proposed and becomes the most intensively investigated technique [80, 81]. It has rectangular-like spectrum and achieves similar spectral efficiency as OFDM. The Nyquist waveform generation can either be realized by optical filter at the output of the transmitter or by digital filter inside the transmitter DSP. The latter offers more precise waveform but requires DAC as for OFDM signal generation.

Experiments have been carried out to compare the performance of OFDM with respect to single-carrier. Equivalent performance between two techniques was demonstrated [74, 82-85].

[82, 83] compare the performance of the 100 Gbps QPSK modulated dual-polarization MB-OFDM and 100 Gbps single-carrier DP-QPSK over 1000 km dispersion-managed (DM) G.652 fiber line and 1000 km DCF-free G.652 fiber line. 100 Gbps DP-QPSK shows a slightly better performance than 100 Gbps MB-OFDM, which is less than half a BER decade in the various configurations under study. In [74], the performance of both 32-Gbaud QPSK and 16-QAM modulated OFDM and N-WDM is investigated over G.652 fiber line. Both OFDM and N-WDM systems have similar BtB receiver sensitivity, as well as similar nonlinear transmission performance.

Therefore, the optimum format of the next generation transmission system will not be determined by their transmission performance, but more likely by some other features, such as their implementation complexity or flexibility.

2.8 Conclusion

In this chapter, we have presented the IFFT/FFT principle of OFDM, frame structure and key DSP procedures for optical communication, such as cyclic prefix concept, clipping, time & frequency synchronization, channel estimation and phase estimation. Experiments are carried out to illustrate the effect of time and frequency synchronization inaccuracy on the back-to-back performance. 16QAM-OFDM is shown to be more sensitive to both synchronization error compared to QPSK-OFDM. Conventional OFDM employs data aided DSP algorithms which add overhead to useful data. The raw and nominal bit rate expressions as well as the overhead calculation have been presented. It is worth noticing that the cyclic prefix overhead increases rapidly with the signal bandwidth. A 400 Gbps OFDM dimensioning has been carried out that takes into consideration real laboratory experimental constraints. A multi-band OFDM approach is adopted in order to relax the bandwidth requirement for electrical components. Using 18 GHz bandwidth per sub-band, QPSK, 8-QAM and 16-QAM modulated multi-band OFDM need 4, 6 and 8 sub-bands, respectively, to achieve 400 Gbps nominal bit rate. An FFT size of 1024 is chosen as a compromise between cyclic prefix overhead and computational complexity, compared to an FFT size of 256 in the 100 Gbps dimensioning using 8-GHz sub-bands. OFDM formats with improved features have been briefly introduced, such as DFT-spread OFDM which presents low transmitter PAPR, or offset-QAM which permits to eliminate cyclic prefix. A large number of experiments have been carried out to investigate the potential of OFDM for future WDM transmission. High order modulation formats, Raman amplification, ULL-LAF or advanced DSP algorithms are implemented in these experiments in order to improve the spectral efficiency and the transmission reach. Experimental comparisons have shown that OFDM and single-carrier technique have equivalent transmission performance. In the next chapter, we will implement 16QAM-OFDM on our experimental test-bed and investigate its back-to-back and transmission performance in various configurations.

CHAPTER 3

EXPERIMENTAL IMPLEMENTATION AND PERFORMANCE EVALUATION OF 16QAM- OFDM

16-QAM modulation achieves a good compromise between spectral efficiency and transmission reach for the long-haul system beyond 100 Gbps. The aim of this chapter is to carry out the experimental implementation of 16QAM-OFDM, based on the QPSK-OFDM test-bed already existing in the laboratory, as well as to investigate its back-to-back (BtB) and transmission performance in various configurations. First of all, in section 1, the sensitivity of QPSK- and 16QAM-OFDM to practical hardware impairments are investigated by numerical simulation, showing the higher sensitivity of 16QAM-OFDM to all of the four impairments simulated. To achieve good BtB performance for 16-QAM by minimizing the hardware impairments, two new sub-band transmitters using different radio frequency (RF)-drivers are built and evaluated in section 2. The impact of CD and PMD on the system performance is also investigated. After that, we describe the transmitter structure of multi-band OFDM constituted of four sub-bands. The transmission performances of QPSK- and 16QAM-OFDM over two typical fibers (G.652 and G.655) are studied in section 3. With the aim to improve the transmission reach of 16QAM-OFDM, nonlinear mitigation techniques (Volterra nonlinear equalizer and digital back-propagation) are implemented and evaluated in section 4. Finally, in section 5, 16QAM-Nyquist-WDM transmission and reception are implemented over the same test-bed as 16QAM-OFDM. Their BtB and transmission performance are studied and compared to that of OFDM.

3.1 Sensitivity to hardware impairments of QPSK- and 16QAM-OFDM

In this section, we investigate and compare numerically the sensitivity of coherent QPSK- and 16QAM-OFDM to practical implementation impairments, such as laser phase noise, ENOB of DAC, I/Q phase detuning and nonlinear transfer function of complex Mach-Zehnder modulator (CMZM).

3.1.1 Simulation set-up

Numerical studies are carried out by using co-simulations between Matlab and VPI Transmission Maker (VPI-TM). The transmitter part of the co-simulation interface is shown in Fig. 3-1. Matlab runs the DSP related to OFDM at the transmitter side and feeds VPI-TM with the OFDM I/Q signal components of two polarizations. Each component goes through a “Numerical to electrical” module, which indicates to the simulator that the data delivered by Matlab is an electrical signal. I/Q components are then amplified by RF-driver before being converted into the optical domain through CMZM. The two polarizations are combined together by a polarization beam combiner (PBC).

The noise loading and receiver part of the co-simulation interface is shown in Fig. 3-2. “Set OSNR” module, in charge of setting the desired OSNR by adding ASE white noise, is placed between the transmitter and receiver. At the receiver side, the polarization-diversity coherent receiver which separates the X/Y polarizations and I/Q signal components is performed with VPI-TM. “Electrical to numerical” modules convert the four outputs of the coherent receiver into the data format that can be analyzed by Matlab. The latter is in charge of the OFDM DSP at the receiver side.

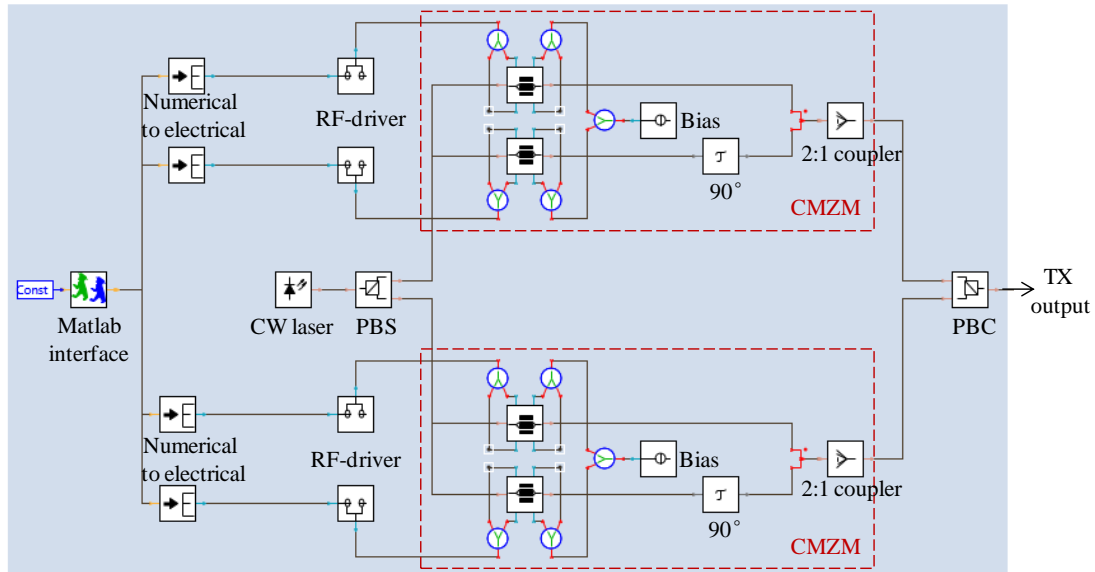


Figure 3-1: Transmitter part of the co-simulation interface, with CW = continuous wave, PBS = polarization beam splitter.

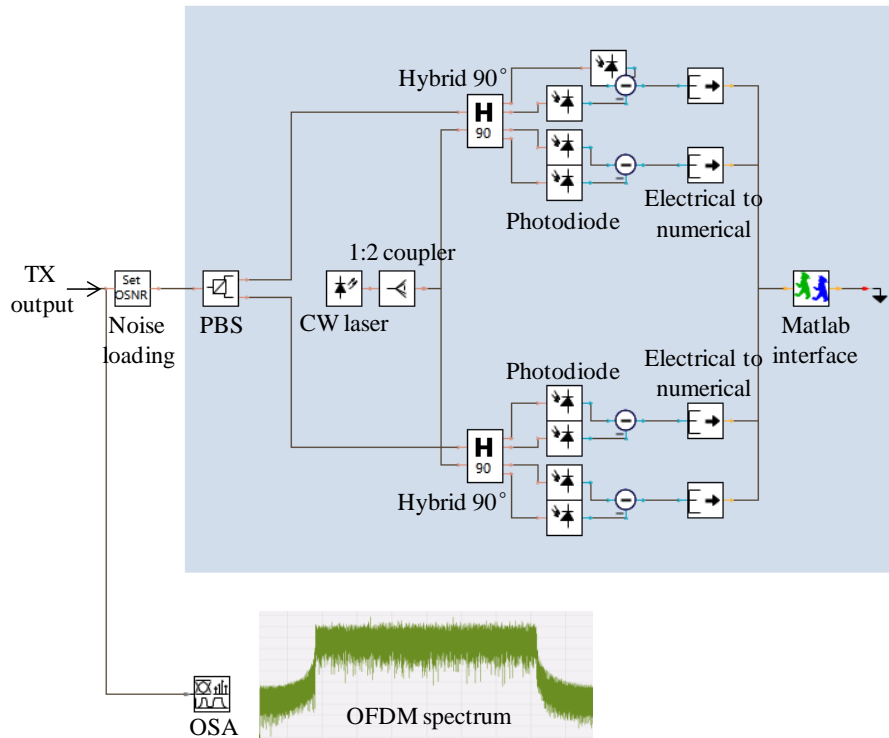


Figure 3-2: Noise loading and receiver part of the co-simulation interface, in inset: the OFDM spectrum observed by VPI-TM optical spectrum analyzer (OSA) module.

3.1.2 Results and discussions

Four co-simulations are performed to study the sensitivity of coherent QPSK- and 16QAM-OFDM to laser phase noise, limited ENOB of DAC, I/Q phase detuning and nonlinear transfer function of the CMZM. We start by the sensitivity to transmitter/receiver laser phase noise. Laser linewidth is specified in the “CW laser” module of VPI-TM. Note that phase noise is added on both transmitter laser and local oscillator. The OSNR penalty (measured for a BER = 10^{-3}) as a function of laser linewidth is shown in Fig. 3-3. Regarding QPSK-OFDM,

the 1-dB OSNR penalty is reached for a linewidth of 300 kHz per laser, whereas 16QAM-OFDM has a significantly more stringent requirement on the laser phase noise, i.e. 70 kHz per laser at 1-dB OSNR penalty.

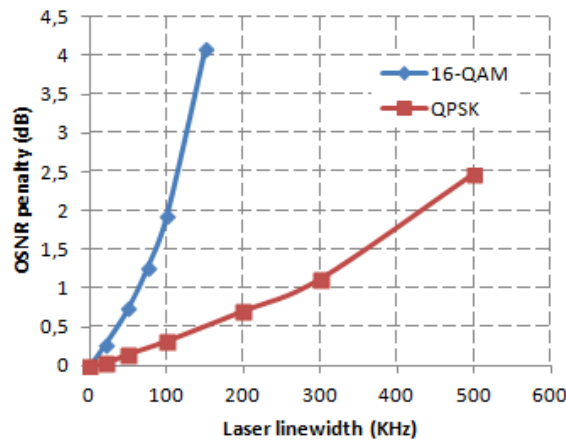


Figure 3-3: OSNR penalty (for a BER= 10^{-3}) versus laser linewidth.

Second, the sensitivity to the ENOB of DAC is investigated. The ENOB assignment is carried out in Matlab by quantizing data before clipping in the DSP part of the transmitter. DAC with an ENOB of 10 bits is taken as reference. OSNR penalties (for a BER = 10^{-3}) are plotted in Fig. 3-4. As expected, 16QAM-OFDM is significantly more sensitive to ENOB degradation than QPSK-OFDM, and it is recommended not to go below an ENOB = 5 bits for 16-QAM and an ENOB = 4 bits for QPSK if we want to limit the OSNR penalty below 1 dB.

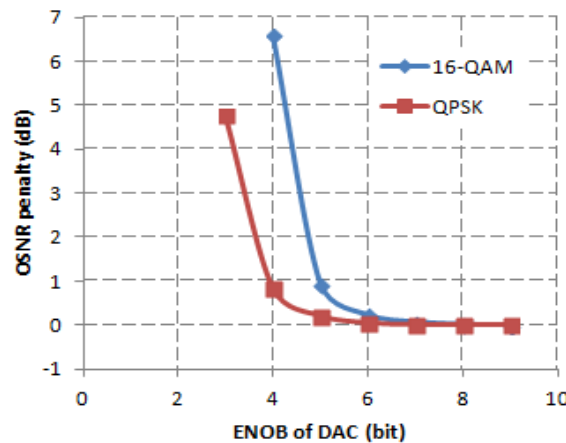


Figure 3-4: OSNR penalty (for a BER= 10^{-3}) versus ENOB of DAC.

The impact of a phase detuning between the I/Q tributaries is studied in Fig. 3-5. The I/Q phase difference is set by the “ τ ” module of the CMZM. The OSNR penalty (at BER = 10^{-3}) is plotted as a function of the I/Q phase difference (the optimal value being 90°). The 1-dB OSNR penalty is reached for an I/Q phase shift of 73° and 82° , respectively, for the QPSK- and 16QAM-OFDM formats. The tolerated deviation with respect to the ideal 90° case is thus equal to 17° with QPSK-OFDM and 8° with 16QAM-OFDM, showing the significantly lower tolerance of 16QAM-OFDM to I/Q phase detuning.

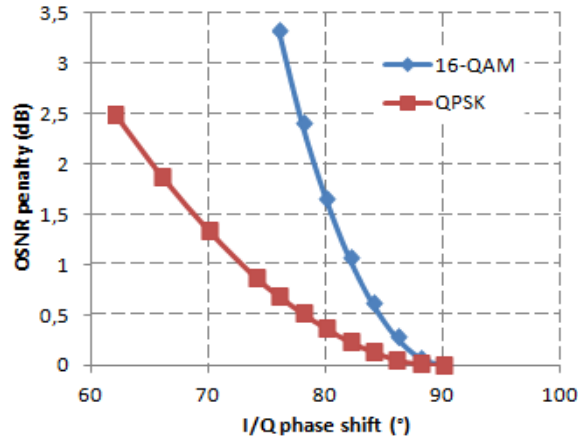


Figure 3-5: OSNR penalty (for a BER= 10^{-3}) versus I/Q phase shift.

Finally, the effect of the CMZM nonlinear transfer function on the OFDM system performance is evaluated in Fig. 3-6. The modulation index (MI), defined as the ratio of the peak-to-peak amplitude of the electrical OFDM signal over the voltage V of the CMZM, is varied in order to excite the CMZM nonlinearities. MI variation is obtained by changing the peak-to-peak amplitude of the electrical OFDM signal, the latter being realized by changing the amplification ratio of RF-driver. For low MI (< 0.5), the CMZM is considered as linear and thus does not degrade the OFDM system performance. At high MI (> 0.5), the nonlinearity of the CMZM transfer function distorts the OFDM signal during the electrical-to-optical conversion, which in turn degrades the OFDM system performance. In Fig. 3-6, the 1-dB OSNR penalty is obtained for a MI ~ 1.75 with QPSK-OFDM and MI ~ 1.25 with 16QAM-OFDM. Once again, 16QAM-OFDM imposes more stringent constraints on the linearity of the electrical-to-optical conversion.

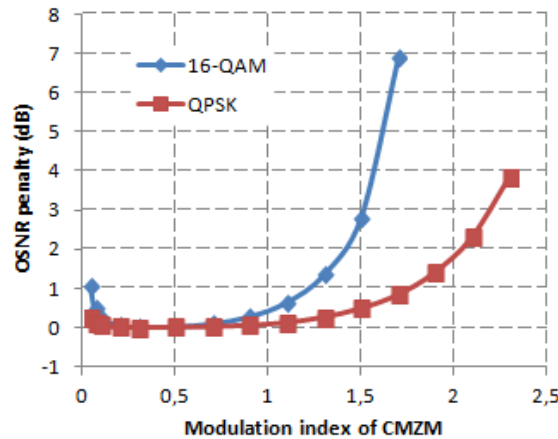


Figure 3-6: OSNR penalty (for a BER= 10^{-3}) versus modulation index of CMZM.

The higher sensitivity of 16QAM-OFDM to implementation limitations has been clearly assessed through the four aforementioned simulation studies. A transmitter that is compliant with QPSK-OFDM may not be able to offer sufficiently good performance for 16QAM-OFDM, due to implementation impairments. This effect can be observed by the appearance of an error floor on the 16QAM-OFDM BtB BER versus OSNR curve. The theoretical BtB OSNR sensitivity difference between the two formats of the same bandwidth is 7 dB, whereas the difference for real transmitters with implementation impairments can be much higher,

especially at high OSNR or low BER values. In the next section, we will show how to optimize the transmitter set-up for 16QAM-OFDM, and report the experimental characterization of the BtB performance of QPSK- and 16QAM-OFDM.

3.2 Back-to-back performance of QPSK- and 16QAM-OFDM

In this section, we will introduce the step by step design of OFDM transmitter and receiver, as well as the back-to-back performance. We will begin by the Tx/Rx design of single sub-band OFDM. We will introduce a first transmitter set-up designed for QPSK-OFDM in 2010 and based on the electrical and optical components available at that time, and then a second transmitter set-up designed for 16QAM-OFDM in 2013. After that, CD and PMD emulation modules will be inserted between the transmitter and the receiver to test the tolerance on linear effects. 20000 ps/nm of CD, 180 ps of first-order PMD and 8030 ps² of second-order PMD will be emulated. Finally we will describe the multi-band OFDM transmitter structure for generating 100 Gbps QPSK-OFDM and 200 Gbps 16QAM-OFDM, as well as the BtB performance of the multi-band signal.

3.2.1 Electrical and optical back-to-back performance

The BtB performance is first evaluated in electrical domain by connecting electrical components of the transmitter to the oscilloscope. After that, single-polarization (SP) optical BtB is performed by adding CMZM and coherent detector. Finally, dual-polarization (DP) optical BtB is carried out by adding polarization-division multiplexing (PDM)-unit.

3.2.1.1 Electrical transmitter design

First-generation QPSK-OFDM electrical transmitter architecture (2010)

Fig. 3-7 shows the electrical part of the transmitter set-up designed for QPSK-OFDM in 2010 with the electrical and optical components available in the market at that moment. Fujitsu FTM7960EX CMZM is used for electrical-to-optical conversion. It is dual-drive and has differential signal inputs, so the RF-driver also requires differential inputs and outputs. In order to feed accordingly the two RF-drivers (one for the I component and another one for the Q component) and IQ modulator, it is necessary to insert a component which generates the signal and its complementary counterpart: this device is denominated as “fanout”. It should work in its linear regime in order to avoid signal distortion, so an attenuation of 16 dB is added at its input. RF-driver is another electrical component that needs to be operated within its linear response zone for OFDM format. Single-carrier signal can be operated at its saturate level, so the requirement over the linearity of RF-driver is much more relaxed compared to OFDM. At the time of this experimental set-up, no RF-driver with large linear response zone designed for coherent OFDM signal generation was commercially available. Therefore two Inphi 2811DZ RF-drivers, which were designed for single-carrier 28 Gbaud DQPSK, were selected. In order to make it work within its linear zone, another attenuation of 6 dB is put before the RF-driver, resulting in a total attenuation of 22 dB overall in the electrical part of the transmitter.

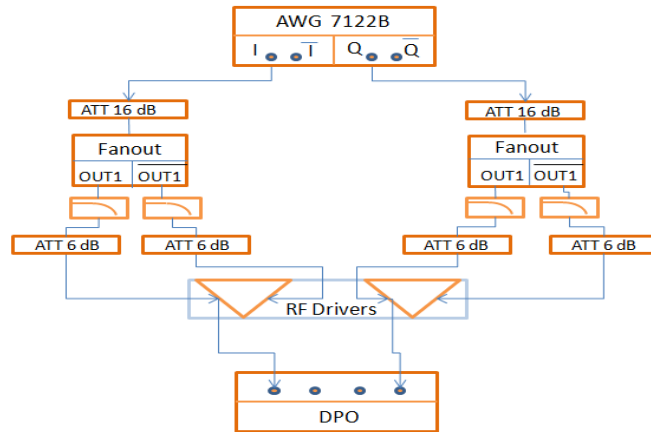


Figure 3-7: Electrical part of the transmitter set-up for differential CMZM. [53]

Tektronix 7122B AWG with a sampling rate of 12 GSa/s is used to generate OFDM baseband signal of 4-GHz bandwidth. Fig. 3-8 shows the baseband signal spectrum in absence of anti-aliasing filter. Aliasing signal appears every 12 GHz which equals to the AWG sampling rate, so the first aliasing signal has a central frequency of 12 GHz and occupies the frequency range from 8 GHz to 16 GHz. Aliasing signals can create crosstalk with other OFDM sub-bands or other channels in the WDM multiplex. Low pass filters (LPF) of 5-GHz bandwidth are added in the transmitter in order to remove aliasing products. The outputs of the RF-driver are connected to Tektronix digital phosphor oscilloscope (DPO) with a sampling rate of 50 GSa/s. Off-line DSP is carried out in Matlab.

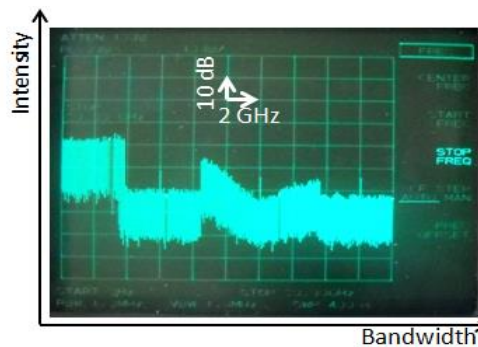


Figure 3-8: OFDM spectrum without anti-aliasing LPF. [53]

Second-generation 16QAM/QPSK-OFDM electrical transmitter architecture (2013)

The electrical part of the transmitter set-up designed for 16QAM-OFDM is depicted in Fig. 3-9. Single-ended Fujitsu FTM7962EP CMZM is used for electrical-to-optical conversion, so that the fanout can be avoided. Two configurations are studied using two different RF-drivers, as shown in Fig 3-9a with Inphi 3212SZ and in Fig. 3-9b with SHF 807. Both RF drives have better linear quality compared to Inphi 2811DZ used in the first transmitter set-up. Inphi 3212SZ is designed for the generation of 100 Gbps single-carrier DP-QPSK, whereas SHF 807 is designed for the generation of single-carrier DP-16QAM and OFDM. An attenuation of 10 dB is added in front of Inphi 3212SZ, in order to achieve linear output. SHF 807 has larger linear range and an attenuation of 3 dB is added in front of it. The output voltage of the AWG is 1 Vpp for both I and Q components, so that the input voltage of Inphi 3212SZ and SHF 807 RF-drivers are 0.3 Vpp and 0.7 Vpp, respectively. The AWG, LPF and DPO remain the same as in the first transmitter set-up. The performance of the electrical transmitter is

evaluated through BER versus SNR curves and will be shown in Fig. 3-11 together with the optical single-polarization transmitter curves. Noise loading is carried out numerically in Matlab at the receiver before the OFDM signal processing procedures. Gaussian white noise is added to the signal according to the desired SNR.

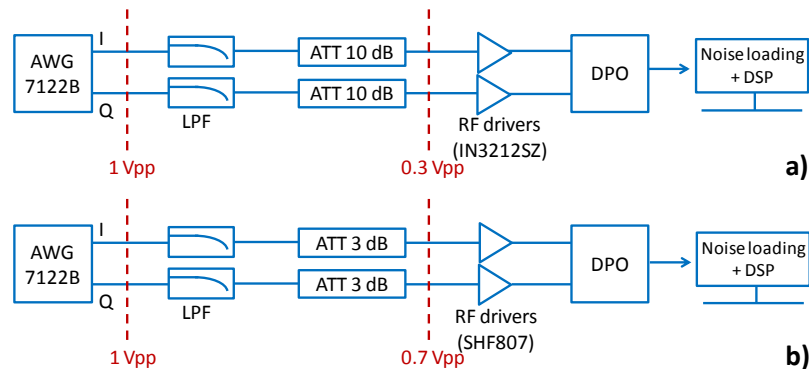


Figure 3-9: Electrical part of the transmitter set-up for single-ended CMZM using (a) RF-driver IN3212SZ, and (b) RF-driver SHF807.

3.2.1.2 Single-polarization back-to-back performance

The next step is to perform electrical-to-optical conversion in the transmitter and the corresponding optical-to-electrical conversion by means of coherent receiver. The transmitter set-up including electrical-to-optical conversion in a single-polarization configuration is depicted in Fig. 3-10. ECL with 100-KHz linewidth at the wavelength of 1552.52 nm feeds the CMZM. A polarization-maintaining (PM) EDFA is placed at the output of the CMZM in order to balance transmitter losses. In the noise loading module, Gaussian white noise is generated, attenuated by variable optical attenuator (VOA) and coupled with the OFDM signal. At the receiver side, an optical band pass filter (OBPF) selects the desired OFDM signal and removes other frequency components. ECL with 100-KHz linewidth is used as local oscillator. Heterodyne detection is implemented, meaning that two different ECLs are used in the transmitter and receiver. The polarization diversity coherent receiver, constituted of two 90° hybrids, allows the separation of the in-phase (I) from the quadrature (Q) component. Their outputs are connected to four balanced photo-receivers, which are themselves coupled to four ADCs of the oscilloscope working at 50 GSa/s.

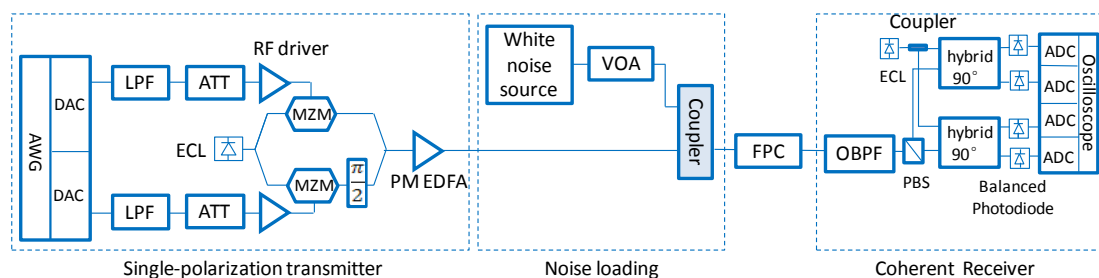


Figure 3-10: SP optical BtB set-up, composed of SP transmitter, noise loading and coherent receiver.

The signal state of polarization (SOP) is changed in the non polarization-maintaining fiber. A fiber polarization controller (FPC) is placed in front of the coherent receiver, in order to align the SOP of the single-polarization signal to that of the x polarization of the receiver. As a result, 100% of the signal power is concentrated on the x polarization and there is only noise

on the y polarization. Only the first two of the four ADCs are activated in the single-polarization configuration.

The BER versus SNR sensitivity curves for two transmitters using Inphi 3212SZ and SHF 807 RF-drivers are shown in Fig. 3-11. The theoretical QPSK and 16-QAM curves are drawn as reference. For the electrical BtB, with the set-up depicted in Fig. 3-9, noise loading is implemented in Matlab before the receiver DSP according to the desired SNR. For the SP optical BtB corresponding to the set-up shown in Fig. 3-10, noise loading is carried out in optical domain between the transmitter and receiver according to the desired OSNR. OSNR is converted to SNR in order to compare electrical and optical BtB sensitivity.

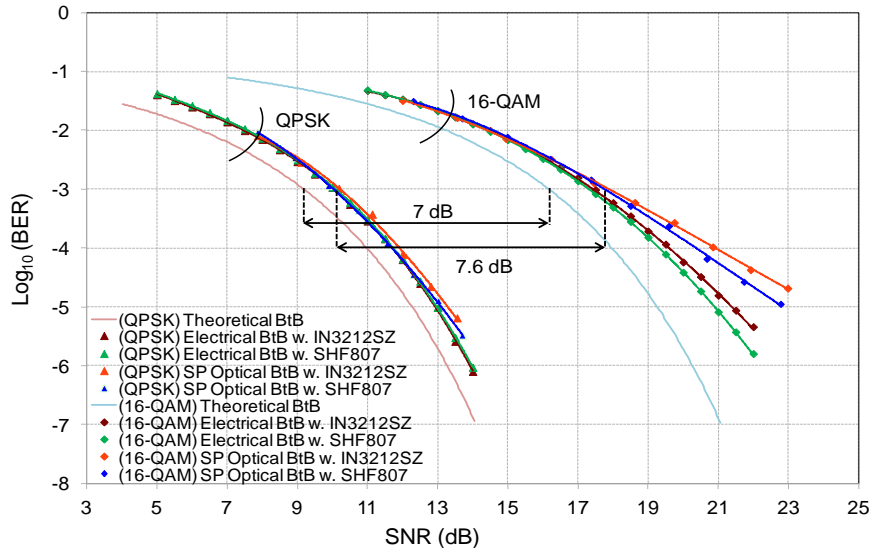


Figure 3-11: BER versus SNR given by theory and measured in electrical and SP optical BtB for QPSK- and 16QAM-OFDM using Inphi 3212SZ and SHF 807 RF-drivers.

As shown in Fig. 3-11, at the same BER, 16QAM-OFDM theoretically requires 7 dB of extra SNR with respect to QPSK-OFDM. For QPSK, equivalent BtB sensitivity is achieved for electrical and SP optical BtB, showing that the electrical-to-optical and optical-to-electrical operations do not have significant impact over the QPSK signal quality. For 16-QAM, a small OSNR sensitivity degradation, which is less than 0.5 dB at $\text{BER} = 1 \times 10^{-3}$, is observed, showing that 16-QAM is more sensitive to CMZM and coherent receiver impairments. There is a sensitivity difference of 7.6 dB between QPSK and 16-QAM at $\text{BER} = 1 \times 10^{-3}$. Besides, the transmitter working with SHF 807 has better performance than the one working with Inphi 3212SZ. The difference is negligible over QPSK curves, but can be clearly noticed over 16-QAM curves, especially at high SNR values.

3.2.1.3 Dual-polarization back-to-back performance

The next step consists in constructing the dual-polarization signal. The DP BtB set-up is depicted in Fig. 3-12. A PDM-unit is added after the PM EDFA, which emulates a dual-polarization OFDM signal. The input signal is duplicated by 3-dB 1:2 coupler. The output on the upper arm is delayed by approximately one OFDM symbol period by means of optical fiber. On the lower arm, a VOA adjusts the optical power in order that the two polarization multiplexed tributaries have the same power. An optical delay line (ODL) gives a fine tuning of the delay. Two polarizers set the upper and lower arm signals onto orthogonal polarizations, before joining the two signals together by PBC. The delay of one OFDM symbol period de-

correlates the signal on the two polarizations. It also facilitates the implementing of the training sequence pattern suggested by Jansen [56] which has the structure [TS 0 TS 0 ... TS 0] on x polarization and [0 TS 0 TS ... 0 TS] on y polarization, where “TS” represents a training symbol filled with known data and “0” represents a zero-padding symbol. Similar to the SP optical BtB configuration, noise loading is carried out by adding Gaussian white noise in the optical domain, followed by the coherent receiver. All of the four ADCs are activated in order to receive the dual-polarization signal.

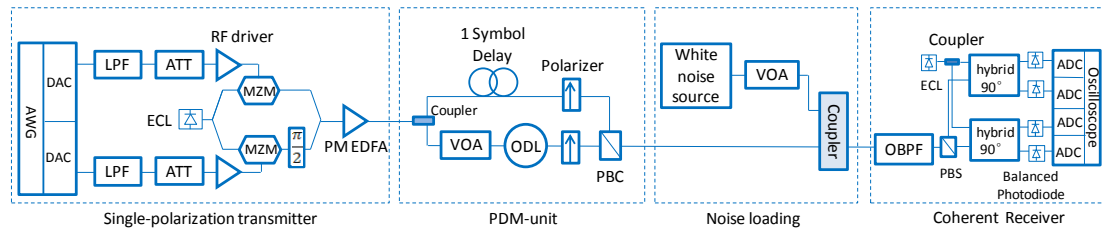


Figure 3-12: DP optical BtB set-up, composed of DP transmitter, noise loading and coherent receiver.

The BER versus OSNR sensitivity curves of SP and DP optical BtB are shown in Fig. 3-13. The QPSK and 16-QAM theoretical curves are given as reference. For the same BER, dual-polarization requires 3 dB of extra OSNR compared to single-polarization. As already depicted in Fig. 3-11, the OSNR sensitivity of 16-QAM is degraded by 7.6 dB with respect to QPSK in the SP configuration, regardless of the type of RF-driver. Whereas in DP configuration, an OSNR sensitivity degradation of 7.8 dB and 8.1 dB are observed, using Inphi 3212SZ and SHF 807, respectively. The performance difference of two RF-drivers is more significant in DP configuration. There is a BER difference of nearly one decade at OSNR = 22 dB between the two 16-QAM DP optical BtB curves.

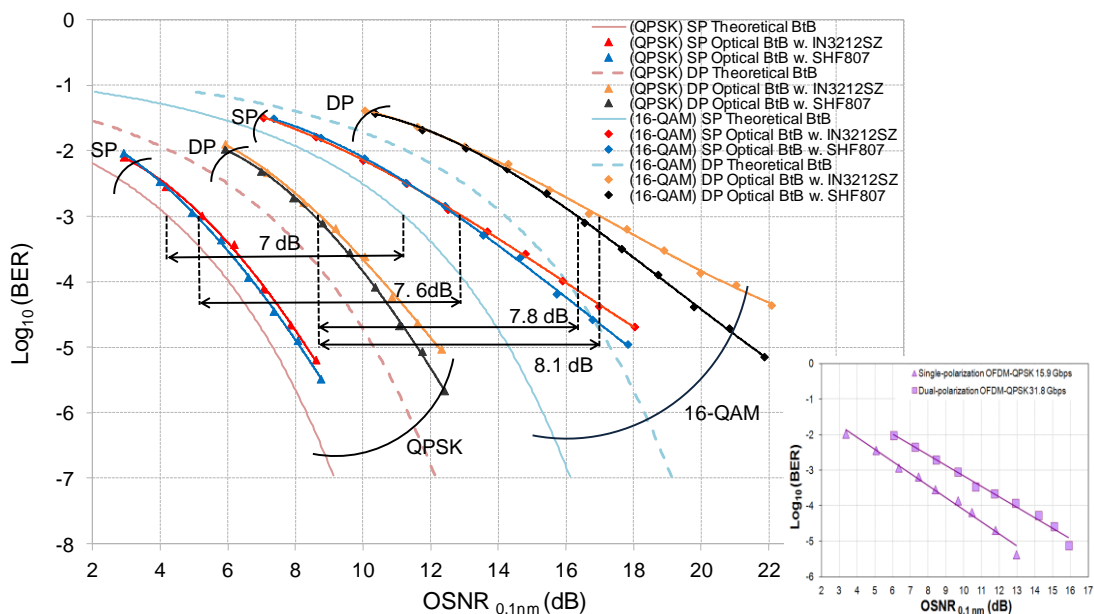


Figure 3-13: BER versus OSNR (in 0.1 nm) given by theory and measured in SP and DP optical BtB for QPSK- and 16QAM-OFDM using Inphi 3212SZ and SHF 807 RF-drivers. In inset, the SP and DP optical BtB for QPSK-OFDM using the transmitter of Fig. 3-7 designed for differential CMZM [53].

The BER versus OSNR curves obtained with the transmitter designed for QPSK-OFDM in 2010 is shown in the inset of Fig. 3-13. The curve with triangle (respectively, rectangular)

points represents the single-polarization (respectively, dual-polarization) QPSK-OFDM BtB sensitivity. At high BER ($= 1 \times 10^{-2}$), the OSNR requirement is approximately 3 dB and 6 dB for SP and DP QPSK-OFDM, respectively. The same OSNR sensitivities are found with the new transmitter. At BER $= 1 \times 10^{-3}$, the OSNR requirement becomes 6.5 dB and 9.5 dB for SP and DP, respectively, which is 1 dB higher than the OSNR sensitivity measured with the new transmitter. At low BER ($= 1 \times 10^{-5}$), the OSNR requirement of the new transmitter is 4-5 dB less. The better BtB performance of the new transmitter is achieved by using more recent RF and optical components. The use of single-ended CMZM permits the removal of fanout and the 16-dB attenuation at its input. Only 3-dB (respectively, 10-dB) attenuation is added to make SHF 807 (respectively, Inphi 3212SZ) operate in its linear response range, compared to 22-dB attenuation in the former transmitter.

We have characterized the electrical, single-polarization and dual-polarization optical BtB performances of transmitters designed for 16QAM-OFDM using two types of RF-drivers. Compared to the first-generation transmitter designed for QPSK-OFDM, significantly better BtB OSNR sensitivity is obtained. The impact of hardware impairment over 16-QAM format is also well controlled. 7.8 dB and 8.1 dB of OSNR sensitivity difference are observed between two modulation formats using Inphi 3212SZ and SHF 807, respectively. Since SHF 807 RF-driver offers better performance, we select the transmitter with this RF-driver for the following experimental studies.

3.2.2 CD and PMD tolerance

As shown in section 2.2.2, thanks to the insertion of cyclic prefix, CD and PMD do not introduce ISI over the OFDM symbol. They only create a constant phase rotation on each subcarrier which can be compensated at the MIMO channel estimation stage, so that there is no need of additional signal processing for CD and PMD compensation. If the cyclic prefix is well dimensioned and the time synchronization is correctly performed, CD and PMD should not induce any impairment on the OFDM signal. In transmission experiments performed over real optical fiber, there is a combination of linear and nonlinear effects which makes it difficult to evaluate if the system is impacted by CD and PMD or not. In this section, we investigate the CD and PMD tolerance of our OFDM system using CD and PMD emulators in BtB configuration before moving to transmission experiments.

The experimental set-up is shown in Fig. 3-14. The dual-polarization OFDM transmitter is connected to CD and PMD module, followed by noise loading module and coherent receiver. Before the PMD emulator, the signal polarization is randomly scrambled by a polarization scrambler (PS) with 70°/ms speed, in order to take into consideration the best case as well as the worst case of PMD during the measurements. The "General Photonics" PMD emulator is able to generate first-order PMD (FOPMD) up to 180 ps and second-order PMD (SOPMD) up to $\sim 8030 \text{ ps}^2$. The second-order PMD effects are represented by frequency dependent terms; the first term known by PDC (polarization dependent chromatic dispersion) is viewed as the chromatic dispersion variation dependent on the polarization. The second term is a result of the rotation of the principle state of polarization (PSP) with frequency. The impact of FOPMD and SOPMD is only a subcarrier polarization rotation that can be easily treated through channel estimation. Two Fixed fiber Bragg grating-based CD emulators (Teraxion ClearSpectrum DCMEX), of 10000 ps/nm each, are used for CD emulation. A total CD of 20000 ps/nm can be emulated. Each of the equipment, i.e. PS, PMD and CD emulator, has an attenuation of 5-8 dB. An EDFA of ~ 20 -dB gain balances the emulator losses.

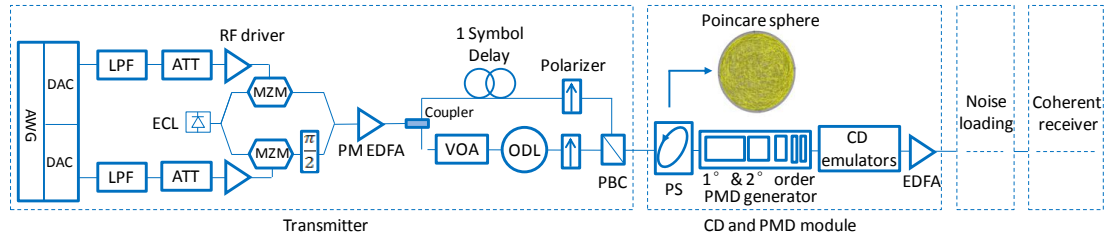


Figure 3-14: Experimental set-up with CD and PMD emulation.

BER versus OSNR results of CD and PMD tolerance are shown in Fig. 3-15. Theoretical curves and BtB curves without (wo.) CD and PMD are plotted as reference for both QPSK and 16QAM-OFDM. A CD of 10000 ps/nm and 20000 ps/nm are emulated, followed by a FOPMD emulation of 180 ps and a SOPMD emulation of 8030 ps². In the "General Photonics" PMD emulator, the generation of FOPMD and SOPMD is coupled. The couple of FOPMD = 126 ps and SOPMD = 8030 ps² makes the highest value of SOPMD for the generator. At last, both CD and PMD emulators are activated to test the tolerance to a maximum value of dispersion. We observe negligible performance degradation for QPSK-OFDM in all configurations and the same for 16QAM-OFDM in most of the configurations. In the last configuration, with a CD of 20000 ps/nm, a FOPMD of 126 ps and a SOPMD of 8030 ps², a slight OSNR penalty arises. This performance degradation is caused by the losses introduced by the PS, the PMD emulator and two CD emulators, which is larger than 20 dB in total. 16-QAM modulation is more sensitive to power losses compared to QPSK.

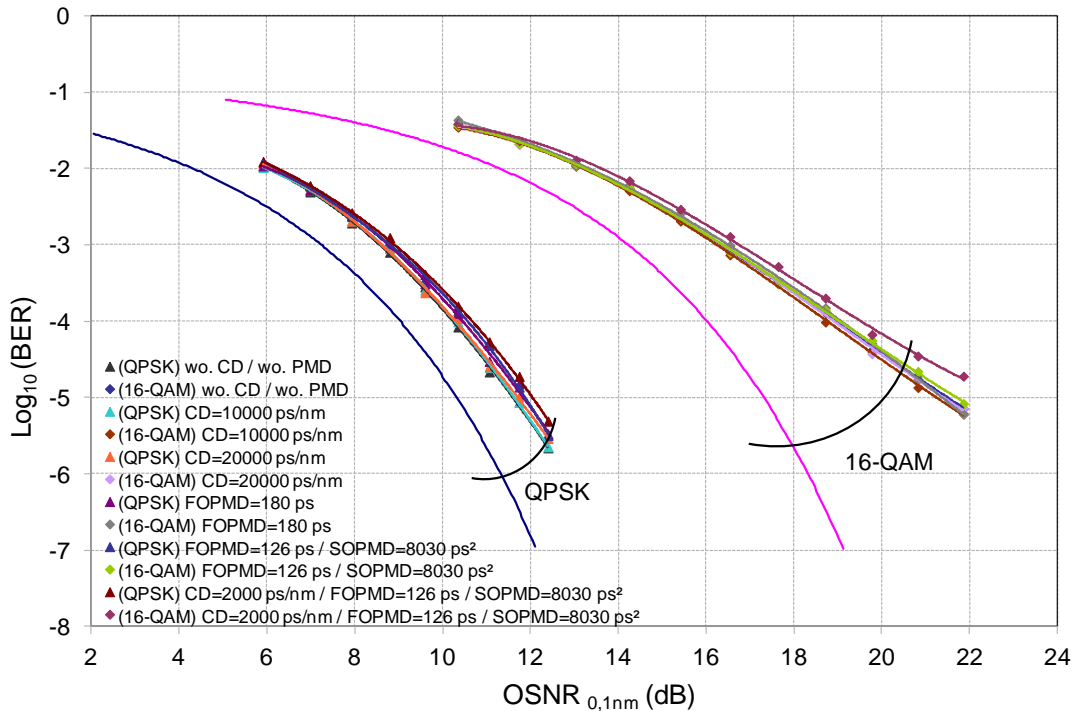


Figure 3-15: BER versus OSNR (in 0.1 nm) given by theory and with various configurations of CD, FOPMD and SOPMD for QPSK- and 16QAM-OFDM.

BtB BER versus OSNR results prove that CD and PMD are totally absorbed by cyclic prefix and do not induce any impairment to OFDM signal. This validates our OFDM dimensioning. The next step is to create a multi-band OFDM channel in order to achieve 100 Gbps (respectively, 200 Gbps) data rate with QPSK (respectively, 16-QAM) modulation.

3.2.3 Multi-band OFDM transmitter

The 100 Gbps QPSK- or 200 Gbps 16QAM-OFDM channel is created by aggregating four OFDM sub-bands. The set-up of DP-MB-OFDM transmitter is depicted in Fig. 3-16. The structure requires two CMZMs and two pairs of DACs, with the first CMZM and the first pair of DAC for the generation odd sub-bands and the second ones for even sub-bands. Four ECLs spaced by 10 GHz are used to locate the four sub-bands. The first and third ECLs, spaced by 20 GHz, are combined together by a PM coupler and amplified by a PM EDFA in order to compensate coupler loss, before feeding the first CMZM. The second and the fourth ECLs feed the second CMZM. A PM EDFA is placed immediately after each CMZM in order to ensure good signal quality. Another PM coupler combines the odd and even sub-bands together, before passing through the PDM-unit. The DP-MB-OFDM signal spectrum is depicted on the right hand side of Fig. 3-16. It occupies a total bandwidth of 38 GHz, and transports 100 Gbps or 200 Gbps of net bit rate depending whether QPSK or 16-QAM is implemented, resulting in a net spectral efficiency of 2.63 bits/s/Hz and 5.26 bits/s/Hz, respectively.

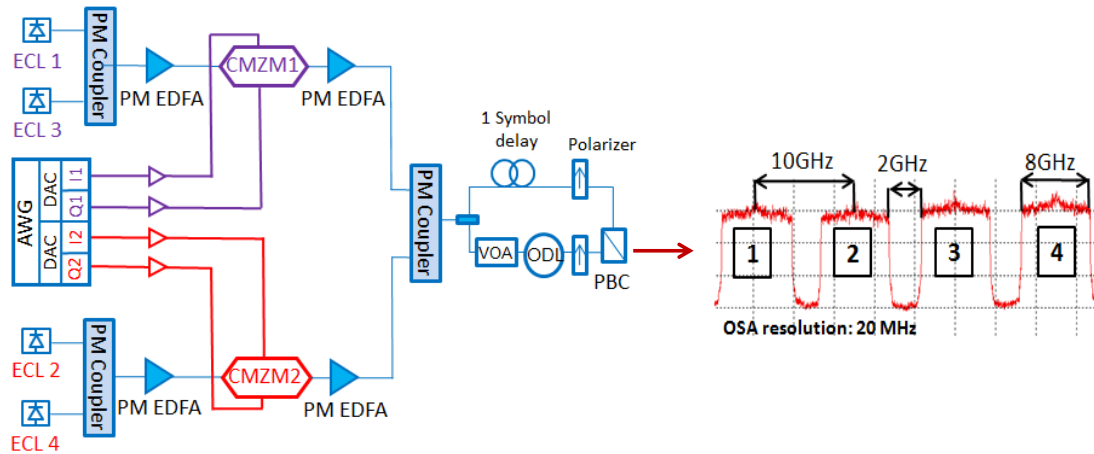


Figure 3-16: (On the left hand side) Set-up of 100 Gbps QPSK or 200 Gbps 16-QAM DP-MB-OFDM transmitter and (on the right hand side) DP-MB-OFDM spectrum.

BER versus OSNR sensitivity curves in BtB of 100 Gbps QPSK and 200 Gbps 16-QAM DP-MB-OFDM are plotted in Fig. 3-17. The soft-decision forward error correction (SD-FEC) threshold is fixed at $BER=2 \times 10^{-2}$, corresponding to a commonly used SD-FEC with 20% overhead [86, 87]. Theoretical predictions are given here as reference. Compared to single sub-band OSNR sensitivity, an extra OSNR of 6 dB is required in order to achieve the same BER. 7.8 dB of OSNR penalty is measured between 100 Gbps QPSK-OFDM (OSNR ~ 14.5 dB at $BER=10^{-3}$) and 200 Gbps 16QAM-OFDM (OSNR ~ 22.3 dB at $BER=10^{-3}$), i.e. the same extra-OSNR penalty (0.8 dB) compared to the single sub-band case, showing that the losses introduced by PM couplers are well compensated by PM EDFAs.

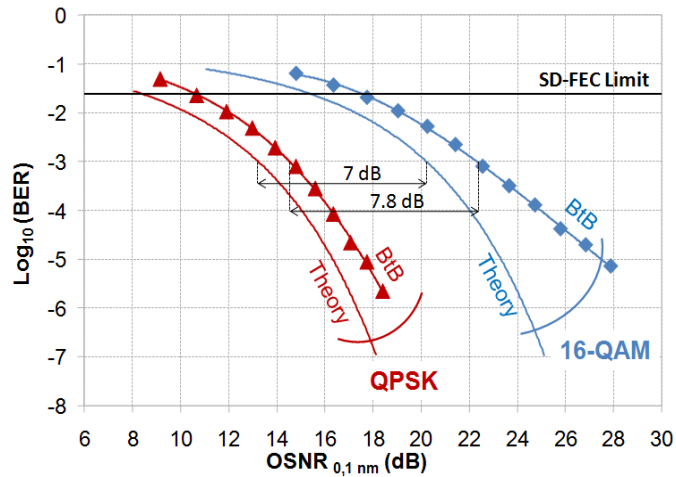


Figure 3-17: BER versus OSNR (in 0.1 nm) given by theory and measured in BtB for 100 Gbps QPSK and 200 Gbps 16-QAM DP-MB-OFDM.

3.3 Transmission experiments over G.652 and G.655 fibers

After having studied the BtB performance of QPSK- and 16QAM-OFDM, it is time to investigate the transmission performance over fiber lines. Two types of fibers: G.652 and G.655, which are the most widely deployed over operators' long-haul WDM links, are chosen for investigation.

3.3.1 Experimental set-up

The transmission test-bed is depicted in Fig. 3-18. The WDM multiplex consists of one 100/200 Gbps DP-MB-OFDM channel at 1552.52 nm carrying QPSK or 16QAM modulation, and 59 other channels modulated at 100 Gbps by single-carrier dual-polarization QPSK (DP-QPSK) format and ranging from 1533.86 nm to 1557.36 nm on the 50 GHz ITU grid. The 100/200 Gbps DP-MB-OFDM generation was described above in Fig. 3-16. Two transmitters are used for the generation single-carrier channels, with one generating odd channels and the other generating even channels. De-correlated $2^{15}-1$ pseudo-random bit sequences (PRBS) are used to drive the I and Q ports of the complex CMZM which generates QPSK constellation. A 10-ns timing delay is introduced between the two replica of the QPSK signal in the PDM-unit in order to generate the DP-QPSK signal. The odd and even 100 Gbps DP-QPSK channels and the 100/200 Gbps DP-MB-OFDM channel are then combined together by means of a 50 GHz interleaver. The WDM signal spectrum recorded at the transmitter side is shown in Fig. 3-19a.

The uncompensated 1000-km transmission line is made of ten 100-km spans of G.652 or G.655 fiber, whose losses are compensated by single-stage EDFA with 20-dB gain and 4.5-dB noise figure. The attenuation, chromatic dispersion (CD) and effective area at 1550 nm of the two fibers under test are: 0.2 dB/km, 17 ps/nm/km and $80 \mu\text{m}^2$ for the G.652 fiber (Corning SMF-28e+®), and 0.2 dB/km, 4.3 ps/nm/km and $72 \mu\text{m}^2$ for the G.655 fiber (Corning LEAF®). A dynamic gain equalizer (DGE) is inserted in the middle of the line in order to flatten the multiplex power. The WDM signal spectrum recovered after the 1000-km transmission is shown in Fig. 3-19b. At the receiver side, the MB-OFDM channel at 1552.52 nm is selected by OBPF and detected by a polarization-diversity coherent receiver using ECL as local oscillator.

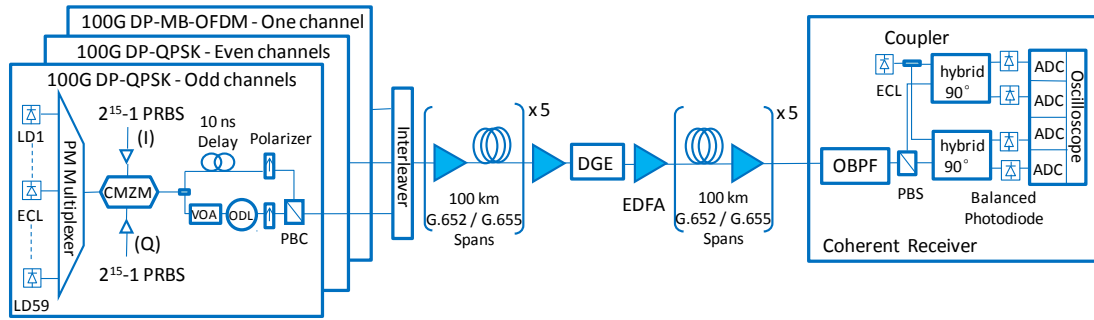


Figure 3-18: Set-up of the 10x100-km transmission test-bed, with the DP-MB-OFDM channel at 1552.52 nm, the 59 odd and even 100 Gbps DP-QPSK channels ranged from 1533.86 nm to 1557.36 nm, the 10x100-km uncompensated G.652/G.655 transmission line, and the coherent receiver.

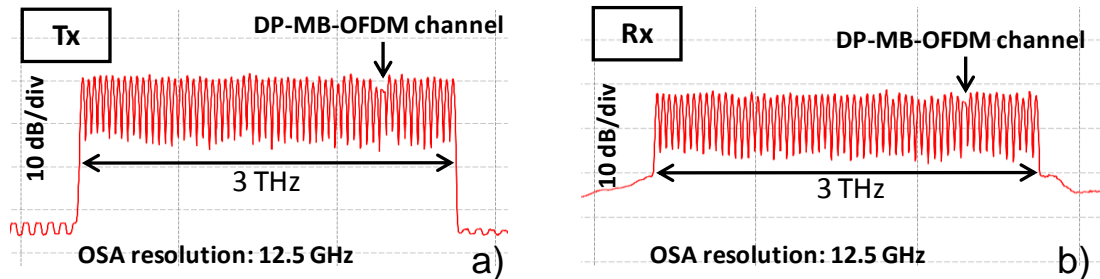


Figure 3-19: (a) Spectrum of the 60 channels at the transmitter side; (b) Spectrum of the 60 channels at the receiver side after the 1000 km of transmission.

3.3.2 Results and discussions

The performance of the 100 Gbps QPSK-OFDM after 1000-km of transmission over either G.652 or G.655 fiber is investigated in Fig. 3-20. In both cases, error free transmission with BERs well below the SD-FEC threshold (fixed here at $\text{BER}=2 \times 10^{-2}$) is achieved. G.652 fiber is significantly more efficient than G.655 fiber in terms of performance: the BER measured over G.652 fiber ($\sim 1 \times 10^{-7}$) at the optimum span input power is 2 decades better than the BER ($\sim 1 \times 10^{-5}$) achieved over the G.655 fiber. Identically, the optimum power injected into the G.652 fiber spans ($P_{\text{in span}} \sim 0$ dBm) is much higher than that injected into the G.655 fiber spans ($P_{\text{in span}} \sim -1.5$ dBm).

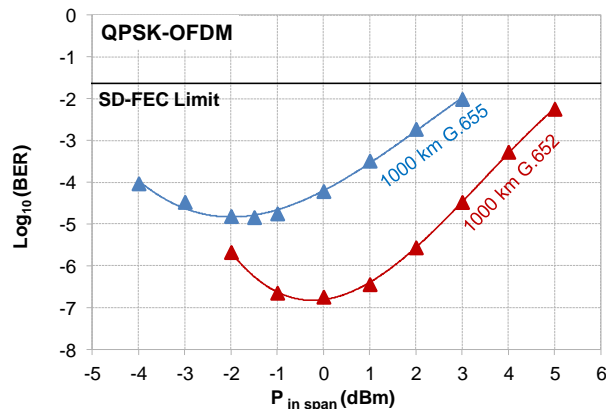


Figure 3-20: BER versus span input power ($P_{\text{in span}}$) for 100 Gbps QPSK-OFDM after 1000 km of transmission over G.652 and G.655 fibers.

The transmission performance of 200 Gbps 16QAM-OFDM is shown in Fig. 3-21. G.652 fiber always gets better performance than G.655 fiber. At the optimum span input power, the BER achieved over the G.652 fiber ($\text{BER} \sim 8 \times 10^{-3}$) is $\frac{1}{2}$ decade better than the BER measured with the G.655 fiber ($\text{BER} \sim 2.3 \times 10^{-2}$). Once more, 1.5 dB higher power can be injected into the G.652 fiber spans when compared to G.655 fiber spans. In order to recover some system margins, a transmission over 500-km of fiber has been finally performed. Over G.655 fiber, BER ($\sim 7 \times 10^{-3}$) is now below the SD-FEC limit and transmission is error-free. Over the G.652 fiber line, nearly one BER decade is recovered after 500-km when compared to the 1000-km case. Note that the optimum span input power over both G.652 and G.655 fibers are approximately identical after 500 km or 1000 km.

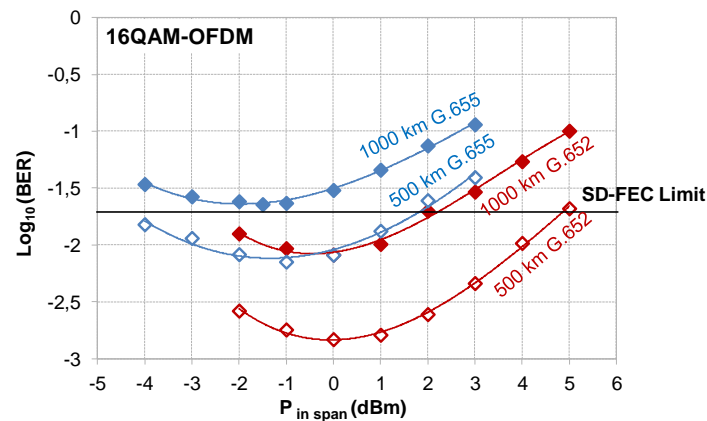


Figure 3-21: BER versus span input power ($P_{in \text{ span}}$) for 200 Gbps 16QAM-OFDM after 1000 km and 500 km of transmission over G.652 and G.655 fibers.

From these comparisons, several conclusions can be drawn. First of all, uncompensated transmission over G.652 fiber with both 100 Gbps QPSK-OFDM and 200 Gbps 16QAM-OFDM is always more efficient than the transmission over G.655 fiber. Due to its higher chromatic dispersion (17 ps/nm/km for the G.652 fiber against 4.3 ps/nm/km for the G.655 fiber) which fully decorrelates the interacting signals and limits the impact of cross-phase modulation (XPM) and four-wave mixing (FWM), G.652 fiber is superior to G.655 fiber. The presence of strong power peaks into the signal constitutes the main limiting factor of uncompensated transmission lines, which have intrinsically high peak-to-average power ratios (PAPR). The fast moving of these peaks over the temporal frame of the signal, as well as their strong temporal decorrelation along the transmission when they belong to different WDM channels are the guarantee that Kerr nonlinearities will not affect too strongly the signal integrity. It can also be noticed that 100 Gbps QPSK-OFDM largely outperforms 200 Gbps 16QAM-OFDM. Its theoretical 7-dB OSNR sensitivity margin provides to QPSK-OFDM modulation a higher robustness to accumulation of ASE noise and fiber nonlinearities than 16QAM-OFDM. Nonetheless, we obtain the outstanding results that error-free transmission is achieved over 1000 km of G.652 fiber with 200 Gbps 16QAM-OFDM.

At last, OSNR sensitivity curves (BER versus OSNR in 0.1 nm) of 100 Gbps QPSK-OFDM and 200 Gbps 16QAM-OFDM (at the optimum span input power) are plotted in Fig. 3-22 and Fig. 3-23. Fig. 3-22 shows that transmission penalties after 1000 km are well-constrained to less than 1 dB (at $\text{BER}=10^{-3}$) with QPSK-OFDM, and that difference between G.652 and G.655 fibers is tiny. The better performance of G.652 fiber is thus explained by its enhanced robustness to fiber nonlinearities permitting to inject higher power into the fiber spans, which

in turn results in better received OSNR (~ 22 dB after 1000 km over G.652 fiber against ~ 20 dB over G.655 fiber). With 16QAM-OFDM at 200 Gbps (see Fig. 3-23), conclusions are identical, except that transmission penalties are superior to those experienced by QPSK-OFDM at 100 Gbps. While no OSNR penalty is observed at $\text{BER}=10^{-2}$ with QPSK-OFDM after 1000 km, already ~ 1 dB of penalty after 500 km of transmission over G.652 fiber and ~ 3 dB after 1000 km are noticeable over the sensitivity curves at this BER value. Note finally that Fig. 3-22 and Fig. 3-23 also explain why the BER differences between G.652 and G.655 fibers are higher after 1000 km of transmission with QPSK-OFDM than with 16QAM-OFDM (2 BER decades against $\frac{1}{2}$). It is simply due to the slope of the OSNR sensitivity curves which is steeper in the range [20-22] dB with QPSK-OFDM than with 16-QAM-OFDM.

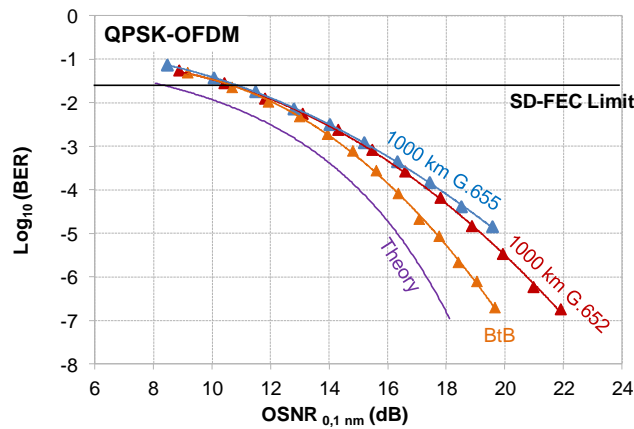


Figure 3-22: BER versus OSNR (in 0.1 nm) given by theory, measured in BtB and after 1000 km of transmission over G.652 and G.655 fibers at the optimum span input power for 100 Gbps QPSK-OFDM.

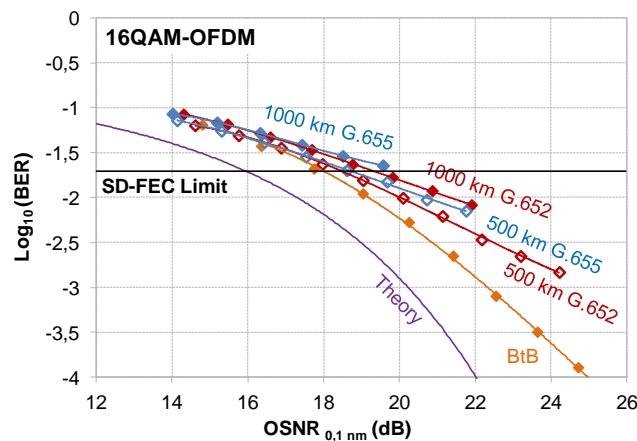


Figure 3-23: BER versus OSNR (in 0.1 nm) given by theory, measured in BtB and after 500 km and 1000 km of transmission over G.652 and G.655 fibers at the optimum span input power for 200 Gbps 16QAM-OFDM.

In this section, we have presented a 10x100km transmission experiment of coherent 100 Gbps QPSK-OFDM and 200 Gbps 16QAM-OFDM over both uncompensated G.652 and G.655 fiber lines. 100 Gbps QPSK-OFDM shows error-free performance after 1000 km of transmission with a $\text{BER} \sim 1 \times 10^{-7}$ over G.652 fiber and $\sim 1 \times 10^{-5}$ over G.655 fiber, providing large OSNR margins for a field implementation. As expected, 200 Gbps 16QAM-OFDM is less efficient, but is still able to achieve 1000 km without error over G.652 fiber line, even if margin with respect to the SD-FEC threshold (fixed at $\text{BER} \sim 2 \times 10^{-2}$) is tiny. We also notice

that G.652 fiber largely outperforms G.655 fiber at 100 Gbps and 200 Gbps whatever the modulation format considered, reinforcing the interest of G.652 fiber infrastructure for modern optical communication systems using high-order QAM.

3.4 Transmission experiments adopting nonlinear mitigation techniques

Transmission reach is the major concern when implementing high order modulation formats, such as 16-QAM, in long-haul WDM systems. Such modulation formats require higher OSNR and have higher sensitivity to nonlinear effects compared to QPSK. As shown in the last section, 16QAM-OFDM achieves 1000-km of transmission reach with little margin with respect to the SD-FEC threshold in a laboratory environment with off-line DSP. The transmission reach of real-time transceivers in a field environment could be reduced to 400 km [13-15], which makes 16-QAM modulation non compliant with long-haul transmission. Nonlinear mitigation techniques improve the transmission reach by compensating fiber nonlinear effects. In this section, the performance of two intra-channel nonlinear mitigation techniques, digital back-propagation split-step Fourier (DBP-SSF) and 3rd order inverse Volterra series transfer function nonlinear equalizer (IVSTF-NLE), are studied experimentally for an OFDM transmission over 10x100 km G.652 fibre line. DBP-SSF is commonly considered as a reference benchmark for nonlinear equalization algorithms. IVSTF-NLE has drawn much attention recently due to its parallel structure, allowing for simultaneous linear and nonlinear compensation of the signal.

The principle of DBP-SSF and IVSTF-NLE is formerly described in the sub-section 1.3.5. We will start by introducing the experimental set-up as well as the three scenarios to be investigated, followed by the experimental results showing the performance of two equalizers.

3.4.1 Experimental set-up

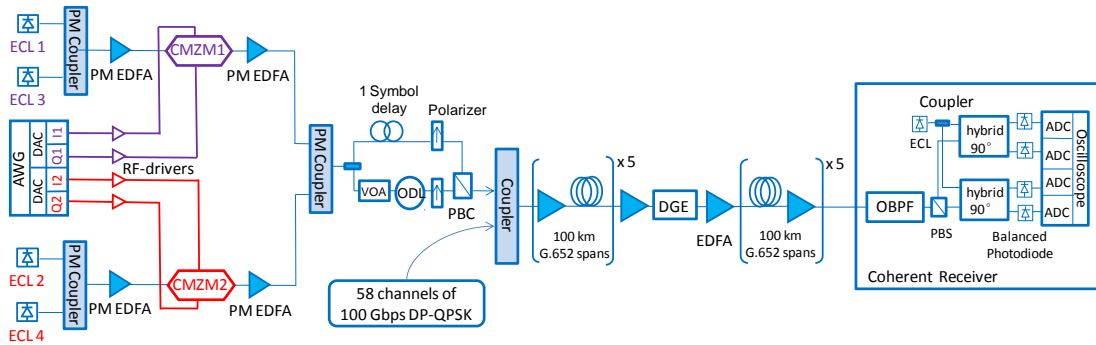


Figure 3-24: Set-up of transmission experiments adopting nonlinear mitigation techniques.

The experimental set-up is depicted in Fig. 3-24, which is similar to that of the aforementioned transmission experiments over G.652 and G.655 fibers. The DP-MB-OFDM channel is combined with fifty-eight 50-GHz-spaced 100 Gbps DP-QPSK channels to form the WDM. The transmission line is constituted of ten spans of 100 km of G.652 SSMF separated by single-stage EDFAs with 20 dB gain and 4.5-dB noise figure. A dynamic gain equalizer (DGE) is introduced in the middle of the link to flatten the multiplex power after 1000 km. At the end of the link, the optical bandpass filter (OBPF) selects the OFDM sub-band under measurement. The latter is detected by a polarization/phase diversity coherent receiver using a 100 KHz linewidth ECL as local oscillator.

The difference between this experimental set-up and the aforementioned BtB and transmission experiments consists in the data rate of DP-MB-OFDM channel. Keysight AWG, with 15-GHz bandwidth and a sampling frequency of 64 GSa/s, is used for the in-phase and quadrature electrical signal generation, in place of the Tektronix AWG 7122B operating at 12 Gsa/s used in the aforementioned BtB and transmission experiments. The new AWG allows the generation of 18-GHz OFDM sub-band, the bandwidth chosen for 400 Gbps 16QAM-OFDM in the OFDM dimensioning section, instead of 8-GHz for 100 Gbps QPSK-OFDM and 200 Gbps 16QAM-OFDM. The ECLs in this configuration are spaced 20 GHz apart, leaving a guard band of 2 GHz between adjacent sub-bands. The spectrum of the 400 Gbps 16QAM-OFDM measured with high spectral resolution (20 MHz) OSA is shown in Fig. 3-25. The total bandwidth of the OFDM channel is 78 GHz corresponding to a nominal spectral efficiency of 5.13 bits/s/Hz.

Hereafter, in order to study the worst case, transmission performances are measured over the third sub-band, which was found to be the most affected among the sub-bands by the various transmission impairments. We use 10^6 bits to evaluate the BER.

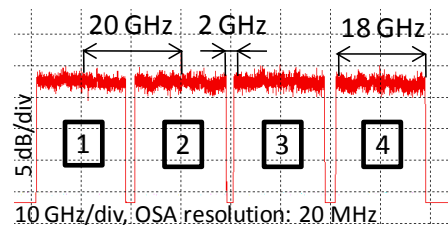


Figure 3-25: Spectrum of 400 Gbps 16-QAM DP-MB-OFDM.

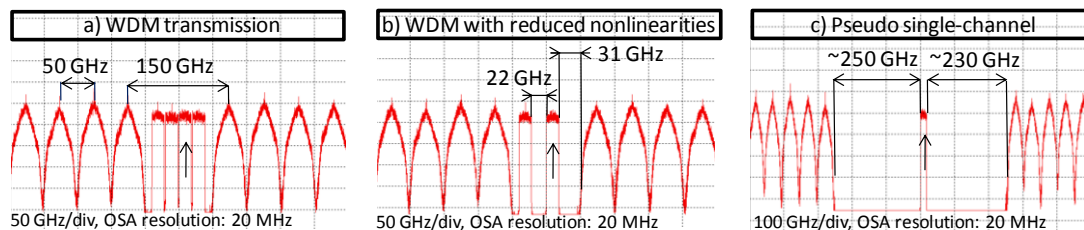


Figure 3-26: Spectra corresponding to the three scenarios under study. The black arrow indicates the sub-band under measurement.

To explore the physical limits of the nonlinear equalizers and the configurations where their performance is maximal, three scenarios are studied. First, a purely WDM transmission scheme with 50-GHz channel spacing is investigated. Then, a configuration with relaxed nonlinear effects is created by turning off the sub-bands 2 & 4. Finally, a pseudo single-channel transmission scheme with only one OFDM sub-band surrounded by large guard-bands is studied. Fig. 3-26 shows optical power spectra recorded for the aforementioned configurations. The first study case, depicted in Fig. 3-26a, is the one which exacerbates as much as possible non-linear effects coming from the channel itself but also from its nearest neighbors. The second one (highlighted in Fig. 3-26b) is an intermediate case, for which nonlinear inter-plays between the channel under study and its neighbors are relaxed. The last one (shown in Fig. 3-26c) corresponds to the pseudo single-channel transmission scenario, for which cross-phase modulation (XPM) and four-wave mixing (FWM) become negligible. As a consequence, the guard-band between the sub-band under measurement and its immediate

left/right neighbors are 2/2 GHz, 22/31 GHz and 250/230 GHz for the case 1, 2 and 3, respectively.

3.4.2 Results and discussions

The transmission performance is first evaluated without any nonlinear equalization (wo. NLE). The Q^2 -factor vs. span input power per sub-band is plotted in Fig. 3-27 for the third sub-band after 1000 km for each study case shown in Fig. 3-26. The optimum Q^2 -factors of all scenarios exceed the 6.25 dB SD-FEC Q^2 threshold (which corresponds to a BER = 2×10^{-2}). Observations from Fig. 3-27 show that the optimum span input power per sub-band increases from ~ -3.5 dBm in the case 1 (the worst one) to ~ -2 dBm in the case 3 (the best one) while at the same time the Q^2 -factor is improved by ~ 1 dB. That demonstrates, as expected, that the pseudo single-channel scenario limits the influence of the non-linear crosstalk between the sub-band 3 and its neighbors.

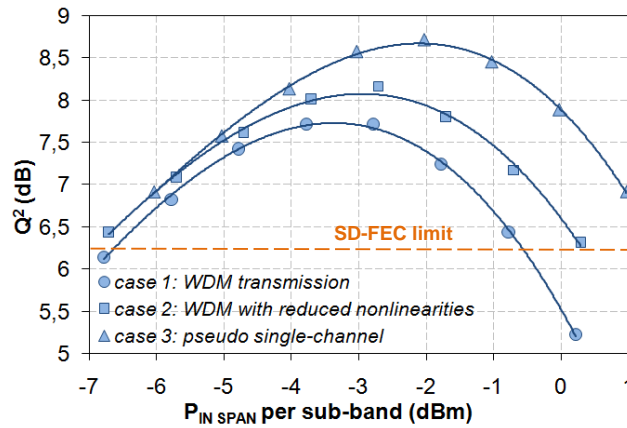


Figure 3-27: Q^2 -factor vs. span input power per sub-band for the three configurations under study.

Subsequently, IVSTF-NLE and DBP-SSF equalizers are introduced into the receiver as a first stage of digital signal processing. Their performances are evaluated Fig. 3-28, Fig. 3-29 and Fig. 3-30. Note that only 1.78 samples per symbol (SpS) is used hereafter for both IVSTF-NLE and DBP-SSF, which corresponds to 32 GSa/s for the sub-band 3 of 18-GHz symbol rate. Further SpS increase provides a marginal performance improvement at the expense of a considerable complexity growth. The abbreviations DBP-SSF1 and DBP-SSF8 denote 1 step-per-span and 8 steps-per-span digital back-propagation equalization, respectively. Note that the Q^2 -factor improvement reaches its maximum at 8 steps per span.

For the first scenario, shown in Fig. 3-28, IVSTF-NLE and DBP-SSF methods yield nearly identical results and provide equivalent Q^2 -factor improvements (i.e. ~ 0.3 dB). At the same time, the optimum span input power per sub-band is increased by ~ 0.5 dB, demonstrating a slight improvement of the nonlinear threshold in the presence of nonlinear equalization. In the second scenario (shown in Fig. 3-29), IVSTF-NLE and DBP-SSF equalizers result in a Q^2 -factor improvement of 0.5 dB and an increase of the span input power per sub-band by ~ 1 dB. Finally, it is in the pseudo single-channel scenario (shown in Fig. 3-30) that IVSTF-NLE and DBP-SSF equalizers are the most efficient. Q^2 -factors are improved by 0.7-0.8 dB, while the non-linear threshold is increased by 1-1.2 dB. Results from the three scenarios show very clearly that nonlinear equalizers are more effective on the compensation of intra-channel nonlinear effects than on the mitigation of inter-channel nonlinear crosstalk.

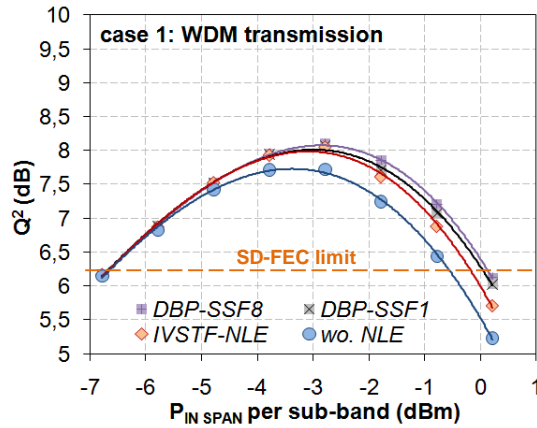


Figure 3-28: Q^2 -factor vs. span input power per sub-band without nonlinear equalization (wo. NLE), with IVSTF-NLE and DBP-SSF for the scenario 1 (WDM transmission).

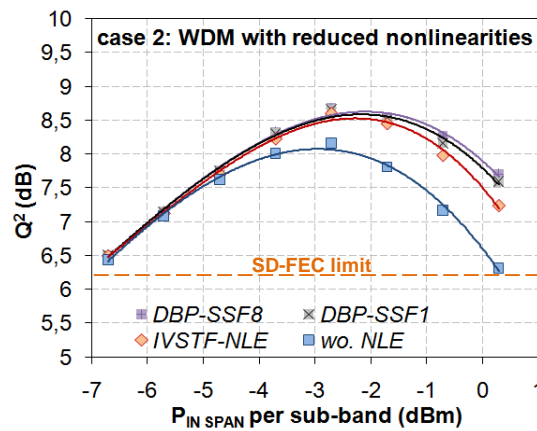


Figure 3-29: Q^2 -factor vs. span input power per sub-band without nonlinear equalization (wo. NLE), with IVSTF-NLE and DBP-SSF for the scenario 2 (WDM with reduced nonlinearities).

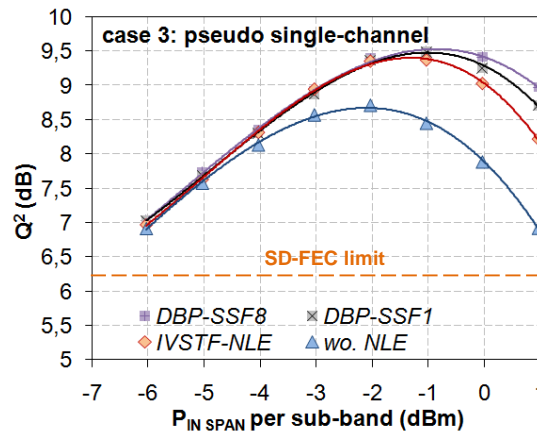


Figure 3-30: Q^2 -factor vs. span input power per sub-band without nonlinear equalization (wo. NLE), with IVSTF-NLE and DBP-SSF for the scenario 3 (pseudo single-channel transmission).

Finally, in Fig. 3-31, we plot the optimum Q^2 -factor as a function of transmission distance (from 500 to 1000 km) for the first scenario. Whatever the distance, the Q^2 -factor improvement (i.e., ~ 0.3 dB) is constant between the case where no nonlinear equalization is implemented and the case where either IVSTF-NLE or DBP-SSF is activated into the receiver. We also notice that the Q^2 -factor at 1000 km with nonlinear equalization is equivalent to the

Q^2 -factor obtained at 900 km without any nonlinear processing. As a consequence, the extra transmission reach provided by both the IVSTF-NLE and the DBP-SSF is about 10% of the overall system reach in the WDM scenario.

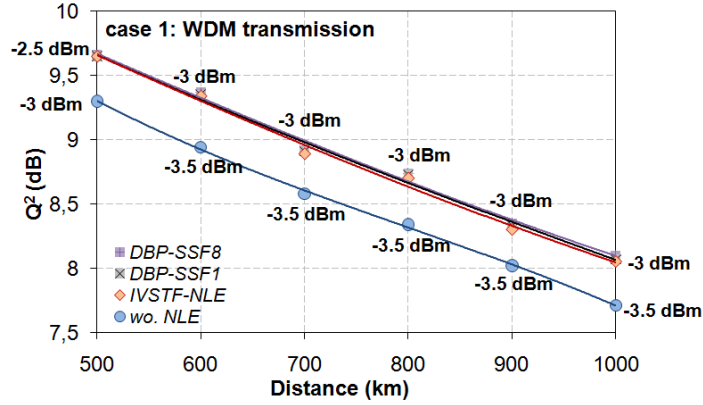


Figure 3-31: Q^2 -factor at optimum span input power vs. distance without nonlinear equalization (wo. NLE), using IVSTF-NLE and DBP-SSF for WDM transmission.

In this section, we have evaluated the performance of both IVSTF-NLE and DBP-SSF equalizers on a 400 Gbps coherent 16-QAM DP-MB-OFDM channel co-propagating with 58 coherent 100 Gbps DP-QPSK channels over a 10x100-km G.652 fiber-based transmission line. We have demonstrated a better performance of the nonlinear equalization in the single-channel configuration, even if the Q^2 -factor improvement reaches ~ 0.3 dB after 1000 km in the WDM scenario, enabling an extension of the transmission reach of 10%. IVSTF-NLE offers equivalent performance with respect to DBP-SSF in WDM scenario. Their future practical implementation will depend on the computational complexity.

3.5 Experimental comparison of OFDM and Nyquist-WDM

16-QAM Nyquist-WDM (N-WDM) is the most widely studied candidate for 400 Gbps and 1 Tbps superchannel (Sp-Ch). It is thus interesting to compare the performance of 16-QAM modulated OFDM and N-WDM. In the literature, there are not many such comparisons carried out over the same test-bed. In [74], the performance of 32-Gbaud 16-QAM OFDM and N-WDM is compared over 2175 km of G.652 fiber line. Same optimum span input power and similar BER are demonstrated. Here we compare the performance of 1 Tbps MB-OFDM and N-WDM Sp-Ch, composed of ten sub-channels, after 400-km, 600-km, 800-km and 1000-km transmission over G.652 fiber using the same test-bed.

3.5.1 Experimental set-up

Both MB-OFDM and N-WDM 1 Tbps Sp-Ch are composed of ten sub-channels carrying each 100 Gbps nominal bit rate. Their spectra are shown in Fig. 3-32. The OFDM (respectively, N-WDM) sub-channels occupy a bandwidth of 18 GHz (respectively, 15 GHz), with a raw bit rate of 144 Gbps (respectively, 120 Gbps). After removing 20% of OFDM redundancy (i.e, cyclic prefix, pilots and training sequence) and 20% of FEC redundancy, the nominal bit rate of OFDM becomes 100 Gbps. Guard-bands of 2 GHz are inserted between OFDM sub-channels. The DSP of N-WDM is based on blind equalization, so that there is only 20% of FEC redundancy. That's why its bandwidth is 3 GHz less than OFDM. N-WDM sub-channels are separated by 5-GHz guard-bands. The total bandwidth of the Sp-Ch is thus ~ 200 GHz, which corresponds to a net spectral efficiency of ~ 5 bits/s/Hz.

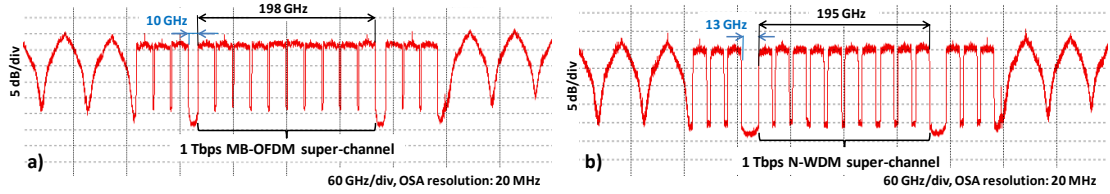


Figure 3-32: Spectra the 1 Tbps superchannel and WDM multiplex used in the experiments (a: MB-OFDM, b: N-WDM).

The hardware used for the generation and detection of MB-OFDM and N-WDM Sp-Chs is identical and described in Fig. 3-33. The 1 Tbps MB-OFDM or N-WDM Sp-Ch is generated thanks to ten 100-kHz linewidth ECL spaced by 20 GHz, which feed two CMZMs. By means of two independent pairs of DACs, data carried by the neighboring sub-bands are totally decorrelated, provided that the first pair of DACs generates the odd Sb-Chs while the second pair generates the even Sb-Chs. Six complementary DFB are used to produce six other OFDM or N-WDM sub-bands (three on each side of the 1 Tbps Sp-Ch), which are introduced to emulate fiber nonlinearities. They are located at 10 GHz from the last right/left-hand Sb-Ch of the Sp-Ch in the case of OFDM, and at 13 GHz in the case of N-WDM. The 16 Sb-Chs are combined together by means of two stages of 8:1 and 2:1 PM couplers. Four PM-EDFA are thus inserted to balance the coupler losses. The PDM-unit remains the same as previously described, except for the time delay. For OFDM, the delay is tuned to one OFDM symbol period (36 ns). For N-WDM, it is tuned to a strict multiple of N-WDM symbol duration (66.7 ps). Finally the 16 sub-bands are combined with 53 channels carrying each 128 Gbps DP-QPSK modulation, which fill the EDFA bandwidth and emulate fiber nonlinearities. The transmission line is composed of N spans of G.652 fiber, with $N = 4, 6, 8$ and 10 . In the middle of the optical link, a dynamic gain equalizer (DGE) is inserted in order to flatten the multiplex power at the receiver side. At the receiver side, one of the middle sub-channels (the sixth sub-channel) of the Sp-Ch is selected for signal processing and BER calculation.

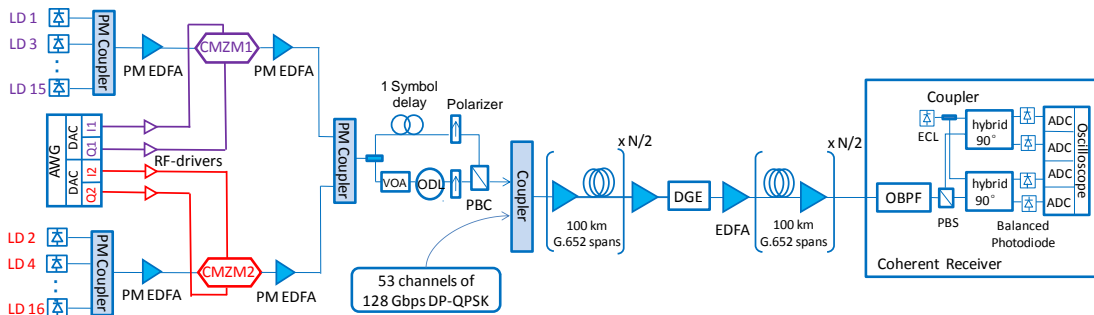


Figure 3-33: Experimental set-up showing the MB-OFDM or N-WDM transmitter, $N \times 100$ -km G.652 fiber-based transmission line, and coherent receiver ($N = 4, 6, 8, 10$).

3.5.2 Signal processing of Nyquist-WDM

The signal processing of N-WDM was developed by ETH Zurich within the framework of the EU-funded "FOX-C" project. At the transmitter side, the pulse shaping is performed using a root-raised-cosine filter with a roll-off factor of 0.05. The information bits are mapped on complex 16-QAM symbols at a symbol rate of 15 Gbaud. Differential encoding is carried out to overcome phase ambiguities. The transmitter DSP implemented at the N-WDM transmitter side can be decomposed as follows. After differential encoding and Nyquist filtering, a pre-equalization is applied over the signal in order to compensate for the amplitude and phase

distortions of the transmitter. The pre-distortion is implemented by a frequency domain equalizer using the "Overlap and Save" method.

At the receiver side, DSP is based on blind equalization in order to avoid any additional overhead and therefore maximize the spectral efficiency. After static frequency-domain compensation of chromatic dispersion, the recorded waveform is normalized and de-skewed in order to compensate for the transceiver imperfections (IQ-imbalance or various path lengths). The received waveform is matched-filtered with a root-raised-cosine filter, which is the complementary of the pulse shaping filter used at the transmitter side. The sampling offset is compensated by a special timing recovery technique based on the modified Godard algorithm and afterwards re-sampled at two samples per symbol [88]. The two polarizations are de-multiplexed, and the signal is compensated for polarization mode dispersion (PMD) and residual chromatic dispersion. This is done by a 2x2 butterfly finite impulse response (FIR) filter structure with 9 taps, which can mitigate dynamically the channel impairments. After a pre-convergence step based on the constant modulus algorithm (CMA) [89], the equalizer is switched to the radius-directed equalization (RDE) method [90]. The carrier frequency offset compensation is done by observing the peak of the spectrum of the m^{th} power signal [91]. The carrier phase compensation comprises two stages: the first stage uses the blind phase search method [92], while the second stage implements the maximum likelihood sequence estimation (MLSE) technique [93]. After carrier recovery, a third equalization stage is applied to further improve the signal quality and eliminate linear signal distortions. This step is realized thanks to a T-spaced decision-directed least mean square (DD-LMS) equalizer with 61 taps. Finally, demodulation and differential decoding are achieved.

3.5.3 Experimental results

The comparison is firstly performed in BtB, as shown in Fig. 3-34. Theoretical curves for 16-QAM modulation are plotted as reference. The OFDM sub-channel has a bandwidth of 18 GHz, whereas the N-WDM sub-channel is 15 GHz. That's why the OFDM theoretical curve is 0.8 dB to the right compared to N-WDM. We find approximately the same difference over BtB measurements. The BtB performance is impacted by hardware impairments and signal processing quality, such as channel estimation, phase noise compensation and CD compensation. Since two formats are tested over the same test-bed, they suffer from the same hardware impairments. These results show that the signal processing used for OFDM and N-WDM in this experiment achieves the same performance.

The transmission performance of OFDM and N-WDM after 400 km, 600 km, 800 km and 1000 km is depicted in Fig. 3-35. BER is plotted as a function of the span input power per sub-channel. OFDM results are presented with solid lines and N-WDM with dotted lines. The optimum span input power of OFDM sub-channel at 1000 km is -4.5 dBm. The optimum power slightly increases when we decrease the transmission distance and becomes -4 dBm at 400 km. The optimum power of N-WDM sub-channel varies from -3 dBm to -2 dBm for different distances, which is 1.5-2 dB higher compared to OFDM, demonstrating better nonlinear performance. For all configurations, the BER at optimum power is under the SD-FEC limit, fixed at 2×10^{-3} , showing error-free transmission for both 16-QAM OFDM and N-WDM. The optimum BER of OFDM sub-channel over 1000 km is 1.2×10^{-2} , while that of N-WDM sub-channel is halved (6.5×10^{-3}). Similar comparison results are observed with other transmission reaches.

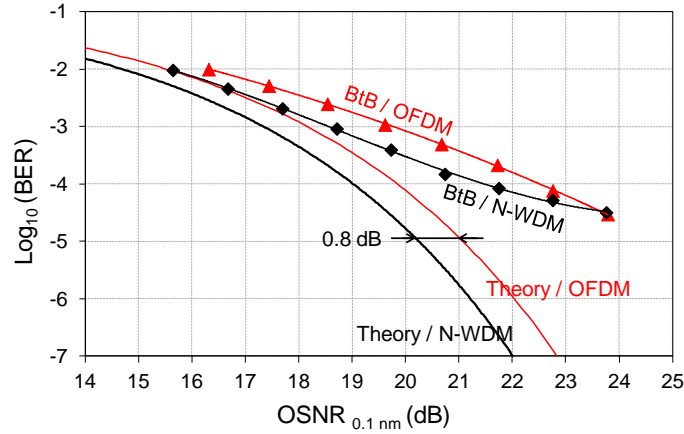


Figure 3-34: BER versus OSNR (in 0.1 nm) given by theory and measured in BtB for 16-QAM modulated OFDM and N-WDM.

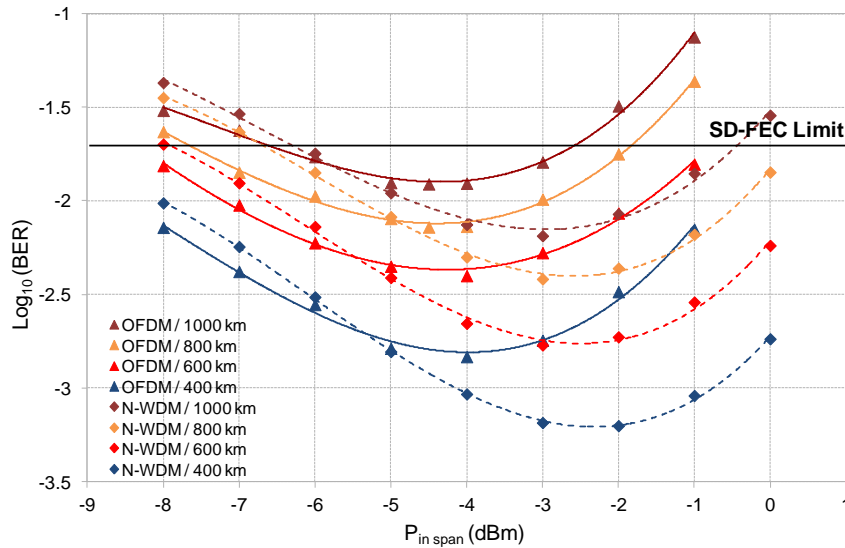


Figure 3-35: BER versus span input power ($P_{in\ span}$) per sub-channel for 16-QAM modulated OFDM and N-WDM after 1000 km, 800 km, 600 km and 400 km of transmission over G.652 fiber.

The aforementioned OFDM and N-WDM transmission experiments were carried out at equal net bit rate, meaning 18-GHz bandwidth / 2-GHz guard-bands for OFDM and 15-GHz bandwidth / 5-GHz guard-bands for N-WDM). We have also checked the performance of OFDM Sp-Ch composed of sub-channels of 15-GHz bandwidth and 5-GHz guard-bands, in order to have the same raw bit rate and the same guard-bands as N-WDM. We do not observe significant increase of optimum span input power with respect to 18-GHz case.

In contrast to the comparison results shown in [74], which demonstrates equivalent nonlinear performance and transmission reach between OFDM and N-WDM, our experiments show higher optimum power over N-WDM, leading to lower BER at the optimum power. The reason of why we get different comparison results still needs to be investigated. This difference may be related to our experimental set-up or DSP procedures. It could also be the intrinsic nonlinear performance difference between OFDM and N-WDM, such as higher XPM or FWM of OFDM signal.

3.6 Conclusion

In this chapter, we have described the 16QAM-OFDM upgrade of an experimental test-bed initially designed for QPSK-OFDM, and we have studied the performance of 16QAM-OFDM in various configurations. Before starting the design of 16QAM-OFDM transmitter, numerical simulations have been carried out to compare the sensitivity of QPSK- and 16QAM-OFDM to four different practical implementation impairments: laser phase noise, ENOB of DAC, I/Q phase detuning and nonlinear transfer function of CMZM. The higher sensitivity of 16QAM-OFDM to implementation limitations has been clearly assessed, proving the importance of optimizing transmitter set-up for high modulation order signals.

After that, we have introduced the step by step design of a carefully-optimized 16QAM-OFDM single sub-band transmitter and receiver, starting from the electrical part of the transmitter to single-polarization configuration till the integral dual-polarization transmitter. Compared to the previous QPSK-OFDM test-bed, more linear RF-drivers and single-ended CMZM are used in the new transmitter. The performance at each step was controlled and validated by means of BtB OSNR sensitivity curves. 16QAM-OFDM is generated with only 7.8-dB OSNR sensitivity difference (at $\text{BER} = 1 \times 10^{-3}$) with respect to QPSK-OFDM. This is only 0.8 dB from the theoretical OSNR penalty that results when switching from QPSK to 16QAM. The tolerance to CD and PMD is validated. The multi-band OFDM transmitter structure is presented and we observe no BtB performance degradation compared to single-band configuration.

Transmission experiments have been carried out over two types of fibers that are the most widely deployed in the field. G.652 fiber outperforms G.655 fiber in all study cases. 100 Gbps QPSK-OFDM shows error-free performance after 1000 km of transmission with a $\text{BER} \sim 1 \times 10^{-7}$ over G.652 fiber and $\sim 1 \times 10^{-5}$ over G.655 fiber, opening large OSNR margins for a field implementation. 200 Gbps 16QAM-OFDM achieves 1000 km without error over G.652 fiber line, but the margin with respect to the SD-FEC threshold (fixed at $\text{BER} \sim 2 \times 10^{-2}$) is tiny.

After highlighting the transmission reach problem of 16-QAM modulation for long-haul system, we have studied typical intra-channel nonlinear mitigation techniques (DBP-SSF and IVSTF-NLE) for the purpose of improving transmission performance. We have demonstrated a better performance of the nonlinear equalization in the single-channel configuration, even if the Q^2 -factor improvement reaches ~ 0.3 dB after 1000 km in the WDM scenario, enabling an extension of the transmission reach of 10%.

At last, we have compared the performance 16QAM-OFDM to that of another popular solution advocated for beyond 100 Gbps system: Nyquist-WDM. The comparison is carried out with 1 Tbps MB-OFDM and N-WDM superchannel, composed of ten sub-channels, after 400-km, 600-km, 800-km and 1000-km transmission over G.652 fiber using the same test-bed. N-WDM has 1.5-2 dB higher optimal launch power, leading to slight lower BER. The reason of why N-WDM outperforms MB-OFDM in our transmission experiments remains to be investigated.

CHAPTER 4

TOWARDS FLEXIBLE OPTICAL TRANSPORT NETWORKS: OFDM SUB- WAVELENGTH OPTICAL SWITCHING

4.1 Context and motivation

In the beyond 100 Gbps WDM era, the intensive research on innovative data transport technologies and network architectures identified the elastic optical networking concept [94] as one of the key enablers to carry on increasing traffic while delaying the expected "capacity crunch". Additionally, a shift of the traffic profile towards rich content video and cloud services is nowadays obvious, imposing high peak to average traffic ratios which result in large bandwidth and capacity variations over time. The key characteristic of the elastic (also referred as flexible) optical networking (EON) concept [95] is that the network resources are always adapted to the traffic demands. Thus, optimized resource utilization is maintained, avoiding the need for over-provisioning due to high traffic fluctuations.

In EON, the adaptability of the network resources to the traffic demands is determined by the characteristics of the defined superchannel (Sp-Ch) and corresponding switching capabilities. A Sp-Ch is formed as one contiguous spectral entity with variable bandwidth that is adapted to the capacity of each demand (or aggregation of demands with same networking requirements). The key characteristic of a Sp-Ch is that it is composed by multiple carriers that are usually set close to one another with minimal guard bands between carriers with the goal to achieve both high spectral efficiency and high capacity channels [69, 94]. Modulation schemes that are compatible with such requirements are for instance OFDM format in its multi-band approach (MB-OFDM) and Nyquist-WDM (N-WDM) format [95]. On the other hand, the properties of the bandwidth adaptive switch determine the EON capabilities and the routing of the Sp-Ch entities [96]. Wavelength selective switches (WSS) are the key network elements with elastic bandwidth characteristics that can be dynamically adapted to the Sp-Ch bandwidth, as the Sp-Ch is routed through the network.

Although the commonly defined Sp-Ch entity in EON addresses the capacity-on-demand issue, it relies on electronic aggregation functions at each node. Thus switching can only be performed transparently at the Sp-Ch level in a similar way to WDM but with the use of flexible bandwidth WSS. Any processing of the Sp-Ch contents (typically with ultra-dense spectral allocation) requires first the reception of the whole superchannel in the node and the electronic processing and switching of its contents. Also, even when switching at the Sp-Ch level is assumed, spectral gaps are required to be inserted between the neighboring Sp-Chs in order to prevent crosstalk. In this case, the switching granularity is restricted to that of the Sp-Ch level, and although in general the minimum Sp-Ch bandwidth can be flexibly defined, the required insertion of a spectral gap between them significantly reduces the overall spectral efficiency.

Fig. 4-1 shows the short-term approach of EON proposed at the time of writing by the system vendors, based on the combination of N-WDM Sp-Ch at 32 Gbauds and mixed 37.5 / 50 GHz spectral grid [97-102]. The sub-channels (Sb-Ch) inside the N-WDM Sp-Ch are spaced by 37.5 GHz, the guard-band between the WDM channels is typically of ~18 GHz, and the capability to optically switch the sub-bands inside the superchannel is not authorized. To further increase the flexibility, the idea is to adapt the capacity carried by the Sb-Chs to the services transported and to adapt the modulation format to the transmission distance. The data-rate carried by the WDM channels are either 50 Gbps (with BPSK), 100 Gbps (with QPSK), 200 Gbps (with 16-QAM), or 400 Gbps for the Sp-Ch grouping two 200 Gbps 16-QAM Sb-Ch [99-101].

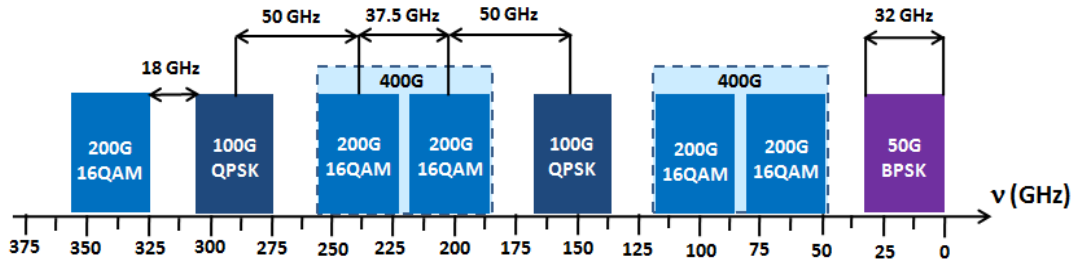


Figure 4-1: An example of the bandwidth management proposed at the time of writing by system vendors, based on N-WDM Sp-Ch working at 32 Gbaud and the mixed 37.5 / 50 GHz spectral grid approach.

In a recent flexible networking proposal, an approach of achieving sub-wavelength circuit switching is proposed [103], based on digitally performed frequency division multiplexing, also referred to as digital subcarrier multiplexing (DSCM). In this proposal, one or more subcarrier frequencies along a path are reserved to connect two edge nodes. These subcarriers are individually switched and routed by digital subcarrier cross-connects (DSXC). A basic DSXC block diagram is shown in Fig. 4-2. It is composed of transponders, high speed DSP for DSCM processing and a crossbar circuit switch. This approach achieves small switching granularity and high spectral efficiency, since there is no need of guard-band inside each wavelength. The drawback is that DSXC requires as many transponders as the number of wavelengths, resulting in very complicated cross-connect structure.

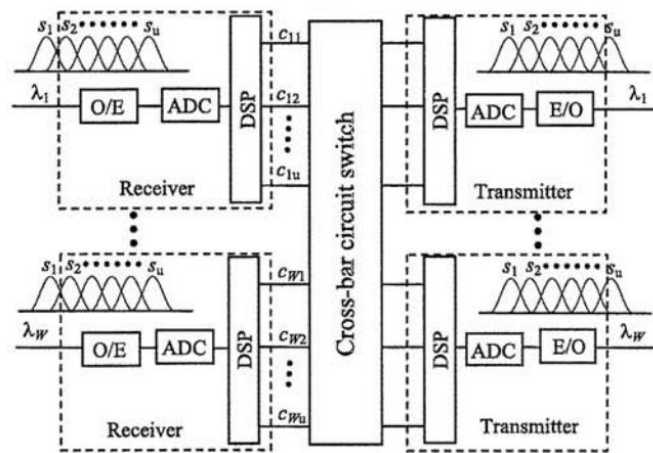


Figure 4-2: DSXC block diagram. [103]

Another approach of achieving small switching granularity is to perform the sub-wavelength switching optically.

4.2 Concept of sub-wavelength optical switching

The concept of sub-wavelength optical switching consists in performing optical aggregation and switching at the Sp-Ch contents level (Sb-Ch level) using ultra-selective optical filters. An example of the spectrum, adapted to the proposed scheme, is shown in Fig. 4-3. In this example, the spectral granularity is 10 GHz, the OFDM Sb-Chs occupy a spectral slot of 10 GHz or 20 GHz and can be grouped together to constitute a Sp-Ch transporting 50 Gbps, 100 Gbps, 200 Gbps, or 400 Gbps. The data-rates carried by each Sb-Ch could take the following values: 12.5 Gbps, 25 Gbps, 33.3 Gbps, 50 Gbps, 66.6 Gbps and 100 Gbps. By using the MB-OFDM technique, this bit-rate elasticity would be obtained by playing both over the modulation format transported by the sub-carriers constituting the OFDM Sb-Chs (i.e.

BPSK, QPSK, 8-QAM, 16-QAM), and over the number of subcarriers constituting each OFDM Sb-Ch (or equivalently over their bandwidth). Thanks to the implementation of ultra-selective optical pass-band and stop-band filters, the optical add-drop of closely spaced OFDM Sb-Chs is possible. The guard-band between the OFDM Sb-Chs can be as small as 2-5 GHz, which will be demonstrated in the experimental studies of this chapter. Techno-economic analysis demonstrates that the proposed ultra-fine switching granularity achieves reduced CAPEX cost for the overall network as well as spectrum saving [104-106].

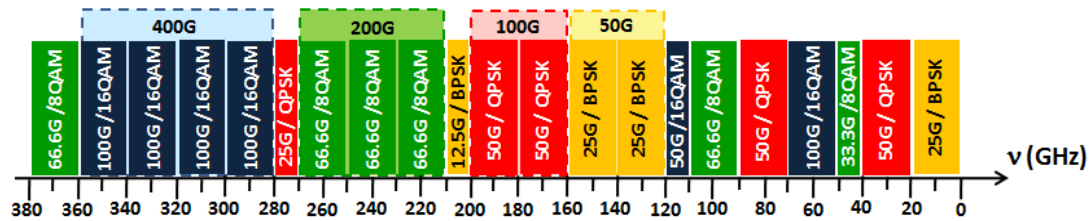


Figure 4-3: An example of the proposed bandwidth management, based on the MB-OFDM technique and 10 GHz spectral grid.

Sub-wavelength optical switching has been realized through experimental demonstrations. In [107], a bit rate variable reconfigurable optical add drop multiplexer (ROADM) function is demonstrated over an OFDM superchannel, composed of 30 OFDM sub-bands with 7-GHz spacing, negligible guard-band and 8-QAM modulation. Their ROADM set-up is shown in Fig. 4-4. In the drop function, the filter bandwidth can be configured at 15 GHz, 30 GHz and 50 GHz, so as to filter out 2, 4 or 7 OFDM sub-bands. The add function is carried out by stopping 5 sub-bands (35 GHz) and then inserting 3 sub-bands (21 GHz), thus creating a gap of 7 GHz on each side, in order to avoid the crosstalk caused by the imperfect filter slope. For performance evaluation, the superchannel passes through 2x80-km SSMF before entering the ROADM. The “add” output of the ROADM goes through another 80-km SSMF.

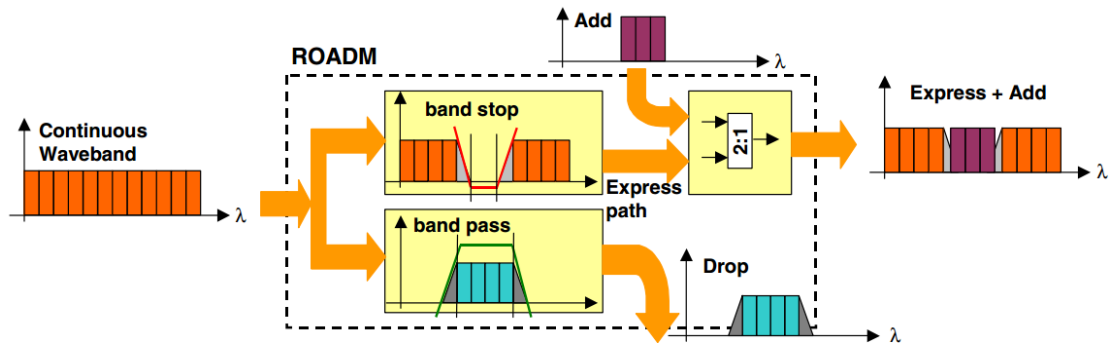


Figure 4-4: Principle setup for drop and add with a continuous waveband spectrum. [107]

In [108], they report an experimental demonstration of OFDM sub-band switching, realized by an optical cross-connect (OXC) architecture depicted in Fig. 4-5. The Finisar Waveshaper 4000S is used as the sub-band selecting switch. It is based on liquid crystals on silicon (LCoS) and has a minimum filtering bandwidth of 10 GHz. The OFDM sub-band has 6.875-GHz bandwidth and 10-GHz spacing. Transmission experiments are carried out by inserting 80-km SSMF before each input of the node and another 80-km SSMF after each output of the node. Experimental results show that the sub-band switching only slightly decreases the Q-factor performance.

Both studies demonstrate sub-wavelength optical switching inside OFDM superchannel with either 7-GHz or 3.125-GHz guard-band between adjacent sub-bands. The transmission over fiber is carried out in metro distance of either 160 km or 240 km. The performance is evaluated over one add/drop operation. The feasibility of realizing such add/drop operation in the middle of a long-haul transmission and the impact of passing through several sub-wavelength OADMs have not yet been investigated.

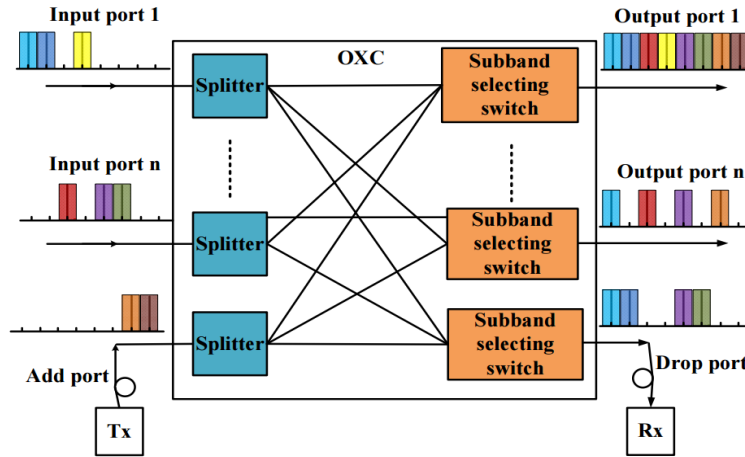


Figure 4-5: An OXC architecture supporting sub-band switching.

In this chapter, we demonstrate successful long-haul transmission with sub-wavelength add/drop in the middle of the link. The cascability of such sub-wavelength add/drop is investigated experimentally. Thanks to ultra-selective optical filters and careful pass-band/stop-band filter bandwidth optimization, long-haul reach (~1000 km) with 5 add/drop cascades is feasible. Sub-wavelength switching inside QPSK modulated 100 Gbps MB-OFDM will be studied in section 4.3. Then, in section 4.4, we extend the study to MB-OFDM modulated with 16-QAM which is more sensitive to filtering impairments. 16-QAM Nyquist-WDM (N-WDM) is also included in the study in order to investigate the sensitivity of Nyquist filtered single-carrier signal to such optical filtering.

4.3 Sub-wavelength optical switching inside 100 Gbps MB-OFDM

In this section, we carry out a sub-wavelength optical switching study inside 100 Gbps QPSK modulated MB-OFDM superchannel, composed of four sub-bands. The assessment of the efficiency of our sub-wavelength OADM to add-drop OFDM sub-bands as narrow as 8 GHz inside the 100 Gbps MB-OFDM superchannel is carried out both in back-to-back and in the 10x100-km G.652 fiber-based transmission line. In particular, the bandwidths of the "drop" and "notch" filters used in the sub-wavelength OADM are optimized as a function of the guard-band separating two consecutive sub-channels. The question of the cascability of the sub-wavelength OADM is studied thanks to the insertion of the add-drop multiplexer into a G.652 fiber-based recirculating loop.

This study is supported by the "FUI9 100GFLEX" collaborative project. The ultra-fine optical pass-band and stop-band filters in the sub-wavelength OADM are designed and realized by the project partner Yenista Optics. The design of these filters as well as the obtained profiles are presented in Appendix A.

4.3.1 Structure of sub-wavelength OADM

The 100 Gbps DP-MB-OFDM superchannel is composed of four sub-bands, with the set-up depicted in Fig. 3-16 in section 3.2 of the last chapter. The sub-band spacing is 10 GHz and each sub-band occupies a bandwidth of 8 GHz, resulting in a guard-band of 2 GHz between adjacent sub-bands. Fig. 4-6 shows the structure of the sub-wavelength OADM. The OADM is constituted of a first 3-dB coupler associated with an optical pass-band filter (OPBF) over its lower arm and an optical stop-band filter (OSBF) over its upper arm. In our experiment, the OSBF removes the third OFDM sub-band of the 100 Gbps DP-MB-OFDM signal, while the OPBF selects it. Once dropped, the third OFDM sub-band enters into another 3-dB coupler, whose lower arm is connected for instance to a coherent receiver and upper arm feeds a 5-km fiber spool. The role of this fiber spool is to de-correlate the signals once the third sub-band will be reinserted into the remaining truncated OFDM multiplex. The "add" operation is carried out by connecting the de-correlating fiber to the OSBF output, as shown in Fig. 4-6. The spectrum of the OFDM signals and filter shapes are measured with a high-resolution (20 MHz) optical spectral analyzer and shown in the insets of Fig. 4-6.

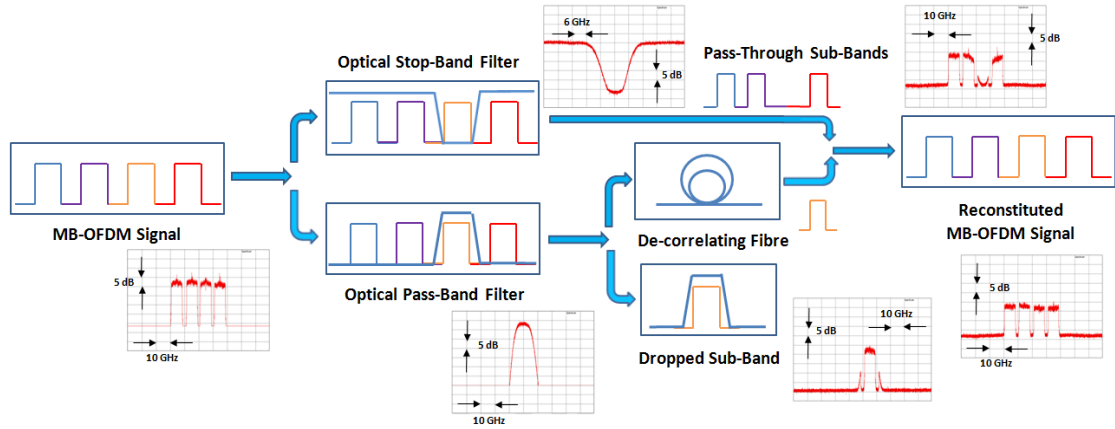


Figure 4-6: Set-up of the OFDM sub-band optical add-drop multiplexer with the spectra of signals and optical filters in insets.

4.3.2 Back-to-back characterization

Our sub-band OADM is firstly evaluated in back-to-back, in which the OADM is inserted between the DP-MB-OFDM transmitter and the coherent receiver. The BER versus OSNR sensitivity curves are measured by degrading the OSNR thanks to a white noise source, which is coupled with the DP-MB-OFDM signal. Fig. 4-7 gives the BER of the dropped sub-band (the third one) versus the OSNR in 0.1 nm for various 3-dB bandwidths (3-dB BW) of the OPBF. From 14 GHz to 6 GHz, the OSNR penalty is acceptable compared to the case where no OADM is inserted, but an error floor at $BER \sim 1 \times 10^{-4}$ appears for a 3-dB BW of 4 GHz. In the following, we choose the 3-dB BW of 10 GHz for the "drop" OPBF, which results in a very low OSNR penalty with respect to the reference case without OADM.

Then, we plot in Fig. 4-8 the BER of the sub-bands 2, 3 and 4 as a function of the 3-dB BW of the OSBF after the "add-drop" operation when the guard-band (GB) is 2 GHz and $OSNR = 18.5$ dB ($OSNR$ required for having a $BER = 10^{-4}$ without OADM for the 100 Gbps DP-MB-OFDM signal). The impact of the crosstalk over the sub-band 3, between the added and remaining residual signals, is maximum (respectively, minimum) at low (respectively, at high) 3-dB BW of the OSBF. It is the opposite observation for the "pass-through" sub-bands

2 and 4, for which a large OSBF results in high spectral distortions. The optimum OSBF 3-dB BW results from a trade-off between the distortions affecting sub-band 3 from one side and sub-bands 2 and 4 from the other side, and is obtained at the intersection of these three measured curves. For a GB = 2 GHz, the optimum OSBF 3-dB BW is equal to ~14 GHz, while the BER of sub-bands 2, 3 and 4 is $\sim 3 \times 10^{-3}$.

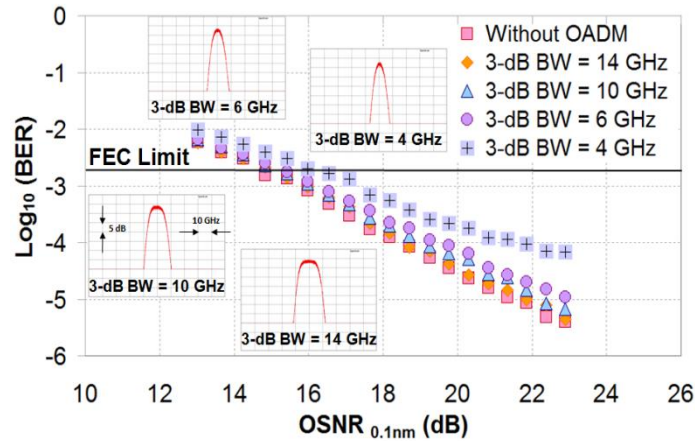


Figure 4-7: BER versus OSNR of the sub-band 3 for various 3-dB BW of the OPBF, with the shapes of the OBPF for various 3-dB BW in insets.

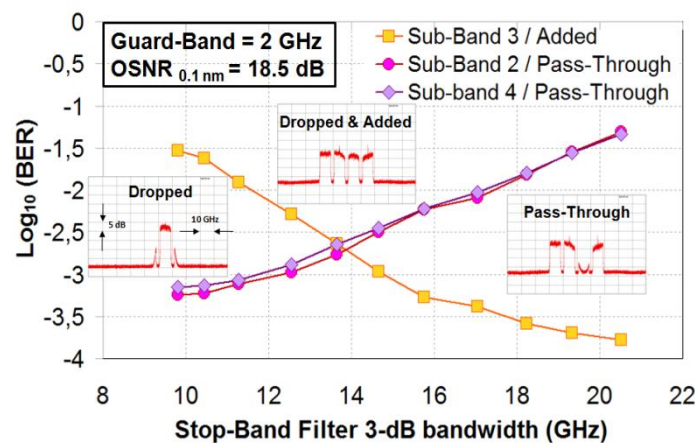


Figure 4-8: BER versus 3-dB BW of the OSBF for the sub-bands 2, 3 & 4 and a GB = 2 GHz. In insets, the spectra of the signals at the optimum.

The same measurements have been carried out in Fig. 4-9 for a GB = 4 GHz and OSNR = 18.5 dB. The optimum 3-dB BW is now equal to ~15.7 GHz, while the BER of sub-bands 2, 3 and 4 has been improved up to $\sim 3 \times 10^{-4}$, i.e. one BER decade better than the BER previously obtained for the GB = 2 GHz.

In Fig. 4-10 is plotted the BER of the dropped sub-band 3, added sub-band 3 and "pass-through" sub-bands 2 and 4 as a function of the OSNR for the optimum tunings of the OPBF and OSBF, obtained with the GB of 2 GHz and 4 GHz. While the BER of the various sub-bands reaches a $\sim 10^{-3}$ error floor (near from the FEC limit fixed here at $\text{BER} = 2 \times 10^{-3}$) at high OSNR for a GB = 2 GHz, the BER results are satisfying for a GB = 4 GHz. The corresponding OSNR penalty compared to the case "without OADM" is less than 1 dB at $\text{BER} = 10^{-3}$. It is the reason why we will evaluate the performance of our sub-wavelength

OADM in the straight-line and in the recirculating loop with a GB tuned over the 4-GHz value.

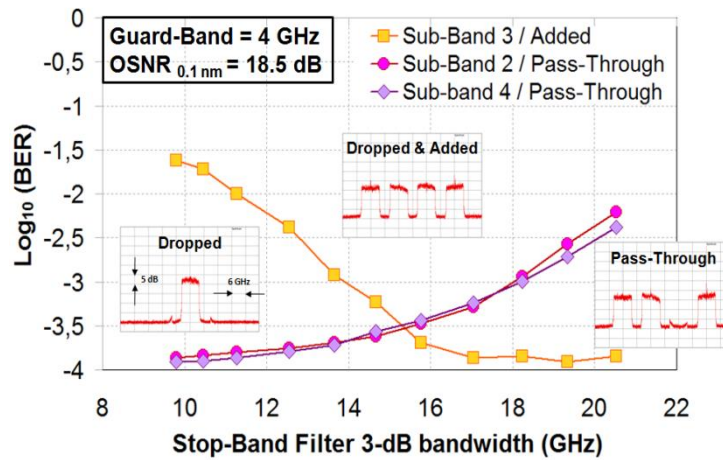


Figure 4-9: BER versus 3-dB BW of the OSBF for the sub-bands 2, 3 & 4 and a GB = 4 GHz. In insets, the spectra of the signals at the optimum.

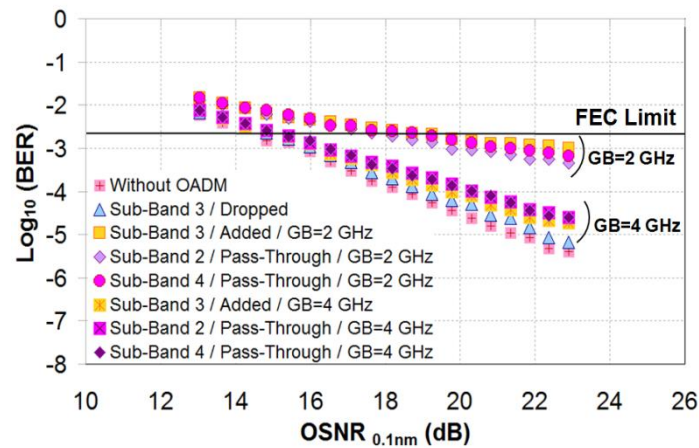


Figure 4-10: BER versus OSNR of sub-bands 2, 3 & 4 in BtB (OADM inserted between the Tx & Rx) for a GB = 2 GHz and GB = 4 GHz.

4.3.3 Straight-line transmission

The sub-wavelength OADM is now studied in the straight-line transmission configuration, as shown in Fig. 4-11. The fiber line is constituted of ten spans of G.652 fiber, amplified by EDFAs with 20-dB gain and 5.5-dB noise figure. The OADM is introduced in the middle of the fiber line after the fifth spans. A 3-dB coupler located at the transmitter side firstly duplicates the 100 Gbps DP-MB-OFDM signal into two identical copies. The first signal replica is combined with the 79 odd and even 100 Gbps DP-QPSK channels and launched into the first five SSMF spans. After an EDFA, a 3-dB coupler sends the WDM multiplex firstly towards an OPBF in order to proceed to the "drop" of the third OFDM sub-band, and secondly towards the OSBF which removes the third OFDM sub-band from the OFDM multiplex. The second replica of the DP-MB-OFDM signal (generated at the transmitter side) is filtered by a second OPBF, which selects the third OFDM sub-band. Thanks to a third 3-dB coupler, this sub-band is re-injected into the truncated OFDM multiplex at the place of the sub-band, which has been removed by the OSBF. Note that here it is not necessary to use a

de-correlating fiber before the "add" operation, as 500 km of fiber separate the added sub-band from the truncated OFDM multiplex (which receives this sub-band). After a DGE, the mix of 100 Gbps DP-MB-OFDM and 100 Gbps DP-QPSK channels is sent into the last five G.652 fiber spans of the transmission link.

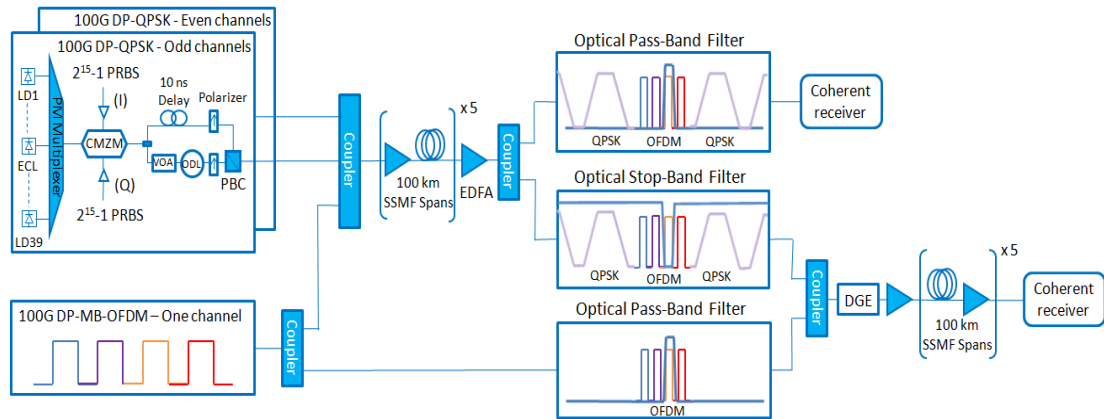


Figure 4-11: Set-up of the 10x100-km transmission test-bed, with the 100 Gbps DP-MB-OFDM channel, the 79 odd and even 100 Gbps DP-QPSK wavelengths, the 10x100-km uncompensated G.652 SSMF transmission line with the sub-wavelength optical switch located in its middle.

We start by looking for the optimum channel span input power of 100 Gbps DP-MB-OFDM over the 10x100-km G.652 fiber-based transmission line without the OADM. The optimum input power is found at ~ 0 dBm, while the corresponding BER and OSNR are $\sim 2 \times 10^{-4}$ and ~ 20 dB, respectively. Note that this optimum power per channel is kept hereafter. The BER is higher than the result previously presented in Fig. 3-20 ($BER = 1 \times 10^{-7}$) because the EDFAs used in this current experiment have higher noise figure.

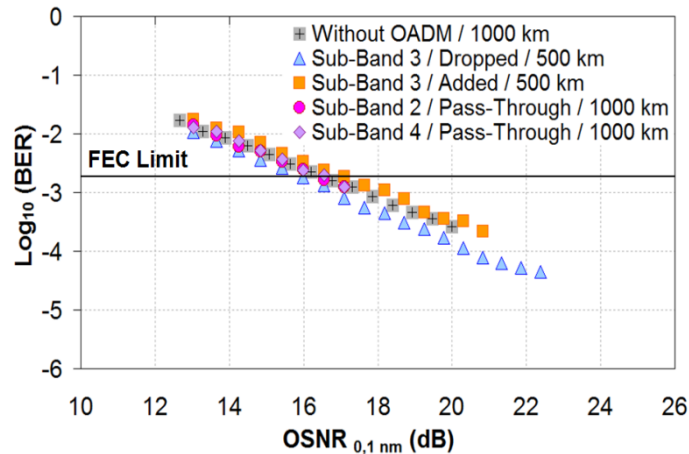


Figure 4-12: BER versus OSNR of sub-bands 2, 3 & 4 after transmission (OADM inserted after 500 km) for a GB = 4 GHz.

Sub-wavelength switching results are presented in Fig. 4-12 by the means of BER versus OSNR sensitivity curves for the sub-bands 2, 3 and 4. Firstly, as a reference, the OSNR sensitivity curve of the 100 Gbps DP-MB-OFDM signal transmitted over the 10x100-km transmission line without the OADM is plotted. The performance of the sub-band 3, dropped after 500 km, and reinserted in the last 500-km of the link (after having been duplicated at the transmitter side) is measured, as well as the performance of the "pass-through" sub-bands 2 &

4 (which are transmitted over 1000 km on the ten SSMF spans). One can notice first that a negligible OSNR penalty is observed at $BER=10^{-3}$ whatever the configuration tested, and secondly that the BER obtained at the best OSNR (measured when the white noise source is not activated) is below the FEC limit for the dropped, added and "pass-through" sub-bands. Note that the best achievable OSNR on the sensitivity curves differ as a function of the configuration considered, since the transmission distance and accumulated ASE are different.

4.3.4 Cascadability of the sub-wavelength OADM

The question of the cascadability of the previously defined sub-wavelength OADM is now studied thanks to the insertion of the add-drop multiplexer into a 2x100-km G.652 fiber-based recirculating loop. The guard-band between the OFDM sub-bands is still fixed at 4 GHz. The 3-dB bandwidths of the OPBF and OSBF are equal to 10 GHz and 15.7 GHz, respectively, as previously optimized. The impact over the sub-band 3 (the sub-band which is dropped and reinserted) but also over the neighboring sub-bands 2 and 4 of the cumulated filtering transfer function as well as the crosstalk inside the OADM is investigated. In the recirculating loop, the architecture of the OADM is identical to the one depicted in Fig. 4-6. After a 3-dB coupler, the 100 Gbps DP-MB-OFDM signal is filtered by an OPBF (respectively, OSBF) which extracts (respectively, removes) the sub-band 3 from the OFDM multiplex. After a 5-km de-correlating fiber, the OPBF and OSBF outputs are re-coupled together, and the reconstituted OFDM multiplex with the "pass-through" and "added" sub-bands is sent into the loop for a new round-trip. This OADM configuration allows us evaluating the impact of the repeated action of the OPBF and OSBF over the OFDM signal (more particularly over the sub-band 2, 3 and 4), both in terms of filtering and crosstalk.

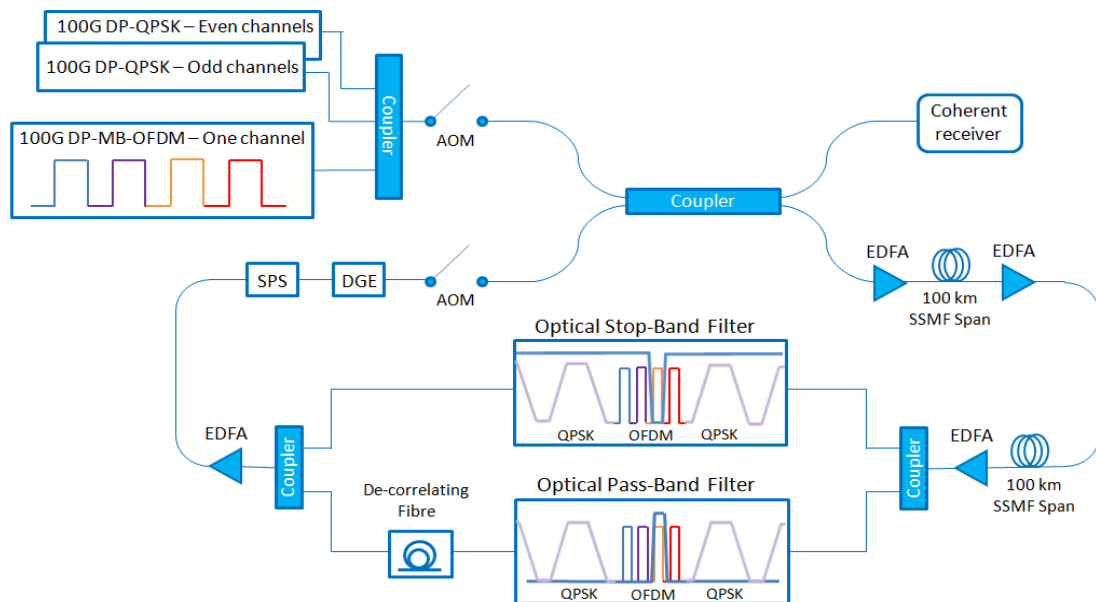


Figure 4-13: Set-up of the 2x100-km G.652 fiber-based recirculating loop including the OFDM sub-band optical switch. AOM = Acoustic-Optical Modulator, SPS = Synchronous Polarization Scrambler, DGE = Dynamic Gain Equalizer.

Fig. 4-13 describes the experimental set-up. The transmitter, depicted in Fig. 3-18, which mixes the 100 Gbps DP-MB-OFDM and the 79 odd and even 100 Gbps DP-QPSK, is connected to the recirculating loop through an acousto-optical modulator (AOM). The loop is constituted of two 100-km spans of G.652 fiber. An EDFA with 20-dB gain and 4.5-dB noise

figure is located at the span input and output, as shown in Fig. 4-13. The OADM described above is then inserted into the loop. The sub-band 3 is firstly dropped and finally reinserted into the OFDM multiplex. It experiences thus the effect of the repeated action of the OPBF (over the "drop" path) and OSBF (over the "stop" path) transfer function, as well as the crosstalk coming from the interaction between the "drop" and "stop" paths. From their side, the sub-bands 2 and 4 experience the repeated distortions of the OSBF. An EDFA compensates for the introduced OADM losses. A DGE and a synchronous polarization scrambler (SPS) achieve power equalization and polarization rotation of the WDM multiplex after each loop round-trip, respectively. The role of the SPS is to stabilize the loop operation. Note that EDFA used in this sub-section are better than those used in the previous sub-section of straight-line experiments (NF = 4.5 dB here against NF = 5.5 dB before), as the objective here is to obtain the best transmission performance so as to cascade the highest possible number of OADM.

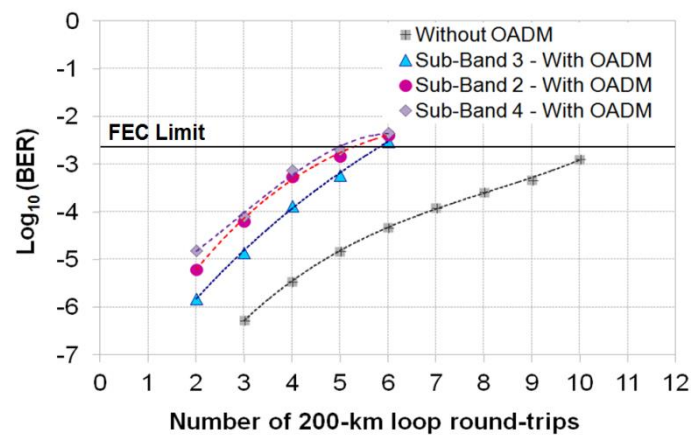


Figure 4-14: BER versus number of 2x100-km loop round-trips for the sub-bands 2, 3 & 4, when the OADM is inserted or not into the loop.

The performance of sub-bands 2, 3 and 4 is shown in Fig. 4-14. The BER is plotted as a function of the number of loop round-trips. For each transmission distance, the span input power per channel is optimized. Two configurations are studied. The case for which no OADM is inserted into the loop is shown as reference. The FEC limit (fixed here at $\text{BER} = 2 \times 10^{-3}$) is reached after 10 loop round-trips or 2000 km. When the OADM is introduced into the loop, the BER of sub-band 3 ($\text{BER} \sim 6 \times 10^{-4}$) after 5 round-trips or 1000 km, including the crossing of 5 OADM, is well below the FEC limit. The BER of sub-bands 2 and 4 ($\text{BER} \sim 1.5 \times 10^{-3}$) is slightly worse than that of sub-band 3. Nonetheless, 5 loop round-trips can be achieved as well. This BER degradation with respect to sub-band 3 comes from the higher distortions which affect the edge sub-carriers of sub-bands 2 and 4 when compared to those of sub-band 3. Indeed, as indicated in the table 0-1 of Appendix A, the edge roll-off of the OSBF (~ 750 dB/nm) and its corresponding frequency selectivity are lower than those of the OPBF (~ 800 dB/nm). The bandwidths of the OPBF and OSBF would have deserved to be re-optimized after each new loop round-trip. However, the performance improvement (respectively, degradation) for the sub-bands 2 and 4 (respectively, for the sub-band 3) would have been limited to less than $\frac{1}{2}$ BER decade (as Fig. 4-14 lets it imagine), and no more than 5 loop round-trips would have been possible. To exhibit the progressive distortion affecting the sub-bands 2, 3 and 4, the spectrum of the MB-OFDM channel after each loop round-trip is also shown in Fig. 4-15.

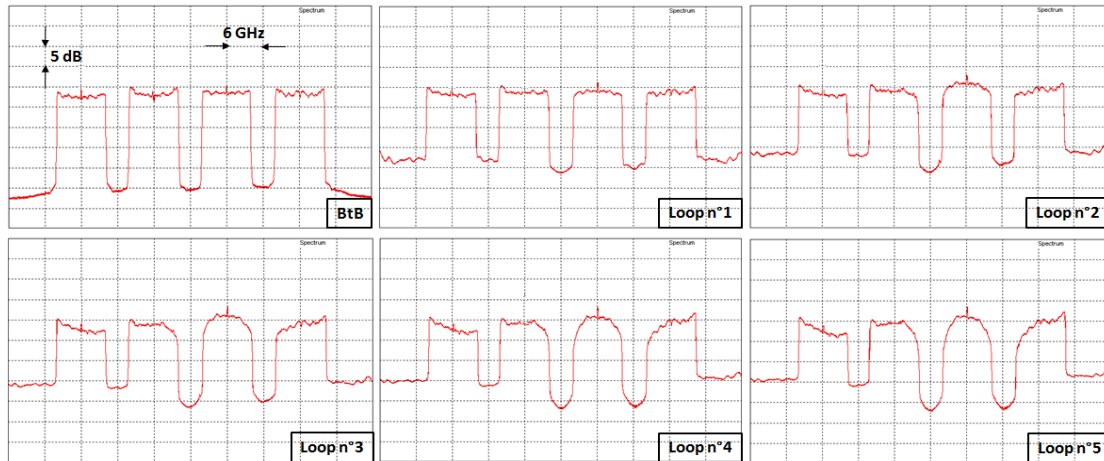


Figure 4-15: Evolution of the 100 Gbps MB-OFDM channel spectrum measured with the high-resolution (20 MHz) OSA after each loop round-trip.

The sensitivity to frequency drift of such ultra-narrow optical pass-band and stop-band filters is also a crucial question when considering their deployment in the field. Indeed, the mechanical or temperature stability of these devices is not as well ensured in the field as in the laboratory. Fig. 4-16 presents the BER evolution of the sub-band 3 (on which the "add-drop" operation is achieved) as a function of the OPBF and OSBF central frequency drift after 5 loop round-trips. In the OPBF case, the FEC limit is reached for absolute values of frequency drift higher than 0.8 GHz, which represents 20% of the OFDM signal bandwidth (fixed here at ~8 GHz) if we consider the whole acceptance window going from -0.8 GHz to +0.8 GHz. When considering now the OSBF, the acceptance window spreads from -1 GHz up to 0.8 GHz, namely 22.5% of the OFDM signal bandwidth. Consequently, the sensitivity of the OFDM signal (here the sub-band 3) to the central frequency drift of the optical filters is slightly higher in the case of the OPBF than in the case of the OSBF. As expected, these values are relatively small, and will require that the optical filters be immunized against both mechanical vibrations and temperature variations.

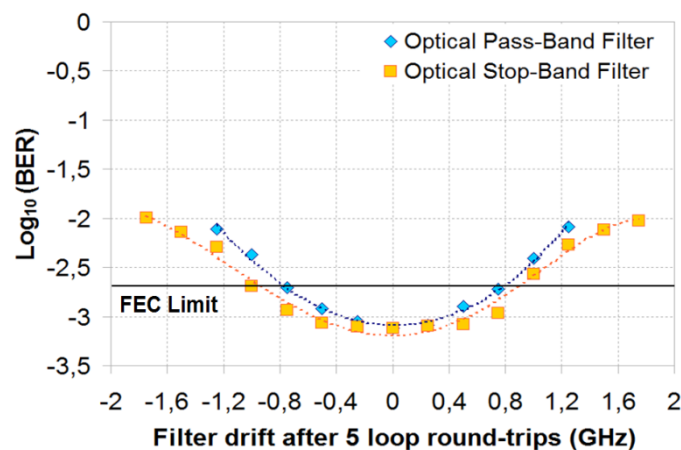


Figure 4-16: BER versus OPBF and OSPF central frequency drift for the sub-band 3 after 5 loop round-trips (or 1000 km).

We have provided an experimental proof of concept of sub-band optical switching over a 100 Gbps QPSK modulated MB-OFDM signal. We successfully perform an optical "add-drop" of an OFDM sub-band as narrow as 8 GHz inside a 100 Gbps DP-MB-OFDM signal constituted

of four sub-bands spaced by 4-GHz guard-bands. The essential elements of this sub-band OADM are composed of two ultra-selective optical pass-band and stop-band filters whose rectangular shape and narrow bandwidth allowed OFDM sub-band extraction and suppression, respectively. The crucial question of the cascability of such ultra-selective optical filters is addressed, by inserting our sub-wavelength OADM into a G.652 fiber-based recirculating loop. We prove that five OADM can be cascaded without degrading too much the transmission performance. These results are very encouraging when considering the introduction of such flexible OADM into meshed optical transport networks, for which several OADM (4 or 5) are often cascaded over a given path.

4.4 Sub-wavelength optical switching inside 1 Tbps MB-OFDM & Nyquist-WDM superchannel

In this section, we extend the sub-wavelength optical switching study to 16-QAM modulated MB-OFDM, which has higher sensitivity to filtering impairments, so that higher requirement over filtering quality. The sub-wavelength add-drop will be carried out inside 1 Tbps MB-OFDM and N-WDM superchannel, composed of ten sub-bands. The transmitter and receiver set-up is the same as Fig. 3-34 in section of "Experimental comparison of OFDM and Nyquist-WDM". The sub-wavelength OADM constructed for this study is named as flexible optical cross-connect node (FOX-C node). This work is supported by the EU-funded "FOX-C" project. Compared to the former study operating over QPSK signal, a more selective high spectral resolution (HSR) optical filter is used in this study over 16-QAM.

We will start the section by introducing the structure of the FOX-C node, before investigating the impact of add-drop operation over 16-QAM signal in BtB by inserting the node between transmitter and receiver. Afterwards, we compare the transmission performance of MB-OFDM and N-WDM with the node in the middle of the fiber line. Finally, by means of recirculating loop, we investigate the impact of repeated add-drop operations over these 16-QAM signals.

4.4.1 Structure of the FOX-C node

The designed FOX-C switching node architecture is based on two switching levels addressing a coarse switching resolution level (when Sp-Chs are extracted from or added to the WDM link) and a fine switching resolution level (when the contents of the Sp-Ch – i.e. the Sb-Chs-are processed).

The FOX-C node is built as follows for the tests (see Fig. 4-17). At its input, a flexgrid LCoS-based WSS (typical switching time < 500 ms) extracts the 1 Tbps Sp-Ch and sends it over one of its outputs. On a second output, the LCoS-WSS sends the remaining WDM multiplex, from which the Sp-Ch has been removed. The Sp-Ch present over the lower output arm of the WSS is replicated by means of a 1:2 coupler. The first signal replica is used for the "drop" operation. The HSR optical pass-band filter (HSR-OPBF) extracts the sixth sub-band from the Sp-Ch. The second copy on the upper arm of the 1:2 coupler is sent into a HSR optical stop-band filter (HSR-OSBF), which deletes this sixth Sb-Ch from the Sp-Ch. A second 1:2 coupler is added in order to duplicate the extracted sixth sub-band. The copy present on the lower arm of the coupler is used for measurements and optimization of the HSR-OPBF bandwidth. The sixth Sb-Ch replica on the upper arm of the coupler is recombined with the truncated Sp-Ch (from which the sixth Sb-Ch has been removed) by means of a third 2:1

coupler. A de-correlating fiber is inserted in order to shift temporally the truncated Sp-Ch and the sixth Sb-Ch during the recombination process. This de-correlating element allows us to emulate a real crosstalk over the sixth Sb-Ch. The FOX-C node termination is constituted of a second flexgrid LCoS-WSS, which reinserts the reconstituted Sp-Ch in the WDM multiplex.

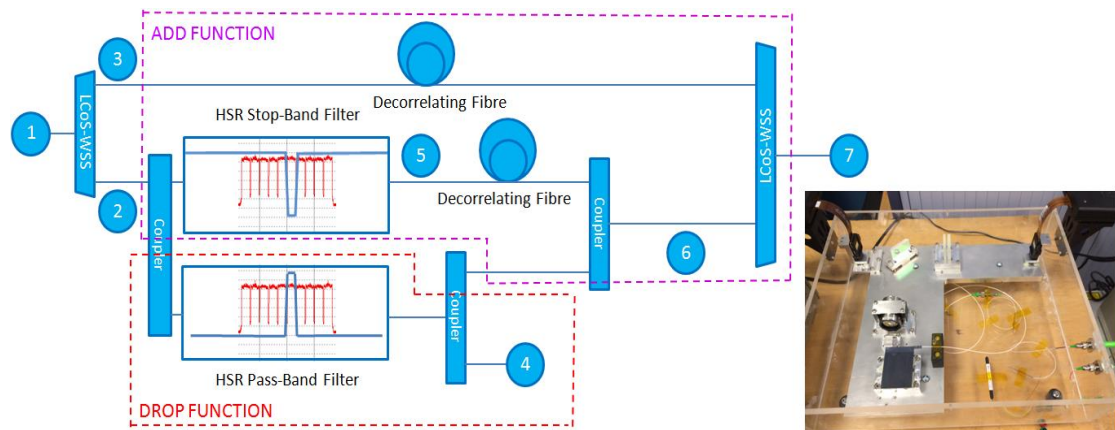


Figure 4-17: Set-up of the FOX-C node with its two levels of optical switching at the superchannel and sub-channel levels. In inset the photo of the HSR pass-band filter whose design is detailed in Appendix B.

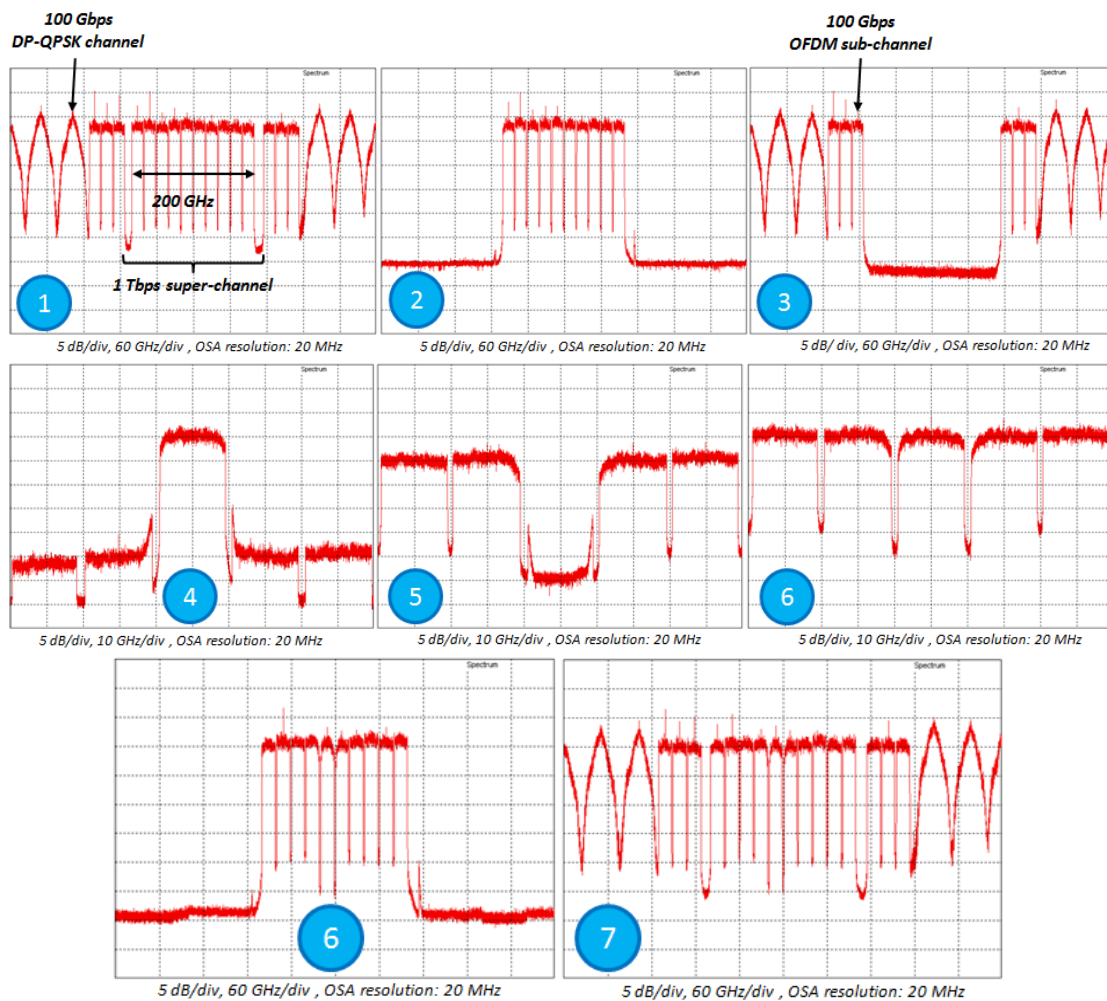


Figure 4-18: Signal spectra at the various "key" locations (labeled by a number going from 1 to 7) inside the FOX-C node in the case of the MB-OFDM superchannel. The location labeled 6 is illustrated by two spectra

in order to look at the overall superchannel as well as a zoom of its central part (where the optical add/drop multiplexing operation is performed).

Compared to the former study operating over QPSK signal, a more selective HSR optical filter is used in this study over 16-QAM. The filter is designed and realized by the project partner Hebrew University of Jerusalem. The design of the filter as well as the obtained profiles are presented in Appendix B. It is capable of being pass-band or stop-band filter. In this study, we use it as the "HSR-OPBF". The Yenista Optics stop-band filter, used in the former sub-wavelength switching study over QPSK signal and whose profile is described in Appendix A, is served as "HSR-OSBF". The signal spectra at the various "key" locations inside the FOX-C node are represented in Fig. 4-18. Note that the HSR-OPBF has a more selective profile, but less extinction ratio (~25 dB) with respect to the HSR-OSBF (~40 dB). That's why the HSR-OPBF does not permit to reject totally the neighboring sub-bands over the spectrum labeled 4.

4.4.2 Back-to-back characterization

The main objective of the BtB characterization is to determine the optimal bandwidth of the optical pass-band and stop-band filters, which are inserted into the FOX-C node, so that the introduction of the HSR OADM function does not induce too much performance penalty, through filtering imperfections and/or signal crosstalk.

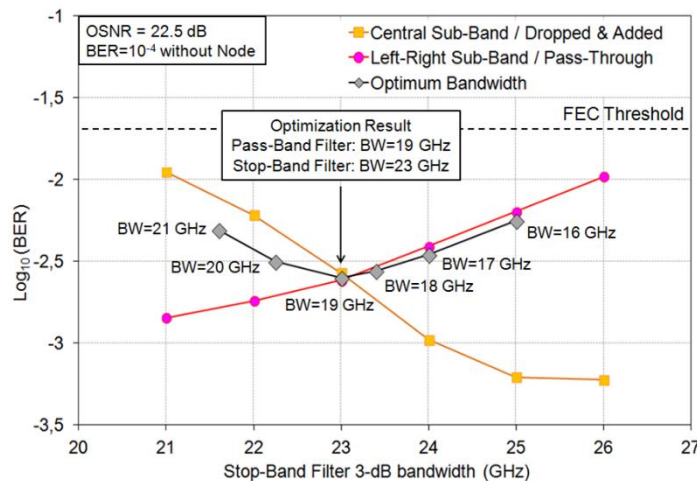


Figure 4-19: BER versus the bandwidth (BW) of the OSBF for the central Sb-Ch 6 and the neighboring left/right-hand Sb-Chs (Sb-Chs 5 and 7), for various BW of the OPBF, in the case of the MB-OFDM Sp-Ch (BW =18 GHz, GB = 2 GHz).

We first fix the OSNR in 0.1 nm to a value of 22.5 dB, which ensures a BER of 10⁻⁴ for the MB-OFDM signal (BW =18 GHz, GB = 2 GHz) in BtB (see Fig. 3-35) when the FOX-C node is not in the experiment. We then introduce the node between the transmitter and receiver. We set the OPBF bandwidth to 19 GHz and vary the OSBF bandwidth from 21 up to 26 GHz, while measuring the BER of Sb-Chs 5, 6 and 7. Fig. 4-19 presents the optimization results. In "orange" color is represented the BER of the central sub-band (sub-band 6). The BER of the neighboring left/right-hand Sb-Chs (Sb-Chs 5 and 7) is shown in "red" color. The crosstalk over the central Sb-Ch, between the added and residual signal, is maximum (respectively, minimum) at low (respectively, at high) bandwidth of the OSBF. The opposite observation can be made for the "pass-through" sub-bands 5 and 7, for which a large OSBF results in high spectral distortions.

The optimum OSBF bandwidth results from a trade-off between the distortions affecting the central Sb-Ch on the one hand, and degradations impairing neighboring Sb-Chs 5 and 7 on the other hand, and is thus obtained at the intersection of the "orange" and "red" curves. This measurement procedure can be reproduced for various OPBF bandwidths going from 16 to 21 GHz. The grey "parabolic" curve is then obtained, and shows that the optimum bandwidths of the HSR-OSBF and HSR-OPBF have values of 23 GHz and 19 GHz, respectively. The corresponding BER is equal to $\sim 2.5 \times 10^{-3}$ for the three sub-bands under concern, which is below the FEC threshold (fixed here at $\text{BER} = 2 \times 10^{-2}$).

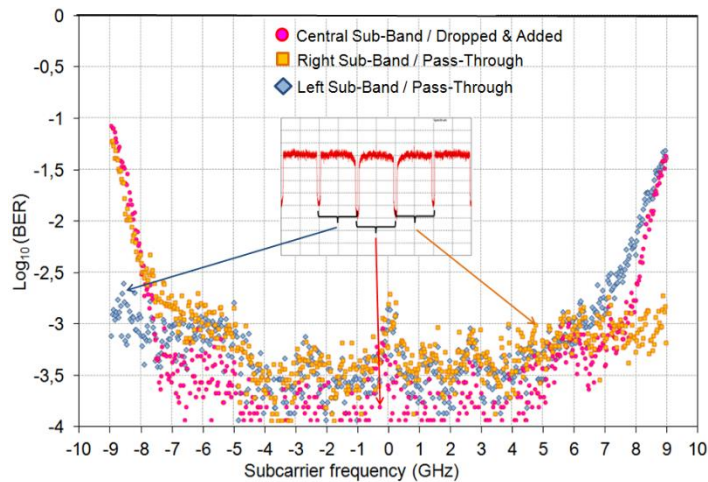


Figure 4-20: BER of the various subcarriers constituting the Sb-Chs 5, 6 and 7 after being routed through the OADM for the optimum bandwidth of the OPBF (BW=19 GHz) and OSBF (BW=23 GHz) in the case of the MB-OFDM Sp-Ch (BW =18 GHz, GB = 2 GHz).

In order to improve the performance of the add/drop process with the perspective of transmission through a number of cascaded FOX-C nodes, we examine in Fig. 4-20 the BER of each subcarrier constituting the OFDM signal for the three Sb-Chs under study (Sb-Chs 5, 6 and 7).

A degradation of the BER performance is observed for the subcarriers which are located at the two edges of the central Sb-Ch (Sb-Ch 6), at the right-hand edge of the left-hand Sb-Ch (Sb-Ch 5) and at the left-hand edge of the right-hand Sb-Ch (Sb-Ch 7). This degradation is due to the distortions experienced by these border subcarriers while going through the OADM, and in particular to the higher attenuation undergone on the sub-band edges. To improve the performance of the add/drop multiplexing process, the idea is to eliminate the most impaired subcarriers from the BER calculation, at the expense of a spectral efficiency reduction.

Fig. 4-21 and Fig. 4-22 present the OSNR sensitivity curves (BER versus OSNR) of the sub-bands 5, 6 and 7 in BtB with and without the FOX-C node for three Sb-Ch bandwidths for BER calculation (18 GHz, 16.5 GHz and 15 GHz) obtained by switching-off 0, 48 and 96 subcarriers, respectively, at the receiver. The theoretical OSNR sensitivity curve is also plotted as reference. It can be observed that modifying the BER calculation bandwidth (at constant OFDM Sb-Ch bandwidth of 18 GHz at the transmitter) does not modify the OSNR sensitivity of the OFDM signal in BtB without the FOX-C node. The situation drastically changes when the FOX-C node is introduced in the experiment. Decreasing the bandwidth removes the error floor present over the OSNR sensitivity curve of the 18 GHz OFDM signal, and permits to limit the OSNR penalty related to the add/drop operation to ~ 1 dB at a $\text{BER} = 1 \times 10^{-3}$ for the 15 GHz OFDM signal, irrespective of the sub-band considered.

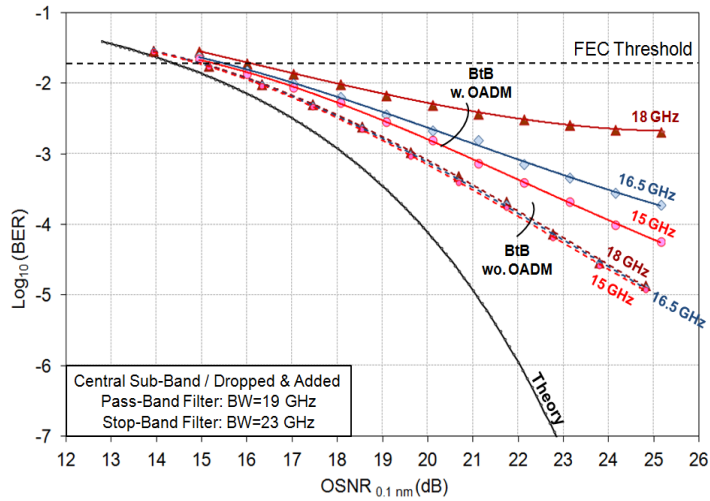


Figure 4-21: BER versus OSNR (in 0.1 nm) of the central Sb-Ch (Sb-Ch 6) in BtB with (w.) and without (wo.) the FOX-C node. Measurements are performed for several BER calculation BW (i.e. 18 GHz, 16.5 GHz and 15 GHz). The OPBF and OSBF are tuned at the previously determined optimum BW values.

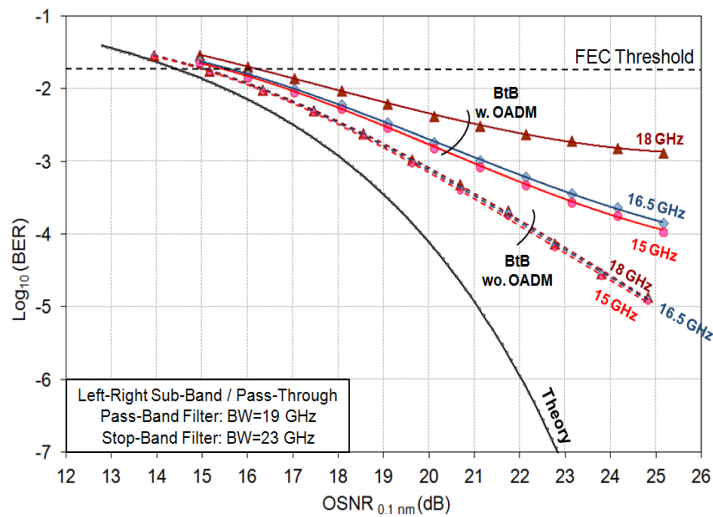


Figure 4-22: BER versus OSNR (in 0.1 nm) of the left/right-hand Sb-Chs (Sb-Chs 5 and 7) in BtB with (w.) and without (wo.) the FOX-C node. Measurements are performed for several BER calculation BW (i.e. 18 GHz, 16.5 GHz and 15 GHz). The OPBF and OSBF are tuned at the previously determined optimum BW values.

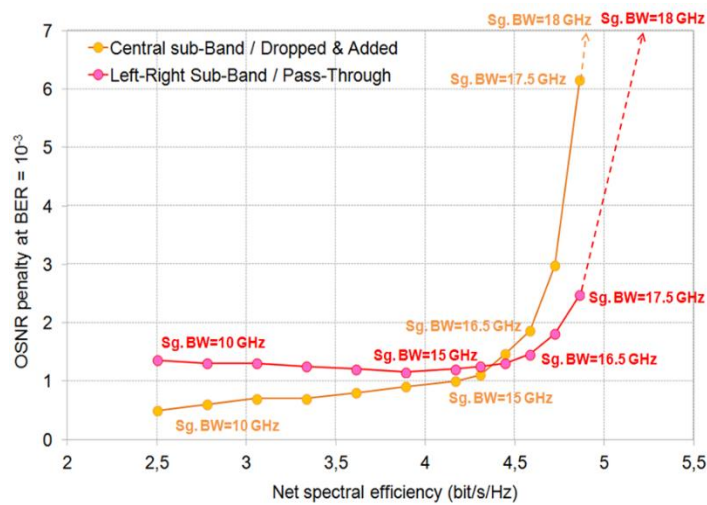


Figure 4-23: OSNR penalty for a $BER=1 \times 10^{-3}$ as a function of the net spectral efficiency for the central Sb-Ch (Sb-Ch 6) and neighboring left/right-hand Sb-Chs (Sb-Chs 5 and 7) after going through the FOX-C node.

OSNR sensitivity curves plotted for various BER calculation bandwidths allow us to infer the OSNR penalty of the OFDM signal as a function of its spectral support. Fig. 4-23 presents OSNR penalty at a BER= 1×10^{-3} for various BER calculation bandwidths “Sg.BW” (or equivalently spectral efficiencies) for Sb-Chs 5, 6 and 7. The net spectral efficiency is defined as the useful bit rate used in the BER calculation after removing edge subcarriers divided by the spectral occupation of the Sb-Ch. OSNR penalty reaches a floor (~ 1 dB) when the spectral efficiencies are lower than 4.16 bit/s/Hz or equivalently when bandwidths are below 15 GHz. The higher floor penalties observed over Sb-Chs 5 and 7 are due to an insufficient rejection of the OPBF (as observed in the spectra 4 of Fig. 4-18).

It is thus now interesting to compare the above results with the performance of the FOX-C node in BtB when the 1 Tbps MB-OFDM Sp-Ch is replaced by its N-WDM counterpart, whose Sb-Chs have a bandwidth of 15 GHz and are separated by 5 GHz guard-bands. OSNR sensitivity curves of N-WDM are plotted in Fig. 4-24 and compared with those of MB-OFDM (in the particular case of a bandwidth of 15 GHz). One can note firstly that the central Sb-Ch shows a better performance than the left/right-hand Sb-Chs. Indeed, the central Sb-Ch suffers from distortions on both sides of its spectrum, while the left/right-hand Sb-Chs experience a single-side but more severe distortion (as shown in spectra 4 and 5 of Fig. 4-18). Furthermore, as explained at the end of the previous paragraph, the insufficient rejection of the OPBF (with respect to the OSBF) generates a higher crosstalk over the edge Sb-Chs 5 and 7. Secondly, Fig. 4-24 shows a slightly better performance of N-WDM compared to MB-OFDM in the presence of the OADM, coming essentially from an improved performance of the N-WDM format in BtB (i.e. without the OADM). However, better performance homogeneity is obtained, after the add/drop multiplexing process, between the central and left/right-hand Sb-Chs for MB-OFDM than for N-WDM. A ~ 1 dB OSNR penalty is measured at BER= 1×10^{-3} for the left/right-hand N-WDM Sb-Chs with respect to the central one. It is probably due to a higher sensitivity of the N-WDM format to distortions of its spectrum with respect to the MB-OFDM scheme.

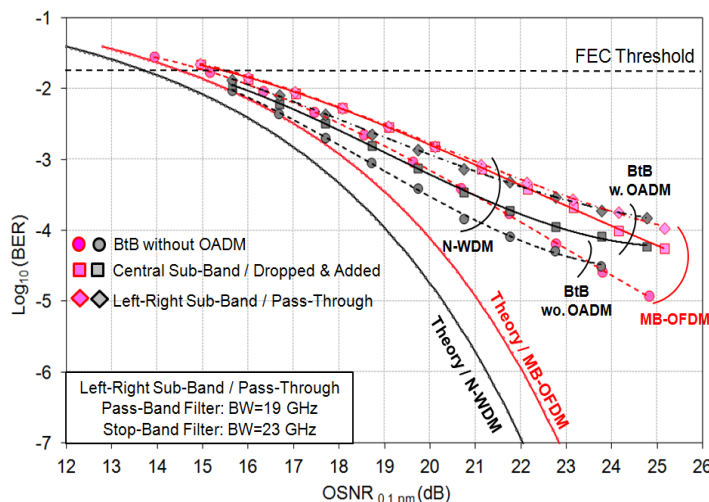


Figure 4-24: BER versus OSNR (in 0.1 nm) in BtB for the N-WDM (black) and MB-OFDM (red) Sp-Chs with or without the FOX-C node. The MB-OFDM Sp-Ch is in its 15-GHz BER calculation BW configuration. The OPBF and OSBF are tuned at the previously determined optimum BW values.

4.4.3 Straight-line Transmission

As depicted in Fig. 4-25, the FOX-C node is now inserted in the Nx100 km G.652 fiber line for transmission evaluation. The transmission line is composed of a maximum of ten spans of

G.652 fiber, separated by EDFA with 20 dB gain and 4.5 dB noise figure. In the middle of the optical link, a dynamic gain equalizer (DGE) is inserted in order to flatten the multiplex power at the receiver side, after 400 km, 600 km, 800 km or 1000 km. This uncompensated transmission configuration is realistic of the coherent 100 Gbps WDM systems currently deployed over optical transport networks, offering significantly enhanced performance compared to legacy dispersion-managed systems.

Transmission without the FOX-C node is firstly performed to determine the optimum power per Sb-Ch to be launched into the G.652 fiber spans. In a second step, the FOX-C node is inserted in the middle of the optical link and the performance degradation is successively measured at a distance of 400 km, 600 km, 800 km and 1000 km for both MB-OFDM and N-WDM Sp-Chs.

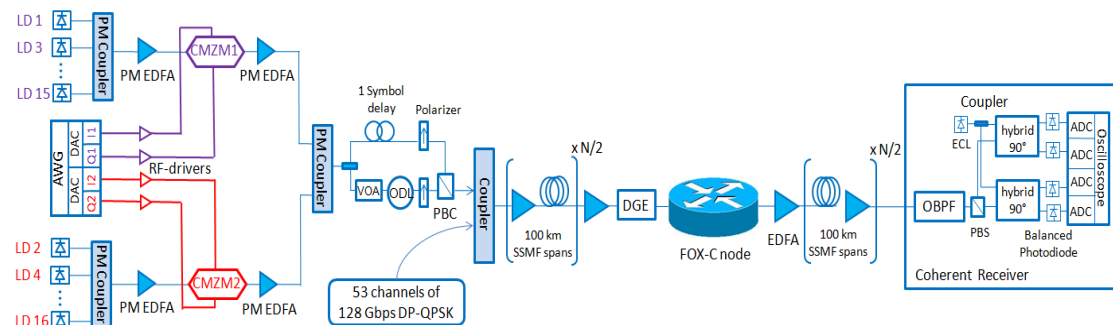


Figure 4-25: Experimental set-up showing the MB-OFDM or N-WDM transmitter, Nx100-km G.652 fiber-based transmission line, and coherent receiver (N = 4, 6, 8, 10).

The curves plotted in Fig. 4-26 and Fig. 4-27 present the BER as a function of the span input power per Sb-Ch in the case of the MB-OFDM Sp-Ch, when no OADM is inserted into the link. These curves allow us to determine the optimum Sb-Ch power to be injected into the fiber spans from 400 km to 1000 km transmission reach. The BER of the central Sb-Ch (Sb-Ch 6) and its left/right-hand neighbors (Sb-Chs 5 and 7) after transmission through N/2 fiber spans, one OADM, and N/2 fiber spans are then measured and placed (gray and purple symbols, respectively) over the graphs. Fig. 4-26 and Fig. 4-27 show the results of 18-GHz and 15-GHz BER calculation BW, respectively. As described above, the 18-GHz configuration takes into account all the subcarriers transmitted in the BER calculation, while the 15-GHz configuration removes 3 GHz of most impacted subcarriers during the BER calculation stage.

From Fig. 4-26, it can be seen that the introduction of FOX-C node has an impact over the transmission performance and makes, for example, the BER after 400 km equivalent to that of 600 km without OADM. At 1000 km with OADM, the BER of central and left/right Sb-Chs are both under the SD-FEC threshold (fixed here at 2×10^{-2}), which means error-free transmission can still be achieved. For 15-GHz configuration (Fig. 4-27), it can be observed that the introduction of the FOX-C node does not degrade too much the transmission performance (less than 2 tenths of a decade). The filtering impairments and spectral crosstalk inside the OADM are thus well-controlled. The BER of the central and left/right-hand Sb-Chs are below the FEC threshold, irrespective of the distance under study, which guarantees error-free transmission up to 1000 km. Good performance homogeneity exists between the central and left/right-hand Sb-Chs.

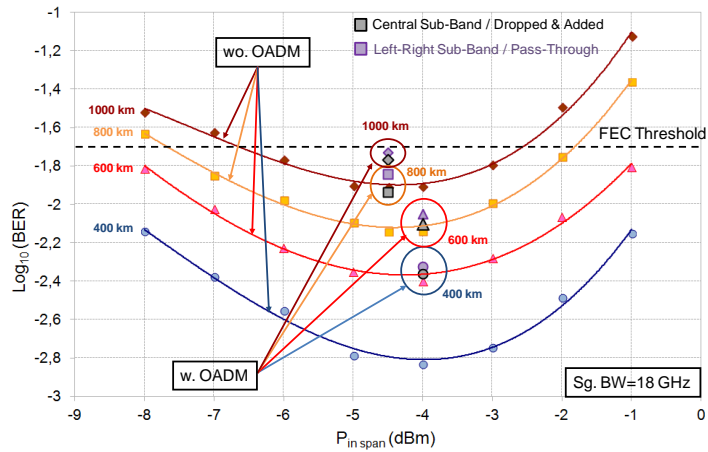


Figure 4-26: BER versus span input power per Sb-Ch for the MB-OFDM Sp-Ch for various transmission distances (400 km, 600 km, 800 km and 1000 km) when the OADM is not inserted into the link. The 18-GHz BER of the central and left/right-hand Sb-Chs (Sb-Chs 5, 6 and 7) after going through the OADM are plotted with gray and purple symbols.

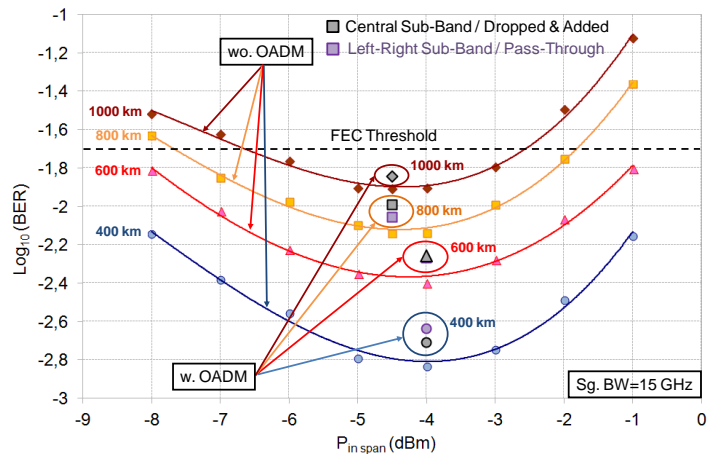


Figure 4-27: BER versus span input power per Sb-Ch for the MB-OFDM Sp-Ch for various transmission distances (400 km, 600 km, 800 km and 1000 km) when the OADM is not inserted into the link. The 15-GHz BER of the central and left/right-hand Sb-Chs (Sb-Chs 5, 6 and 7) after going through the OADM are plotted with gray and purple symbols.

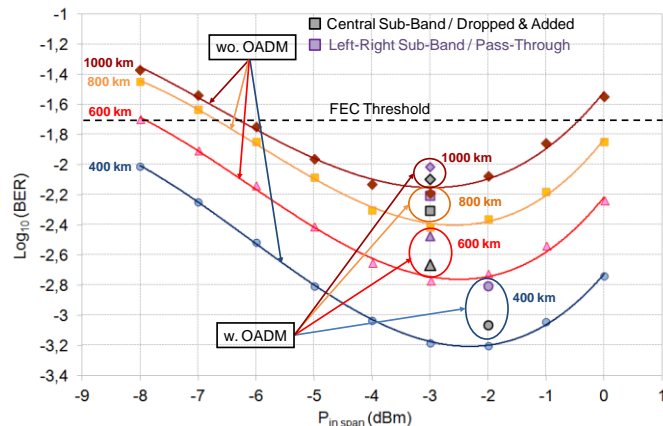


Figure 4-28: BER versus span input power per Sb-Ch for the N-WDM Sp-Ch for various transmission distances (400 km, 600 km, 800 km and 1000 km) when the OADM is not inserted in the link. The BER of the central and left/right-hand Sb-Chs (Sb-Chs 5, 6 and 7) after going through the OADM are also plotted over this graph (gray and purple symbols, respectively).

Fig. 4-28 is equivalent to Fig. 4-27 but for the N-WDM Sp-Ch with 15-GHz Sb-Ch bandwidth. When the OADM is not inserted into the optical link, we observe a small improvement of the BER with respect to MB-OFDM (oscillating between 2 and 4 tenths of a decade), combined with an increase of the optimum span input power per Sb-Ch (going from 1.5 to 2 dB). This means that N-WDM is more robust to fiber nonlinearities than MB-OFDM. The BER of the central and left/right-hand Sb-Chs after going through the transmission line and OADM are also plotted over this graph at the optimum span input power per Sb-Ch. As previously reported in BtB, lesser homogeneity exists between the performance of the central and left/right-hand Sb-Chs with N-WDM than with MB-OFDM (in particular, at 400 km and 600 km). As for MB-OFDM Sp-Ch, from 400 km up to 1000 km, the BER of the central and left/right-hand Sb-Chs of the N-WDM Sp-Ch are largely below the SD-FEC threshold after going through the OADM.

4.4.4 Cascadability of sub-wavelength OADM

The question of the cascadability of the FOX-C node is now addressed over MB-OFDM Sp-Ch. The same as the sub-wavelength OADM study over QPSK modulated 100 Gbps MB-OFDM, the repeated add-drop operations are realized by recirculating loop composed of fiber spans and one sub-wavelength OADM. In the previous cascadability study, pure EDFA was used as the only amplification scheme, and 1000-km transmission as well as five cascades were achieved. Compared to QPSK modulation, 16-QAM has intrinsically less transmission reach and the BER after 1000 km is already close to the SD-FEC threshold. In order to push the transmission reach of 16-QAM, besides pure EDFA configuration, hybrid Raman-EDFA amplification is implemented in this study. In addition, we suppose an SD-FEC threshold of 3.8×10^{-2} [109] instead of 2×10^{-2} for the 16-QAM signal after repeated add-drop operations.

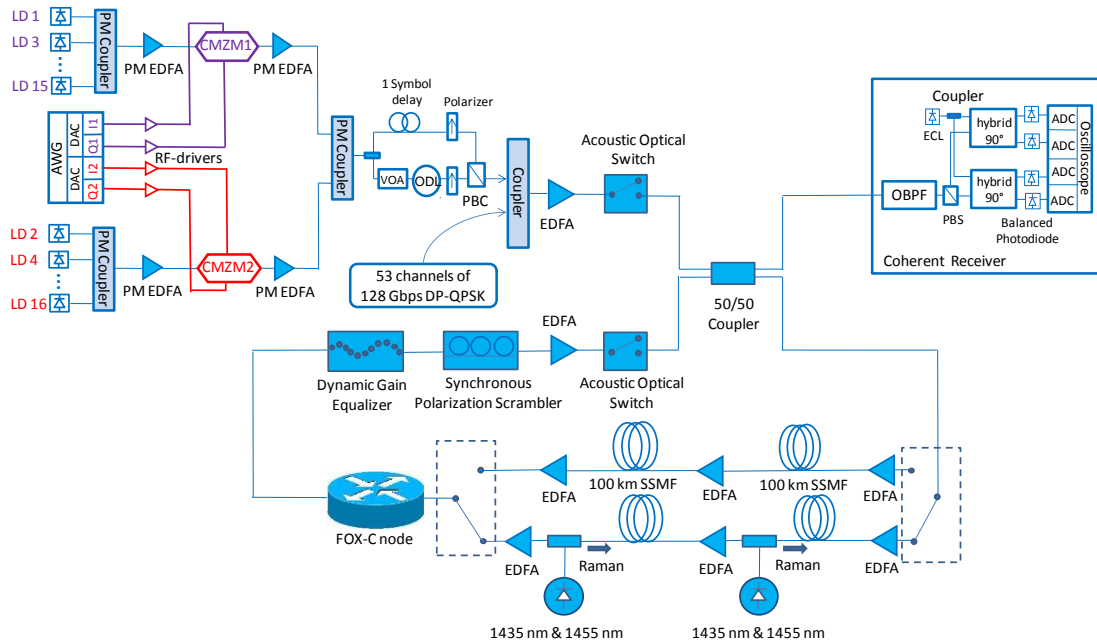


Figure 4-29: Set-up of the OFDM transmitter and the 2×100 -km G.652 fiber-based recirculating loop equipped with pure EDFA or Raman-EDFA.

The experimental set-up is depicted in Fig. 4-29. The transmitter and receiver remain the same as in BtB characterization and straight-line transmission. The transmitter is connected to the recirculating loop through an acousto-optic (AO) switch. The loop consists of two 100-km

spans of G.652 fiber equipped with either pure EDFA or hybrid Raman-EDFA. In the first configuration, EDFAs have 20-dB gain and 4.5-dB noise figure. In the second, two Raman pumps at 1435 nm and 1455 nm offer 12 dB of backward Raman gain, with an additional EDFA compensating for the remaining loss. The ROADM node is inserted after the fiber span. A dynamic gain equalizer and a synchronous polarization scrambler achieve power equalization and polarization rotation of the WDM multiplex after each loop round-trip.

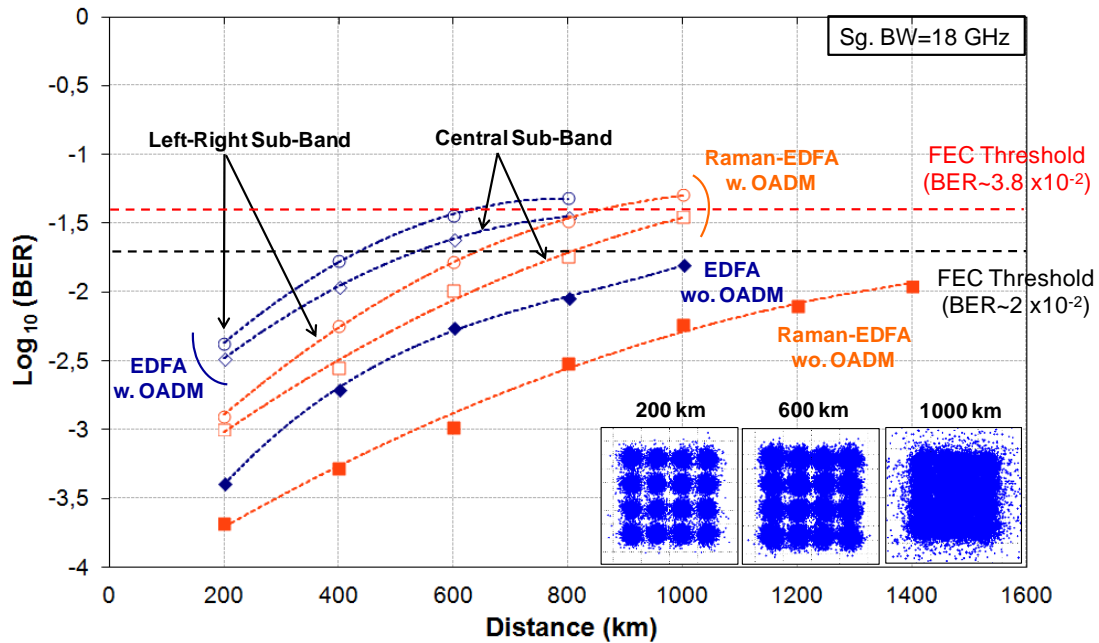


Figure 4-30: BER versus distance with (w.) and without (wo.) the ROADM node for the MB-OFDM Sp-Ch in the 18-GHz BER calculation BW configuration. Insets show constellations of the central Sb-Ch with the ROADM node and hybrid Raman-EDFA after 200, 600 and 1000 km (1,3 and 5 loops).

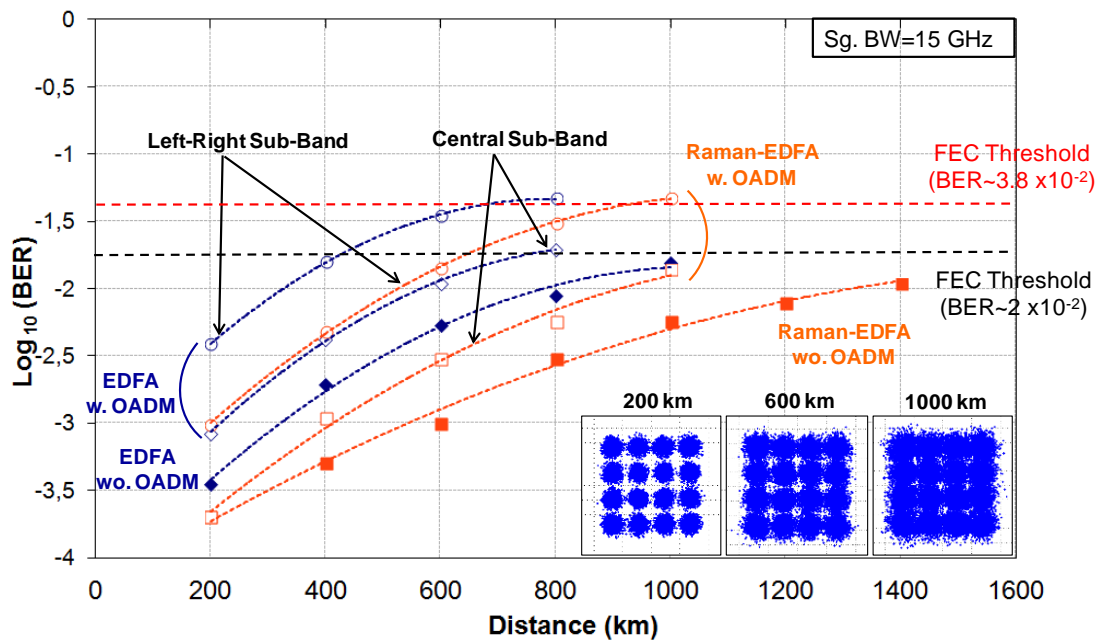


Figure 4-31: BER versus distance with (w.) and without (wo.) the ROADM node for the MB-OFDM Sp-Ch in the 15-GHz BER calculation BW configuration. Insets show constellations of the central Sb-Ch with the ROADM node and hybrid Raman-EDFA after 200, 600 and 1000 km (1,3 and 5 loops).

The transmission results with and without the ROADM node for BER calculation BW of 18 GHz and 15 GHz are shown in Fig. 4-30 and Fig. 4-31. Without the node, the BER is below 2×10^{-2} after 1000 km and 1400 km for pure EDFA and hybrid Raman-EDFA, respectively. With the node and at 18-GHz BW (Fig. 4-30), error free transmission with a FEC threshold of 2×10^{-2} is achieved over 400 km and 800 km for the central Sb-Ch using pure EDFA and hybrid Raman-EDFA, respectively. Increasing the FEC threshold to 3.8×10^{-2} allows error-free transmission over 800 km and 1000 km, respectively. These distances correspond to 4 and 5 loop round-trips with one add/drop operation in each loop round-trip. The transmission reach of the left-right Sb-Ch in the same configuration is 600 km and 800 km respectively, slightly worse than that of the central Sb-Ch. Decreasing the BW from 18 GHz to 15 GHz (Fig. 4-31) gives significant performance improvements for the central Sb-Ch, however, the left-right Sb-Ch only exhibits a slight performance improvement.

4.5 Conclusion

In this chapter, we have described the concept of sub-wavelength optical switching, which performs optical aggregation and switching at the Sp-Ch contents level using ultra-selective optical filters. The proposed switching scheme achieves reduced CAPEX cost for the overall network as well as spectrum saving. In a meshed optical network, the Sp-Ch contents are supposed to pass through several sub-wavelength switching elements, which may introduce large impairments to the signal. Few experimental studies were carried out in state-of-art to demonstrate the feasibility of such repeated add-drop operations at the Sp-Ch contents level. In this chapter, we have successfully proven the cascability of such sub-wavelength switching over QPSK and 16-QAM signal; owing to the use of ultra-fine optical filters, the careful design of sub-wavelength OADM and the use of optimized recirculating loop.

The sub-wavelength switching is first realized inside QPSK modulated 100 Gbps MB-OFDM superchannel, composed of four 8-GHz sub-bands with 2- or 4-GHz guard-bands. After pass-band and stop-band filters' bandwidth optimization and the BtB performance evaluation, we decide to continue with 4-GHz guard-band configuration for the transmission study. We observe negligible performance degradation after 10x100-km's transmission with one sub-wavelength OADM in the middle of the link. In the cascability study, error-free transmission is achieved at five loop round-trips including 1000-km's fiber line and 5 sub-wavelength add-drops, which shows the feasibility of such sub-wavelength switching over closely spaced QPSK modulated OFDM signal.

The experimental proof-of-concept is then extended to 16-QAM modulation. The sub-wavelength switching is realized inside 1Tbps MB-OFDM and N-WDM superchannel, composed of ten 18-GHz or 15-GHz sub-bands with 2- or 5-GHz guard-bands. More selective pass-band and stop-band filter is developed by project partner and implemented in the sub-wavelength OADM, which permits the sub-wavelength add-drop of 16-QAM signal with small guard-bands. With SD-FEC threshold fixed at 2×10^{-2} , both MB-OFDM and N-WDM demonstrate error-free transmission of 10x100 km with one sub-wavelength OADM in the middle of the link. Considering that 16-QAM has a higher OSNR requirement compared to QPSK, hybrid Raman-EDFA and higher SD-FEC threshold (3.8×10^{-2}) are considered in the cascability study. Under this condition, 4-5 loop round-trips can be realized, corresponding to a transmission reach of 800-1000 km and 4-5 sub-wavelength add-drops. Through these results, we show the feasibility of sub-wavelength switching using a high order modulation format such as 16-QAM.

CHAPTER 5

NEXT GENERATIONS OF ULTRA-HIGH BIT RATE TRANSCEIVERS AND TECHNOLOGIES

In chapter 3 and 4, we have focused the study on coherent multi-band OFDM (MB-OFDM) technique in the form of 100 Gbps, 400 Gbps and 1 Tbps superchannel with either QPSK or 16-QAM modulation. We have shown its capability to address various long-haul transmission schemes. In the elastic optical networking (EON) context, the feasibility of sub-wavelength optical switching has been demonstrated inside QPSK and 16-QAM modulated MB-OFDM and Nyquist-WDM (N-WDM) superchannel. These studies rely on off-line signal processing and some non-industrialized components, such as ultra-selective optical filters. Besides these medium or long term studies, operators are also interested in short-term research topics which may open new possibilities in the near future.

The 100 Gbps coherent DP-QPSK is considered as a credible technique following the 10 Gbps NRZ-OOK in long-haul network and commercial transceivers are available in the market. The next question that concerns the operators would be the further reduction of the cost of the 100 Gbps transceivers. Recently, Silicon photonics make it possible the integration of a coherent 100 Gbps transmitter-receiver with advanced digital signal processing (DSP) and soft-decision FEC (SD-FEC) into a C-form factor pluggable (CFP) module of 3.2 x 5.7 inches [110]. This technology will potentially permit significant reduction of cost and power consumption. In the first section of this chapter, we will introduce 100 Gbps digital coherent CFP module and investigate its capability of addressing different transmission scenarios.

Besides transceivers, optical fiber is also an essential element of optical transport networks. Up to now, operators adapted the fiber type to the specificities of their networks. For instance, ITU-T G.652.D [111] fibers were deployed over regional and core transport networks. In France, ARCEP (the French telecommunication regulator) imposes to use ITU-T G.657.A2 [112] fiber for building wiring and connection boxes, because it tolerates bends of 15-mm diameter while being fully compliant with G.652 pigtails. Today, operators would like to deploy G.657.A2 fiber in regional networks, and it is more than likely that this uniformity process will be extended soon to ultra-long-haul (ULH) networks. In the second section of this chapter, we will investigate G.657.A2 fiber with a realistic long-haul transmission scenario and compare its performance with the currently deployed G.652.D fiber.

Since 100 Gbps solution is under massive deployment, operators begin to search for the next mature technology capable of supporting higher bit rate. Recently, equipment suppliers propose 400 Gbps coherent WDM interface using dual-carrier Nyquist-filtered DP-16QAM [113]. It achieves a spectral efficiency of 5.33 bit/s/Hz, which is improved by 166% compared to 100 Gbps. However, recent laboratory and field trials have reported no more than 500 km of error-free transmission distance over uncompensated G.652 fiber line with 400 Gbps coherent dual-carrier DP-16QAM, EDFA only and no OSNR margin [13-15]. For operators, the primary concern is to reuse at 400 Gbps the existing G.652/G.655 fiber-based long-haul transparent meshed optical transport networks, and to limit as much as possible the need for electrical regeneration. In the section 3 of this chapter, we demonstrate for the first time uncompensated error-free transmission of 400 Gbps real-time coherent dual-carrier DP-16QAM over 1000 km (resp. 500 km) of G.652 (resp. G.655) fiber using purely EDFA amplification.

5.1 100 Gbps digital coherent CFP interface for short reach, regional, and ultra-long-haul optical communications

Silicon photonics [114] drive an incredible technological breakthrough in the field of ultra-high bit-rate coherent WDM interfaces. Integrating a coherent 100 Gbps transmitter-receiver with advanced digital signal processing (DSP) and soft-decision FEC (SD-FEC) into a C-form factor pluggable (CFP) module of 3.2 x 5.7 inches is today possible [110]. This high level of miniaturization results in a drastic reduction of cost, power consumption and size of 100 Gbps WDM interfaces while, in parallel, the performance degradation in transmission is strictly constrained. For operators facing an exponential growth of their IP traffic and a continuous erosion of their average revenue per user (ARPU), there is a triple advantage to introduce 100 Gbps digital coherent CFP (DCO-CFP) into their optical transport network. Beyond the cost and power consumption reduction enabling lower capital and operational expenditures, the banalization of 100 Gbps client and WDM ports (thanks to a standardized electrical interface) makes attractive and credible IP over WDM scenario, while the high level of flexibility of the interface make it adaptable to various contexts going from purely passive network element (NE) interconnection up to regional, and ultra-long-haul WDM transmission applications.

In this section, after a brief description of the characteristics and capabilities of the 100 Gbps DCO-CFP under test, we evaluate its performance in various transmission scenarios. When LR4/ER4 client 100 GbEthernet (GbE) CFP reach (10/40 km) is too short to connect two NE (for instance, two IP routers), 100 Gbps digital coherent CFP offers a cost-effective alternative to cover passively typical distances of 80-120 km. In the regional context, it can address 100 Gbps upgrade of 10 Gbps dispersion-managed WDM systems at the optimal cost. In the ultra-long-haul (ULH) scenario with full 100 Gbps transmission, it covers nearly all the needs of a pan-European backbone with maximum transmission distances of ~2000 km over uncompensated G.652 fiber line.

5.1.1 100 Gbps digital coherent CFP module

The highest benefit of 100 Gbps DCO-CFP is to halve the price of common 100 Gbps WDM interfaces, while drastically reducing the size (divided by four) and the power consumption (divided by three when considering Optical Internetworking Forum (OIF) requirements). When the Turbo-Product-Code (TPC) FEC with three iterations is activated and the chromatic dispersion (CD) and polarization mode dispersion (PMD) compensation are at their maximum value (i.e. 34000 ps/nm for CD and 25 ps for PMD), the power consumption is only of 27 W. The main features of the interface are summarized in Tab. 5-1. Fig. 5-1 shows the size of OIF 100 Gbps WDM interface, 100 Gbps client LR4 CFP and 100 Gbps DCO-CFP.

Table 5-1: Compared features of a OIF 100 Gbps WDM interface and the 100 Gbps DCO-CFP under test.

	OIF 100G WDM interface	100G digital coherent CFP
Line Rate	128 Gbps	120 Gbps
FEC Threshold	SD-FEC (LDPC) BER ~ 2.5×10^{-2}	SD-FEC (TPC) BER ~ 1.5×10^{-2}

CD	~50000 ps/nm	~34000 ps/nm
Distance	Up to 3000 km	Up to 2000 km
PMD	Up to 30 ps	Up to 25 ps
Sensitivity	-22 dBm	-28.4 dBm
Wavelength Range	Full C-Band	Full C-Band
Power Consumption	~80 W (OIF) ~200 W (others)	27 W
Size	9" x 9"	3.2" x 5.7"

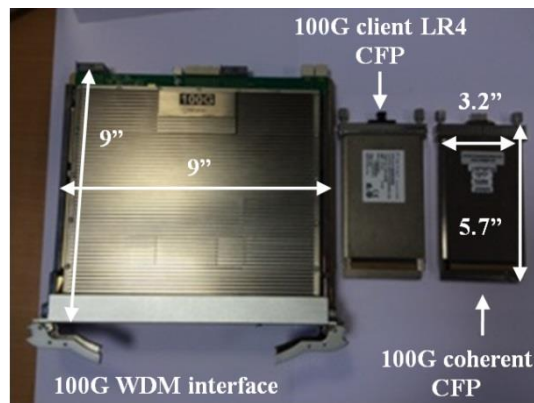


Figure 5-1: OIF 100 Gbps WDM interface, 100 Gbps client LR4 CFP and 100 Gbps DCO-CFP.

The SD-FEC used in the module is a TPC [86], with a pre-FEC BER threshold of 1.5×10^{-2} , a net coding gain (NCG) of 11.1 dB at 10^{-15} and an overall overhead of 15%. As shown in Fig. 5-7, the OSNR in 0.1 nm at the FEC threshold is equal to 13 dB. The flexibility of the module is very high and it can adapt its features to the specificities of the link. Beyond the automatic CFP adaptation to CD or PMD, the ability to choose the number of iterations (up to 3) of the TPC or to deactivate the SD-FEC for an energy-efficient hard-decision FEC (HD-FEC) is possible, while the capability to adapt the size of the common phase estimation (CPE) window to the transmission impairment (amplified spontaneous emission noise or nonlinear effects) is offered.

5.1.2 Passive interconnection of distant NE

In a first step, the capability of the interface to interconnect two distant network elements (NE) without the insertion of an EDFA is evaluated. The experimental set-up is depicted in Fig. 5-2. A 100 GbE LR10 client CFP module and a 100 Gbps DCO-CFP interface are plugged together into the ACACIA evaluation board. The 100GbE LR10 CFP is connected to a 100 GbE tester for long-duration BER measurements, while the coherent CFP feeds a G.652 fiber line. Its output optical power is tuned at its maximum value (i.e. +3 dBm). Inside the evaluation board, the two CFP communicate together thanks to a 100G attachment unit interface (CAUI). We first vary the fiber length by step of 25 km and measure the pre-FEC BER by verifying in the same time that transmission is error-free thanks to the 100GbE tester.

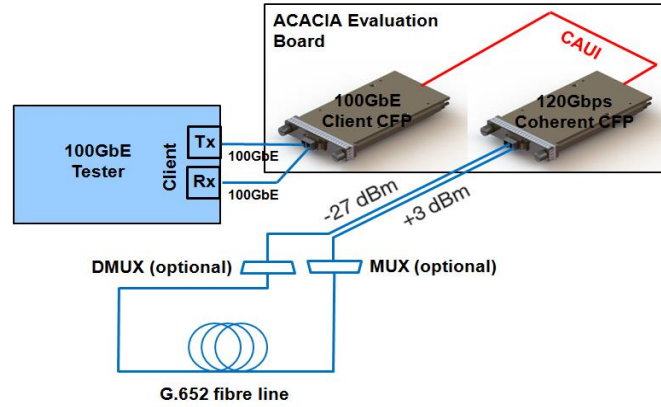


Figure 5-2: Experimental setup for the NE interconnection test without EDFA.

Results are summarized in Fig. 5-3. An error-free transmission distance of 150 km (corresponding to a received CFP power P_{in-Rx} of -27 dBm) is achieved with a pre-FEC BER of 2.7×10^{-3} , far from the FEC limit fixed here at 1.5×10^{-2} . In case of fiber shortage to interconnect NE, it could be interesting to combine several 100 Gbps channels of different wavelengths into one fiber (still without the help of an EDFA) thanks to the insertion of a WDM multiplexer (resp. demultiplexer) at the transmitter (resp. receiver) side. The results of Fig. 5-3 show that it is possible to reach 125 km when the cumulative MUX-DMUX losses are 4.5 dB. In order to evaluate precisely the receiver sensitivity of the CFP interface, the fiber line is replaced by an attenuator. The FEC threshold is then reached for $P_{in-Rx} = -28.4$ dBm.

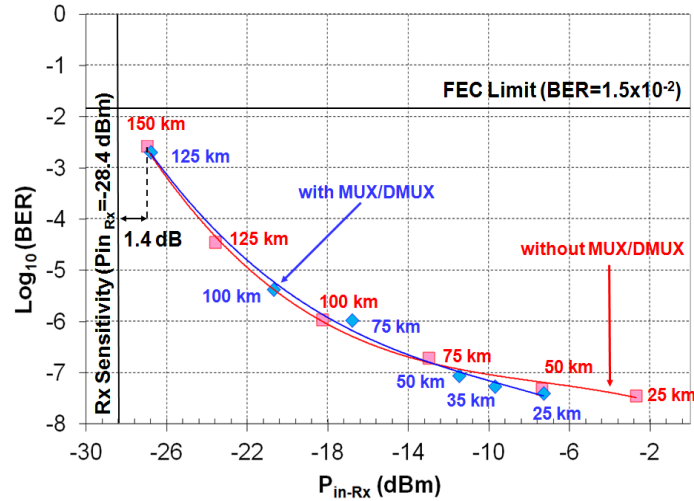


Figure 5-3: BER versus received CFP power P_{in-Rx} for various lengths of G.652 fiber.

5.1.3 100 Gbps up-grade of metro-regional 10 Gbps WDM systems

Another interesting use case for the deployment of 100 Gbps DCO-CFP interface is the up-grade at 100 Gbps of existing metro-regional WDM systems operating at 10 Gbps. The experimental setup is shown in Fig. 5-4. The wavelength generated by the 100 Gbps DCO-CFP interface is inserted in a 79x10 Gbps NRZ WDM multiplexer and injected into a 10x100 km dispersion-managed (DM) G.652 fiber line. The span losses (~ 20 dB) are overcome by double-stage EDFA with 6-dB noise figure, whose inter-stage receives 90-km dispersion compensation fiber (DCF-90) module. A pre-compensation fiber of -1000 ps/nm

broadens the pulses before their insertion into the line. A dynamic gain equalizer (DGE) located after 500 km flattens the WDM multiplex. A -700 ps/nm post-compensation stage closes the line.

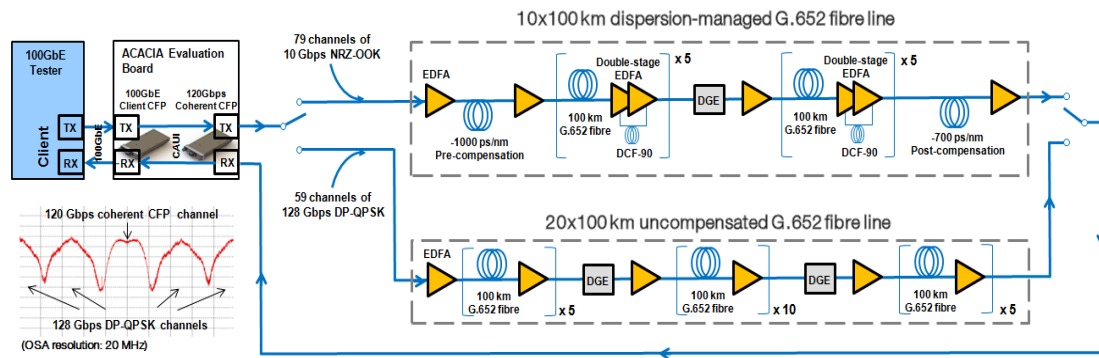


Figure 5-4: Experimental setup in the mixed 10/100 Gbps system configuration and full 100 Gbps transmission scenario.

Results are displayed in Fig. 5-5. BER are plotted as a function of the span input power per channel ($P_{in\ span} / Channel$). In the first configuration (continuous blue line), the 100 Gbps channel propagates together with the 10 Gbps multiplex without any guard interval (GI) nor power difference $\Delta P = P_{100G} - P_{10G}$. As shown in Fig. 5-5, error-free transmission is achieved up to 700 km. For longer distances, the 100 GbE tester measures some errors periodically caused by inter-channel nonlinear effects. To increase the system reach up to 1000 km, a GI (dashed red curve with triangles) or a power difference $\Delta P = P_{100G} - P_{10G}$ (dashed red curve with star-squares) between the 10 Gbps channels and the 100 Gbps signal has to be introduced. Long-term BER measurements show that a 100 GHz GI is required in the first case and a $\Delta P = P_{100G} - P_{10G} = +2.5$ dB power difference in the second case to effectively reach 1000 km. Note that the BER of 10 Gbps neighboring channels is not disturbed by these operations.

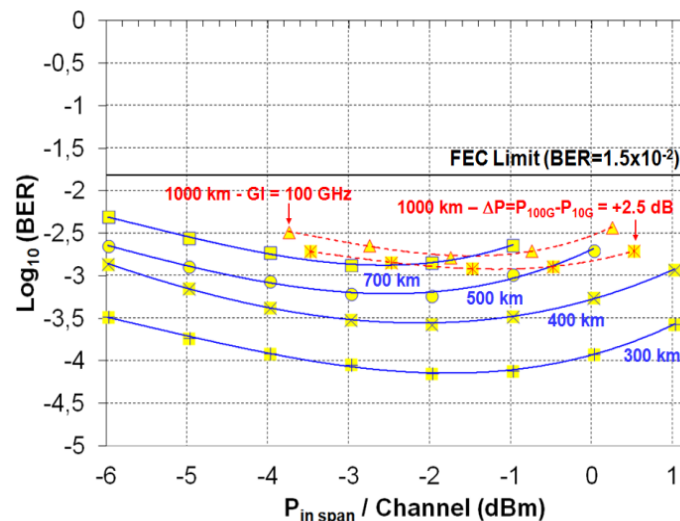


Figure 5-5: BER vs. Pin span / Channel for the 100 Gbps DCO-CFP under test in the mixed 10/100 Gbps WDM system.

5.1.4 Full 100 Gbps ULH WDM transmission

Finally, the scenario of a full 100 Gbps ULH uncompensated WDM transmission is studied. The experimental set-up is shown in Fig. 5-4. The wavelength generated by the 100 Gbps

DCO-CFP interface is inserted in a 59x100 Gbps DP-QPSK WDM multiplex and injected into a 20x100 km uncompensated G.652 fiber line. The span losses (~20 dB) are balanced by single-stage EDFA with 4.5-dB noise figure. Two DGE flattens the WDM multiplex at 500 km and 1500 km. BER versus $P_{in\ span} / Channel$ curves are plotted in Fig. 5-6 for various distances. Note that only one DGE is kept when system reach is lower than 1000 km. Error-free transmission is achieved up to 2000 km with a significant margin ($BER=6.7 \times 10^{-4}$) with respect to the FEC limit.

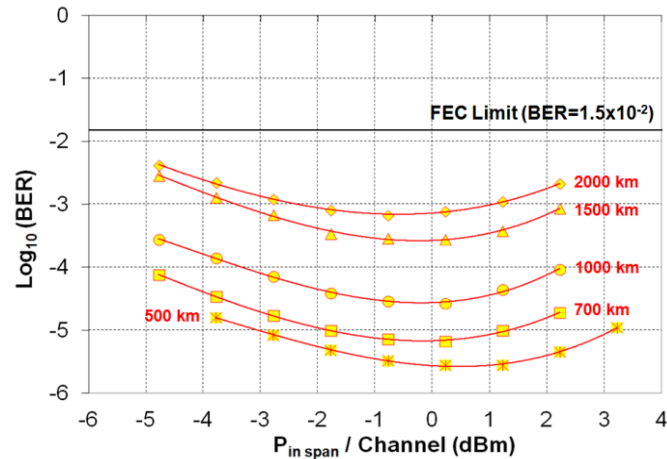


Figure 5-6: BER vs. $P_{in\ span} / Channel$ for the 100 Gbps DCO-CFP under test in the full 100 Gbps system configuration.

Finally, in Fig. 5-7, the optimum of each BER versus $P_{in\ span} / Channel$ curves is reported over a BER versus OSNR graph, where are also plotted the back-to-back (BtB) sensitivity curves of the laboratory 100 Gbps DP-QPSK reference and 100 Gbps DCO-CFP under test. After 2000 km, the non-linear effect (NLE) penalty is equal to ~2 dB, and ~1.4 BER decade margin is present with respect to the FEC limit.

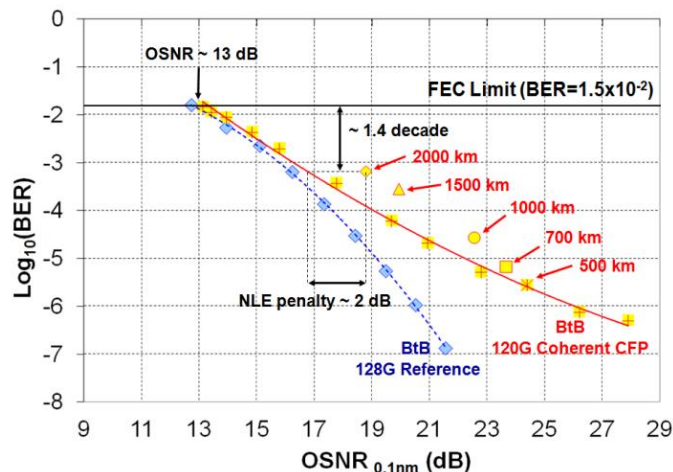


Figure 5-7: BER vs. OSNR 0.1 nm in BtB for our off-line laboratory 100 Gbps reference and for the 100 Gbps DCO-CFP under test. BER vs. OSNR points at the optimum $P_{in\ span} / Channel$ for various distances.

We have shown here that 100 Gbps DCO-CFP interface is a low-cost and power-efficient modular solution to address short-reach (interconnection of distant NE without EDFA in single or multi-wavelength environment), regional (with 100 Gbps upgrade of legacy 10 Gbps WDM systems) and ultra-long-haul (with full 100 Gbps WDM transmission) applications. It

will be an essential element of future ultra-high bit-rate optical transport networks with a large field of applications from the IP routers up to metro and core transport networks, and a strong factor of convergence of IP and optical world.

5.2 Performance comparison of G.657.A2 and G.652.D fibers

Optical fiber is an essential element of optical transport networks. Up to now, operators adapted the fiber type to the specificities of their networks. For instance, ITU-T G.652.D [111] fibers were deployed over regional and core transport networks. In France, ARCEP (the French telecommunication regulator) imposes to use ITU-T G.657.A2 [112] fiber for building wiring and connection boxes, because it tolerates bends of 15-mm diameter while being fully compliant with G.652 pigtailed. Thanks to its advantageous properties, G.657.A2 fiber has also been chosen in optical access networks to connect optical line terminals (OLT) to optical networks units (ONU). As a consequence, its large spreading has made easier the fiber/cable management in fiber-to-the-home (FTTH) networks. Today, operators would like to deploy G.657.A2 fiber into regional networks, and it is more than likely that this uniformity process will be extended soon to ultra-long-haul (ULH) networks. However, to make it relevant for such applications, the tolerance of G.657.A2 fiber to nonlinear effects has to be deeply investigated.

In this section, we compare the performance of G.657.A2 and G.652.D fibers over a 20x100 km uncompensated transmission line. We repeat the experiment with two 100 Gbps interfaces in order to confirm the comparison results: 100 Gbps Optical Internetworking Forum (OIF) multi-source agreement (MSA) coherent transceiver [115] (dedicated to ultra-long-haul applications) and 100 Gbps digital coherent C-form factor pluggable (DCO-CFP) interface [110] (devoted to low-cost metro-oriented applications). We show that G.657.A2 and G.652.D fibers have similar performance at 100 Gbps, while both OIF-MSA and DCO-CFP interfaces have comfortable system margins with respect to forward error correction (FEC) code threshold after 2000 km.

5.2.1 G.657.A2 versus G.652.D fibers

Table 5-2: Compared features of the G.652.D and G.657.A2 fibers under test.

	G.652.D	G.657.A2
Mode Field Diameter 1550 nm	10.4 ± 0.5 μm	9.7 ± 0.5 μm
Attenuation 1310 – 1625 nm	≤ 0.40 dB/km	≤ 0.40 dB/km
Attenuation 1550 nm	0.20 dB/km (typ.)	0.195 dB/km (typ.)
Dispersion 1550 nm	≤ 18 ps/(nm.km)	≤ 18 ps/(nm.km)
PMD Link Design Value	≤ 0.06 ps/nm ^{1/2}	≤ 0.06 ps/nm ^{1/2}
	Macro-Bend Loss at 1625 nm	
Mandrel Diameter	60 mm	60 / 15 mm
Number of turns	100	100 / 1
Attenuation	≤ 0.1 dB	≤ 0.05 / ≤ 1 dB

The main interest of G.657.A2 fiber resides in its high robustness to bends. For instance, the loss is lower than 1 dB for a curvature of 15-mm diameter at 1625 nm and less than 0.05 dB if the fiber is hundred-fold turned over a 60-mm mandrel. The trench-assisted index-profile structure also lowers micro-bending sensitivity and cable-induced loss effects. The other parameters are identical to those of G.652.D fiber, except the attenuation and mode field diameter at 1550 nm which are slightly lower for the G.657.A2 fiber (see Tab. 5-2) with a possible effect over the sensitivity to nonlinear effects.

5.2.2 Experimental set-up

The 120 Gbps DP-QPSK wavelengths generated by the OIF-MSA interface at 1548.51 nm and the DCO-CFP module at 1547.72 nm are inserted in a 58x120 Gbps DP-QPSK 50-GHz spaced WDM multiplex and injected into an uncompensated fiber line of 20x100 km constituted of the two fibers under test (see Fig. 5-8). The 19.5 / 20-dB span losses of the G.657.A2 / G.652.D fiber spans are balanced by single-stage EDFA with 4.5-dB noise figure. Two dynamic gain equalizers (DGE) flatten the WDM multiplex at 500 and 1500 km. At the receiver side, a 0.4-nm flat-top optical band-pass filter (OBPF) selects the right channel, while an optical switch sends it over the right transceiver.

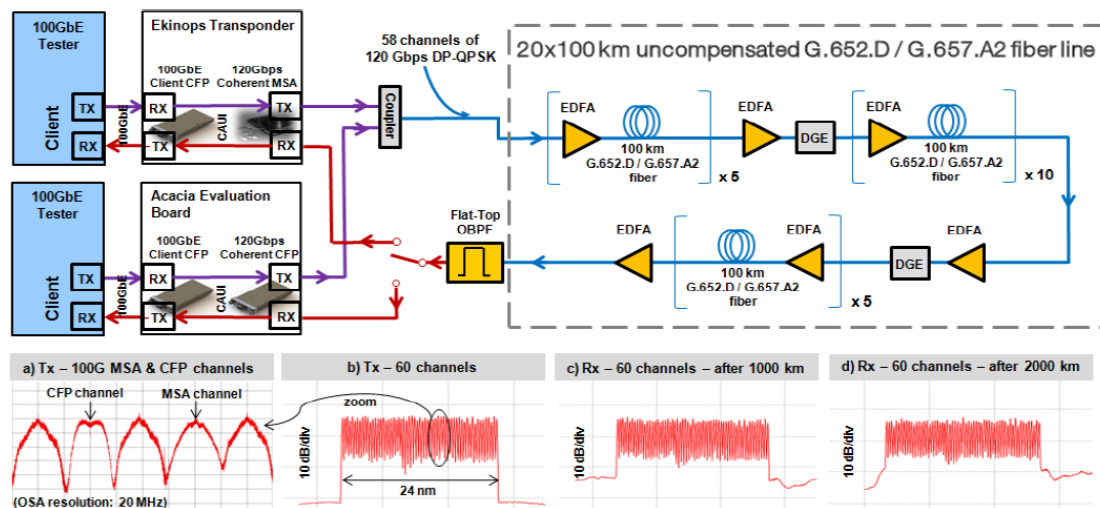


Figure 5-8: Experimental setup with, in insets, the spectrum at the transmitter side (a & b), after 1000 km (c) and 2000 km (d).

The 120 Gbps coherent OIF-MSA transceiver [86, 115] ($7^{\circ} \times 5^{\circ}$) compensates CD up to 60000 ps/nm and PMD up to 30 ps. It implements a soft-decision FEC (SD-FEC) based on a turbo product code (TPC), with a pre-FEC BER of 1.8×10^{-2} , a NCG of 11.1 dB at 10^{-15} and an overhead of 15%. Its energy consumption is ~ 100 W. The 120 Gbps DCO-CFP ($5.7^{\circ} \times 3.2^{\circ}$) mitigates 40000 ps/nm of CD and 25 ps of PMD. It uses a TPC-based SD-FEC with a pre-FEC BER threshold of $\sim 1.5 \times 10^{-2}$, a NCG of ~ 11 dB at 10^{-15} and an overhead of 15% for an energy consumption of only 28 W. As shown in Fig. 5-11, the OSNR limit at the FEC threshold is equal to 12.3 dB for the OIF-MSA transceiver and 13.1 dB for the DCO-CFP. Two 100 GbE LR10 client CFP modules are plugged into the Ekinops transceiver (which embeds the OIF-MSA transceiver) and the Acacia evaluation board (which hosts the DCO-CFP). Each of the two 100GbE LR10 CFP is connected to a 100 GbE tester for long-duration BER measurements. Inside the Ekinops transceiver and Acacia evaluation board, the WDM transceiver and client interface communicate together thanks to a 100 Gbps attachment unit interface (CAUI).

5.2.3 Results and discussion

For various distances, BER versus span input power per channel ($P_{in\ span} / Channel$) curves are plotted in Fig. 5-9 for each of the two fibers and each of the two interfaces under test. Note that only one DGE is kept when the system reach is lower than 1000 km. It can be observed first that the performances of G.657.A2 and G.652.D fibers are similar at the optimum $P_{in\ span} / Channel$, whatever the distance. Secondly, the optimum $P_{in\ span} / Channel$ is 0.5 to 1-dB lower for the G.657.A2 than for the G.652.D fiber spans. It means that G.657.A2 fiber is slightly more sensitive to nonlinear effects. This can be explained by two factors. Firstly, mode field diameter and effective area of G.657.A2 fiber are smaller than those of G.652.D fiber (see Tab. 5-2). Secondly, the lower attenuation of G.657.A2 fiber slightly increases the effective length L_{eff} (i.e. the length where nonlinearities are induced) of G.657.A2 fiber spans ($L_{eff} = 22$ km for 100 km spans) with respect to G.652.D fiber ($L_{eff} = 21.5$ km for 100 km spans).

Now comparing the performance of the two 100 Gbps interfaces, it can be inferred from Fig. 5-9 that the OIF-MSA solution works better than the DCO-CFP one. After 2000 km, the pre-FEC BER is one decade better with the OIF-MSA transceiver ($BER \sim 1 \times 10^{-4}$) than with the DCO-CFP interface ($BER \sim 1 \times 10^{-3}$). However, in the both cases, the optimum pre-FEC BER is far to reach the FEC threshold. In particular, for the DCO-CFP, more than one BER decade margin exists between the performance after 2000 km and the FEC threshold ($BER = 1.5 \times 10^{-2}$).

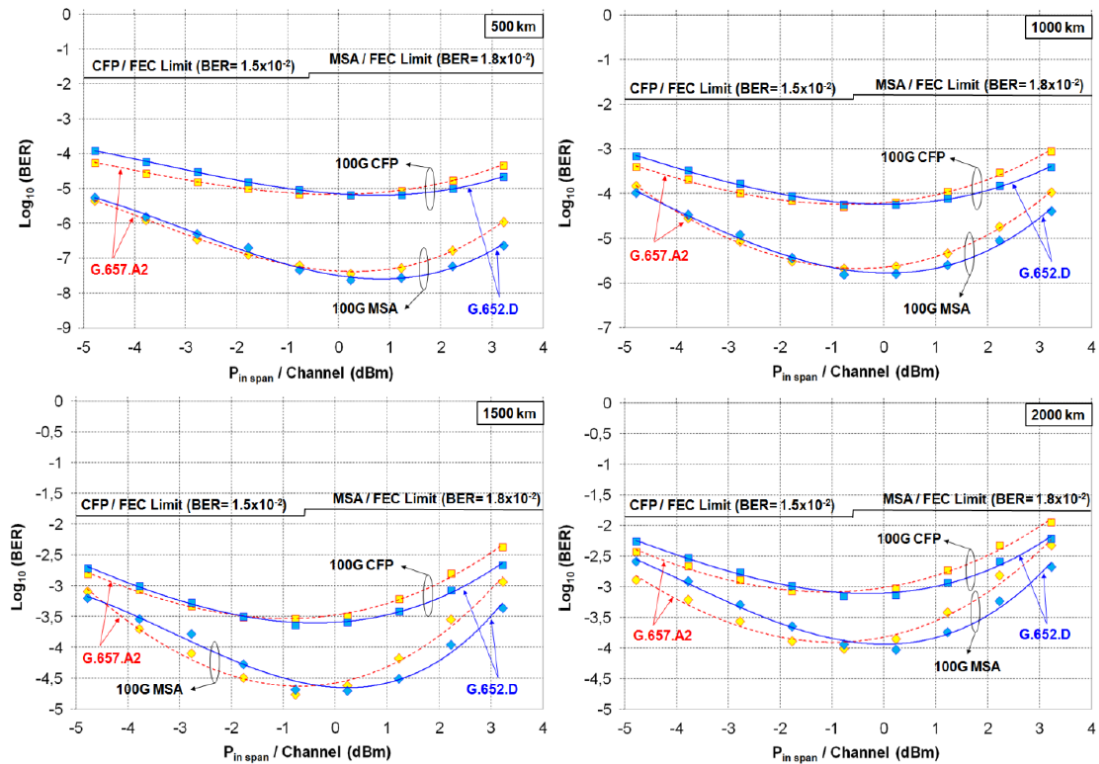


Figure 5-9: BER vs. $P_{in\ span} / Channel$ for the 100 Gbps OIF-MSA / DCO-CFP transceivers and the G.652.D / G.657.A2 fibers.

Fig. 5-10 confirms these results. Whatever the distance, the performance of G.657.A2 and G.652.D fibers are equivalent, and the OIF-MSA performs better than the DCO-CFP, with large BER margins with respect to the FEC threshold. BER measurements during 24 hours with the 100 GbE testers confirm that error-free transmission is achieved after 2000 km whatever the configuration under study.

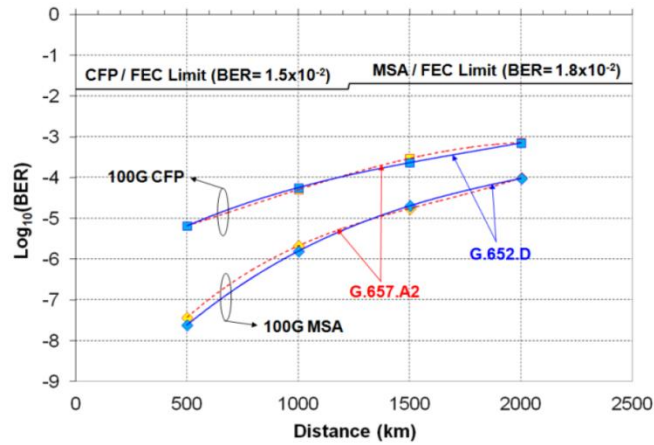


Figure 5-10: BER vs. transmission distance at the optimum $P_{in\ span} / Channel$ for the 100 Gbps OIF-MSA / DCO-CFP transceivers and the G.652.D / G.657.A2 fibers.

Finally, in Fig. 5-11, the optimum of each BER versus $P_{in\ span} / Channel$ curves is reported over a BER versus OSNR graph, where are also plotted the BtB sensitivity curves of the OIF-MSA and DCO-CFP interfaces. Transmission penalties are roughly similar for the two fibers under test, and the OSNR (in 0.1 nm) after 2000 km is ~ 18.5 dB, i.e. very far from the OSNR limits at the FEC threshold (12.3 dB for the OIF-MSA transceiver and 13.1 dB for the DCO-CFP interface).

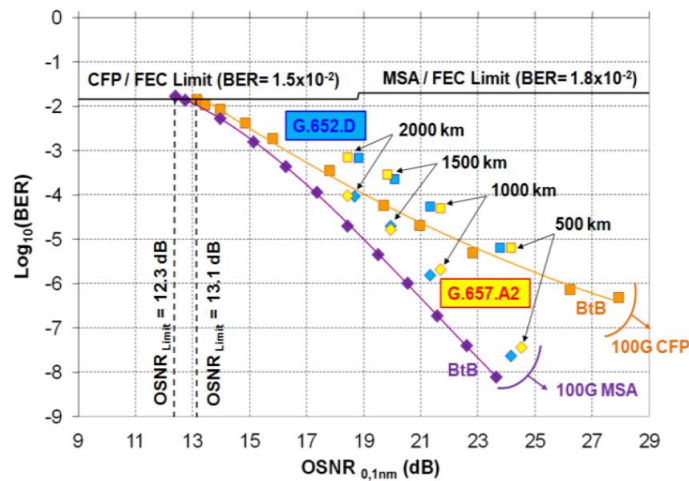


Figure 5-11: BER vs. OSNR 0.1 nm in BtB for the 100 Gbps OIF-MSA and DCO-CFP transceivers. BER vs. OSNR points at the optimum $P_{in\ span} / Channel$ for various distances.

We have demonstrated here for the first time that G.657.A2 fiber can address long-haul transmission applications, and be employed over regional and core transport networks. Indeed, its transmission performance at 100 Gbps is equivalent to that of G.652.D fiber, and more than 2000 km can be achieved with both coherent OIF-MSA transceiver and DCO-CFP module with significant system margins.

5.3 400 Gbps real-time coherent Nyquist-WDM DP-16QAM transmission over legacy G.652 or G.655 fiber infrastructure with 2 dB margins

Equipment suppliers presently propose 400 Gbps coherent WDM interfaces to operators in order to improve by a factor of two the spectral efficiency of WDM links in existing optical transport networks. The upgrade from 100 Gbps to 400 Gbps is obtained by means of coherent dual-carrier dual-polarization 16QAM (DP-16QAM) modulation operating at 32 Gbaud [113]. With Nyquist filtering performed at the transmitter side, a spectral efficiency of 5.33 bit/s/Hz (improved by 166% when compared to 100 Gbps) can be achieved. In parallel, recent laboratory and field trials have reported no more than 500 km of error-free transmission distance over uncompensated G.652 fiber line with 400 Gbps coherent dual-carrier DP-16QAM, EDFA only and no industrial margin [13-15]. For operators, the primary concern is to reuse at 400 Gbps the existing G.652/G.655 fiber-based long-haul transparent meshed optical transport networks, and to limit as much as possible the need for electrical regeneration.

In this study, we experimentally demonstrate for the first time uncompensated error-free transmission of 400 Gbps real-time coherent dual-carrier DP-16QAM over 1000 km (resp. 500 km) of G.652 (resp. G.655) fiber using purely EDFA amplification. By considering realistic industrial margins of ~ 2 dB for fiber/system aging and time-varying transmission effects, we obtain error-free transmission distance of 500 km (resp. 300 km) over G.652 (resp. G.655) fiber. The two 200 Gbps sub-carriers which constitute the 400 Gbps superchannel are Nyquist-filtered, spaced by 37.5 GHz and occupy a total bandwidth of 75 GHz resulting in a spectral efficiency of 5.33 bit/s/Hz. The BER (resp. OSNR in 0.1 nm) threshold of the forward error correction (FEC) code implemented in this first generation of industrial 400 Gbps WDM interface is $\sim 2.4 \times 10^{-2}$ (resp. ~ 19.4 dB) in back-to-back.

5.3.1 Experimental setup

The experimental transmission test-bed is depicted in Fig. 5-12. The WDM transmitter consists of one 400 Gbps dual-carrier DP-16QAM superchannel at 1549.91 nm (central wavelength), and 58 other channels ranging from 1533.86 nm to 1557.36 nm on the 50 GHz ITU grid and modulated at 100 Gbps by dual-polarization QPSK (DP-QPSK). As shown in Fig. 5-12a), the 400 Gbps dual-carrier DP-16QAM signal is constituted of two Nyquist-filtered 200 Gbps sub-channels at 1549.76 nm and 1550.06 nm spaced by 37.5 GHz. A guard-band of 12.5 GHz is inserted between the 400 Gbps signal and each of its two 100 Gbps neighbours. The 400 Gbps superchannel is generated by a real-time WDM interface hosted in the Huawei OSN 9800 equipment [113] and able to transmit two 200 Gbps sub-carriers. The SD-FEC implemented over the board has 20% overhead, a NCG of 11.3 dB and results in a data-rate of 256 Gbps per sub-channel. The tolerance to polarization mode dispersion and chromatic dispersion is typically of ~ 30 ps and ~ 50000 ps/nm, respectively. The 400 Gbps interfaces are connected to an OTN cross-connect, itself linked to 2x100GbE/OTU4 and 16x10GbE/OTU2/OTU2e/FC1200 client interfaces, themselves connected to bit-error rate testers (BERT) for long-duration BER measurements. At the transmitter side, the two 200 Gbps sub-channels are combined together by means of a flexgrid wavelength selective switch (WSS) and coupled with the previously mentioned 58 DP-QPSK channels at 100 Gbps. The resulting WDM signal spectrum recorded at the transmitter side is shown in Fig. 5-12b).

The uncompensated 1000-km transmission line is constituted of ten 100-km spans of G.652 [116] or G.655 fiber [117], whose losses are compensated by single-stage EDFA with 20-dB gain and 4.5-dB noise figure. These fibers are the most deployed worldwide over the legacy infrastructures of operators. A dynamic gain equalizer (DGE) is inserted in the middle of the transmission line in order to flatten the multiplex power. The WDM signal spectrum recovered after 1000-km of G.652 fiber is shown in Fig. 5-12c).

At the receiver side, the 400 Gbps DP-16QAM superchannel at 1549.91 nm is extracted by a 100-GHz bandwidth flat-top optical band-pass filter (OBPF) and detected by a second 400 Gbps real-time WDM interface. The two 200 Gbps sub-carriers are simultaneously sent to each of the two 200 Gbps ports by means of a splitter, and separated by the coherent receivers embedded into the interface. After analog-to-digital conversion (ADC) and real-time digital signal processing, the two 200 Gbps sub-carriers are processed by the OTN cross-connect and transferred to the BERTs through the previously described client interfaces.

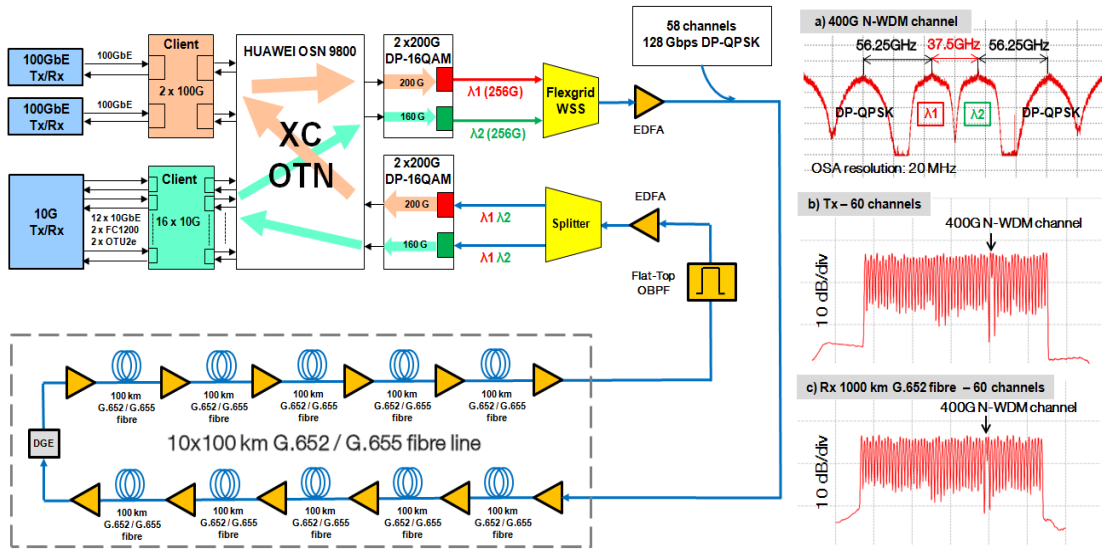


Figure 5-12: Set-up of the 10x100-km transmission test-bed, with the real-time coherent Nyquist-WDM (N-WDM) DP-16QAM transmitter/receiver at 1549.91 nm, the 58 DP-QPSK channels at 100 Gbps ranged from 1533.86 nm to 1557.36 nm, the 10x100-km uncompensated G.652 or G.655 transmission line, the OTN cross-connect and the 2x100GbE/OTU4 and 16x10GbE/OTU2/OTU2e/FC1200 client interfaces connected to the BERTs. In insets, the spectrum of the 400 Gbps N-WDM superchannel at the transmitter side (a), the spectra of the 59 channels at the transmitter side (b) and receiver side after 1000-km of transmission over the G.652 fiber (c).

5.3.2 Back-to-back characterization, transmission performances and discussions

BER versus OSNR are firstly plotted in BtB for the 400 Gbps real-time Nyquist-WDM DP-16QAM WDM interface and for the 100 Gbps DP-QPSK reference in Fig. 5-13. Noise loading is used to vary the OSNR at the receiver side. The FEC threshold is reached for a $BER \sim 2.4 \times 10^{-2}$ and an OSNR in 0.1 nm of ~ 19.4 dB. This is ~ 7 dB away from the OSNR measured at the FEC threshold for the 100 Gbps DP-QPSK reference, as predicted by theory. At the opposite side of the sensitivity curve and as already shown in [118, 119], an error floor is observed for high OSNRs.

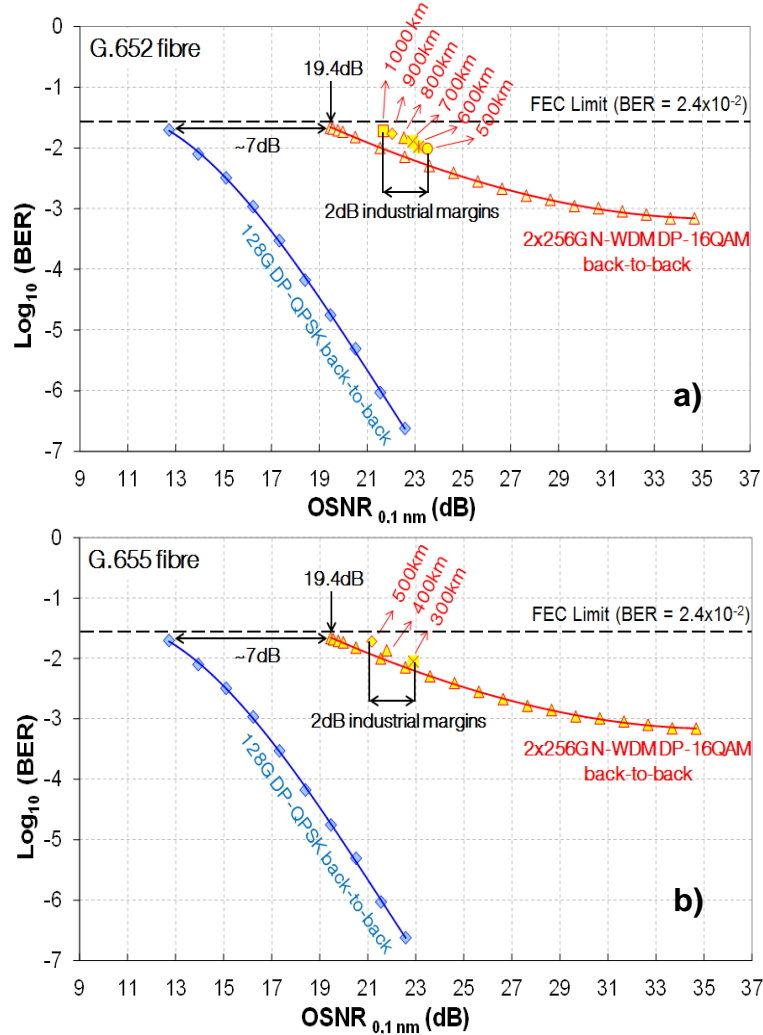


Figure 5-13: BER vs. OSNR (in 0.1 nm) in BtB for 128 Gbps DP-QPSK and 2x256 Gbps N-WDM DP-16QAM. BER vs. OSNR points at the optimum span input power per channel for 500 km, 600 km, 700 km, 800 km, 900 km and 1000 km of transmission over G.652 fiber (a), and for 300 km, 400 km and 500 km of transmission over G.655 fiber (b) are also reported for the 400 Gbps real-time coherent N-WDM DP-16QAM interface.

The performance of the 400 Gbps real-time coherent Nyquist-WDM DP-16QAM interface is secondly evaluated over the previously described G.652 / G.655 transmission test-bed. BERs as a function of the span input powers per channel ($P_{IN\ SPAN}$ /channel) are plotted for various transmission distances over both G.652 (Fig. 5-14a) and G.655 (Fig. 5-14b) fibers. Over G.652 fiber, the optimum span input power decreases from 0 dBm per channel at 500 km to -0.5 dBm per channel at 1000 km. A long-duration measurement of 60 hours without errors has been successfully achieved over the 100GbE/OTU4 and 10GbE/OTU2/OTU2e/FC1200 client flows after 1000 km. Over G.655 fiber, the optimum span input power decreases from -1 dBm per channel at 300 km to -1.5 dBm per channel at 500 km. A long-duration error-free transmission of 60 hours has also been performed over the G.655 fiber after 500 km. Interestingly and as expected, the best performance is obtained over the G.652 fiber, with a maximum transmission distance two-fold higher (1000 km) than over the G.655 fiber (500 km), demonstrating a better robustness of G.652 fiber to nonlinear effects. Due to its larger chromatic dispersion which fully decorrelates the interacting signals and limits the impact of cross-phase modulation and four-wave mixing, G.652 fiber turns out to be superior to G.655 fiber.

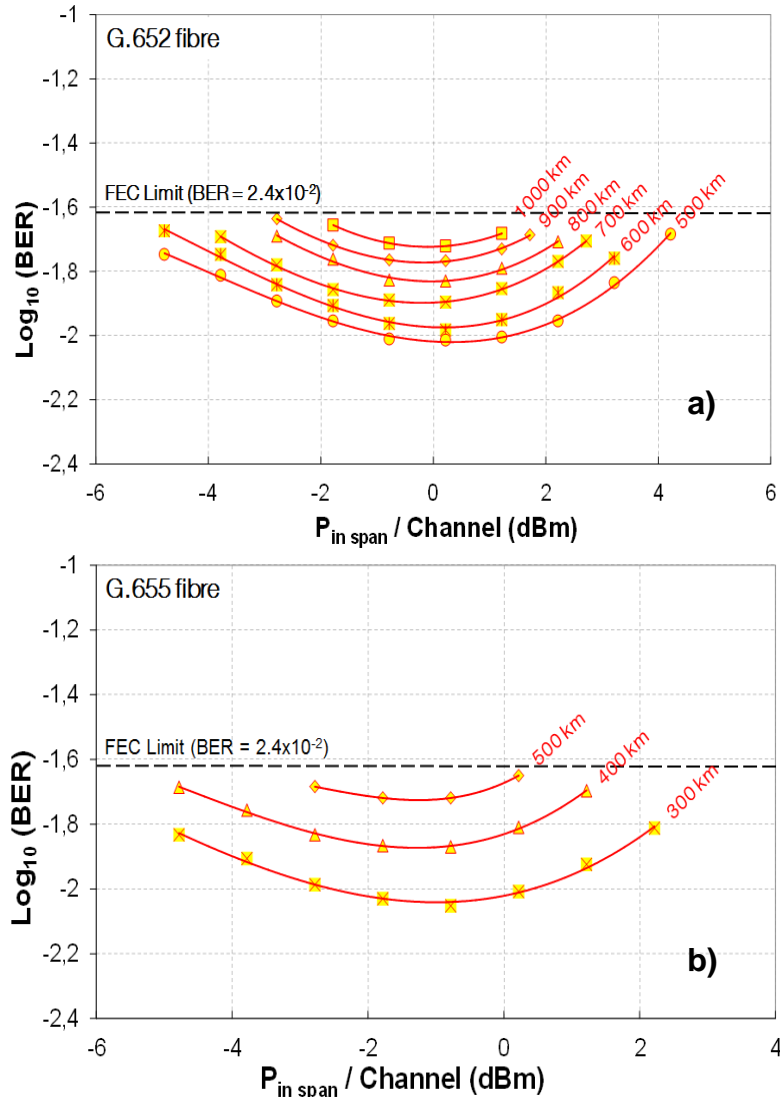


Figure 5-14: BER vs. span input power per channel after 500 km, 600 km, 700 km, 800 km, 900 km and 1000 km of transmission over the G.652 fiber (a), and after 300 km, 400 km and 500 km of transmission over the G.655 fiber (b) for the 400 Gbps real-time coherent N-WDM DP-16QAM interface.

The optimum of each BER versus $P_{\text{IN SPAN}}/\text{channel}$ curves is now reported over the BER versus OSNR graphs of Fig. 5-13 for the various transmission distances and the two fibers under test. The OSNR penalty engendered by the transmission over 1000 km of G.652 fiber is ~ 2 dB. Even if the BER is steady and post-FEC BER is better than 1×10^{-15} after 1000 km, the fiber/system aging and time-varying transmission effects (polarization-dependant loss, cross-polarization modulation, ...) oblige operators to take industrial margins over the OSNR in order to make the system robust during its lifetime (i.e. 6-7 years). Provisioning ~ 2 dB of industrial OSNR margins is usual and ensures that the WDM transmission system will be operational during its lifetime without wasting too much CAPEX by over-dimensioning these margins. Fig. 5-13a shows that the provisioned 2 dB industrial margins oblige to reduce the maximum transmission distance of the 400 Gbps Nyquist-WDM DP-16QAM system from 1000 km to 500 km. By considering now G.655 fiber, the OSNR penalty engendered by the transmission over 500 km is ~ 1.5 dB. It is a bit lower when compared to the G.652 fiber line because the transmission distance considered here (500 km) is two-fold lower than that considered previously over the G.652 fiber (1000 km). The previously introduced 2 dB industrial margins shorten the maximum transmission distance of the system to 300 km.

Nonetheless, we obtain the remarkable result that error-free transmission can be achieved over 1000 km (resp. 500 km) of G.652 (resp. G.655) fiber with the 400 Gbps real-time coherent interface under test, while other industrial 400 Gbps WDM interfaces evaluated up to now in field trials using purely EDFA amplification did not reach more than 400-500 km (with no industrial margin) [13-15].

We have successfully evaluated a 400 Gbps real-time coherent dual-carrier Nyquist-WDM DP-16QAM interface over 1000 km (resp. 500 km) of uncompensated G.652 (resp. G.655) fiber with purely EDFA amplification and no industrial margin. By taking into account ~ 2 dB of industrial margins for fiber/system aging and time-varying transmission effects, the maximum transmission distance is reduced to 500 km over the G.652 fiber and 300 km over the G.655 fiber. To our knowledge, it is the first time that such long transmission distances are achieved at 400 Gbps with a real-time coherent dual-carrier Nyquist-WDM DP-16QAM interface. These results let hope that 400 Gbps DP-16QAM technology will be compliant with transmission distances higher than 1000 km over legacy long-haul transparent meshed optical transport networks, in particular thanks to the help of hybrid Raman/EDFA amplification.

5.4 Conclusion

In this chapter, we have addressed some short-term research topics that concern telecom operators. First of all, we have shown here that 100 Gbps DCO-CFP interface is a low-cost and power-efficient modular solution to address short-reach (interconnection of distant NE without EDFA in single or multi-wavelength environment), regional (with 100 Gbps upgrade of legacy 10 Gbps WDM systems) and ultra-long-haul (with full 100 Gbps WDM transmission) applications. It will be an essential element of future ultra-high bit-rate optical transport networks with a large field of applications from the IP routers up to metro and core transport networks, and a strong factor of convergence of IP and optical world.

Secondly, we have demonstrated that G.657.A2 fiber can address long-haul transmission applications, and be employed over regional and core transport networks. Indeed, its transmission performance at 100 Gbps is equivalent to that of G.652.D fiber, and more than 2000 km can be achieved with both coherent OIF-MSA transceiver and DCO-CFP module with significant system margins.

At last, we have shown the capability of the 400 Gbps real-time coherent dual-carrier Nyquist-WDM DP-16QAM interface to achieve 1000 km (resp. 500 km) error-free transmission over uncompensated G.652 (resp. G.655) fiber with purely EDFA amplification. To our knowledge, it is the first time that such long transmission distances are achieved at 400 Gbps with a real-time coherent dual-carrier Nyquist-WDM DP-16QAM interface. The transmission reach is halved when we reserve ~ 2 dB OSNR margins, but these results show the potential of 400 Gbps real-time DP-16QAM technology to address legacy long-haul transport networks, with the change of amplification scheme or some DSP improvements in the transceiver.

CONCLUSIONS AND PERSPECTIVES

Conclusions

In this thesis, we have studied 400 Gbps and 1 Tbps 16-QAM MB-OFDM, a potential candidate for the next generation of long-haul transmission systems, in the context of elastic optical networking.

We have first demonstrated through numerical simulation that 16QAM-OFDM is more sensitive to various practical implementation impairments with respect to QPSK-OFDM, showing the importance of optimizing transmitter set-up for high order modulation signals. The transmitter design for 16-QAM MB-OFDM has been described and 16QAM-OFDM has been generated with only 7.8-dB OSNR sensitivity difference (at $\text{BER} = 1 \times 10^{-3}$) with respect to QPSK-OFDM. Both 100 Gbps QPSK-OFDM and 200 Gbps 16QAM-OFDM achieve error free transmission over 1000 km of G.652 SSMF. The latter has tiny margin with respect to the SD-FEC threshold (fixed at $\text{BER} \sim 2 \times 10^{-2}$). G.652 SSMF outperforms G.655 LEAF for both modulation formats, conforming that SSMF is a better choice for coherent systems. Nonlinear mitigation techniques (DBP-SSF and IVSTF-NLE) give ~ 0.3 dB of Q^2 -factor improvement in the 1000 km WDM scenario, enabling a transmission reach extension of 10%. We have then compared the performance of 1 Tbps 16-QAM MB-OFDM and N-WDM over the same test-bed. We observe slight lower BER and 1.5-2 dB higher launch power in favor to N-WDM. The reason of why N-WDM outperforms MB-OFDM in our test remains to be investigated.

After that, we have described the concept of sub-wavelength optical switching, which consists in performing optical aggregation and switching at the Sp-Ch contents level using ultra-selective optical filters. Few experimental studies were carried out in state-of-art to demonstrate the feasibility of such repeated add-drop operations at the Sp-Ch contents level. We have successfully proven the cascability of such sub-wavelength switching over QPSK and 16-QAM signal; owing to the use of ultra-fine optical filters, the careful design of sub-wavelength OADM and the use of optimized recirculating loop. We have first realized the sub-wavelength switching inside QPSK modulated 100 Gbps MB-OFDM superchannel, composed of four 8-GHz sub-bands with 2- or 4-GHz guard-bands. Error-free transmission is achieved at five loop round-trips including 1000-km's fiber line and 5 sub-wavelength add-drops. The experimental proof-of-concept is then extended to 16-QAM modulation. The sub-wavelength switching is realized inside 1Tbps MB-OFDM and N-WDM superchannel, composed of ten 18-GHz or 15-GHz sub-bands with 2- or 5-GHz guard-bands. More selective pass-band and stop-band filter is developed by project partner and implemented in the sub-wavelength OADM, which permits the sub-wavelength add-drop of 16-QAM signal with small guard-bands. Using hybrid Raman-EDFA and by considering high SD-FEC threshold (3.8×10^{-2}), 4-5 loop round-trips are realized, corresponding to a transmission reach of 800-1000 km and 4-5 sub-wavelength add-drops.

Furthermore, we have addressed some short-term research topics that concern telecom operators. We have shown that the modular 100 Gbps DCO-CFP interface is capable of addressing short-reach, regional and ultra-long-haul applications, meaning that there is choice for lower-cost and more power-efficient transponders for optical networks. We have also

demonstrated that G.657.A2 fiber, conventionally used for building wiring, can address long-haul transmission applications. This result makes it possible to deploy access, metro and long-haul network with one unique type of fiber. At last, we have shown the capability of the 400 Gbps real-time coherent dual-carrier DP-16QAM N-WDM interface to achieve 1000 km (resp. 500 km) error-free transmission over uncompensated G.652 (resp. G.655) fiber with purely EDFA amplification. The transmission reach is halved when we reserve ~2 dB OSNR margins. It still requires further progress in optical fiber infrastructure and signal processing techniques to support the deployment of such beyond 100 Gbps systems in long-haul network.

Perspectives

Based on former results and observations, our future research work can be headed towards some of these short-term or long-term directions:

- **Nonlinearity limitations of OFDM superchannel:** We have compared the performance of 1 Tbps 16-QAM MB-OFDM and N-WDM over the same test-bed and have found that OFDM is slightly more sensitive to fiber nonlinear effects. OFDM signal is composed of a certain number of subcarriers situated at different frequencies, so that there are nonlinear interactions between subcarriers inside OFDM sub-channel and between subcarriers from different sub-channels. The nonlinear effects, especially FWM and XPM, impact the OFDM signal in a different way with respect to single-carrier signal such as N-WDM. The possible research direction would be, through theoretical calculations or experimental tests, to investigate the nonlinear mechanism of OFDM superchannel. Some parameters, such as the number of subcarriers or the signal PAPR, may influence the nonlinear performance.
- **Performance improvement for sub-wavelength optical switching:** We have successfully proven the cascading of sub-wavelength optical switching over QPSK and 16-QAM signal. Error-free transmission has been achieved after 4-5 loop round-trips, corresponding to a transmission reach of 800-1000 km and 4-5 sub-wavelength add-drops. However, we notice serious waveform distortion after passing through several ROADM functions, especially on the edges of the spectrum due to the imperfect transform function of optical filters. As a consequence, most of the bit errors come from edge subcarriers. One of the potential improvements would be to perform bit and power loading according to the performance of each OFDM subcarrier. Other directions could be using more selective optical filters or further optimization over the bandwidth of optical bandpass and bandstop filters.
- **Transmission reach of 16-QAM modulated OFDM or N-WDM:** 16-QAM modulated signal is a high potential candidate for the next generation of long-haul transmission. It doubles the spectral efficiency of currently deployed 100 Gbps DP-QPSK systems. Although we have demonstrated error-free transmission over 1000 km of G.652 fiber using off-line 16QAM-OFDM and 16QAM N-WDM real-time interface, the BER margin with respect to the SD-FEC limit is very tiny. 16-QAM modulated transponders are not yet compliant with the long-haul transmission reach. Changing legacy fiber requires huge investments and does not seem to be short-term solution. Other directions, such as using hybrid amplification schemes and advanced signal processing

techniques, may open ways to the deployment of 16-QAM. Nonlinear mitigation algorithms improve the BER and optimum launch power, but in a WDM scenario with large inter-channel nonlinearities, the benefice is very limited. Inter-channel nonlinear mitigation techniques may contribute to the extension of transmission reach.

- **OFDM in space-division multiplexing (SDM):** As cited in the introduction of the thesis, the global IP traffic will triple from 2015 to 2020. The use of high order modulation formats permits the increase of spectral efficiency, but at the expense of transmission reach. SDM over multi-mode fibers (MMF) and multi-core fibers (MCF) opens another degree of freedom that is not yet exploited. However, the differential impairment and crosstalk between modes or cores seriously deteriorate the performance of the system. OFDM signal processing techniques offer some computational advantages. For instance, by using a cyclic prefix longer than the maximum differential modal dispersion, modes can be decoupled by a single-tap frequency domain filter. One of the long-term research directions would be to study OFDM in MMF or MCF.

APPENDIX

Appendix A

Ultra-fine optical pass-band & stop-band filters designed by Yenista Optics

A double target is followed for the design and building of the optical pass-band and stop-band filters used in the sub-wavelength optical switching inside 100 Gbps QPSK modulated MB-OFDM. They have to be ultra-selective to extract and suppress OFDM sub-bands as narrow as 8 GHz, while having a transfer function as rectangular as possible in order not to distort too much the neighbouring sub-bands. Free-space optical technology integrating a bulk diffraction grating has been chosen here [120] to obtain typical full-width-half-maximum (FWHM) of 10 GHz and edge roll-off of 1000 dB/nm. The tunability of the filter central wavelength and bandwidth constitutes also an important feature of the developed devices. The optical pass-band and stop-band filters employ the same basic architecture. The main difference comes from the filtering slit, which is specific either to the pass-band or to the stop-band optical filter. The filter architecture is shown in Fig. 0-1, and is detailed below.

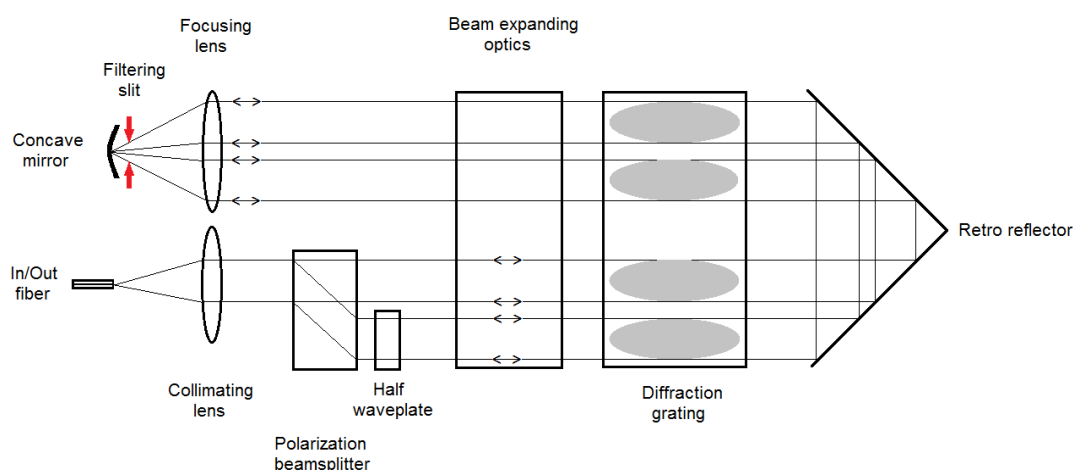


Figure 0-1: Typical architecture of the ultra-narrow pass-band and stop-band optical filters used in the sub-band OADM.

Table 0-1: Typical features of the pass-band and stop-band optical filters

	Optical Pass-Band Filter	Optical Stop-Band Filter
Insertion Loss	5 dB typical	5.5 dB typical
Edge roll-off	> 800 dB/nm	> 750 dB/nm
3-dB Bandwidth	32 pm / 4 GHz	65 pm / 8 GHz
Isolation	60 dB typical	Not Applicable
Rejection	Not Applicable	60 dB typical

The input divergent beam coming from the In/Out single mode fiber is collimated thanks to a lens, whose focal point is adjusted on the In/Out fiber. The filter architecture uses a

polarization-diversity configuration in order to deal with the x and y polarizations independently. A polarization beam splitter separates the two polarization components and generates two elementary parallel light beams. A half wave-plate inserted over the lower beam turns its polarization by 90° . The diffraction grating is thus fed by two beams polarized in a direction perpendicular to the grating grooves. An optical expander is inserted before the grating, in order to spread the beams on the whole grating length and to maximize the separation strength of the Littman-Metcalf set-up. A dihedron is placed after the grating as a retro-reflector, to increase the resolution of the device by doubling the number of passage into the grating. The beams are then sent to the upper filtering stage, and are finally focused onto a concave mirror, after passing through a slit. The role of this slit is to filter the signal either in the pass-band or stop-band configuration. The slit is fixed over a translation stage and can be moved into the beam: it allows changing the bandwidth of the filters. The filter central frequency is chosen thanks to a rotation of the retro-reflector. In the case of the pass-band filter, the slit shape is triangular. Note that the concave mirror has limited dimensions in the dispersion plane. Thus, the wavelengths corresponding to the beam portion reflected onto the concave mirror and not stopped by the slit are re-coupled on the way back in the In/Out fiber. This last one is connected to a circulator, which enables to de-correlate the input from the output signals. The optical configuration chosen here is symmetrical when considering the input and output beams, that in turn results in very low polarization dependant losses (PDL) for both the optical pass-band and stop-band filters. The typical PDL is equal to 0.2 dB and is mainly due to the circulator. Table 0-1 gives the main optical features of the developed filters. Their insertion losses do not exceed 5 dB for the pass-band filter and 5.5 dB for the stop-band filter. Their edge roll-off are typically higher than 800 dB/nm for the pass-band filter and 750 dB/nm for the stop-band filter. The minimum 3-dB bandwidth is equal to 32 pm (or 4 GHz) for the pass-band filter and 65 pm (or 8 GHz) for the stop-band filter. The isolation of the pass-band filter and rejection of the stop-band filter are typically 60 dB.

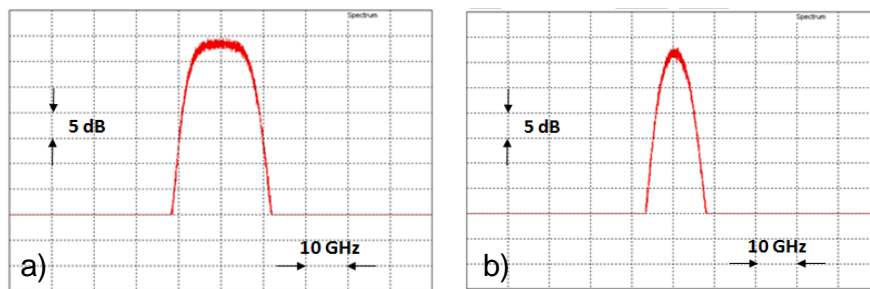


Figure 0-2: Typical transfer function of the optical pass-band filter when its 3-dB bandwidth is a) ~ 14 GHz and b) ~ 4 GHz.

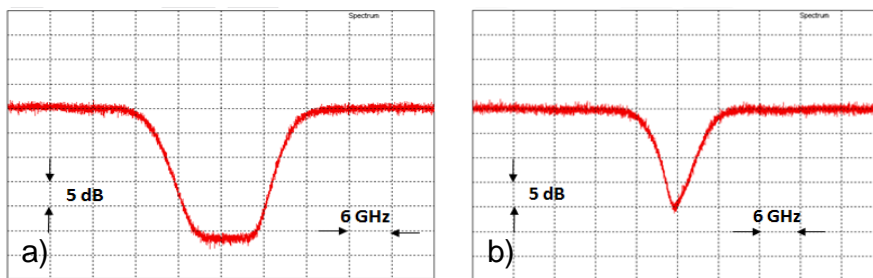


Figure 0-3: Typical transfer function of the optical stop-band filter when its 3-dB bandwidth is a) ~ 20 GHz and b) ~ 10 GHz.

Fig. 0-2 presents the typical profiles of the pass-band optical filter for 3-dB bandwidths equal to ~14 GHz and ~4 GHz, respectively. For the 14-GHz bandwidth, the filter is nearly rectangular. Reduction of its bandwidth up to 4 GHz involves a modification of its profile, which becomes Gaussian. Fig. 0-3 shows the typical transfer function of the stop-band optical filter for 3-dB bandwidths of ~20 GHz and ~10 GHz, respectively. While the "notch" function is nearly rectangular when the 3-dB bandwidth is ~20 GHz, it becomes triangular when the 3-dB bandwidth is decreased up to ~10 GHz. Further reduction of the filter bandwidth is limited by several factors: firstly, the slit size cannot be reduced indefinitely and have to be higher than 20 μm ; secondly, limitation over the number of lines of the diffraction gratings limits the grating dispersion strength; and finally, chromatic and spherical aberrations affecting optics degrade the resolution of the filters.

Appendix B

High spectral resolution filter designed for the FOX-C node

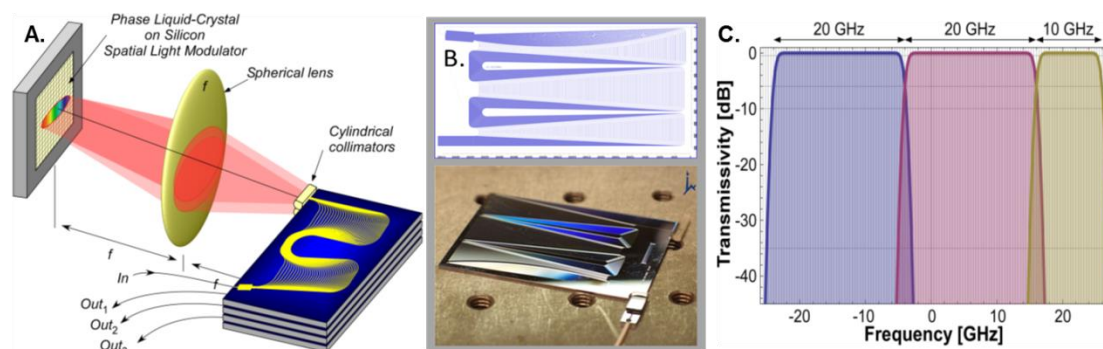


Figure 0-4: Fine-resolution WSS based on a high resolution filter employing one input and several output AWGs for high resolution dispersion as well as an LCoS switching engine (A); the AWG design and implementation providing <1 GHz optical resolution and 400 MHz spectral granularity (B); calculated fine spectral filter performance characteristics for three flexible sub-channels (C).

The high spectral resolution (HSR) optical filter is designed by FOX-C partners R. Rudnick and D. M. Marom from Hebrew University of Jerusalem. The operating principle of the HSR filter [121], used as a building block for the fine resolution WSS shown in Fig. 0-4, is similar to that of a WSS with a liquid crystal on silicon (LCoS) processor for flexible bandwidth allocation (see Fig. 0-4A). However, the bulk diffraction grating dispersive element is replaced by an engineered phase array waveguide grating (AWG) designed to provide fine optical resolution over a finite bandwidth. A state-of-the-art phase array implemented in a silica-on-silicon platform was reported in [122], where a high resolution AWG was designed to achieve < 1 GHz optical resolution (i.e. the edge roll-off bandwidth from -0.5 dB or 90% down to -10 dB or 10%) and 400 MHz spectral granularity (i.e. the tuning precision for the filter edge placement), operating over a free 200 GHz spectral range (FSR). Since the length difference between the shortest and longest waveguides is ~250 mm in silica waveguides (to obtain the <1 GHz resolution), the waveguides are folded three times within the planar lightwave circuit (PLC), as shown in Fig. 0-4B, resulting in a total size of 50×10 mm.

The multi-port HSR filter, depicted in Fig. 0-4A, can consist of a stack of AWGs, each representing an input/output port, a free-space optical arrangement for dispersing the optical signal onto an LCoS spatial light modulator (SLM), itself controlled by a computer that can assign spectral quanta as fine as the spectral granularity to subdivide the Sp-Ch into its finer tributaries. One fiber port (i.e. one of the AWGs) accepts a Sp-Ch of any bandwidth up to the FSR limit of the AWG. The Sp-Ch is then dispersed with a lens on the LCoS-SLM at fine resolution. The LCoS-SLM selects the spectral bandwidth (which can be adapted to the spectral width of one or several Sb-Chs) that will be routed to an individual output AWG. This output AWG is assigned to a "drop" side (where the filter performs a pass-band function) and a "through" destination (where the filter realizes a stop-band function), which will then be re-multiplexed with new "add" data to form the new Sp-Ch for upstream transmission. Since the optical resolution of the AWG is at record fidelity, the band transitions are extremely sharp, enabling the separation of the Sp-Ch into any combination (not necessarily spectrally contiguous) of its tributaries with minimal guard-bands.

In Fig. 0-4C, the calculated finer HSR filter performance characteristics are shown, when variable bandwidth channels are deployed at a spectral granularity of 400 MHz (denoted by vertical grid lines) and an optical resolution of 1 GHz. This reveals the capability to extract even 10 GHz channels with minimum spectral guard-band of 2 GHz between them, while achieving crosstalk suppression close to 25 dB. The versatility of the AWG-based HSR filter is enabled by the LCoS-SLM processing, which is applied to the spatially-dispersed light (independently of the dispersion scheme). However, the challenge of this approach is the accuracy to which the AWG must conform. Briefly stated, all the AWG arms must radiate at the exact same relative phase while providing path length differences required to provide the spectral resolution value. Two techniques for correcting fabrication phase errors have been successfully demonstrated by the results obtained in [122].

REFERENCES

1. Cisco visual networking index: Forecast and methodology, 2015–2020. 2016: White paper.
2. Essiambre, R.-J., et al., *Capacity limits of optical fiber networks*. Journal of Lightwave Technology, 2010. **28**(4): p. 662-701.
3. Wilder, M.R. *Understanding and measuring chromatic dispersion*. 2000; Available from: <http://www.fiberopticonline.com/doc/understanding-and-measuring-chromatic-dispers-0002>.
4. Poole, C. and R. Wagner, *Phenomenological approach to polarisation dispersion in long single-mode fibres*. Electronics Letters, 1986. **19**(22): p. 1029-1030.
5. Dal Forno, A., et al., *Experimental and theoretical modeling of polarization-mode dispersion in single-mode fibers*. IEEE Photonics Technology Letters, 2000. **12**(3): p. 296-298.
6. Agrawal, G.P., *Fiber-Optic Communication Systems*.
7. Kaminow, I.P. and T.L. Koch, *Optical Fiber Telecommunications III*. Vol. 1. 1997: Academic Press.
8. Pincemin, E., et al. *Coherent Optical Transmission at 40 and 100 Gbps over 1000 km of DCF-free G. 652 and G. 655 Fibre Infrastructure*. in *Optical Fiber Communication Conference*. 2014. Optical Society of America.
9. Pincemin, E., et al. *100 Gbps DP-QPSK performance over DCF-free and legacy system infrastructure*. in *IEEE Photonics Conference 2012*. 2012. IEEE.
10. DeLange, O.E., *Wide-band optical communication systems: Part II—Frequency-division multiplexing*. Proceedings of the IEEE, 1970. **58**(10): p. 1683-1690.
11. Sun, H., K.-T. Wu, and K. Roberts, *Real-time measurements of a 40 Gb/s coherent system*. Optics Express, 2008. **16**(2): p. 873-879.
12. Cho, K. and D. Yoon, *On the general BER expression of one-and two-dimensional amplitude modulations*. IEEE Transactions on Communications, 2002. **50**(7): p. 1074-1080.
13. Pagano, A., et al. *400Gb/s real-time trial using rate-adaptive transponders for next generation flexible-grid networks*. in *Optical Fiber Communication Conference*. 2014. Optical Society of America.
14. "France Telecom-Orange and Alcatel-Lucent deploy world's first live 400 Gbps per wavelength optical link," www.orange.com.
15. Zhou, Y.R., et al. *Real-Time Gridless 800G Super-channel Transport Field Trial over 410km Using Coherent DP-16 QAM*. in *Optical Fiber Communication Conference*. 2014. Optical Society of America.
16. Awwad, E., *Emerging space-time coding techniques for optical fiber transmission systems*. 2015, Télécom ParisTech.
17. Desurvire, E. and M.N. Zervas, *Erbium-doped fiber amplifiers: principles and applications*. Physics Today, 1995. **48**: p. 56.
18. Bromage, J., *Raman amplification for fiber communications systems*. Journal of Lightwave Technology, 2004. **22**(1): p. 79-93.
19. Raman, C.V. and K.S. Krishnan, *A new type of secondary radiation*. Nature, 1928. **121**: p. 501-502.
20. Pelouch, W.S., *Raman Amplification: An Enabling Technology for Long-Haul Coherent Transmission Systems*. Journal of Lightwave Technology, 2016. **34**(1): p. 6-19.
21. Mizuoichi, T., et al. *Progress in soft-decision FEC*. in *National Fiber Optic Engineers Conference*. 2011. Optical Society of America.

22. Leven, A. and L. Schmalen, *Status and recent advances on forward error correction technologies for lightwave systems*. Journal of Lightwave Technology, 2014. **32**(16): p. 2735-2750.
23. Xie, C., et al. *FEC for high speed optical transmission*. in *Communications and Photonics Conference and Exhibition, 2011. ACP. Asia*. 2011.
24. Ip, E. and J.M. Kahn, *Compensation of dispersion and nonlinear impairments using digital backpropagation*. Journal of Lightwave Technology, 2008. **26**(20): p. 3416-3425.
25. Yaman, F. and G. Li, *Nonlinear impairment compensation for polarization-division multiplexed WDM transmission using digital backward propagation*. IEEE Photonics Journal, 2010. **2**(5): p. 816-832.
26. Liu, L., et al., *Intrachannel nonlinearity compensation by inverse Volterra series transfer function*. Lightwave Technology, Journal of, 2012. **30**(3): p. 310-316.
27. Peddanarappagari, K.V. and M. Brandt-Pearce, *Volterra series transfer function of single-mode fibers*. Lightwave Technology, Journal of, 1997. **15**(12): p. 2232-2241.
28. Gao, Y., et al., *Assessment of intrachannel nonlinear compensation for 112 Gb/s dual-polarization 16QAM systems*. Journal of Lightwave Technology, 2012. **30**(24): p. 3902-3910.
29. Du, L.B. and A.J. Lowery, *Improved single channel backpropagation for intra-channel fiber nonlinearity compensation in long-haul optical communication systems*. Optics express, 2010. **18**(16): p. 17075-17088.
30. Guiomar, F.P., et al. *Parallel split-step method for digital backpropagation*. in *Optical Fiber Communication Conference*. 2015. Optical Society of America.
31. Napoli, A., et al., *Reduced complexity digital back-propagation methods for optical communication systems*. Journal of lightwave technology, 2014. **32**(7): p. 1351-1362.
32. Chang, R.W., *Synthesis of band-limited orthogonal signals for multichannel data transmission*. Bell System Technical Journal, The, 1966. **45**(10): p. 1775-1796.
33. Salz, J. and S. Weinstein. *Fourier transform communication system*. in *Proceedings of the first ACM symposium on Problems in the optimization of data communications systems*. 1969. ACM.
34. Peled, A. and A. Ruiz. *Frequency domain data transmission using reduced computational complexity algorithms*. in *Acoustics, Speech, and Signal Processing, IEEE International Conference on ICASSP'80*. 1980. IEEE.
35. Armstrong, J., *OFDM for optical communications*. Lightwave Technology, Journal of, 2009. **27**(3): p. 189-204.
36. Shieh, W., *OFDM for flexible high-speed optical networks*. Journal of Lightwave Technology, 2011. **29**(10): p. 1560-1577.
37. Winzer, P.J., *High-spectral-efficiency optical modulation formats*. Lightwave Technology, Journal of, 2012. **30**(24): p. 3824-3835.
38. Lowery, A.J. and L.B. Du, *Optical orthogonal division multiplexing for long haul optical communications: A review of the first five years*. Optical Fiber Technology, 2011. **17**(5): p. 421-438.
39. Tang, Y., W. Shieh, and B.S. Krongold, *DFT-spread OFDM for fiber nonlinearity mitigation*. Photonics Technology Letters, IEEE, 2010. **22**(16): p. 1250-1252.
40. Chen, X., et al., *Experimental demonstration of improved fiber nonlinearity tolerance for unique-word DFT-spread OFDM systems*. Optics express, 2011. **19**(27): p. 26198-26207.
41. Xie, C., *Chromatic dispersion estimation for single-carrier coherent optical communications*. Photonics Technology Letters, IEEE, 2013. **25**(10): p. 992-995.
42. Berger, C.R., et al., *Theoretical and experimental evaluation of clipping and quantization noise for optical OFDM*. Optics express, 2011. **19**(18): p. 17713-17728.

43. Jiang, T. and Y. Wu, *An overview: peak-to-average power ratio reduction techniques for OFDM signals*. IEEE transactions on broadcasting, 2008. **54**(2): p. 257.
44. Boyd, S., *Multitone signals with low crest factor*. 1986, DTIC Document.
45. Tarokh, V. and H. Jafarkhani, *On the computation and reduction of the peak-to-average power ratio in multicarrier communications*. Communications, IEEE Transactions on, 2000. **48**(1): p. 37-44.
46. Jones, A.E., T.A. Wilkinson, and S. Barton, *Block coding scheme for reduction of peak to mean envelope power ratio of multicarrier transmission schemes*. Electronics letters, 1994. **30**(25): p. 2098-2099.
47. Feng, Z., et al., *Performance Enhanced Direct Detection Optical OFDM Transmission with CAZAC Equalization*.
48. Wang, X., T.T. Tjhung, and C. Ng, *Reduction of peak-to-average power ratio of OFDM system using a companding technique*. Broadcasting, IEEE Transactions on, 1999. **45**(3): p. 303-307.
49. Jiang, T., Y. Yang, and Y.-H. Song, *Exponential companding technique for PAPR reduction in OFDM systems*. Broadcasting, IEEE Transactions on, 2005. **51**(2): p. 244-248.
50. Jiang, T. and G. Zhu, *Nonlinear companding transform for reducing peak-to-average power ratio of OFDM signals*. Broadcasting, IEEE Transactions on, 2004. **50**(3): p. 342-346.
51. Schmidl, T.M. and D.C. Cox, *Robust frequency and timing synchronization for OFDM*. Communications, IEEE Transactions on, 1997. **45**(12): p. 1613-1621.
52. Minn, H., V.K. Bhargava, and K. Letaief, *A robust timing and frequency synchronization for OFDM systems*. Wireless Communications, IEEE Transactions on, 2003. **2**(4): p. 822-839.
53. Karaki, J., *100 Gbps coherent MB-OFDM for long-haul WDM optical transmission*. 2013, Paris, ENST.
54. Fludger, C., et al. *10 x 111 Gbit/s, 50 GHz spaced, POLMUX-RZ-DQPSK transmission over 2375 km employing coherent equalisation*. in *National Fiber Optic Engineers Conference*. 2007. Optical Society of America.
55. Van Zelst, A. and T.C. Schenk, *Implementation of a MIMO OFDM-based wireless LAN system*. Signal Processing, IEEE Transactions on, 2004. **52**(2): p. 483-494.
56. Jansen, S.L., et al., *Long-haul transmission of 16x 52.5 Gbits/s polarization-division-multiplexed OFDM enabled by MIMO processing*. Journal of Optical Networking, 2008. **7**(2): p. 173-182.
57. Pollet, T., M. Van Bladel, and M. Moeneclaey, *BER sensitivity of OFDM systems to carrier frequency offset and Wiener phase noise*. Communications, IEEE Transactions on, 1995. **43**(2/3/4): p. 191-193.
58. Yi, X., W. Shieh, and Y. Tang, *Phase estimation for coherent optical OFDM*. IEEE Photonics technology letters, 2007. **19**(9/12): p. 919.
59. Randel, S., S. Adhikari, and S.L. Jansen, *Analysis of RF-pilot-based phase noise compensation for coherent optical OFDM systems*. Photonics Technology Letters, IEEE, 2010. **22**(17): p. 1288-1290.
60. Jansen, S.L., et al., *Coherent optical 25.8-Gb/s OFDM transmission over 4160-km SSMF*. Journal of Lightwave Technology, 2008. **26**(1): p. 6-15.
61. Jansen, S.L., et al., *121.9-Gb/s PDM-OFDM transmission with 2-b/s/Hz spectral efficiency over 1000 km of SSMF*. Journal of Lightwave Technology, 2009. **27**(3): p. 177-188.
62. Liu, X., et al., *448-Gb/s reduced-guard-interval CO-OFDM transmission over 2000 km of ultra-large-area fiber and five 80-GHz-grid ROADMs*. Lightwave Technology, Journal of, 2011. **29**(4): p. 483-490.

63. Plant, D.V., et al. *Flexible transceivers using adaptive digital signal processing for single carrier and OFDM*. in *Proceedings of Optical Fiber Communication Conference (OFC)(17–21 March 2013)*. 2013.
64. Zhao, J., *DFT-based offset-QAM OFDM for optical communications*. *Optics express*, 2014. **22**(1): p. 1114-1126.
65. Zhao, J. and A.D. Ellis, *Offset-QAM based coherent WDM for spectral efficiency enhancement*. *Optics express*, 2011. **19**(15): p. 14617-14631.
66. Hillerkuss, D., et al., *26 Tbit s⁻¹ line-rate super-channel transmission utilizing all-optical fast Fourier transform processing*. *Nature Photonics*, 2011. **5**(6): p. 364-371.
67. Yu, J., et al. *30-Tb/s (3× 12.84-Tb/s) signal transmission over 320km using PDM 64-QAM Modulation*. in *Optical Fiber Communication Conference and Exposition (OFC/NFOEC), 2012 and the National Fiber Optic Engineers Conference*. 2012. IEEE.
68. Sano, A., et al., *No-guard-interval coherent optical OFDM for 100-Gb/s long-haul WDM transmission*. *Journal of Lightwave Technology*, 2009. **27**(16): p. 3705-3713.
69. Ellis, A.D. and F.C.G. Gunning, *Spectral density enhancement using coherent WDM*. *Photonics Technology Letters, IEEE*, 2005. **17**(2): p. 504-506.
70. Qian, D., et al. *Transmission of 115× 100G PDM-8QAM-OFDM Channels with 4bits/s/Hz Spectral Efficiency over 10,181 km*. in *European Conference and Exposition on Optical Communications*. 2011. Optical Society of America.
71. Zhang, S., et al., *Transoceanic transmission of 40× 117.6 Gb/s PDM-OFDM-16QAM over hybrid large-core/ultralow-loss fiber*. *Journal of Lightwave Technology*, 2013. **31**(4): p. 498-505.
72. Liu, X., et al. *Generation and FEC-decoding of a 231.5-Gb/s PDM-OFDM signal with 256-iterative-polar-modulation achieving 11.15-b/s/Hz intrachannel spectral efficiency and 800-km reach*. in *Optical Fiber Communication Conference*. 2012. Optical Society of America.
73. Liu, X., et al. *Transmission of a 448-Gb/s reduced-guard-interval CO-OFDM signal with a 60-GHz optical bandwidth over 2000 km of ULAF and five 80-GHz-Grid ROADMs*. in *National Fiber Optic Engineers Conference*. 2010. Optical Society of America.
74. Lu, Y., et al. *Experimental comparison of 32-Gbaud Electrical-OFDM and Nyquist-WDM transmission with 64GSa/s DAC*. in *39th European Conference and Exhibition on Optical Communication (ECOC 2013)*. 2013.
75. Huang, M.-F., et al., *EDFA-only WDM 4200-km transmission of OFDM-16QAM and 32QAM*. *Photonics Technology Letters, IEEE*, 2012. **24**(17): p. 1466-1468.
76. Liu, X., et al. *3x 485-Gb/s WDM transmission over 4800 km of ULAF and 12x 100-GHz WSSs using CO-OFDM and single coherent detection with 80-GS/s ADCs*. in *Optical Fiber Communication Conference*. 2011. Optical Society of America.
77. Liu, X., et al. *Single coherent detection of a 606-Gb/s CO-OFDM signal with 32-QAM subcarrier modulation using 4× 80-Gsamples/s ADCs*. in *36th European Conference and Exhibition on Optical Communication*. 2010.
78. Zhu, B., et al., *Transmission performance of a 485-Gb/s CO-OFDM superchannel with PDM-16QAM subcarriers over ULAF and SSMF-based links*. *Photonics Technology Letters, IEEE*, 2011. **23**(19): p. 1400-1402.
79. Downie, J.D., et al., *Study of EDFA and Raman system transmission reach with 256 Gb/s PM-16QAM signals over three optical fibers with 100 km spans*. *Optics express*, 2013. **21**(14): p. 17372-17378.
80. Renaudier, J., et al. *Long-haul transmission of 1-Tb/s superchannels, 175-GHz spaced, over SSMF using Nyquist pulse shaping and flex-grid WDM architecture*. in *39th European Conference and Exhibition on Optical Communication (ECOC 2013)*. 2013.

81. Buchali, F., et al. *1-Tbit/s dual-carrier DP 64QAM transmission at 64Gbaud with 40% overhead soft-FEC over 320km SSMF*. in *Optical Fiber Communication Conference*. 2013. Optical Society of America.
82. Karaki, J., et al., *Dual-polarization multi-band OFDM versus single-carrier DP-QPSK for 100 Gb/s long-haul WDM transmission over legacy infrastructure*. *Optics express*, 2013. **21**(14): p. 16982-16991.
83. Giacomidis, E., et al. *100 Gb/s coherent optical polarization multiplexed Multi-band-OFDM (MB-OFDM) transmission for long-haul applications*. in *Transparent Optical Networks (ICTON), 2012 14th International Conference on*. 2012. IEEE.
84. Prat Gomà, J.J., et al. *Comparison of single carrier and OFDM with back-propagation and RF pilot tone for a 9x224Gb/s POLMUX-16QAM system*. in *2011 IEEE Photonics Conference (PHO)*. 2011.
85. Bosco, G., et al., *Performance limits of Nyquist-WDM and CO-OFDM in high-speed PM-QPSK systems*. *Photonics Technology Letters, IEEE*, 2010. **22**(15): p. 1129-1131.
86. Nelson, L.E., et al., *A robust real-time 100G transceiver with soft-decision forward error correction [Invited]*. *Journal of Optical Communications and Networking*, 2012. **4**(11): p. B131-B141.
87. Onohara, K., et al., *Soft-decision-based forward error correction for 100 Gb/s transport systems*. *Selected Topics in Quantum Electronics, IEEE Journal of*, 2010. **16**(5): p. 1258-1267.
88. Josten, A., et al. *Multiplier-Free Real-Time Timing Recovery Algorithm in the Frequency Domain Based on Modified Godard*. in *Signal Processing in Photonic Communications*. 2015. Optical Society of America.
89. Godard, D.N., *Self-recovering equalization and carrier tracking in two-dimensional data communication systems*. *Communications, IEEE Transactions on*, 1980. **28**(11): p. 1867-1875.
90. Winzer, P.J. and A.H. Gnauck. *112-Gb/s polarization-multiplexed 16-QAM on a 25-GHz WDM grid*. in *2008 34th European Conference on Optical Communication*. 2008.
91. Selmi, M., Y. Jaouën, and P. Ciblat, *Accurate digital frequency offset estimator for coherent PolMux QAM transmission systems*. *ECOC 2009*, 2009.
92. Pfau, T., S. Hoffmann, and R. Noé, *Hardware-Efficient Coherent Digital Receiver Concept With Feedforward Carrier Recovery for M -QAM Constellations*. *Journal of Lightwave Technology*, 2009. **27**(8): p. 989-999.
93. Zhou, X. *Hardware efficient carrier recovery algorithms for single-carrier QAM systems*. in *Signal Processing in Photonic Communications*. 2012. Optical Society of America.
94. Jinno, M., et al., *Spectrum-efficient and scalable elastic optical path network: architecture, benefits, and enabling technologies*. *Communications Magazine, IEEE*, 2009. **47**(11): p. 66-73.
95. Gerstel, O., et al., *Elastic optical networking: A new dawn for the optical layer?* *Communications Magazine, IEEE*, 2012. **50**(2): p. s12-s20.
96. Ryf, R., et al., *Wavelength blocking filter with flexible data rates and channel spacing*. *Lightwave Technology, Journal of*, 2005. **23**(1): p. 54-61.
97. Morea, A., et al. *Impact of reducing channel spacing from 50GHz to 37.5 GHz in fully transparent meshed networks*. in *Optical Fiber Communication Conference*. 2014. Optical Society of America.
98. Zami, T. *Interest of the MIXGRID setup for elastic spectral efficiency*. in *Optical Communication (ECOC 2013), 39th European Conference and Exhibition on*. 2013. IET.
99. www.ciena.com, *Corestream Agility Optical Transport System brochure*.
100. www.alcatel-lucent.com, *1830 Photonic Service Switch brochure*.

101. Laperle, C. and K. Roberts. *Flexible transceivers*. in *Eur. Conf. Opt. Commun., Amsterdam, The Netherlands*. 2012.
102. Gringeri, S., E.B. Basch, and T.J. Xia, *Technical considerations for supporting data rates beyond 100 Gb/s*. *Communications Magazine, IEEE*, 2012. **50**(2): p. s21-s30.
103. Hui, R., et al., *Digital subcarrier optical networks and cross-connects*. *Journal of High Speed Networks*, 2013. **19**(1): p. 55-69.
104. Pincemin, E., et al., *Multi-band OFDM transmission at 100 Gbps with sub-band optical switching*. *Journal of Lightwave Technology*, 2014. **32**(12): p. 2202-2219.
105. Thouénon, G., et al. *All-Optical vs. Electrical aggregations CAPEX comparisons in a fully-flexible multi-layer transport network*. in *Optical Communication (ECOC), 2015 European Conference on*. 2015. IEEE.
106. Thouénon, G., et al. *Electrical v/s optical aggregation in multi-layer optical transport networks*. in *Photonics in Switching (PS), 2015 International Conference on*. 2015. IEEE.
107. Dischler, R., F. Buchali, and A. Klekamp. *Demonstration of bit rate variable ROADM functionality on an optical OFDM superchannel*. in *Optical Fiber Communication Conference*. 2010. Optical Society of America.
108. Chen, Y., et al. *Experimental demonstration of subband switching functionality on optical OFDM superchannel*. in *Optical Fiber Communication Conference*. 2012. Optical Society of America.
109. Yang, M., W.E. Ryan, and Y. Li, *Design of efficiently encodable moderate-length high-rate irregular LDPC codes*. *Communications, IEEE Transactions on*, 2004. **52**(4): p. 564-571.
110. Mikkelsen, B., *Challenges and key technologies for coherent metro 100G transceivers*. *Lightwave Magazine*, 2012: p. 14-18.
111. *Characteristics of a single-mode optical fiber and cable*. Ed. 11/2009, ITU-T G.652 recommendation.
112. *Characteristics of a bending-loss insensitive single-mode optical fiber and cable for the access network*. Ed. 10/2012, ITU-T G.657 recommendation.
113. *Alcatel-Lucent 1830 PSS brochure*, www.alcatel-lucent.com; *Ciena 6500 Packet Optical Platform brochure*, www.ciena.com; *Huawei OSN 9800 brochure*, www.huawei.com.
114. Doerr, C.R. *Photonic integrated circuits for high-speed communications*. in *Conference on Lasers and Electro-Optics*. 2010. Optical Society of America.
115. *Multi-source agreement for 100G long-haul DWDM transmission module*. 2010, OIF recommendation.
116. *Corning SMF-28e+® Optical Fibre brochure*, www.corning.com.
117. *Corning LEAF® Optical Fibre brochure*, www.corning.com.
118. Bertran-Pardo, O., et al. *Experimental assessment of transmission reach for uncompensated 32-GBaud PDM-QPSK and PDM-16QAM*. in *Optical Fiber Communication Conference*. 2012. Optical Society of America.
119. Xia, T.J., et al. *Transmission of 400G PM-16QAM channels over long-haul distance with commercial all-distributed Raman amplification system and aged standard SMF in field*. in *Opt. Fiber Commun. Conf., San Francisco, CA, USA*. 2014.
120. Lefevre, H., *Rectangular response optical filter for partitioning a limited spectral interval*. 2004, Google Patents.
121. Rudnick, R., et al. *Sub-banded/single-sub-carrier drop-demux and flexible spectral shaping with a fine resolution photonic processor*. in *Optical Communication (ECOC), 2014 European Conference on*. 2014. IEEE.

122. Goldshtein, N., et al., *Fine Resolution Photonic Spectral Processor Using a Waveguide Grating Router with Permanent Phase Trimming*. *Lightwave Technology, Journal of*, 2016. **34**(2): p. 379-385.

PUBLICATIONS

Presented in chapter 3:

- [1] Song, M., Pincemin, E., Grot, D., Guillosoy, T., Jaouën, Y., & Le Bidan, R. (2014, July). Robustness of coherent 100 Gbps QPSK and 200 Gbps 16QAM-OFDM to practical implementation impairments. In *Signal Processing in Photonic Communications* (pp. SM3E-5). Optical Society of America.
- [2] Song, M., Pincemin, E., Grot, D., Guillosoy, T., Jaouen, Y., & Le Bidan, R. (2014, October). Robustesse des modulations QPSK-OFDM à 100 Gbps et 16QAM-OFDM à 200 Gbps aux imperfections d'implémentation pratique et de transmission. In *JNOG 2014: 34èmes Journées Nationales d'Optique Guidée*.
- [3] Song, M., Pincemin, E., Grot, D., Guillosoy, T., Jaouën, Y., & Le Bidan, R. (2015, July). Coherent 100/200 Gbps QPSK/16QAM-OFDM transmission over 1000 km of G. 652 or G. 655 fibre. In *2015 17th International Conference on Transparent Optical Networks (ICTON)* (pp. 1-5). IEEE.
- [4] Song, M., Pincemin, E., Vgenopoulou, V., Roudas, I., Amhoud, E. M., & Jaouën, Y. (2015, September). Transmission performances of 400 Gbps coherent 16-QAM multi-band OFDM adopting nonlinear mitigation techniques. In *Digital Communications (TIWDC), 2015 Tyrrhenian International Workshop on* (pp. 46-48). IEEE.
- [5] Pincemin, E., Song, M., Loussouarn, Y., Thouenon, G., & Betoule, C. (2013, June). Towards 400G/1T flexible optical transport networks. In *2013 15th International Conference on Transparent Optical Networks (ICTON)* (pp. 1-13). IEEE.

Presented in chapter 4:

- [6] Pincemin, E., Song, M., Karaki, J., Poudoulec, A., Nicolas, N., Van Der Keur, M., ... & Froc, G. (2013, September). Multi-band OFDM transmission with sub-band optical switching. In *Optical Communication (ECOC 2013), 39th European Conference and Exhibition on* (pp. 1-3). IET.
- [7] Pincemin, E., Song, M., Karaki, J., Zia-Chahabi, O., Guillosoy, T., Grot, D., ... & Van der Keur, M. (2014). Multi-band OFDM transmission at 100 Gbps with sub-band optical switching. *Journal of Lightwave Technology*, 32(12), 2202-2219.
- [8] Betoule, C., Thouenon, G., Pincemin, E., Song, M., Klondis, D., & Tomkos, I. (2014, July). Impact of optical flexibility and sub-band switching on multi-layer transport network architectures. In *2014 16th International Conference on Transparent Optical Networks (ICTON)* (pp. 1-8). IEEE.

- [9] SONG, M., & PINCEMIN, E. Pre-Distortion of an Optical Signal with Frequency Division Multiplexed Sub-Carriers. *U.S. Patent* No 20,150,318,931, 5 nov. 2015.
- [10] Song, M., Pincemin, E., Josten, A., Baeuerle, B., Hillerkuss, D., Leuthold, J., ... & Thouenon, G. (2016). Flexible Optical Cross-Connects for High Bit Rate Elastic Photonic Transport Networks [Invited]. *Journal of Optical Communications and Networking*, 8(7), A126-A140.

Presented in chapter 5:

- [11] Loussouarn, Y., Song, M., Pincemin, E., Miller, G., Gibbemeyer, A., & Mikkelsen, B. (2015, September). 100 Gbps coherent digital CFP interface for short reach, regional, and ultra long-haul optical communications. In *Optical Communication (ECOC), 2015 European Conference on* (pp. 1-3). IEEE.
- [12] Pincemin, E., Song, M., Loussouarn, Y., Guillosoy, T., Evanno, N., Lissillour, F. (2016, July). Low-cost 100 Gbps Transport Solution based on DCO-CFP and G.657.A2 Fibre for Long-haul WDM Transmission. In *2016 18th International Conference on Transparent Optical Networks (ICTON)*. IEEE.
- [13] Loussouarn, Y., Pincemin, E., Song, M., Gauthier, S., Chen, Y., & Shengqian, Z. (2015, March). 400 Gbps real-time coherent Nyquist-WDM DP-16QAM transmission over legacy G. 652 or G. 655 fibre infrastructure with 2 dB margins. In *Optical Fiber Communication Conference* (pp. W3E-3). Optical Society of America.

Other publications:

- [14] Gavignet, P., Le Rouzic, E., Pincemin, E., Han, B., Song, M., & Sadeghioon, L. (2015, September). Time and spectral optical aggregation for seamless flexible networks. In *Photonics in Switching (PS), 2015 International Conference on* (pp. 43-45). IEEE.
- [15] Song, M., Pincemin, E., Baeuerle, B., Josten, A., Hillerkuss, D., Leuthold, J., & Tomkos, I. (2016, July). Fibre Nonlinearity Limitations of 1 Tbps (10x100 Gbps) Multi-Band e-OFDM Super-Channel. In *Signal Processing in Photonic Communications* (pp. SpW1G-2). Optical Society of America.
- [16] Josten, A., Baeuerle, B., Song, M., Pincemin, E., Hillerkuss, D., & Leuthold, J. (2016, July). Modified Godard Algorithm Applied on a Fractional Oversampled Signal to Correct CD, Polarization, and CFO. In *Signal Processing in Photonic Communications* (pp. SpTu2F-3). Optical Society of America.

INTRODUCTION

Les systèmes de fibres optiques jouent un rôle important dans les réseaux de communication modernes. Les caractéristiques de la fibre optique en font le moyen de transmission le plus adapté pour les communications à débit élevé à longue distance. Depuis son introduction dans les années 1970, la capacité des systèmes de fibre optique a considérablement augmenté grâce à diverses avancées technologiques. L'invention d'EDFA permet une transmission longue distance sans besoin de régénération électrique périodique coûteuse. La grande fenêtre d'amplification d'EDFA permet l'introduction du multiplexage en longueur d'onde (WDM) permettant la transmission de 80 canaux dans une fibre optique et des signaux NRZ-OOK de 10 Gbps dans chaque canal dans les années 1990. L'application d'une détection cohérente dans les systèmes optiques est une autre percée majeure, permettant l'utilisation de formats de modulation multiniveaux, de signaux à multiplexage de polarisation et de traitement du signal numérique. Les systèmes cohérents 100 Gbps DP-QPSK placés sur une infrastructure WDM de grille de 50 GHz ont commencé à être déployés depuis 2012. Ils sont capables d'offrir une portée longue distance de ~ 2000 km et de fournir dix fois la capacité par rapport à 10 Gbps NRZ-OOK.

En raison des fortes croissances de trafic, l'augmentation de la capacité dans les systèmes optiques est toujours requise. Selon l'indice Cisco [1], le trafic IP mondial multipliera presque par trois entre 2015 et 2020. La prochaine génération de systèmes optiques longue distance visera un débit par canal de 400 Gbps ou 1 Tbps ou même plus élevé. L'utilisation de formats de modulation d'ordre supérieure, tels que 16-QAM, est un moyen d'augmenter l'efficacité spectrale, mais au détriment de la portée de la transmission. Pour éviter la régénération électrique coûteuse, la longue portée d'un système de transmission est très importante pour les opérateurs de télécommunications. La performance d'un signal de débit élevé pourrait être améliorée grâce à la mise à niveau de l'infrastructure de fibre optique (telles que les nouvelles fibres optiques et les schémas d'amplification hybrides) ou des techniques de traitement du signal numérique plus puissantes (telles que des algorithmes avancés de correction d'erreur et des techniques de compensation des effets non-linéaires).

Outre les formats de modulation mono-porteuse, l'OFDM (en anglais : coherent orthogonal frequency division multiplexing) a commencé à attirer l'attention depuis l'arrivée de la détection cohérente et la possibilité d'effectuer le traitement du signal numérique dans l'émetteur et le récepteur. Il s'est avéré avoir une performance de transmission équivalente par rapport aux formats mono-porteuse. L'OFDM présente plusieurs caractéristiques intéressantes. Le signal OFDM a un spectre intrinsèquement quasi rectangulaire. Les canaux adjacents peuvent être placés près l'un de l'autre sans générer de diaphonie spectrale sérieuse, ce qui permet une efficacité spectrale élevée. Grâce à l'insertion du préfixe cyclique, le CD et le PMD peuvent être compensés avec une complexité de calcul très faible grâce à un égaliseur de simple étape. L'OFDM permet également une mise en œuvre facile des techniques de codage espace-temps capables de mitiger la perte dépendante de la polarisation (PDL). En outre, le signal OFDM est composé d'un grand nombre de sous-porteuses modulées individuellement. Le chargement de bit et de puissance peut être réalisé sur chaque sous-porteuse en cas de non-homogénéité de performance, par exemple en raison d'un effet de filtrage optique.

En raison de la limitation de la bande passante des composants électriques et optiques, la capacité future de 400 Gbps ou 1 Tbps ne peut plus être portée par un seul canal. "Superchannel", composé d'un certain nombre de sous-canaux à faible débit, devient une approche prometteuse pour faire face à la demande de débit ultra-élevé. La grille fixe de 50 GHz sera remplacée par une granularité de grille flexible. Les futurs super-canaux optiques seront élastiques, capables d'adapter la capacité du super-canal à la variation de la demande de trafic dans le temps. OFDM et Nyquist-WDM sont deux candidats prometteurs pour ce futur réseau optique flexible à haute capacité.

Dans cette thèse, nous avons l'intention d'étudier le potentiel de l'OFDM dans le contexte du réseau optique super-canal et souple. Nous avons d'abord étudié la performance de 400 Gbps et 1 Tbps 16QAM-OFDM dans diverses configurations, et comparé à celui de Nyquist-WDM. Nous avons ensuite réalisé une nouvelle étude de la commutation optique de sous-longueur d'onde grâce à la démonstration expérimentale, offrant un réseau optique plus flexible en exploitant la forme spectrale intrinsèquement rectangulaire de l'OFDM. Nous avons également étudié certains sujets de recherche à court terme qui concernent les opérateurs de télécommunications utilisant des interfaces en temps réel.

Chapitre 1: donne un aperçu des systèmes de transmission optique longue distance. Nous commençons par introduire les principales déficiences physiques de la fibre optique monomode. Nous décrivons ensuite l'évolution des systèmes de transmission WDM actuellement déployés et des technologies au-delà de 100 Gbps.

Chapitre 2: donne un aperçu de la technique OFDM pour les systèmes de transmission optique longue distance. Nous présentons les algorithmes DSP de l'émetteur et du récepteur, le dimensionnement du signal OFDM, les formats OFDM avec des fonctionnalités améliorées, l'état de l'art des expériences de transmission OFDM ainsi que des comparaisons avec des techniques mono-porteuse.

Chapitre 3: étude de la mise en œuvre expérimentale du 16QAM-OFDM. Nous présentons la sensibilité du 16QAM-OFDM à des imperfections matérielles, sa performance dos à dos, sa tolérance au CD et au PMD, ses performances de transmission sur deux types de fibres, la performance des techniques de compensation des effets non-linéaires et les comparaisons expérimentales avec 16QAM-Nyquist-WDM.

Chapitre 4: étudie la faisabilité de la commutation optique de sous-longueur d'onde à l'intérieur d'un super-canal OFDM et Nyquist-WDM. Nous présentons la structure d'insertion et d'extraction de sous-longueur d'onde, l'optimisation des largeurs de bande des filtres optiques et la cascabilité des insertions / extractions optiques de sous-longueur d'onde dans les super-canaux modulés QPSK et 16-QAM.

Chapitre 5: se concentre sur les sujets de recherche à court terme qui concernent les opérateurs de télécommunications. Nous présentons la performance de la CFP cohérente numérique à 100 Gbps basée sur les technologies photoniques sur silicium, la capacité de la fibre optique ITU-T G.657.A2 à répondre à la transmission longue distance et la performance de l'interface temps réel 400 Gbps DP-16QAM cohérente à double porteuses.

CHAPTER 1

SYSTEMES DE TRANSMISSION OPTIQUE LONGUE DISTANCE

Ce chapitre est un aperçu des systèmes de transmission optique longue distance. Nous allons commencer par introduire les principales déficiences physiques de la fibre optique monomode. Nous décrirons ensuite l'évolution des systèmes de transmission longue distance en mettant l'accent sur deux techniques de détection: la détection directe et la détection cohérente. Enfin, nous discuterons au-delà des technologies de 100 Gbps: les formats de modulation haute qualité ainsi que les améliorations du traitement du matériel et du signal.

1.1 Principales déficiences physiques en fibre monomode

Les signaux optiques subissent plusieurs inconvénients lors de la propagation le long de la fibre. Nous allons d'abord décrire les principaux effets linéaires consistant en la perte de fibres, la dispersion chromatique (CD) et la dispersion du mode de polarisation (PMD). Le principal phénomène non linéaire: l'effet Kerr sera également brièvement introduit.

1.1.1 Perte de fibres

Un paramètre fibreux important est la perte de puissance pendant la propagation du signal à l'intérieur de la fibre. La puissance de signal $P(z)$ à la sortie de la fibre peut être exprimée comme

$$P(z) = P(0)\exp(-\alpha z) \quad \text{Eq. 1-1}$$

où $P(0)$ est la puissance du signal à l'entrée de la fibre, z est la longueur de la fibre et α est le coefficient de perte de fibre en néper/m. Le coefficient de perte de fibre est habituellement exprimé en dB/km avec la relation de 1 néper/m = 8686 dB/km.

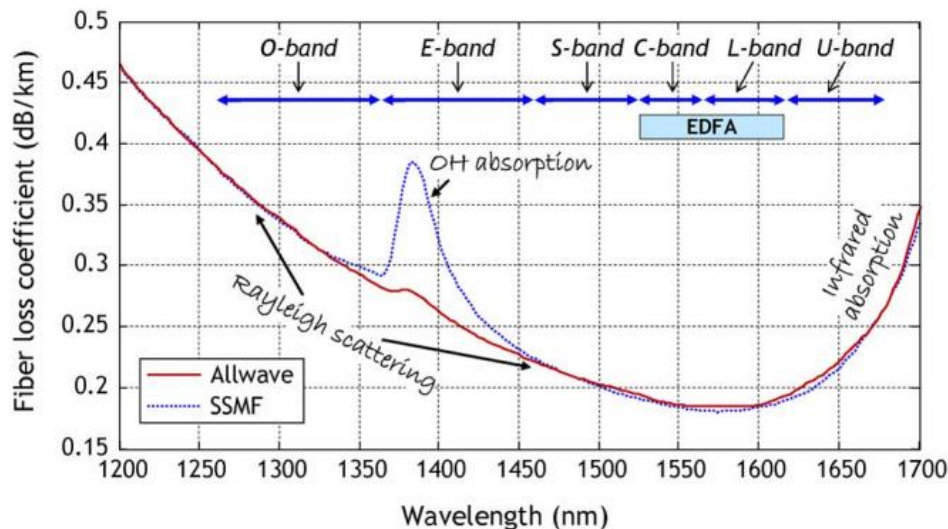


Figure 1-1: Dépendance spectrale du coefficient de perte de fibre pour la fibre monomode standard (SSMF) et une fibre sans le pic d'absorption d'eau (Allwave). [2]

La perte de fibre dépend de la longueur d'onde du signal représentée sur la Fig. 1-1. Les sources principales régissant le profil d'atténuation sont la diffusion Rayleigh et l'absorption du matériau. La diffusion de Rayleigh provient des fluctuations de densité congelées dans la silice fondue pendant la fabrication. Les fluctuations locales résultantes de la lumière de dispersion de l'indice de réfraction dans toutes les directions. Il affecte de courtes longueurs d'ondes plus que longues dans la région infrarouge proche (1200-1715 nm). Outre la diffusion de Rayleigh, l'absorption du verre de silice, forte à longue longueur d'onde de fibre ainsi que

la présence d'impuretés, contribuent également à la perte de fibres. L'absorption OH est responsable du pic à 1380 nm représenté sur la Fig. 1-1 sur SSMF. Le pic OH peut être éliminé dans la fabrication actuelle de fibres.

Les longueurs d'onde avec une perte de fibres modérée (de 1300 à 1700 nm) sont considérées comme utilisables pour la transmission longue distance. Dans les implémentations pratiques, la bande passante utilisable est limitée par la bande passante des technologies d'amplification. Les amplificateurs à fibre dopée à l'Erbium (EDFA) couvrent la bande C et la bande L, qui coïncident avec les zones minimales de longueur d'onde de perte de fibre.

1.1.2 Dispersion chromatique

La dispersion chromatique (CD) représente le fait que différentes couleurs ou longueurs d'ondes se déplacent à des vitesses différentes dans la fibre optique. La dispersion totale est essentiellement la combinaison de dispersion de matériau et de dispersion de guide d'onde. La dispersion du matériau est causée par des variations de l'indice de réfraction du matériau fibreux par rapport à la longueur d'onde. La dispersion Waveguide se réfère à des différences dans la vitesse du signal en fonction de la répartition de la puissance optique sur le noyau et du revêtement de la fibre optique. Lorsque la longueur d'onde du signal optique augmente, un plus grand signal sera porté par la gaine, qui a un indice de réfraction différent par rapport au noyau de fibre.

L'effet de la dispersion des fibres s'explique par l'expansion de la constante de propagation β dans une série de Taylor autour de la fréquence centrale ω_0

$$\beta(\omega) = n(\omega) \frac{\omega}{c} = \beta_0 + \beta_1(\omega - \omega_0) + \frac{1}{2}\beta_2(\omega - \omega_0)^2 + \dots \quad \text{Eq. 1-2}$$

où $n(\omega)$ est l'indice de réfraction et c la vitesse de la lumière sous vide. La constante de propagation β , également appelée constante de phase, représente le changement de phase par unité de longueur le long du chemin parcouru par l'onde à tout instant. Le coefficient β_0 est un déphasage constant et β_1 est l'inverse de la vitesse du groupe ($\beta_1 = 1/V_g$), ou en d'autres termes le délai de groupe par unité de longueur. La deuxième dérivée, β_2 , est responsable de CD et s'appelle le paramètre de dispersion de vitesse de groupe (GVD). Le paramètre le plus couramment utilisé pour indiquer la quantité de dispersion en fibre est le paramètre de dispersion D , défini comme la variation du retard de groupe par unité de longueur avec la longueur d'onde. Il est lié à β_2 par la relation

$$D = \frac{d\beta_1}{d\lambda} = -\frac{2\pi c}{\lambda^2} \beta_2 \quad \text{Eq. 1-3}$$

Figure. 1-2 montre le profil de dispersion le long de la longueur d'onde pour la fibre monomode standard (SSMF) de l'Union internationale des télécommunications (ITU) G.652, qui est la fibre la plus largement déployée pour l'application longue distance, ainsi que le profil de ses deux contributeurs: dispersion des matériaux et dispersion des guides d'ondes. La dispersion zéro tombe sur la longueur d'onde de ~1310 nm. Il a un D de ~17 ps/(nm·km) à la longueur d'onde de 1550 nm.

Le CD provoque un élargissement des impulsions et entraîne une interférence inter-symboles (ISI). Dans les systèmes hérités de 10 Gbps non retournés à zéro (NRZ-OOK) avec détection directe de modulation d'intensité (IM/DD), le CD est géré en insérant une fibre de

compensation de dispersion (DCF) avec un coefficient de dispersion négatif après Chaque portée de fibre. Une autre approche consiste à changer le profil de dispersion de la fibre. La fibre découpée par dispersion (DSF) avec une dispersion nulle à 1550 nm est définie dans l'UIT G.653. La fabrication de DSF peut être réalisée en modifiant l'indice de réfraction du noyau. Cependant, la fibre de dispersion nulle est très sensible à l'effet non linéaire du mélange à quatre ondes (FWM), ce qui rend impossible la transmission WDM. La fibre décalée à dispersion non nulle (NZDSF) définie dans l'ITU G.655 déplace la dispersion zéro à environ 1510 nm, afin d'obtenir à la fois une faible dispersion et des effets non linéaires inférieurs par rapport à DSF. Les quantités de dispersion à 1550nm et d'autres caractéristiques de plusieurs NZDSF sont données dans le tableau 1-1 à la sous-section 1.3.3. Avec l'arrivée d'une détection cohérente, la dispersion chromatique, qui est un effet quasi déterministe, peut être entièrement compensée par le traitement du signal numérique.

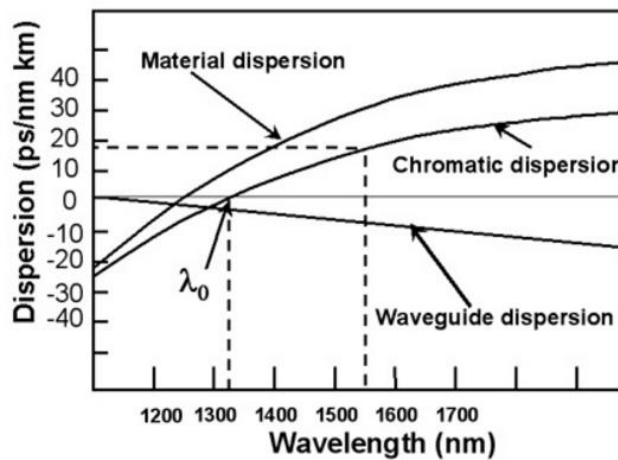


Figure 1-2: Le profil de la dispersion chromatique d'un G.652 SSMF ainsi que ses deux contributeurs: la dispersion des matériaux et la dispersion des guides d'ondes. [3]

1.1.3 Dispersion modale de polarisation

Un rayon de lumière peut être considéré comme composé de deux modes de polarisation orthogonaux. En fibre parfaitement circulaire, les deux états de polarisation possèdent les mêmes caractéristiques de propagation. Cependant, en réalité, les imperfections dans la géométrie du guide d'onde combinées aux contraintes mécaniques et aux variations de température dans le champ entraînent une biréfringence. Dans un milieu biréfringent, les signaux se propageant sur les deux modes de polarisation présentent un indice de réfraction différent, donc se déplacent à une vitesse de groupe différente.

Sur la base de [4], il existe deux états orthogonaux de polarisation (PSP). Lorsqu'un signal optique est aligné avec l'un des PSP, sa polarisation de sortie est invariante au premier ordre avec des changements de fréquence, ce qui signifie que les composantes spectrales du signal de sortie ont tous le même état de polarisation. Les PSP sont également appelés les modes de polarisation rapide et lente. Le mode de polarisation rapide maximise la vitesse du groupe et le ralentit le minimise. La différence de temps de propagation entre deux PSP est appelée différentielle différentielle (DGD).

Les PSP varient aléatoirement le long de la fibre et changent avec le temps, de sorte que le DGD est également aléatoire. Pour les fibres longues, ce qui est le cas pour la transmission longue distance, on constate que les valeurs DGD suivent la distribution maxwellienne [5]

dont la moyenne est proportionnelle à la racine carrée de la longueur de la fibre. Le coefficient de dispersion du mode de polarisation de premier ordre (PMD), habituellement exprimé en $\text{ps}/\sqrt{\text{km}}$, est utilisé pour caractériser la dispersion moyenne d'une fibre donnée. Le PMD typique d'un SSMF G.652 est de $0.1 \text{ ps}/\sqrt{\text{km}}$. L'impact de PMD sur un signal optique dépend à la fois du retard de groupe différentiel et de l'intensité relative de la lumière dans les PSP. L'altération est maximale lorsque des quantités égales de lumière sont couplées dans les deux PSP et l'altération est négligeable lorsque toute la lumière est couplée à une seule PSP.

En plus du PMD de premier ordre, les effets de biréfringence dépendent de la longueur d'onde. Cette fonctionnalité résulte en PMD de second ordre, y compris une dépendance du PMD avec la longueur d'onde appelée dispersion chromatique dépendant de la polarisation et un décalage de PSP avec la longueur d'onde.

1.1.4 Effets non linéaires

La perte de fibre, le CD et le PMD sont des effets linéaires dont l'impact est indépendant de la puissance optique. Outre les effets linéaires, l'indice de réfraction de la fibre change également avec l'intensité de la lumière. Ce phénomène est connu sous le nom d'effet Kerr [6, 7]. L'indice de réfraction n en fonction de la puissance optique à l'intérieur de la fibre est exprimé par

$$n(\omega, P) = n(\omega) + n_2 \cdot I = n(\omega) + n_2 \frac{P}{A_{eff}} \quad \text{Eq. 1-4}$$

où n est la partie linéaire de l'indice de réfraction, n_2 est l'indice de réfraction non linéaire, I est l'intensité optique, P est la puissance optique et A_{eff} est la zone centrale efficace. La valeur de n est d'environ 1,5 et n_2 a des valeurs typiques de $2-3 \cdot 10^{-20} \text{ m}^2/\text{W}$. A_{eff} de G.652 SSMF est autour de $80-100 \mu\text{m}^2$ à 1550 nm selon la conception de la fibre. De l'équation 1-4, on peut en déduire que la puissance optique élevée ou le petit A_{eff} augmentent l'impact Kerr. Le coefficient non linéaire γ est exprimé par

$$\gamma = \frac{n_2 \omega}{c A_{eff}} \quad \text{Eq. 1-5}$$

Dans une bobine de fibre, la puissance optique est importante pour les premiers kilomètres et descend à une faible valeur au bout de la portée. En conséquence, l'effet non linéaire diminue le long de la portée de la fibre. La longueur effective de la fibre, en tenant compte de l'atténuation de la fibre est exprimée comme

$$L_{eff} = \frac{1 - \exp(-\alpha L)}{\alpha} \quad \text{Eq. 1-6}$$

où L est la longueur totale de la fibre et α est le coefficient d'atténuation. Le décalage de phase non linéaire introduit par une fibre de longueur L est donné par

$$\Phi_{NL} = \gamma \cdot L_{eff} \cdot P_0 \quad \text{Eq. 1-7}$$

où P_0 est la puissance de pointe dans la portée.

Dans un système WDM, nous sommes intéressés par l'impact de Kerr sur chaque canal. Pour un canal donné, le changement de phase induit par sa propre variation de puissance est appelé

modulation auto-phase (SPM). L'indice de réfraction dépend également de la variation de puissance d'autres canaux de multiplication et aboutit à un effet de modulation en phase croisée (XPM). Un autre effet inter-canaux est le mélange à quatre ondes (FWM), représenté sous forme de canaux de multiplication interagissant entre eux pour créer des signaux à de nouvelles fréquences. En outre, les PSP d'un canal peuvent être affectés par les PSP d'autres canaux de multiplication. Cet effet est nommé comme modulation de polarisation croisée (XPoIM).

L'altération créée par les effets non linéaires est également liée à la quantité de dispersion des fibres. Les fibres à dispersion élevée ont une meilleure performance non linéaire. Il est démontré que G.652 SSMF ($D = 17$ ps/nm/km) dépasse G.655 LEAF ($D = 4.3$ ps/nm/km) dans des transmissions cohérentes de 40 Gbps et 100 Gbps WDM [8]. Les systèmes cohérents atteignent de meilleures performances par rapport à la ligne de fibre sans DCF par rapport à la ligne de fibre gérée par la dispersion traditionnelle [9].

1.2 Évolution des systèmes de transmission optique longue distance

1.2.1 Systèmes de modulation d'intensité / détection directe

La fibre optique a été introduite dans la première moitié des années 1970. Dans ses premières années, les systèmes de fibre optique ont vu une augmentation de la capacité lisse et la fenêtre de transmission a été graduellement basculée de 800 à 1300 à 1550 nm vers les plus petites longueurs d'onde d'atténuation. Le schéma de modulation était la modulation d'intensité / détection directe (IM/DD). À l'émetteur, l'information est codée sur l'amplitude du signal; Au récepteur, la décision est prise en fonction de l'intensité du signal au moyen d'un photo-détecteur. Le non-retour-à-zéro on-off-keying (NRZ-OOK) est le format de modulation IM/DD le plus utilisé.

L'invention des amplificateurs à fibre dopée à l'Erbium (EDFA) à la fin des années 1980 est une excellente percée pour les communications optiques à longue distance. Il permet d'amplifier périodiquement le signal atténué, évitant ainsi la régénération électrique coûteuse. EDFA présente une grande fenêtre d'amplification qui coïncide avec la faible fenêtre d'atténuation de la fibre optique. Des canaux multiples à différentes longueurs d'onde peuvent être amplifiés simultanément par EDFA unique, permettant l'introduction du multiplexage par répartition en longueur d'onde (WDM).

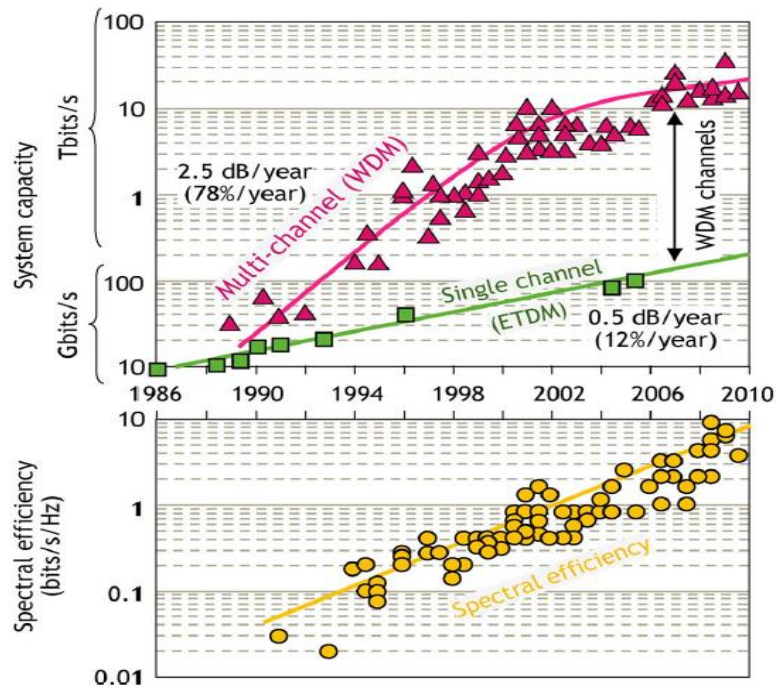


Figure 1-3: Capacités démontrées du système (carrés verts: systèmes monocanal, triangles rouges: systèmes WDM) et des évolutions de l'efficacité spectrale. [2]

2,5 Gbps NRZ-OOK a été le premier format déployé dans les systèmes WDM constitués de 40 canaux. La portée de la transmission était de 800 km sur G.652 SSMF. Une augmentation supplémentaire du débit de données a été limitée par le CD accumulé. La déficience générée par CD est proportionnelle au carré de débit en bauds. Le taux de données augmente de 2,5 Gb à 10 Gbit / s a été rendu possible grâce au déploiement de la fibre de compensation de dispersion (DCF) et à l'utilisation de codes de correction d'erreur directe (FEC). 10 Gbps NRZ-OOK déployé dans les systèmes WDM de 80 canaux offre un débit de données de ~ 1 Tbps par fibre. Fig. 1-3 montre les capacités de système démontrées des systèmes monocanal et WDM, ainsi que l'évolution de l'efficacité spectrale de 1986 à 2010.

1.2.2 Systèmes de détection cohérente

Les communications cohérentes ont d'abord été introduites par DeLange en 1970 [10] et ont beaucoup étudié dans les années 1980 en raison de leur plus grande sensibilité du récepteur (10-15 dB) par rapport aux schémas de détection directe. Cependant, leur développement a été interrompu pendant près de 20 ans, en raison du déploiement des systèmes EDFA et WDM qui ont fait de la IM/DD le format simple et parfait pour atteindre les longs trajets et faire face à la demande de trafic. Dans les années 2000, la charge de trafic a continué d'augmenter, de sorte que la capacité par fibre devait suivre. Le nombre de canaux dans les systèmes WDM est limité par la bande passante d'amplification d'EDFA. L'approche la plus simple serait d'augmenter le débit par canal des systèmes IM/DD.

L'augmentation de capacité de 10 Gbps NRZ-OOK à 40 Gbps NRZ-OOK a fait face à plusieurs défis: d'une part, 40 Gbps nécessitent 6 dB d'extra-OSNR par rapport à 10 Gbps afin d'obtenir le même taux d'erreur de bits. En d'autres termes, sur le même lien de fibre, la portée de la transmission de 40 Gbps est environ quatre fois plus courte que celle de 10 Gbps. En outre, les fibres existantes présentent des valeurs élevées de PMD. La sensibilité à la déficience PMD est proportionnelle au débit en bauds. Alors que le récepteur de 10 Gbps a

une tolérance PMD de 10 ps ce qui correspond à 10% de la durée du symbole, la tolérance du récepteur de 40 Gbps est de seulement 2,5 ps. En outre, le canal NRZ-OOK de 40 Gbps occupe une gamme spectrale de plus de 50 GHz, ce qui le rend pas conforme au système WDM de grille 50 GHz à 80 canaux, en particulier avec les multiplexeurs optiques configurables à la grille 50 GHz (ROADM) Déployé dans le réseau.

Face aux difficultés de 40 Gbps NRZ-OOK et à la disponibilité d'ADC à grande vitesse, une détection cohérente a retrouvé l'attention. Les systèmes cohérents en temps réel en phase en quadrature à double polarisation de 40 Gbps (DP-QPSK) ont d'abord été démontrés par Nortel en 2008 [11]. La détection cohérente permet d'accéder à l'amplitude et à la phase du signal optique, permettant l'utilisation des formats de modulation avancés avec une efficacité spectrale accrue. La capacité par canal est encore doublée par multiplexage de polarisation. En outre, une détection cohérente rend possible le traitement du signal numérique (DSP), ce qui permet de lutter contre les effets linéaires et non linéaires numériquement. Le CD peut être compensé dans le domaine électrique, en évitant l'utilisation de DCF. Des systèmes DP-QPSK de 100 Gbps, ayant une portée de transmission de ~ 2000 km et conformes à la grille WDM de 50 GHz, sont déployés dans des réseaux long-courriers depuis 2012.

1.3 Technologies au-delà de 100 Gbps

La prochaine génération de systèmes long-courriers aura une capacité par canal supérieure à 100 Gbps. La façon directe d'augmenter la capacité par canal serait l'utilisation de formats de modulation haute qualité. Cependant, leur portée de transmission est largement réduite par rapport à QPSK. L'amélioration de l'infrastructure des fibres et le développement de techniques DSP avancées sont des approches potentielles pour augmenter la portée de la transmission. Les développements récents sur les fibres optiques, les schémas d'amplification optique, les codes de correction d'erreur directe et les techniques d'atténuation non linéaire seront décrits dans cette section.

1.3.1 Formats de modulation d'ordre supérieure

L'augmentation de l'efficacité spectrale (SE), qui consiste à transmettre plus de bits par seconde par hertz, est un moyen direct de faire face à l'augmentation de la demande de trafic. Les systèmes DP-QPSK de 100 Gbps actuellement déployés dans un canal de grille fixe de 50 GHz ont un SE de 2 bits/s/Hz. La modulation QPSK, également appelée 4-QAM, dont le diagramme de constellation est illustré à la figure 1-4, comporte 4 points de constellation et porte 2 bits par symbole. Les formats de modulation d'ordre supérieur permettent de transporter plus de bits par symbole. 8-QAM, 16-QAM, 32-QAM et 64-QAM portent respectivement 3, 4, 5 et 6 bits par symbole. Ils atteignent un SE de 3, 4, 5 et 6 bits/s/Hz, respectivement, si nous adoptons le même taux de symboles que dans les systèmes DP-QPSK de 100 Gbps.

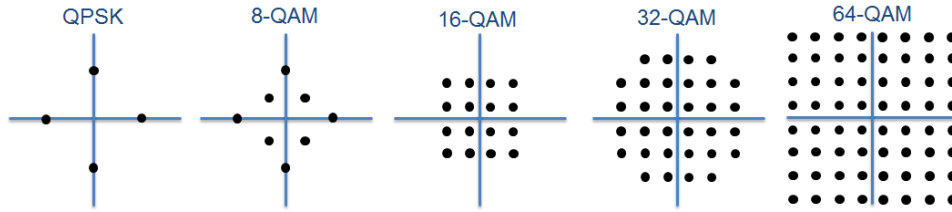


Figure 1-4: Exemples de constellations M-QAM.

L'ordre de modulation croissant permet de rapprocher les points de constellation adjacents, ce qui le rend plus sensible au bruit. Les courbes de fréquence d'erreur de bit (BER) contre le rapport signal sur bruit (SNR) par bit de QPSK, 16-QAM et 64-QAM sont tracées dans la Fig. 1-5a, selon l'expression BER des formats QAM fournis dans [12]. Par exemple, pour obtenir un BER de 10^{-3} , le SNR théorique demandé par QPSK, 16-QAM et 64-QAM est respectivement de ~ 6 dB, ~ 10 dB et ~ 15 dB. Cela signifie que, au même débit, nous devons fournir 4 dB de SNR supplémentaire pour 16-QAM et 9 dB de SNR supplémentaire pour 64-QAM, afin d'obtenir les mêmes performances BER que QPSK.

Nous voudrions également comparer l'exigence SNR de différents formats de modulation au même taux de symboles. Les courbes BER contre SNR par symbole sont tracées dans la Fig. 1-5b. Cette fois, pour obtenir un BER de 10^{-3} , le SNR théorique par symbole requis par QPSK, 16-QAM et 64-QAM est respectivement de ~ 9 dB, ~ 16 dB et ~ 22 dB. Au même taux de symboles, par exemple, les signaux QPSK 100 Gbps, 200 Gbps 16-QAM et 300 Gbps 64-QAM, 16-QAM nécessite 7 dB de SNR supplémentaire et 64-QAM nécessite 13 dB de SNR supplémentaire par rapport à QPSK.

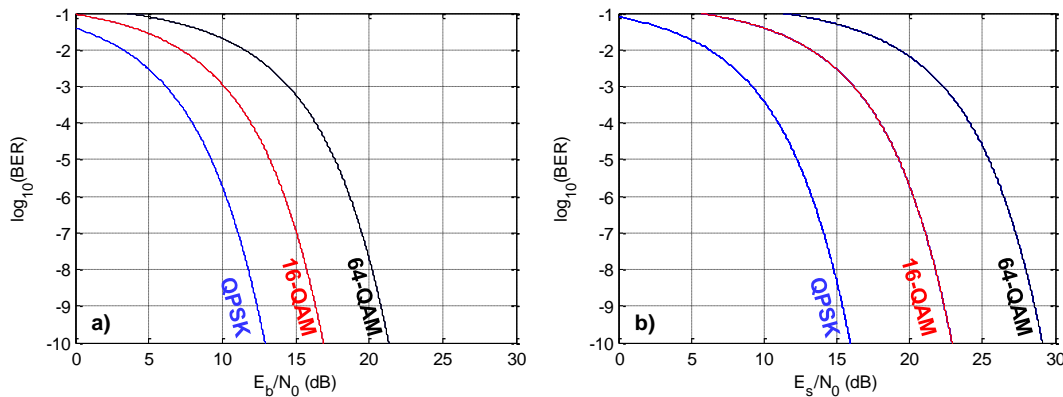


Figure 1-5: a) BER en fonction du SNR par bit; b) BER en fonction du SNR par symbole.

La portée de la transmission des systèmes DP-QPSK actuels de 100 Gbps est d'environ 2000 km, ce qui satisfait les besoins du réseau européen en réseau sans régénération électrique. En l'absence d'effets non linéaires, nécessitant 7 dB de SNR supplémentaire, il faut diviser la portée de transmission d'un facteur 5, ce qui signifie que la portée des systèmes DP-16-QAM de 200 Gbps ne sera que d'environ 400 km. Cette prédiction théorique est vérifiée par divers essais sur le terrain avec des transpondeurs en 16-QAM en temps réel et une infrastructure de fibre héritée (SSMF avec amplification EDFA) [13-15]. En outre, les formats de modulation d'ordre supérieur sont également plus sensibles aux altérations matérielles, telles que le nombre effectif de bits (ENOB) dans les convertisseurs numérique-analogique (DAC) et les

convertisseurs analogique-numérique (ADC), qui seront présentés en Section 3.1 par simulation numérique.

Les formats de modulation en ordre élevé permettent une augmentation de SE mais ont un problème majeur de portée de transmission. Les améliorations apportées à l'infrastructure fibreuse (tels que les schémas d'amplification et les fibres optiques) et les algorithmes de traitement de signal numérique (tels que les codes de correction d'erreur directe et les égaliseurs non linéaires) joueront un rôle important pour pousser la mise en œuvre de formats de modulation haut de gamme dans les réseaux long-courriers.

1.3.2 Systèmes d'amplification

L'amplificateur optique est un élément important dans les systèmes de transmission optique longue distance. EDFA est de loin l'amplificateur optique le plus utilisé. Il peut amplifier efficacement la lumière dans la région de 1550 nm où la perte de fibre est minimale. L'amplification Raman distribuée offre une image de bruit plus faible et une plus grande fenêtre d'amplification. Nous allons présenter brièvement le principe et les caractéristiques des amplificateurs EDFA et Raman.

1.3.2.1 EDFA

Dans un EDFA, l'amplification du signal est réalisée à l'intérieur d'une fibre dopée à l'Erbium mono-mode de quelques mètres de long. Les pompes laser d'environ 980 nm ou 1450 nm excitent les ions erbium (Er^{3+}) dans un niveau d'énergie plus élevé. Le diagramme de niveau d'énergie est représenté sur la Fig. 1-6. L'amplification se produit lorsque les photons entrants stimulent les ions erbium à l'état sortant pour se détendre, tout en libérant des photons ayant la même énergie et la même phase que les photons entrants. Ces photons répéteront le processus, fournissant ainsi un gain au signal. La gamme d'amplification classique d'une EDFA est la bande C (de 1530 nm à 1565 nm). Il peut également être optimisé pour l'amplification du signal en bande L (de 1565 nm à 1625 nm).

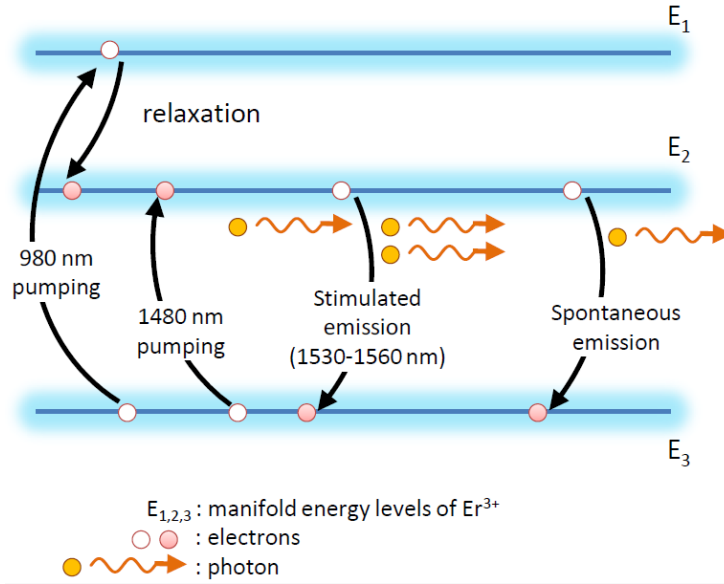


Figure 1-6: Schéma de niveau énergétique d'un EDFA. [16]

En plus des émissions stimulées, quelques-uns des ions Er^{3+} excités se décomposent au niveau du sol par émission spontanée. Dans ce cas, des photons bruyants à phase aléatoire sont émis et amplifiés par la relaxation des ions Er^{3+} . Ce processus s'appelle émission spontanée amplifiée (ASE). Le bruit ASE est généralement considéré comme un bruit Gaussien blanc additif. Il se caractérise par une figure de bruit NF qui est définie comme le rapport entre OSNR d'entrée et de sortie. NF peut également être exprimé en termes de gain G et facteur d'émission spontané (ou facteur d'inversion de la population) n_{sp} [17]

$$NF = 2n_{sp} \frac{(G-1)}{G} \approx 2n_{sp} \quad \text{Eq. 1-8}$$

Au haut G , ce qui est le cas pour une portée de fibre de 50-100 km, la NF peut être estimée à $2n_{sp}$. Un amplificateur parfait avec $n_{sp} = 1$ a une NF de 2, correspondant à 3 dB en unité de décibels. Dans la pratique, les EDFA ont un NF entre 4 et 6 dB.

Une transmission longue distance est composée d'un certain nombre de périodes, chacune suivie d'une EDFA. En conséquence, le bruit ASE est accumulé. En supposant un lien avec des fibres de longueur de portée égale et des amplificateurs avec le même gain et la même figure de bruit, le rapport signal / bruit optique (OSNR) à la sortie de la liaison peut être exprimé comme

$$OSNR = \frac{GP_{in}}{2N_{spans}N_{ASE}B_{ref}} \quad \text{with } N_{ASE} \approx \frac{1}{2}NF \cdot hfG \quad \text{Eq. 1-9}$$

où P_{in} est la puissance du signal à l'entrée de l'EDFA, N_{spans} est le nombre de portées dans le lien, N_{ASE} est la densité spectrale de puissance du bruit ASE dans une polarisation, B_{ref} est la bande passante de référence, h est la constante de Planck et f est La fréquence de la lumière. De l'équation 1-9, l'OSNR en dB peut être écrit comme

$$OSNR_{dB} = P_{in_{dB}} - NF_{dB} - 10 \log_{10}(N_{spans}) - 10 \log_{10}(hfB_{ref}) \quad \text{Eq. 1-10}$$

Nous remarquons que le rapport signal / bruit est positivement lié à la puissance du signal à l'entrée de l'EDFA $P_{in_{dB}}$ et lié négativement à la figure de bruit de l'EDFA NF_{dB} et au nombre de bobines N_{spans} .

1.3.2.2 Amplificateur Raman

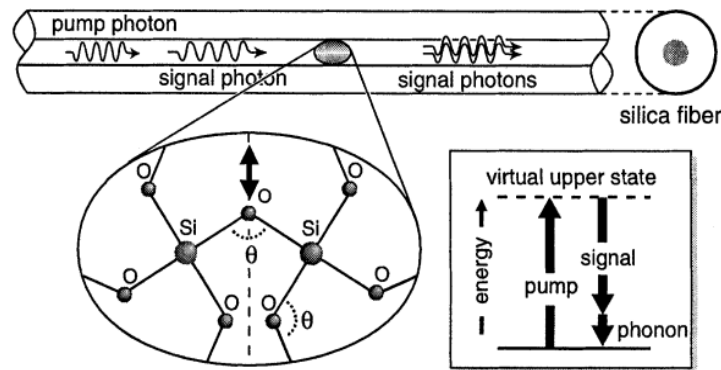


Figure 1-7: Schéma représentant l'amplification par diffusion Raman en fibre optique. L'interaction Raman Stokes entre une pompe, le photon signal et les molécules de silice convertit les pompes en une réplique du photon signal, produisant un phonon optique. [18]

La diffusion spontanée de Raman a d'abord été découverte par Raman [19], pour laquelle il a reçu le prix Nobel de physique en 1930. Les photons optiques sont dispersés inélastiquement par des vibrations moléculaires appelées phonons optiques [18]. La diffusion Raman peut se produire dans tous les matériaux. Dans le verre de silice, il est dominé par le mouvement de flexion de la liaison Si-O-Si (voir l'angle de liaison θ sur la figure 1-7). La diffusion Raman peut être stimulée par le signal lumineux à un changement de fréquence approprié d'une pompe, ce qui entraîne une diffusion Raman stimulée (SRS). Le diagramme de niveau d'énergie est représenté sur la Fig. 1-7. Dans ce processus, un photon de pompe est converti en une réplique exacte du photon de signal, et l'énergie restante produit un phonon optique. Par conséquent, le photon de signal initial est amplifié.

Il existe un certain nombre de configurations différentes dans lesquelles l'amplification Raman peut être utilisée sur une portée de fibre. Les pompes Raman peuvent se multiplier avec le signal (Raman vers l'arrière) et / ou se propager avec le signal (avant Raman). En outre, la puissance de la pompe résiduelle de Raman peut alimenter un amplificateur à pompe optique à distance (ROPA). Un ROPA est généralement une fibre dopée à l'Erbium placée entre 60 et 140 km du nœud de l'équipement et exerce essentiellement la fonction d'une moyenne médiation EDFA [20]. Figure. 1-8 montre différents profils de puissance de signal pour différents schémas d'amplification.

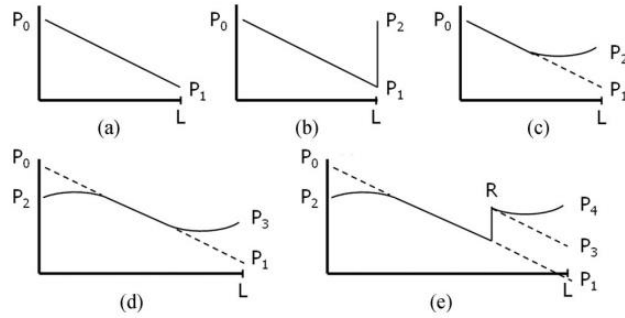


Figure 1-8: Profils de puissance de signal (dBm) pour différents schémas d'amplification d'extension dans une longueur L (km). Les lignes pointillées montrent des profils d'alimentation sans amplification Raman (pas à l'échelle). (A) span, (b) EDFA, (c) Raman vers l'arrière, (d) vers l'avant + Raman vers l'arrière, (e) vers l'avant + Raman + ROPA vers l'arrière. [20]

L'amplification Raman a une flexibilité spectrale, car le gain Raman dépend de la séparation de fréquence entre une pompe et un signal. Tant que la lumière de la pompe avec la longueur d'onde appropriée est disponible, on peut construire des amplificateurs pour toute bande de longueurs d'onde de signal. En combinant plusieurs longueurs d'onde de pompe, les systèmes Raman sont compatibles avec une fenêtre de transmission large bande (jusqu'à 100 nm de large). Un autre avantage de l'amplification de Raman est son faible niveau de bruit. Prenons le cas de Raman en arrière comme exemple, comme le montre la Fig. 1-8c, et supposons que le reste de la perte est équilibré par un EDFA. Cette configuration peut être modélisée en cascade de deux amplificateurs. La figure de bruit total d'une chaîne d'amplificateur en cascade est donnée par [17]

$$NF_{total} = NF_1 + \frac{NF_2 - 1}{G_1} + \frac{NF_3 - 1}{G_1 G_2} + \dots \quad \text{Eq. 1-11}$$

Où NF_i et G_i sont la figure de bruit et gagnent (en unités linéaires) pour le i ème amplificateur dans la chaîne. Si le gain du premier amplificateur (G_1) est suffisamment élevé, la figure de bruit total sera dominée par la figure de bruit du premier amplificateur (NF_1) qui est la figure de bruit du Raman en arrière dans notre cas. Alors que le bruit de l'EDFA pur est toujours supérieur à 3 dB, la figure de bruit total du Raman-EDFA hybride peut être négative dans l'unité de décibels. [20] démontre qu'un OSNR bénéficie d'environ 4,75 dB en utilisant Raman-EDFA hybride par rapport à l'EDFA pur.

Plusieurs effets entraînent des pénalités de transmission lors de l'utilisation de l'amplification Raman. L'une des pénalités provient de l'interférence multi-voies (MPI), qui se produit lorsque le signal lumineux atteint le récepteur par plus d'un chemin optique. Le MPI est principalement causé par la double diffusion Rayleigh (DRS) et peut être traité comme une source de bruit supplémentaire. En pratique, le MPI doit être maintenu au-dessous de -20 dB [20]. Le niveau de MPI est lié à la puissance du signal, ce qui limite le gain Raman de l'amplificateur à environ 25 dB. Le MPI pour Raman gagne moins de 15 dB est assez insignifiant. D'autres inconvénients, tels que le gain dépendant de la polarisation (PDG), le FWM avec les pompes Raman et le transfert de bruit des pompes vers le signal, doivent également être pris en compte lors de la conception des amplificateurs Raman.

Par rapport aux amplificateurs EDFA, Raman ou Raman-EDFA hybrides ont un coût plus élevé et des procédures d'ingénierie plus compliquées, telles que des exigences de sécurité plus strictes en raison des pompes à haute puissance. En retour, il fournit une plus grande

fenêtre d'amplification et une image de bruit plus faible par rapport à EDFA, ce qui en fait l'un des facteurs potentiels de la transmission longue distance avec un débit ultra-élevé.

1.3.3 Fibres optiques

Le média de transmission: la fibre optique a un impact important sur les performances de transmission dans les systèmes long-courriers. Comme décrit dans la section 1.1, plusieurs paramètres clés (c'est-à-dire perte de fibre, CD, PMD et effets non linéaires) caractérisent la fibre.

- **Coefficient d'atténuation α** : détermine la perte de fibre d'une longueur de portée donnée. Cela affecte directement le $P_{in_{dB}}$ dans l'équation. 1-10, de sorte que l'OSNR du signal reçu.
- **CD**: a été considéré comme un effet indésirable dans les systèmes IM/DD. Nous avons l'intention de concevoir des fibres avec un CD inférieur, afin de réduire la longueur de la fibre de compensation de dispersion. Dans les systèmes cohérents, le CD n'est plus une altération indésirable, car il s'agit d'un processus quasi-déterministe et peut être compensé par le traitement du signal numérique. En outre, la présence de CD réduit les effets non linéaires de la fibre, de sorte que les fibres avec un coefficient de dispersion élevé sont souhaitées.
- **PMD**: était un autre effet indésirable dans les systèmes IM/DD, entraînant une dégradation des performances. Dans les systèmes cohérents, PMD peut être compensé dans le processus de démultiplexage de polarisation dans le récepteur.
- **Surface effective**: a été définie dans le but de calculer des effets non linéaires qui dépendent de la densité de puissance de la lumière injectée dans la fibre. Plus la zone effective est grande, plus la densité de puissance est faible et donc l'impact des effets non linéaires.

Différents types de fibres ont été conçus pour obtenir le meilleur rendement dans différents cas d'utilisation. L'ITU a développé un certain nombre de normes pour classer différents types de fibres, parmi lesquelles G.652, G.655 et G.654 sont les plus étudiés et déployés pour les systèmes long-courriers. G.652 représente la fibre monomode standard (SSMF) avec un α de $\sim 0,2$ dB/km et une dispersion de $\sim 16-18$ ps/(nm.km) à 1550 nm. G.655 représente une fibre décalée à dispersion nulle (NZDSF) avec un α de $\sim 0,2$ dB/km et une dispersion de $\sim 4-10$ ps/(nm.km). G.654 désigne la fibre décalée avec une grande surface efficace, de sorte que des effets non linéaires faibles. Initialement conçu pour les systèmes de transmission sous-marine pour atteindre une distance ultra-longue distance. Le tableau 1-1 montre les paramètres clés de certaines fibres industrielles conçues dans les normes G.652, G.655 et G.654 ITU.

Table 1-1: Principaux paramètres de certaines fibres industrielles

Product	ITU standard	α @1550 nm (dB/km)	CD @1550 nm (ps/nm/km)	PMD (ps/km ^{1/2})	Effective area @1550 nm (μm^2)
Corning SMF-28e+	G.652	≤ 0.20	≤ 18.0	≤ 0.06	85
Corning LEAF	G.655	≤ 0.19	4.5-6.0	≤ 0.04	72
Draka TeraLight	G.655	≤ 0.22	5.5-10	≤ 0.04	63
TrueWave REACH	G.655	≤ 0.20	5.5-8.9	≤ 0.04	55
Draka LongLine	G.654	≤ 0.19	≤ 23	≤ 0.04	120
Corning Vascade EX2000	G.654	0.160	20.2	≤ 0.05	112
Corning Vascade EX3000	G.654	0.158	20.8	≤ 0.05	150

La plupart des fibres actuellement déployées dans les systèmes terrestres long-courriers sont des fibres G.652 et G.655 avec un α de $\sim 0,2$ dB/km et une surface efficace inférieure à $85 \mu\text{m}^2$. Il est possible d'améliorer l'OSNR ainsi que la performance non linéaire en adoptant une perte ultra-basse, un grand CD et de grandes fibres efficaces. Cependant, il convient de noter que l'évolution de l'infrastructure des fibres exige d'énormes investissements pour les opérateurs. En conséquence, cette option ne sera considérée que si toutes les autres solutions moins coûteuses ont été mises en œuvre.

1.3.4 Solutions FEC avancées

Le code correcteur d'erreur (FEC) est basé sur l'ajout d'informations redondantes à la séquence de bits d'information. Après la transmission sur un canal bruyant tel que la fibre optique, un système de décodage tente d'exploiter les informations redondantes pour la récupération complète de la séquence de bits source. FEC est un élément essentiel de la transmission optique de débit à haut débit d'aujourd'hui. Une transmission "sans erreur" nécessite un BER post-FEC jusqu'à 10^{-12} ou 10^{-15} .

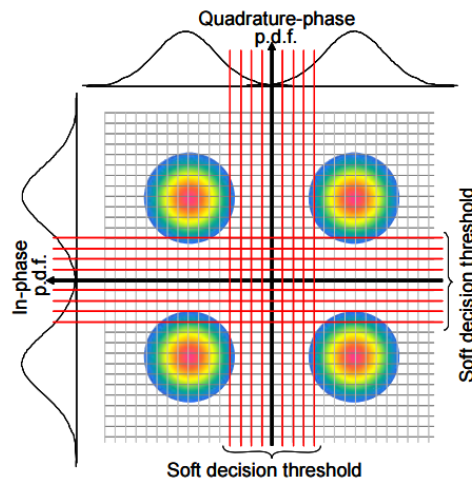


Figure 1-9: Exemple de décision souple à 3 bits pour le signal QPSK. [21]

Le décodage FEC peut être réalisé avec deux systèmes de décision: décision dure (HD) et décision souple (SD). Un HD-FEC fonctionne avec la séquence de données sortant de la démodulation (dégagement de symboles) composé uniquement de "1" et "0". Une décision souple ne donne pas seulement la décision conventionnelle «1» contre «0», mais indique également à quel point nous sommes certains de la décision. Une structure typique de décision souple d'une modulation QPSK est représentée sur la Fig. 1-9. Les seuils de décision 2^N-1 sont placés entre les points de constellation. Dans le cas de $N = 3$, le bit démodulé sera

représenté par un vecteur binaire allant de [000] à [111]. Le bit le plus à gauche correspond à la décision difficile, et les deux autres bits sont des chiffres d'information indiquant la probabilité de '1' ou '0'. Le gain de codage net théorique (NCG) de HD et SD-FEC en fonction des frais généraux est tracé avec des lignes noires et rouges dans la Fig. 1-10. La limite théorique de SD-FEC est inférieure de 2 dB par rapport à HD-FEC.

L'évolution des FEC dans les systèmes de communication optique est habituellement classée en trois générations. La première génération utilise des codes de décision difficiles classiques. Le plus représentatif est le code Reed-Solomon (255,239) normalisé par l'ITU-T G.709, qui a une surcharge de ~7% et un NCG à BER = 10^{-12} de ~ 6 dB. Les systèmes FEC de la deuxième génération sont basés sur le code de produit concaténé, ce qui signifie que le flux de bits est d'abord codé par un code algébrique simple et que plusieurs de ces mots de code sont entrelacés; Après le partitionnement, la sortie de l'entrelaceur est à nouveau codée par un simple code algébrique [22]. Les FEC de la deuxième génération, représentés par les schémas FEC normalisés par l'ITU-T G.975.1, possèdent généralement un NCG de 7 à 9 dB. Avec l'utilisation de la détection cohérente et des ADC haute résolution, la FEC de troisième génération: SD-FEC devient un moyen attractif pour augmenter le NCG. Deux types de codes SD-FEC sont les plus largement implémentés: codes à faible densité (LDPC) et codes de produits turbo (TPC). À 20% de frais généraux, le NCG atteint ~ 11 dB. Figure. 1-10 montre le NCG de G.975.1 FEC et certains FEC avancés récemment publiés.

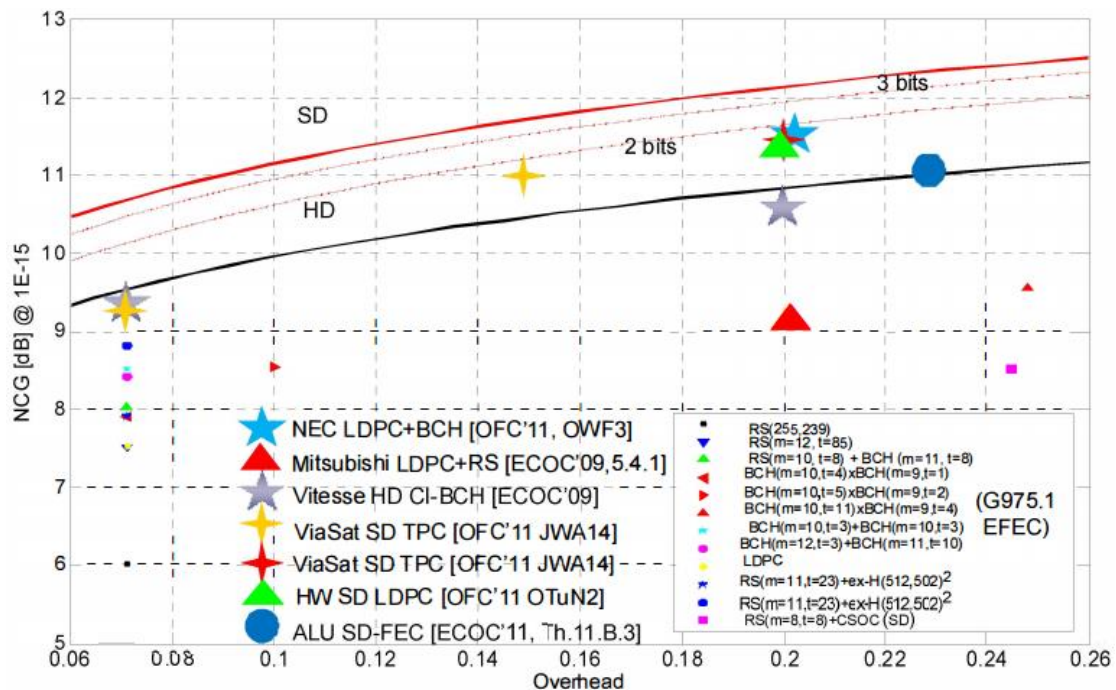


Figure 1-10: NCG théorique de HD-FEC et SD-FEC pour le canal de bruit Gaussien blanc additif (AWGN) ainsi que le NCG de G.975.1 FECs et FEC avancés récemment publiés. [23]

FEC puissant est l'un des facilitateurs du débit binaire ultra-élevé dans les systèmes long-courriers. La performance de nouveaux codes FEC approche la limite de Shannon. Une approche pour augmenter encore le NCG est de créer des FEC avec des frais généraux plus élevés, mais au détriment du débit de données. Certains autres axes de recherche, tels que le décodage optimal vers un canal non linéaire non AWGN, et le codage et la modulation des articulations, peuvent aider les futurs FEC à fournir plus de gain de codage.

1.3.5 Egaliseurs non linéaires

La performance de transmission par rapport à la fibre optique est limitée par le rapport signal à bruit à faible puissance de lancement et limitée par les effets non linéaires de fibre à haute puissance. Des égalisations numériques non linéaires sont développées pour atténuer les non-linéarités des fibres intra-canaux. La rétro-propagation numérique (DBP) réalisée par la méthode Fourier (SSF) en deux étapes [24, 25] est la plus étudiée et généralement considérée comme référence de référence des algorithmes de compensation non linéaire. Récemment, l'égaliseur non linéaire inversé de série de Volterra d'ordre 3 (IVSTF-NLE) [26, 27] a attiré l'attention en raison de sa structure parallèle, permettant une compensation linéaire et non linéaire simultanée. Le principe de DBP-SSF et IVSTF-NLE sera détaillé dans cette sous-section.

1.3.5.1 Rétro-propagation numérique

La propagation du signal dans la fibre optique peut être décrite par l'équation non linéaire de Schrödinger (NLSE)

$$\frac{\partial E}{\partial z} - j \frac{\beta_2}{2} \frac{\partial^2 E}{\partial t^2} + \frac{\alpha}{2} E = -j\gamma |E|^2 E \quad \text{Eq. 1-12}$$

où $E = E(t, z)$ est l'enveloppe de champ électrique du signal optique, β_2 est le paramètre de dispersion du second ordre, α est le coefficient d'atténuation des fibres, et γ est le coefficient non linéaire de la fibre. Le NLSE peut être résolu numériquement à l'aide de la méthode SSF d'une manière asymétrique non opérationnelle, où la fibre est modélisée en concaténation de sections linéaires et non linéaires, comme représenté sur la Fig. 1-11. h correspond à la taille de l'étape de la méthode SSF. La précision du modèle s'améliore lorsque la taille de l'étape diminue. La puissance du signal est la plus forte à l'entrée de la section des fibres, de sorte que les non-linéarités des fibres. C'est pourquoi la section non linéaire est généralement modélisée avant la section linéaire. Eq. 1-13 montre la transformation du signal dans la section non linéaire. Cela correspond à une rotation de phase dans le domaine temporel. Eq. 1-14 montre l'effet de l'atténuation des fibres et du CD dans la section linéaire, qui est une rotation de phase dans le domaine de la fréquence. $E_n(w, z + h)$ et $E(w, z + h)$ correspondent aux représentations de domaine fréquentiel de $E_n(t, z + h)$ et $E(t, z + h)$.

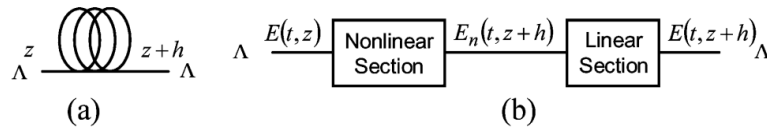


Figure 1-11: (a) Section de la fibre de z à $z + h$; (b) Modèle mathématique. [24]

$$E_n(t, z + h) = E(t, z) \exp(j\gamma h |E(t, z)|^2) \quad \text{Eq. 1-13}$$

$$E(w, z + h) = E_n(w, z + h) \times \exp\left(-\left(\frac{\alpha}{2} + j \frac{\beta_2}{2} \omega^2\right) h\right) \quad \text{Eq. 1-14}$$

Dans le cas de la double polarisation, la propagation du signal le long de la fibre peut être décrite par l'équation de Manakov avec $\gamma' = \frac{8}{9}\gamma$:

$$\frac{\partial E_{x/y}}{\partial z} - j \frac{\beta_2}{2} \frac{\partial^2 E_{x/y}}{\partial t^2} + \frac{\alpha}{2} E_{x/y} = -j\gamma' (|E_x|^2 + |E_y|^2) E_{x/y} \quad \text{Eq. 1-15}$$

Les signaux de sortie des sections non linéaire et linéaire deviennent:

$$E_{n,x/y}(t, z + h) = E_{x/y}(t, z) \exp(j\gamma' h (|E_x(t, z)|^2 + |E_y(t, z)|^2)) \quad \text{Eq. 1-16}$$

$$E_{x/y}(w, z + h) = E_{n,x/y}(w, z + h) \times \exp\left(-\left(\frac{\alpha}{2} + j\frac{\beta_2}{2}\omega^2\right)h\right) \quad \text{Eq. 1-17}$$

La rétroprojection numérique utilisant la méthode SSF consiste à effectuer numériquement l'opération inverse pour estimer le signal transmis, de sorte que:

$$E'_{n,x/y}(w, z + h) = E_{x/y}(w, z + h) \times \exp\left(\left(\frac{\alpha}{2} + j\frac{\beta_2}{2}\omega^2\right)h\right) \quad \text{Eq. 1-18}$$

$$E'_{x/y}(t, z) = E'_{n,x/y}(t, z + h) \exp(-j\varepsilon\gamma' L_{eff} (|E'_{n,x}(t, z)|^2 + |E'_{n,y}(t, z)|^2)) \quad \text{Eq. 1-19}$$

où $E'_{n,x/y}(t, z + h)$ et $E'_{x/y}(t, z)$ sont les signaux intermédiaires et transmis estimés d'une étape donnée. L_{eff} représente la longueur effective de l'étape qui équivaut à $\frac{1 - \exp(-\alpha h)}{\alpha}$. Un paramètre empirique ε ($0 < \varepsilon < 1$) est généralement appliqué pour des performances BER optimales.

La DBP nécessite généralement de petites étapes de compensation, ce qui signifie plusieurs étapes par portée pour obtenir de bonnes performances de péréquation, ce qui entraîne une complexité de calcul élevée. Plusieurs études ont été réalisées pour simplifier l'implémentation matérielle de la DBP [28-31].

1.3.5.2 Egaliseur Volterra d'ordre 3

La solution du NLSE peut être écrite avec des noyaux VSTF allant jusqu'à un troisième ordre comme [27]:

$$E(\omega, z) = H_1(\omega, z)E(\omega) + \int_{-\infty}^{\infty} \int_{-\infty}^{\infty} H_3(\omega_1, \omega_2, \omega - \omega_1 + \omega_2, z) \times E(\omega_1)E^*(\omega_2)E(\omega - \omega_1 + \omega_2)d\omega_1d\omega_2 \quad \text{Eq. 1-20}$$

$$H_1(\omega, z) = \exp(-\alpha z/2) \exp(-j\omega^2\beta_2 z/2) \quad \text{Eq. 1-21}$$

$$H_3(\omega_1, \omega_2, \omega - \omega_1 + \omega_2, z) = -\frac{j\gamma}{4\pi^2} H_1(\omega, z) \times \frac{1 - \exp(-[\alpha + j\beta_2(\omega_1 - \omega)(\omega_1 - \omega_2)]z)}{\alpha + j\beta_2(\omega_1 - \omega)(\omega_1 - \omega_2)} \quad \text{Eq. 1-22}$$

où $E(\omega) = E(\omega, 0)$ est le signal optique dans le domaine fréquentiel à l'entrée de la fibre, $H_1(\omega, z)$ et $H_3(\omega_1, \omega_2, \omega - \omega_1 + \omega_2, z)$ sont les noyaux Volterra premier et troisième, respectivement. Un IVSTF-NLE de troisième ordre calcule l'inverse de $H_3(\omega_1, \omega_2, \omega - \omega_1 + \omega_2, z)$ en tant que compensateur non linéaire.

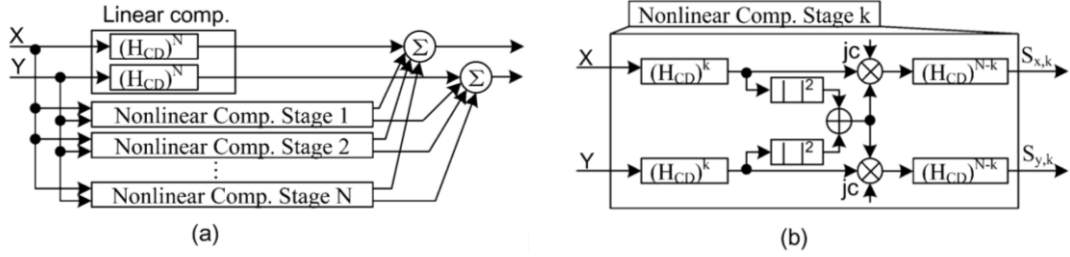


Figure 1-12: Réalisation de la troisième ordre IVSTF-NLE pour double polarisation. (A) Schéma de principe du régime de compensation global. (B) réalisation détaillée de l'étape de compensation non linéaire k . [26]

Figure. 1-12a montre le schéma de principe d'un troisième ordre IVSTF-NLE à double polarisation proposé dans [26]. L'égaliseur considère une liaison de fibre N-span amplifiée optiquement sans compensation de dispersion en ligne. Une simplification dans la formule de l'inverse du troisième ordre est obtenue en ignorant la distorsion de la forme d'onde dans une portée. La compensation est composée d'une partie linéaire et d'une partie non linéaire fonctionnant en parallèle. La partie linéaire compense la dispersion chromatique. La partie non linéaire contient N étapes, où N est le nombre de travées.

La réalisation détaillée de l'étape de compensation non linéaire k est représentée sur la Fig. 1-12b. $H_{CD} = \exp\left(\frac{j\omega^2\beta_2L}{2}\right)$ compense le CD de chaque portée, où L désigne la longueur de la portée. c est une constante dont la valeur théorique est égale à γL_{eff} . Dans la mise en œuvre pratique sur le test de test expérimental, la valeur optimale de c est généralement différente de sa valeur théorique et doit être optimisée pour chaque configuration. Dans la k ème étape de compensation non linéaire, nous récupérons d'abord l'effet de dispersion de k spans en appliquant $(H_{CD})^k$, puis calculons les non-linéarités à travers $jc(| \cdot |^2_x + | \cdot |^2_y)(\cdot)_x$ et $jc(| \cdot |^2_x + | \cdot |^2_y)(\cdot)_y$, où le signal est multiplié par une constante jc et par la puissance totale Des deux polarisations. Enfin, nous supprimons la dispersion résiduelle en appliquant $(H_{CD})^{N-k}$.

L'étape de compensation linéaire et chaque étape de la compensation non linéaire sont des réalisations respectives de:

$$K_1(\omega) = H_1^{-1}(\omega) = \exp\left(\frac{j\omega^2\beta_2NL}{2}\right) \quad \text{Eq. 1-23}$$

$$K_{3,k}(\omega_1, \omega_2, \omega - \omega_1 + \omega_2) \approx \frac{j\gamma'}{4\pi^2} \times \frac{1 - \exp(-\alpha L)}{\alpha} \times K_1(\omega) \exp(jk\beta_2L\Delta\Omega) \quad \text{Eq. 1-24}$$

où K_p désigne l'ordre p th inverse d'un système non linéaire donné H , γ' assume la valeur de $\frac{8}{9}\gamma$ présent dans l'équation de Manakov pour la double polarisation et $\Delta\Omega = (\omega_1 - \omega)(\omega_1 - \omega_2)$.

Les égaliseurs non linéaires améliorent considérablement la portée de la transmission du signal à débit élevé, en particulier dans la configuration à un seul canal. [28] démontre une amélioration de la portée de 68% et 43% sur les systèmes DP-16QAM de 112 Gbps en appliquant DBP de 4 étapes par bobine et 0,2 étape par bobine, respectivement. La péréquation non linéaire est l'un des facteurs potentiels de mise en œuvre du format de modulation de grande taille dans les systèmes long-courriers. Cependant, sa complexité informatique est encore une barrière empêchant sa mise en œuvre en temps réel. En outre, la bande passante des ADC développés actuellement ne permet que la détection d'un seul canal,

ce qui rend incapable pour le récepteur DSP d'avoir la connaissance des canaux adjacents. En conséquence, SPM est le seul effet non linéaire atténué. Dans les systèmes WDM avec un grand nombre de canaux de multiplication, la performance des égaliseurs non linéaires intracanaux est très limitée. Peu d'expériences ont comparé leurs performances dans une seule chaîne et des configurations WDM. Dans la section 3.4, nous allons étudier la performance de DBP-SSF et IVSTF-NLE sur le signal OFDM de 400 Gbps et comparer leurs performances dans trois scénarios avec différentes quantités de non-linéarités inter-canaux.

1.4 Conclusion

Dans ce chapitre, nous avons présenté des déficiences physiques principales en fibre optique monomode, y compris la perte de fibre, la dispersion chromatique, la dispersion du mode polarisation et l'effet Kerr. Nous avons ensuite fourni une brève description de l'évolution des systèmes de transmission optique longue distance. WDM a été la première percée majeure permise par l'invention d'EDFA. L'évolution de 10 Gbps à 40 Gbps avec une approche IM/DD a rencontré plusieurs difficultés techniques, favorisant le renouveau de la détection cohérente. Des systèmes DP-QPSK cohérents à 100 Gbps sont actuellement en déploiement massif. La génération suivante au-delà des systèmes long-courriers de 100 Gbit / s utilisera des formats de modulation haute qualité pour fournir une efficacité spectrale élevée. Leur portée de transmission devient la principale barrière. La transmission longue distance avec des formats de modulation haut de gamme peut être activée par une infrastructure fibreuse ou des améliorations DSP, telles que la fibre de grande surface efficace à grande perte, les nouveaux schémas d'amplification, les codes avancés de correction des erreurs avancées et les techniques d'atténuation non linéaire. Dans le chapitre suivant, nous donnerons un aperçu de la technique OFDM pour les systèmes de transmission optique WDM.